

Growth Simulations of InAs/GaAs Quantum-Dots

vorgelegt von
Diplom-Physiker
Thomas Hammerschmidt

der Fakultät II-Mathematik und Naturwissenschaften
der Technischen Universität Berlin
zur Erlangung des akademischen Grades
DOCTOR RERUM NATURALIUM

genehmigte Dissertation

Promotionsausschuss:

Vorsitzender: Prof. Dr. Mario Dähne

Berichter: Prof. Dr. Eckehard Schöll

Berichter: Prof. Dr. Matthias Scheffler

Tag der wissenschaftlichen Aussprache: 10.7.2006

Berlin 2006

D 83

Abstract

Semiconductor nanostructures, and particularly quantum dots (QDs), have promising potential for technical applications such as light-emitting diodes, lasers, new devices, and quantum computers. But the big number of QDs needed, less than billions are hardly useful, is far beyond the means of normal manufacturing methods. For this nanotechnology to prevail, the QDs have to build themselves by self-assembly and self-organization. In this work, we study the growth of InAs QDs on GaAs substrates.

For this purpose we developed a many-body potential of the Abell-Tersoff type that is able to account for the energetic balance of strain relief and QD side-facet formation during QD growth. It simultaneously captures many microscopic quantities of In, Ga, As, GaAs, and InAs bulk phases, as well as GaAs and InAs surface structures as obtained from experiment and density-functional theory (DFT) calculations with good overall accuracy. Its predictions for biaxial strained GaAs and InAs are in good agreement with DFT calculations and analytic results of continuum-elasticity theory.

Based on recent STM results, we set up detailed atomic structures of InAs QDs with In-As wetting layers and homogenous InAs films on GaAs, relax them with our potential, and compare the resulting total energies. We show that the lateral elastic interaction of ‘hut’-like QDs dominated by $\{317\}$ facets is significantly larger than that of ‘dome’-like QDs dominated by $\{101\}$ facets. A strain-tensor analysis suggests that this effect is due to the relative orientations of the QD side facets to the elastic principal axes. Our calculated onset of the Stranski-Krastanov growth mode with respect to the InAs coverage is in good agreement with experimentally deduced values. The critical nucleus for QD formation is approximately 70 In atoms in size and poses an energy barrier of 5.3 eV. Furthermore, we can explain the experimentally observed shape sequence of ‘hut’-like QDs and ‘dome’-like QDs through the finding of distinct stability regimes. The regime separation depends strongly on the chemical potentials and the QD density. The experimental finding of vertical growth correlation in QD stacks can be explained by a distinct minimum in the potential-energy-surface (PES) of free-standing QDs in different lateral positions above overgrown QDs. This effect vanishes with increasing distance between the stacked QDs. The energy gain observed in our calculations can lower the energy barrier for QD formation to 3.5 eV and the size of the critical nucleus to only 25 In atoms.

Additionally, we calculated the PES for In adsorption on surfaces that correspond to major side facets of ‘hut’- and ‘dome’-like QDs by means of DFT to study possible kinetic effects. The dominating diffusion paths are perpendicular and parallel to the QD contour lines on $\{317\}$ facets, but only perpendicular on $\{101\}$ facets. The In incorporation on $\{317\}$ facets could be kinetically limited due to the high barrier of approximately 1 eV for breaking As dimers. The diffusion barriers on $\{101\}$ facets are lowered near the bottom of ‘dome’-like QDs, which supports the interpretation of the $\{317\}$ facets on top as kinetic effect.

Zusammenfassung

Halbleiter Nanostrukturen, insbesondere Quanten-Punkte (QP), haben vielversprechendes Potenzial für technische Anwendungen wie Leucht-Dioden, Laser, neue Bauelemente und Quanten-Computer. Die große Zahl benötigter QP (weniger als Milliarden sind kaum nützlich) übersteigt jedoch die Möglichkeiten normaler Herstellungsmethoden. Zum Durchbruch dieser Nanotechnologie müssen sich die QP durch Selbst-Aufbau und Selbst-Organisation selbst bilden. In dieser Arbeit untersuchen wir InAs QP Wachstum auf GaAs Substraten.

Dazu haben wir ein Viel-Körper-Potenzial vom Abell-Tersoff Typ entwickelt, welches die Energie-Bilanz des Verspannungs-Abbaus und der Bildung von QP Flächen während des QP Wachstums beschreiben kann. Es reproduziert mit guter Genauigkeit simultan viele, experimentell und mit Dichte-Funktional-Theorie (DFT) Rechnungen bestimmte, mikroskopische Eigenschaften von In, Ga, As, GaAs, und InAs Kristallen, sowie GaAs und InAs Oberflächen. Die Vorhersagen für biaxial verspanntes GaAs und InAs stimmen gut mit DFT Rechnungen und analytischen Ergebnissen aus Kontinuums-Elastizitäts-Theorie überein.

Anhand von neuen STM Resultaten konstruieren wir detaillierte atomare Strukturen von InAs QP mit InAs Benetzungs-Filmen und homogene InAs Filme auf GaAs, relaxieren sie mit unserem Potenzial und vergleichen die gewonnenen Gesamt-Energien. Wir zeigen, daß die laterale elastische Wechselwirkung bei „hut“-artigen QP, die von $\{317\}$ Flächen dominiert werden, deutlich stärker ist als bei „dome“-artigen QP, die von $\{101\}$ Flächen dominiert werden. Eine Verspannungs-Tensor Analyse zeigt, daß dieser Effekt von der relativen Lage der QP Flächen zu den elastischen Hauptachsen stammt. Das berechnete Einsetzen des Stranski-Krastanov Wachstums bezüglich der InAs Bedeckung stimmt gut mit experimentellen Daten überein. Der kritische Keim für QP Bildung ist etwa 70 In Atome groß und stellt eine Energie-Barriere von 5.3 eV dar. Die experimentell beobachtete Abfolge von QP Formen können wir durch das Auftreten unterschiedlicher Stabilitäts-Regime erklären. Deren Grenze hängt stark von chemischen Potenzialen und der QP Dichte ab. Die experimentell gefundenen vertikalen Wachstums-Korrelationen in gestapelten QP Lagen können mit einem deutlichen Minimum in der Potenzial-Energie-Oberfläche (PEO) von freistehenden QP in verschiedenen lateralen Positionen über vergrabenen QP erklärt werden. Bei größerem Abstand der gestapelten QP wird dieser Effekt kleiner. Der berechnete Energie-Gewinn kann die Energie-Barriere für QP Nukleation auf 3.5 eV und die kritische Keim-Größe auf 25 In Atome verringern.

Ferner haben wir zur Untersuchung eventueller kinetischer Effekte mit DFT Rechnungen die PEO für In Adsorption auf Flächen, die „hut“- und „dome“-artige QP dominieren, berechnet. Die Haupt-Diffusionspfade sind senkrecht und parallel zu den QP Höhenlinien auf $\{317\}$ Flächen, aber nur senkrecht dazu auf $\{101\}$ Flächen. Der In Einbau auf $\{317\}$ Flächen könnte wegen der hohen Barriere zur Spaltung der As Dimere von etwa 1 eV kinetisch limitiert sein. Die Diffusionsbarriere auf $\{101\}$ Flächen ist am Fuß von „dome“-artigen QP erniedrigt und stützt damit die Interpretation der $\{317\}$ Flächen an der Spitze als kinetischen Effekt.

Inhaltsverzeichnis

1	Introduction	1
1.1	Quantum Dot Experiments	2
1.2	Challenge for Theory: Length and Time Scales	5
1.3	Goal of this Work	7
2	Electronic-Structure Calculations	12
2.1	The Many-Body-Problem and Solutions	12
2.1.1	Born-Oppenheimer Approximation	13
2.1.2	e-e Interaction: Exchange and Correlation	13
2.2	Density-Functional Theory	14
2.2.1	Kohn-Sham Formalism	14
2.2.2	Approximations to the XC-Functional	17
2.2.3	Solving the Kohn-Sham Equations	18
2.3	Electron-Ion Interaction: Pseudo-Potentials	20
2.4	Minimization of the Kohn-Sham Energy	21
2.5	Forces in the Ionic System	21
3	Thermodynamic Concepts in Surface Physics	23
3.1	Physical Events During Growth	23
3.2	Surface Energy and Chemical Potential	24
3.3	Crystal Growth	27
3.4	Nucleation Theory	29
4	Continuum-Elasticity Theory and Atomistic Strain	32
4.1	Introduction	32
4.2	Elastic Constants of Cubic Systems	34
4.3	Biaxial Strain in Systems with Cubic Symmetry	36
4.3.1	General Strain Tensor	37
4.3.2	General Linear Elastic Response	38

4.4	Atomistic Strain-Tensor	40
5	Many-Body Potential	45
5.1	Introduction	45
5.2	Bond-Order Potentials	47
5.2.1	Derivation from Tight-Binding Bond Model	47
5.2.2	Abell-Tersoff Functional	48
5.3	Geometric Interpretation of Parameter Optimization	50
5.3.1	Example: Lennard-Jones Potential	51
5.3.2	Practical Consequences	53
5.4	Determination of the Parameters	54
5.4.1	Reference Data	54
5.4.2	Optimization Procedure	55
5.4.3	Parameters	56
6	Applicability of Many-Body Potential to In, Ga, As, InAs, and GaAs	58
6.1	Bulk Properties	58
6.2	Biaxial Poisson-Ratio and Elastic Energy	66
6.3	GaAs and InAs Surfaces	72
6.4	Surface Stress	80
6.5	Adatom Diffusion on Surfaces: Limitations of MBP	82
6.5.1	Ga / GaAs(001) β 2(2x4): Comparison of MBP with DFT	82
6.5.2	In / InAs(110): Analysis of Artifacts	83
7	Self-Assembled QD Growth	87
7.1	Experimental Findings	87
7.2	Calculations of QD Nanostructures	89
7.2.1	Initialization	89
7.2.2	Relaxation and Formation Energy	89
7.3	Wetting Layer	90
7.4	Convergence with Substrate Thickness	92
7.5	Elastic Energy in Lateral QD Array	95
7.6	Regimes of Thermodynamic Stability	97
7.7	Critical Nucleus	104
8	QD Superlattices	107
8.1	Experimental Findings	107
8.2	Truncated Pyramids in a QD Superlattice	109
8.3	Growth Correlations in Stacked QD Layers	111
8.3.1	Initialization	111

8.3.2	Potential-Energy Surface of Stacked QD Layers	112
8.3.3	Effect of Lateral QD-QD Spacing and Spacer Thickness	116
8.3.4	Spatially Resolved Critical Nucleus	118
9	Kinetic Aspects of QD Growth	120
9.1	Introductory Remarks	120
9.2	Diffusion on Side Facets of Hut-Shaped QDs	121
9.2.1	Potential-Energy Surface of In/InAs(137)	121
9.2.2	Binding Sites at As Surface-Dimer	122
9.3	Diffusion on Side Facets of Dome-Shaped QDs	124
9.3.1	Potential-Energy Surface of In/InAs(101)	124
9.3.2	Dependence of Diffusion Barriers on Biaxial Strain	125
	Summary and Outlook	126
	Appendix	131
A.	DFT Calculations	131
B.	Implementation of Many-Body Potential	133
C.	Initialization of QD Supercells	136
D.	Surface Area of QD Side Facets	138
	Bibliography	139
	Publications and Presentations	155
	Acknowledgments	158
	Index	160

Abbildungsverzeichnis

1.1	Band-gap energy versus lattice constant of common semiconductors	3
1.2	High-resolution STM results of QD ensemble and single QD	4
1.3	Length and time scales of QD growth and computational methods	6
2.1	Schematic illustration of pseudo-potential concept	20
3.1	Elementary modes of crystal growth	28
3.2	Critical nucleus in classical nucleation theory	31
4.1	Poisson ratio and elastic energy of GaAs and InAs upon biaxial strain	40
4.2	Atomistic calculation of strain tensor	41
4.3	Comparison of strain tensor obtained by different methods	43
5.1	Solution manifolds in the parameter space of a Lennard-Jones Potential	52
6.1	Conventional unit-cells of stable Ga, As, In, and InAs	59
6.2	Pauli relation of Ga, In, and As	65
6.3	Pauli relation of GaAs and InAs	65
6.4	Survey of MBP accuracy for lattice constants and cohesive energies	66
6.5	Poisson ratio of InAs for biaxial strains in different planes	69
6.6	Low-index reconstructions of the (001) surface of GaAs and InAs	73
6.7	High-index reconstructions of the (001) surface of GaAs and InAs	74
6.8	Applicability of MBP to GaAs and InAs surfaces: Survey and phase diagram	78
6.9	Surface energies as obtained from DFT, previously published MBP and ours	79
6.10	Dependence of surface energy on strain for GaAs and InAs surfaces	81
6.11	PES of a Ga atom adsorbed on GaAs(001) $\beta 2(2 \times 4)$ obtained with MBP	82
6.12	Splitting of As surface-dimer: MBP vs DFT	84
6.13	Topview of InAs(110) and In adsorption	85
6.14	Number of neighbors and z coordinate of In/InAs(110) obtained with MBP	86
7.1	Atomically resolved QD shapes from high-resolution STM experiments	88

7.2	Structure and formation energy of InAs(001) α 2 (2 \times 4) wetting layer	91
7.3	Convergence of QD formation energy with substrate thickness	93
7.4	Strain tensor of elastically (non-)interacting QDs	94
7.5	Repulsive lateral interaction of <i>hut</i> -shaped QDs	96
7.6	Atomic representation of QDs in experimentally observed shapes	98
7.7	Stability regimes of different QD shapes with dependence on $\mu(\text{As})$	101
7.8	Dependence of <i>hut-dome</i> transition on $\mu(\text{As})$ and QD density	103
7.9	Critical nucleus of QD formation from a homogenous film	105
8.1	Experimental findings of QD stacks	108
8.2	Sketch and formation energy of overgrown QD in different shapes	110
8.3	Sketch of PES calculation for QD stack	111
8.4	Line scans of QD-stack PES in all four quadrants	113
8.5	Effect of shapes of stacked QD on formation energy	114
8.6	Line scans of PES of formation energies for different QD shapes	115
8.7	Effect of spacer thickness and QD density on vertical correlation	116
8.8	Strain-tensor overlap in QD stacks with different spacer thickness	117
8.9	Critical nucleus for different QD stacking arrangements	119
9.1	Adsorption energy of an In atom on InAs(137) obtained by DFT calculations	122
9.2	Adsorption sites of In adatom at surface As dimer of InAs(137)	123
9.3	Adsorption energy of an In atom on InAs(101) obtained by DFT calculations	124
9.4	Effect of biaxial strain on diffusion of In on InAs(101)	125
A.1	Convergence tests of DFT calculations	131
B.1	Convergence of structural relaxation and order-N scaling of MBP	134
C.1	Derivation of atomistic representations of experimentally observed QD shapes	137
C.2	Analytic calculation of areas of side facets for <i>hut</i> - and <i>dome</i> -shaped QD . . .	138

Tabellenverzeichnis

5.1	Parameter sets for the different interactions	57
6.1	Equilibrium properties of different Ga phases	60
6.2	Equilibrium properties of different In phases	61
6.3	Equilibrium properties of different As phases	62
6.4	Equilibrium properties of different GaAs phases	63
6.5	Equilibrium properties of different InAs phases	64
6.6	Effect of internal relaxation on Poisson ratio of biaxially strained InAs	70
6.7	Poisson ratio for biaxial strain from DFT and different MBP	71
6.8	Elastic energy for biaxial strain from DFT and different MBP	71
6.9	Comparison of calculated properties of GaAs surfaces	76
6.10	Comparison of calculated properties of InAs surfaces	77
6.11	Comparison of adsorption energies of Ga/GaAs(001) β 2(2x4): MBP and DFT	83
7.1	Structural parameters of investigated <i>hut</i> -shaped QDs	99
7.2	Structural parameters of investigated <i>dome</i> -shaped QDs	100
7.3	Coefficients of formation energy for <i>hut</i> - and <i>dome</i> -shaped QDs	102
7.4	Structural parameters of unstable <i>hut</i> -shaped QDs	105
9.1	Minima and transition states of In adatom on InAs(137)	121
9.2	Minima and transition states of In adatom on InAs(101)	125

Kapitel 1

Introduction

We are living in an age of data storage, transport, and procession. The amounts of data are increasing at a breathtaking speed and no limitation can yet be seen. In recent decades we witnessed revolutionary developments that made it possible to increase the power of storage, transport, and procession by an incredible amount. Light-emitting diodes made of semiconductor materials are the backbone of transportable high-density storage media and broadband glass-fiber cable connections. In addition, they are a possible realization of solid-state lighting with the aim to replace light bulbs not only in traffic lights, but in fact everywhere. The integrated circuit faced enormous development to increase the efficiency of the data processing device itself, we are already heading for devices with single-electron transistors. These technologies have reached a level of miniaturization where quantum-mechanical effects become apparent, often referred to as nanotechnology. The first major impact of the peculiar optical properties of nanoparticles dates back to the work of the chemist and glass manufacturer J. Kunckel in the 17th century. He was able to realize the fabrication of ruby glass by embedding small gold particles in crystal glass, an effort that brought the color red to many church windows long before this effect was understood. The focus of present research endeavors is more in the ultra-violet and the nanoparticles are semiconductor materials, embedded in other semiconductor materials. In contrast to these ancient times we can now often predict the optical properties of nanostructures but we are still facing similar problems in manufacturing them. We will need billions or trillions of quantum dots, the nanoparticles studied in this work, to be useful. Because of this big number, normal manufacturing methods will be useless and the nanostructures have to build themselves for nanotechnology to become relevant. This possibly very complex process is called self-assembly, with some ingredients from self-organization. The nanoparticles of this work are InAs quantum dots that form on GaAs surfaces and we will use the help of information-age machinery to understand it.

1.1 Quantum Dot Experiments

The transition from flat (2D) islands to raised (3D) islands during semiconductor hetero-epitaxy [1] was incipiently an undesirable effect for the fabrication of semiconductor heterostructures. Further investigations, however, showed that these islands were crystalline with photoluminescence lines at lower energies and very high intensity as compared to ‘island-free’ heterostructures, such as quantum wells [2]. The evidence that this self-assembly process can in fact be utilized to create quantum dots (QDs) was first supplied for vicinal GaAs(001) [3], and later for nominal GaAs(001) substrates [4, 5]. Shortly after that, the theoretically predicted δ -like density of states in such quantum dots was proven experimentally [6, 7], and the first demonstration of lasing from self-assembled QDs was reported [8]. These findings led to a change in paradigm of semiconductor technology and initiated a tremendous research effort that is still going on. The topics range from the fabrication of new, customized optoelectronic and single-electron devices to the realization of quantum computing and quantum cryptography. It took no more than 10 years to develop a secure quantum-cryptography connection over more than 100 km, based on QDs as single photon-sources [9]. With this rapid evolution, it is no wonder that the ARDA roadmap for solid-state quantum-computing [10] considers the development of a small-scale hybrid conventional/quantum processor possible by the year 2012. A major issue for materials science in this context is a thorough understanding of the processes underlying the self-assembled formation of semiconductor nanostructures. In this chapter we give a survey of previous experimental and theoretical achievements to expound the starting point and goal of this work.

The key to semiconductor technology is the ability to engineer the electronic structure by combining different materials to achieve the desired alignment of valence and conduction band. A proper band arrangement can form a confinement potential that delimits the charge-carriers to a certain region. In *quantum dots*, the mobility of the charge carriers is reduced to zero dimensions by a three dimensional confinement potential. The energy spectrum of these charge-carriers will no longer be continuous but form discrete levels if the confinement potential is narrow enough to localize them sufficiently. It depends on the particular material combination if the alignment of the valence and conduction band-edge acts as an effective quantum-well or quantum-barrier. The QDs with a confinement of both electrons and holes (e.g. InAs/GaAs) are named *type-I QDs*, whereas those with a confinement of either electrons or holes (e.g. GaSb/GaAs) are called *type-II QDs*. Calling such islands with a sufficiently narrow confinement potential *quantum dots* pays tribute to the manifestation of *nanophysics* that is not just ‘down-scaling’, but rather involves the appearance of qualitatively new features such as quantized energy-levels. The visualization of the electron wave-function in such levels with scanning-tunneling microscopy as has only recently been achieved [11], is an expressive demonstration of new physics at the bottom of solid-state length-scales.

The formation of such semiconductor objects with nanometer-scale dimensions perpendicular to the growth direction is beyond the resolution of conventional lithography techni-

ques used in contemporary semiconductor device technology. A promising way of realizing electronic-structure engineering at this length scale is the *self-assembly* of semiconductor nanostructures. The key to create technologically useful QDs is to find material combinations with a lattice-mismatch that lead to the self-assembled formation of 3D islands, but at the same time exhibit an alignment of valence and conduction band that confines the charge carriers to inside the island. A guide to the identification of possible candidates is the dependence of the band-gap energy on the lattice constant of the different semiconductor materials shown in Fig. 1.1. The best studied material combinations for QD formation are Si/Ge and

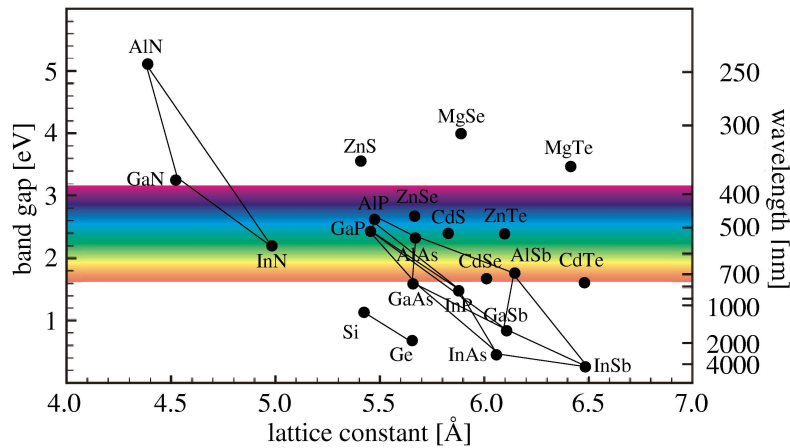


Abbildung 1.1: The map of band-gap energy versus lattice constant allows one to identify combinations of semiconductor materials that form by self-assembly and pose a confinement potential for the charge carriers, and are thus suitable for QDs (after Ref. [12]).

InAs/GaAs, but many others are of high interest for certain applications. A prominent example are diodes with wide-gap semiconductors (e.g. III-N) that emit light at short wavelengths, a key technology e.g. for the Blu-ray Disc [13] and solid-state lighting. In this study, we focus on InAs/GaAs QD nanostructures that are very well characterized and exhibit a comparably large lattice-mismatch.

The research efforts of the last decades established a number of experimental techniques for self-assembled QD growth (see e.g. Refs. [14, 15, 16, 17]), such as molecular-beam epitaxy (MBE), metalorganic chemical vapor deposition (MOCVD), liquid-phase deposition (LPD), and metalorganic vapor phase epitaxy (MOVPE). Good conditions for systematic investigations of QD growth are given in the case of MBE: The substrates are prepared atomically clean in ultra-high vacuum (UHV) in contrast to MOCVD where residues of reactant gases are unavoidable. The deposition of material can be accomplished at comparably low temperatures, and the coverage is controllable down to the sub-monolayer regime. Furthermore,

the possibility to perform *in-situ* RHEED measurements during MBE growth allows to follow the growth transition from 2D films to 3D islands. The investigations performed in this work address InAs/GaAs QD nanostructures grown by MBE.

The structure of freestanding semiconductor nanostructures can be characterized by direct imaging techniques like scanning tunneling microscopy (STM) and atomic force microscopy (AFM), or by transmission electron microscopy (TEM). A lot of insight was gained recently from fascinating high-resolution STM experiments: The side facets of QDs on substrates of several orientations could be identified in different growth stages for both, InAs/GaAs and Ge/Si (see e.g. Refs. [18, 19]). We will use such STM results of InAs QDs on GaAs(001) as shown in Fig. 1.2 to investigate the self-assembled QD growth (as described in Chap. 7 and 8). The detailed structure of overgrown semiconductor nanostructures, that are in fact more relevant for technical applications, has been determined with cross-sectional STM experiments (see e.g. Refs. [20, 21]). Diffraction methods like e.g. reflection high-energy electron diffraction

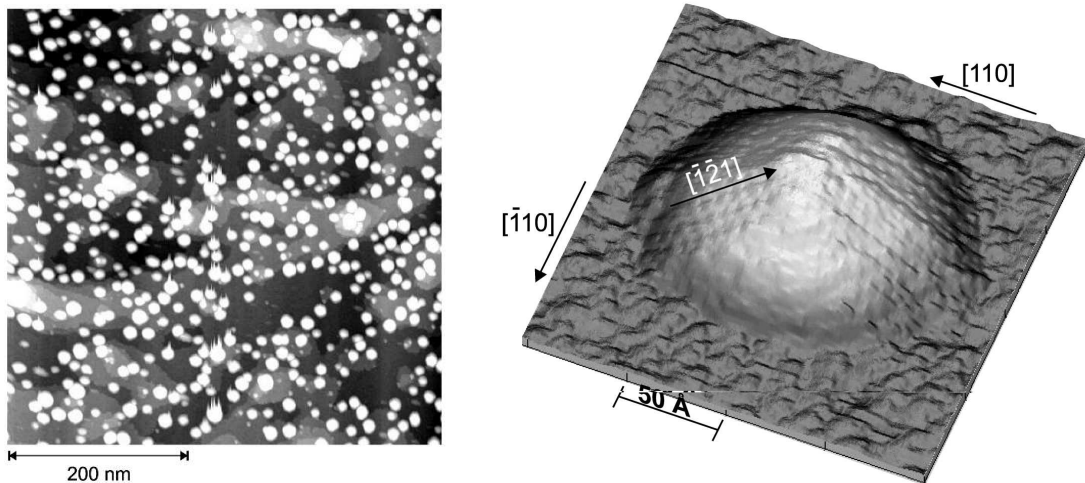


Abbildung 1.2: Recent STM experiments of QD ensembles (left panel) allowed to investigate QD size distributions [22, 23] and to identify QD side facets of single QDs (right panel) [18].

(RHEED) and (grazing-incidence) X-ray diffraction ((GI)-XRD) provide additional information about the side facets and the chemical composition of QD ensembles. The interested reader may gain more insight on direct-imaging and diffraction techniques from Ref. [16, 17]. An indirect and more subtle way of investigating QD nanostructures is the comparison of optical properties observed by e.g. photoluminescence (PL), photoluminescence excitation (PLE) or cathodoluminescence (CL) spectroscopy with theoretical results that were obtained under certain assumptions on shape and chemical composition (see e.g. Ref. [24] for a review of microscopic approaches): The relative position of hole and electron energy levels

that determine the optical transition-energies depend not only on the band gap of the QD material shown in Fig. 1.1, but also on the detailed energy levels that arise from the particular confinement potential. A meaningful comparison with experimentally observed optical and electronic properties thus may require a consideration of realistic shapes and compositions of QDs, as well as accurate descriptions of the resulting strain tensor. A very convincing example of such an approach given recently [25] compared PL spectra with $k \cdot p$ /CI calculations and concluded a discrete QD size distribution in increments of full monolayers. In this work, we present accurate investigations of the structural stability of realistic, atomically detailed QD nanostructures. Some of these results are currently used by A. Kleinsorge to determine the electronic properties of the investigated QD nanostructures with an atomistic tight-binding approach and to connect to the above indirect comparison.

1.2 Challenge for Theory: Length and Time Scales

In this work, we address the issue of QD growth by self-assembly with approaches of computational physics that allow us to solve complex problems in a numerical manner. The success of computational physics in recent years is not only due to the exponential increase of the CPU integration-density according to Moore's 'law' [26] and the resulting gain of computational power. It is also and particularly the methodical development of the recent decades that allows to overcome several obstacles: The solution of typical tasks, such as matrix diagonalization, Fourier transformation, and minimization of a function, with highly efficient algorithms are already standard. In addition, much progress was made in modeling the evolution of a system in time. This requires to either integrate the equations of motion with Molecular Dynamics (see e.g. Ref. [27]) or to employ statistical approaches like kinetic Monte Carlo (see e.g. Refs. [28, 29]). The latter is a strong motivation for improving the methods to determine the reaction pathways (see e.g. Ref. [30]), and in particular the transition states between two (meta)stable configurations. However, such algorithms can by no means replace physical intuition. (Or, free after Seneca: *There is no good algorithm for those who don't know where to go.*) The computational effort to determine relaxation and time evolution depends on the expenses of the various physical approaches to calculate the forces on the atoms. It can differ by many orders of magnitude, and, of even greater concern, its scaling with the characteristic system-length is typically less advantageous for methods with higher accuracy.

Within an overall CPU time of t_c one can perform N steps of CPU time τ_c , and thereby advance the physical time by t_p in steps of τ_p , i.e. $t_c = N\tau_c$ and $t_p = N\tau_p$. The best known scaling of the numerical effort with the number of atoms N is linear, the so-called order- N scaling. The physical time reachable in a given CPU time for a system with characteristic length L and characteristic density $\rho = N/V = N \cdot L^{-3}$ is then

$$t_p = Ct_c\tau_p \cdot L^{-3} \tag{1.1}$$

with a prefactor C that depends on the underlying method for force evaluation. A comparison of different methods to study QD nanostructures within a given amount of CPU time is given in Fig. 1.3. The regimes of ab-initio calculations (DFT, see Chap. 2) and many-body

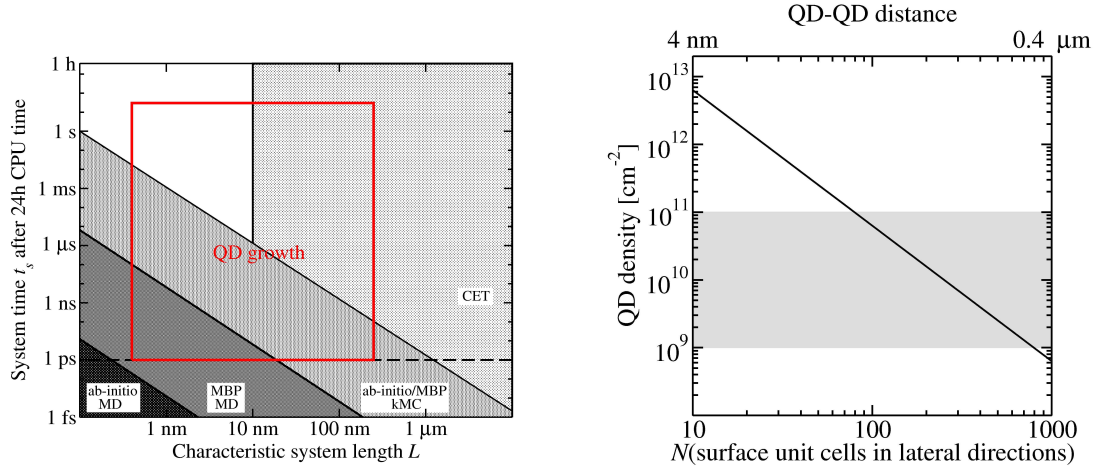


Abbildung 1.3: Physical times and sizes of QD nanostructures that are accessible by different methods within a CPU time of $t_c = 24\text{h}$ and a time increment of $\tau_p = 1\text{fs}$ (left). The computational effort of a typical relaxation with the MBP is also indicated (left: dashed line.) The region of QD growth (red box in left panel) can be deduced (text) from the experimentally observed QD densities (right, gray area), the relation between QD density and QD-QD distance (right: line), and the reported typical formation times of a few seconds (c.f. Ref. [18] and Sec. 7.7).

potentials (MBP, see Chap. 5) are shown according to the CPU times observed in this work (Ref. [31] and Appendix B). The typical regime of kinetic Monte-Carlo simulations (not performed in this work) is also indicated. The regime of continuum-elasticity theory (CET) is shown as being independent from the physical time to indicate that it is primarily a static approach. The range of validity of CET for QD nanostructures is somewhat questionable: In the literature, the numbers for the minimum QD size that can be treated properly by CET range from about 1000 atoms [32, 33] to about 5000 atoms [34], corresponding to QD base lengths of about 1 nm and 10 nm, respectively (Tab. 7.1 and 7.2). The latter is consistent with a recent rigorous investigation [35] which showed that applying CET to QD of sub-10 nm sizes introduces appreciable deviations in the strain tensor and shifts of the conduction band. The additionally shown dashed line indicates the computational effort of relaxing a QD nanostructure with the many-body potential: For large systems, as investigated in this work, the computational effort of performing an iteration of a relaxation or a step in a molecular-dynamics simulations is mainly determined by the cost of evaluating forces on the atoms and therefore is very similar in both cases. If therefore the effort of the typically

required 1000 iterations of the relaxation would instead have been spent in 1000 steps of a molecular dynamics simulation with a physical-time step of 1 fs, the physical time would be increased by 1 ps.

The method of choice is typically dictated by either the characteristic length-scale L or the characteristic system time-scale. The lower bound of L is given by the resolution that is needed to capture possibly relevant details. The upper bound of L is the length of the irreducible super cell, i.e. the smallest super cell that still allows one to capture the anticipated essential effects. In many cases like studies of surface stability, the problem can be captured by irreducible supercells of a few nanometer extension. For QD growth studied in this work, the long-range strain fields increase the characteristic length to about half the lateral distance between two QDs. From the experimentally observed lateral QD densities of $10^{11} - 10^9 \text{cm}^{-2}$ we expect L to be as large as 25 – 250 nm. The lower bound of the characteristic length-scale of about 1 nm is needed to resolve different surface reconstructions, but also QD edges and kinks. The region of interest for this work (red box in the left panel of Fig. 1.3) is spanned by the shortest time-scale during growth (see e.g. Ref. [36]) and the typical time interval for QD formation. The advantage of the many-body potential is its ability to describe the full range of length scales that possibly play a role in self-assembled QD growth. The disadvantage of such an approach is the simplified description of the quantum-mechanical nature of chemical bonding. This can be a severe limitation in studies of structures with characteristic length scales below about 5 nm: In such cases, the many-body potential may not be adequate to describe e.g. quantum-size effects or changes of the surface reconstruction. The difficulty and the art of a *successful* study with a many-body potential is the detailed knowledge of limitations and a proper balance of inaccuracy and new insight.

1.3 Goal of this Work

Previous theoretical investigations of the self-assembled growth and structural stability of semiconductor nanostructures initially started out with continuum approaches: The first explanation for shape transitions of QDs was given in terms of a balance of energy contributions from surfaces, interfaces and elastic relaxation [37]. The work of Shchukin et al. [38] suggested that the material constants and the lattice mismatch determine if islands are stable or undergo ripening. These authors neglected the existence of a wetting layer, but Daruka et al. [39] found that the stability of islands depends sensitively on the thickness of the wetting layer and gave a detailed ‘phase-diagram’ of growth close to thermodynamic equilibrium. An important step beyond a pure continuum-model of QD growth was the development of a hybrid approach [40] that combined DFT calculations of microscopic properties, particularly surface energies and stresses, with long-range strain fields determined by CET. Using this approach, it could be shown that the equilibrium shape of InAs QDs on GaAs(001) substrates is also dependent on the volume of the QDs [33]. It was furthermore applied to show that a narrow

distribution of QD sizes can be explained by a constraint equilibrium of wetting-layer and QD [34], without the invocation of elastic QD-QD interactions proposed earlier [38, 39]. Rather, the particular island size is a consequence of the chosen growth conditions and nominal coverage [41]. Similar applications of this hybrid approach to the case of Ge QDs on Si(001) substrates [42, 43] demonstrated quantitatively that the strain dependence of the surface energies of experimentally observed QD side facets effectively stabilizes small QDs. Furthermore, this approach was able to reveal a discontinuous change of the chemical potential in the islands during a structural transition at a later growth stage [44].

In this work, we want to address issues of nanostructure self-assembly that require a further increase in the level of detail in modeling and ultimately reach the limit of atomic resolution: Instead of combining DFT results of microscopic systems with CET solutions of macroscopic structures in a *hybrid* approach, we develop an *all-in-one* approach that is based on microscopic properties, but is still able to describe systems of macroscopic size in atomic detail. Such an atomistic approach has some major advantages over continuum approaches:

- *Atomistic approaches are in principle complete in the sense that they can be directly applied to arbitrary structures.* For reasons of feasibility, some previously presented investigations with a hybrid approach neglected elastic QD-QD interactions, the energy contributions (and strain dependency) of steps, edges and kinks. Furthermore, the use of CET with no intrinsic length-scale yields a strain tensor that is independent from the size of the QD, an approximation that may introduce errors for small QDs. An additional approximation is that the dependency of the surface energies of QD side-facets on the local strain tensor is usually considered only with respect to the averaged biaxial strain without off-diagonal components. But the most severe drawback of the above hybrid approach is supposedly the necessity to extend them by additional DFT calculations for every new surface that is modeled in the QD nanostructure.
- *Studies of possible effects of the detailed structure require an atomistic treatment.* The hybrid approach developed so far provides no possibility to account for structural details on an atomic length-scale. However, This natural feature of atomistic methods allows the realization of static, kinetic, or even dynamic studies in atomic detail. The latter are needed for an understanding of e.g. adatom diffusion and clustering on (strained) substrates and QD side facets, the evolution of facet growth, the preferred formation site of dislocations, and the preferred site of QD nucleation with respect to steps or the surface reconstruction. A minor issue in this context is that continuum approaches can hardly account for the finite character of structural motifs: This is of importance particularly for small QDs with side-facet areas in the range of the according surface unit-cells.
- *The system-wide composition stoichiometry is a natural and well-defined quantity in an atomistic treatment.* The relative stability of structures with different composi-

on stoichiometry depends on the chemical potentials of the involved elements. These composition stoichiometries of nanostructures with free-standing QDs depend on contributions from surfaces, edges and corners and are therefore not obvious in the hybrid approaches.

Even with the vast computing power currently available, there are only few atomistic approaches that allow systematic investigations of the structural evolution of million-atom systems within an acceptable CPU time: First-principles methods can be applied to already relaxed nanostructures of up to about 10^4 atoms [45], but they are computationally too expensive for the required structural relaxations. Lower-level electronic-structure methods such as tight-binding have a lot of potential for the near future, even for structural relaxation of nanostructures. At the moment, however, classical interatomic potentials seem to be the only feasible way of modeling macroscopically-sized systems in atomic detail and with a reasonable accuracy. Among the many different classes of classical interatomic potentials, we have chosen a bond-order potential of the Abell-Tersoff type (see Chap. 5), a many-body potential that has proven to be useful in previous studies of group IV and III-V semiconductors.

The first goal of this work is to validate the applicability of this atomistic approach to the modeling of semiconductor heterostructures with interfaces and surfaces. To this end we collected a large number of theoretical and experimental reference values of the properties of stable and meta-stable In, Ga, As, InAs, and GaAs bulk structures, as well as reconstructed GaAs and InAs surfaces. As a result of detailed tests we found that the previously published parameterizations left some room for improving the interaction parameters of the potential to capture a larger portion of the reference data (Chap. 6). This required the development of a flexible fitting environment, and computationally efficient implementations of energy and force evaluations (technical details: Appendix B). We confirmed the applicability of the new parameterization to the description of biaxially strained InAs by a comparison with results from CET and DFT calculations. To this end we derived general expressions for the elastic response upon biaxial strain in arbitrary planes from CET that have in fact a much broader range of applicability (Chap. 4). In particular they strongly simplify numerical calculations of elastic response to biaxial strain, and enable us to isolate non-linear elastic response by comparing the results obtained within CET with those from DFT calculations.

Our second goal is to clarify the applicability of the newly parameterized many-body potential to kinetic and dynamic growth simulations. We compared the potential-energy surfaces of adatom diffusion on different reconstructed GaAs and InAs surfaces with corresponding results of DFT calculations that were performed previously and in the framework of this study. Of particular interest for combining our approach with a kinetic Monte-Carlo scheme is the effect of strain on the energy barriers of adatom diffusion. Additionally, we were interested in realizing a kMC scheme for heteroepitaxy that allows for an on-the-fly search of diffusion events, and therefore tested the Dimer method for transition-state search employing

our many-body potential. Studies of growth simulations with (conventional and accelerated) molecular dynamics are subject of a collaboration with M. Mignogna and Prof. K. Fichthorn at the Pennsylvania State University (University Park, PA, USA).

The third goal is to develop a framework for initializing and relaxing nanostructures in macroscopically sized simulation cells.. This requires a mapping of experimentally observed free-standing QDs to atomic coordinates that we accomplish by truncating a sufficient amount of zinc blende bulk material with specified QD side facets and by ‘reconstructing’ the resulting structure according to surface unit-cells as obtained from relaxation with DFT calculations (technical details: Appendix C). The routines for structural relaxation are optimized to achieve a linear scaling of the computational effort with the number of atoms in these systems. The calculation of the resulting strain tensor is implemented with linear scaling, too, and is compared to results of a Green’s function approach for a simple model structure (Chap. 4). The QD nanostructures obtained with our approach are already used in follow-up calculations of the electronic structure with tight binding, and will soon be combined with a kMC scheme for modeling heteroepitaxy.

The fourth goal is to understand several aspects of self-assembled growth of free-standing QDs. After having reproduced the experimentally observed coverage at the growth transition from a 2D film to 3D islands, we determine the size of the corresponding critical nucleus. Our approach allows us to quantify the lateral elastic interactions between QDs in experimentally observed shapes, which so far was investigated only in an approximative manner. The aspect of major importance however, is to identify if the experimentally observed shape transition upon QD growth is driven by the kinetic evolution or rather an equilibrium effect. In this context we will exploit the atomistic character of our method to investigate the influence of the chemical potentials and the lateral QD density on the shape transition (Chap. 7).

As a fifth goal we want to explain growth correlations in QD stacks by quantifying the effect on the critical nucleus in the topmost layer. Until now, these experimentally observed growth correlations were explained in a qualitative manner only. But due to the subtle balance of energy contributions from strained surfaces and bulk regions, the relative importance of strain-mediated diffusion and elastic interactions remained unclear. Our approach allows us to settle this issue in line with experimental observations and to determine the size of the critical nucleus for different stacking arrangements.

The sixth goal of this work is to study adatom diffusion on QD side facets. For this purpose we performed DFT calculations to determine the potential-energy surfaces of In adsorption on InAs(137) and InAs(101) surfaces (Chap. 9) which appear as dominant side facets of small and large QDs. By means of additional DFT calculations we studied the importance of the breaking of the As dimer on InAs(137) as a possible rate-limiting process and the strain dependence of In diffusion on InAs(101) as an origin of kinetic effects.

With the achievement of the above goals we extend the study of InAs/GaAs QD nanostructures to the atomistic level that is not yet accessible with other approaches. We thereby

aim to gain a deeper understanding of the role of kinetic and thermodynamic effects of QD self-assembly. Our results and the supplied method will hopefully stimulate future work on the physics of these exciting tiny pieces of nature.

Kapitel 2

Electronic-Structure Calculations

This chapter is intended to give a brief overview of the theory behind *ab-initio* electronic-structure calculations. The interested reader might refer to one of the excellent review papers [46, 47, 48, 49] and textbooks [50, 51] for further information.

2.1 The Many-Body-Problem and Solutions

Electronic structure theory describes atoms, molecules and solids as non-relativistic (spin is a non-relativistic, spin-orbit coupling is a relativistic effect), isolated N-electron systems. The quantum-mechanical description of the ground-state of these systems is the time-independent Schrödinger equation for ions (i.e. the atomic nuclei) and electrons for a many-body wavefunction $|\Psi\rangle$:

$$(\mathbf{H} - E)|\Psi\rangle = (\mathbf{T}_e + \mathbf{T}_i + V_{e-e} + V_{e-i} + V_{i-i} - E)|\Psi\rangle = 0. \quad (2.1)$$

The terms V_{e-e} , V_{e-i} and V_{i-i} denote the Coulomb interactions between electrons and electrons, electrons and ions, as well as ions and ions. The kinetic energies are given by

$$\mathbf{T}_e = \sum_i \frac{\mathbf{p}_i^2}{2m}, \quad \mathbf{T}_i = \sum_j \frac{\mathbf{P}_j^2}{2M_j} \quad (2.2)$$

where \mathbf{p}_i , m and \mathbf{P}_j , M are momentum and mass of the electrons and ions, respectively. The structure and properties of all static many-body systems can be determined by solving the above Schrödinger equation. Dynamic phenomena are treated by solving the time-dependent Schrödinger equation within the so-called time-dependent density-functional theory (see e.g. Ref. [52]).

2.1.1 Born-Oppenheimer Approximation

The task of solving Eq. 2.1 is much simplified by the Born-Oppenheimer approximation [53] that reduces the complexity of the quantum-mechanical many-body problem. The mass of the electrons is much smaller than the mass of the ions ($\frac{m}{M_j} \ll 1$). By neglecting the movement of the ions, the equations of motion for the electrons at the positions $\mathbf{r} = (\mathbf{r}_1, \dots, \mathbf{r}_N)$ and the ions at $\mathbf{R} = (\mathbf{R}_1, \dots, \mathbf{R}_K)$ decouple. The (fixed) positions of the ions only modulate the wavefunction of the electrons and the overall wavefunction can be written as:

$$\Psi(\mathbf{r}, \mathbf{R}) = \Phi(\mathbf{R})\Psi_{\text{BO}}(\mathbf{r}, \mathbf{R}). \quad (2.3)$$

Here $\Psi_{\text{BO}}(\mathbf{r}, \mathbf{R})$ is the solution of the Schrödinger equation without kinetic energy of the ions T_i . This approximation is reasonable in cases where electron-phonon coupling has no considerable effect on the investigated system properties. The hyper-surface that is formed by the values of the total energy as a function of the ion positions is called the Born-Oppenheimer surface.

2.1.2 e-e Interaction: Exchange and Correlation

The remaining complexity of the quantum-mechanical many-body problem is mainly due to the interaction of the electrons among each other. This interaction is determined by the Coulomb potential and the Pauli principle. The Coulomb forces between the electrons lead to spatial separation, balanced against the increase in kinetic energy. This is an early problem of quantum-mechanics and there are several theories addressing this issue. The earliest approach, the *Hartree* theory [54] treats the Coulomb interaction by an average potential. The many-body wavefunction $|\Psi\rangle$ is approximated by a product of single-particle wavefunctions $|\psi_i\rangle$. Each of them satisfies a single-particle Schrödinger equation in an average, self-consistent potential arising from the other particles. For electrons the Pauli principle holds and requires an anti-symmetric wavefunction. In the *Hartree-Fock* theory [55, 56] the Fermi statistics for the electrons is accounted for by constructing Ψ with the Slater determinant for a set of N orthogonal spin-orbitals $\psi_i(\mathbf{x})$ (where \mathbf{x} comprises spatial coordinates \mathbf{r} and spin s):

$$\Psi(\mathbf{x}_1, \dots, \mathbf{x}_N) = \frac{1}{\sqrt{N!}} \det|\psi_i(\mathbf{x})|, \quad \psi_i(\mathbf{x}) = \phi_i(\mathbf{r})\chi_\alpha(s). \quad (2.4)$$

$$\text{orthonormality : } \int \psi_i^*(\mathbf{x})\psi_j(\mathbf{x})d\mathbf{x} = \delta_{ij} \quad (2.5)$$

This imposes an additional, nonlocal exchange-term, but the single-particle picture remains unchanged. The wavefunction of the ground-state is determined by the minimization of the

total energy with respect to $\psi_i(\mathbf{x})$. Usage of the Lagrangian multipliers ε_i yields the Hartree-Fock equations:

$$\int d^3\mathbf{x}' \left(-\frac{1}{2}\nabla^2\delta(\mathbf{x}-\mathbf{x}') + V_{e-i}(\mathbf{x})\delta(\mathbf{x}-\mathbf{x}') + V_H(\mathbf{x})\delta(\mathbf{x}-\mathbf{x}') + V_X(\mathbf{x},\mathbf{x}') \right) \psi_i(\mathbf{x}) = \sum_i \varepsilon_i \psi_i(\mathbf{x}) \quad (2.6)$$

with the Hartree term $V_H(\mathbf{x})$ and the exchange term $V_X(\mathbf{x},\mathbf{x}')$. These equations need to be solved self-consistently. The additional term results in a spatial separation between two electrons with equal spin, thereby reducing the Coulomb-energy of these two electrons. This reduction in energy of the electronic system due to the antisymmetric wavefunction is called *exchange-energy*. The Coulomb-energy is further reduced by the spatial separation of electrons with different spin (on the cost of kinetic energy). This difference (between the many-body-energy of an electronic system and the energy calculated in the Hartree-Fock-approximation) is called the *correlation-energy*. The *Thomas-Fermi model* can be seen as the origin of the density-functional theory. It uses statistical considerations to approximate the distribution of electrons in an atom. This is based on two assumptions: electrons are distributed uniformly in phase-space per h^3 -volume (h is Planck's constant) and there is an effective potential that is determined by the charge of the nuclei and the electrons. The Thomas-Fermi model is too simple to give good accuracies for atoms and fails to predict molecular binding. This model can be regarded as an approximation of the density-functional theory for ground states. In the next section we will introduce the *density-functional theory*, a formally exact theory with an exact energy functional $E[\rho]$ and an exact variational principle. The Kohn-Sham formalism, the core of DFT calculations, is based on the electronic ground-state density. The latter determines the full many-body Hamiltonian and would in principle allow the treatment of excitations which are the origin of most of the commonly measured spectra. The limitations of the currently known exchange-correlation functionals, however, limits DFT to the description of properties of the electronic ground-state. Other approaches try to overcome this limitation: The *GW-formalism* is based on many-body perturbation-theory with DFT as zero-order solution. An extension to 'static' DFT is *time-dependent DFT*, which uses a time-dependent external potential and a time-dependent exchange-correlation functional (review: Ref. [57]).

2.2 Density-Functional Theory

2.2.1 Kohn-Sham Formalism

The electron density The electron density ρ is the basic variable in density functional theory. It describes the number of electrons per unit volume in a given state as expressed by

$$\rho(\mathbf{r}_1) = N \int \dots \int |\Psi(\mathbf{x}_1, \dots, \mathbf{x}_N)|^2 d\mathbf{x}_2 d\mathbf{x}_N. \quad (2.7)$$

This is a non-negative simple function of \mathbf{r} that integrates to the total number of electrons

$$\int \rho(\mathbf{r})d\mathbf{r} = N. \quad (2.8)$$

For an atom in its ground state the electron density $\rho(\mathbf{r})$ decreases monotonically away from the nucleus. The electron density of molecules is not only a superposition of the atomic densities, but shows higher density in the regions of chemical bonding.

Hohenberg-Kohn theorem The Hohenberg-Kohn theorem [58] deals with the ground state Ψ of an interacting electron gas in an external potential $v(\mathbf{r})$ and consists of two parts. The first part legitimizes the use of the electronic density $\rho(\mathbf{r})$ as basic variable. Hohenberg and Kohn showed that, *within an additive constant c , there is a one-to-one correspondence between the external potential $v(\mathbf{r})$ and the electronic density $\rho(\mathbf{r})$:*

$$\text{HK1 : } \quad v = v[\rho(\mathbf{r})] + c. \quad (2.9)$$

Note that the ground-state electron density $\rho(\mathbf{r})$ of a system of interacting electrons in some external potential $v(\mathbf{r})$ determines this potential uniquely up to an additive constant and that $\rho(\mathbf{r})$ determines implicitly all properties derivable from the Hamiltonian through the solution of the time-independent Schrödinger equation. The similar Runge-Gross theorem is a generalization to the time-dependent Schrödinger equation [52]. The second part of the Hohenberg-Kohn theorem establishes the energy variational principle in analogy to the variational principle for wavefunctions. The full many-body wavefunction Ψ is a unique functional of the electron density $\rho(\mathbf{r})$, since $v(\mathbf{r})$ fixes the Hamilton operator:

$$\Psi = \Psi[\rho(\mathbf{r})]. \quad (2.10)$$

As Ψ is a functional of $\rho(\mathbf{r})$, so is the kinetic and interaction energy. A universal functional $F[\rho]$ that is valid for any number of particles and any external potential can be defined as

$$F[\rho(\mathbf{r})] = (\Psi, (T + U)\Psi). \quad (2.11)$$

With this expression, an energy functional $E_v[\rho]$ for a given potential $v(\mathbf{r})$ can be defined that equals the ground-state energy E for the correct electronic density $\rho(\mathbf{r})$:

$$E_v[\rho] = \int v(\mathbf{r})\rho(\mathbf{r})d\mathbf{r} + F[\rho]. \quad (2.12)$$

With the restriction for the admissible functions $\tilde{\rho}$

$$N[\tilde{\rho}] = \int \tilde{\rho}(\mathbf{r})d\mathbf{r} = N. \quad (2.13)$$

Hohenberg and Kohn proved that *the functional $E_v[\rho]$ assumes its minimum value E_0 for the correct ground state density $\rho(\mathbf{r})$* , which means that

$$\text{HK2 : } \quad E_0 \leq E_v[\tilde{\rho}]. \quad (2.14)$$

It can be shown that these expressions also hold for a degenerate ground-state. For a known functional $F[\rho(\mathbf{r})]$ the problem of determining the ground-state density and energy for a given external potential reduces to the minimization of the energy functional $E_v[\rho(\mathbf{r})]$ with respect to the density. But an analytic expression for $F[\rho(\mathbf{r})]$ can be given only for the two limiting cases of nearly constant density and slowly varying density. For realistic systems the complexity of the many-electron problem arises from the determination of the functional $F[\rho(\mathbf{r})]$. The Thomas-Fermi theory approaches the unknown functional $F[\rho(\mathbf{r})]$ directly by assuming explicit expressions for $F[\rho(\mathbf{r})]$. This leads to analytic expressions depending on the electronic density $\rho(\mathbf{r})$ alone, but the applicability is very limited due to the rather crude approximation for the functional. The density-functional theory is based on an indirect approach to the unknown functional $F[\rho(\mathbf{r})]$ from Kohn and Sham and allows one to perform rigorous calculations.

Kohn-Sham equations Kohn and Sham [59] transformed the many-body problem to an exactly equivalent set of self-consistent one-electron equations with an auxiliary non-interacting system with the same electron density. These so-called Kohn-Sham equations form the core of density functional calculations (and are denoted by KS in the following equations). The unknown functional $F[\rho(\mathbf{r})]$ of a *system of interacting electrons* can be written in terms of the ground-state kinetic energy $T_0[\rho(\mathbf{r})]$ of a *system of non-interacting electrons* and the classical electrostatic self-interaction of the electronic density as

$$F[\rho(\mathbf{r})] = T_0[\rho(\mathbf{r})] + \int \frac{\rho(\mathbf{r})\rho(\mathbf{r}')}{|\mathbf{r} - \mathbf{r}'|} d\mathbf{r}d\mathbf{r}' + E_{xc}[\rho(\mathbf{r})]. \quad (2.15)$$

This equation defines the so-called exchange-correlation energy functional $E_{xc}[\rho(\mathbf{r})]$. For a fixed number of electrons, the variation of this energy functional for a system of interacting electrons with respect to $\rho(\mathbf{r})$ leads to an equation that is formally the same as the one that holds for a system of noninteracting electrons in an effective potential v_{eff} , the so-called Self-Consistent-Field (SCF), that is given by:

$$\text{KS1} \quad v_{\text{eff}}(\mathbf{r}) = v_{\text{SCF}}(\mathbf{r}) = v(\mathbf{r}) + v_{\text{H}}(\mathbf{r}) + v_{\text{xc}}(\mathbf{r}) \quad (2.16)$$

$$\text{with } v_{\text{H}}(\mathbf{r}) = \int \frac{\rho(\mathbf{r}')}{|\mathbf{r} - \mathbf{r}'|} d^3\mathbf{r}', \quad \text{and } v_{\text{xc}}(\mathbf{r}) = \frac{\delta E_{xc}[\rho(\mathbf{r})]}{\delta \rho(\mathbf{r})}. \quad (2.17)$$

Here v_{H} is the Hartree-potential of the electrons and v_{xc} is the exchange-correlation potential. With this *mapping of the interacting many-electron system onto a system of noninteracting electrons* moving in an effective potential due to the other electrons, we can write the

Schrödinger equation for an electron in the non-interacting system as:

$$\text{KS2} \quad \left[-\frac{1}{2}\nabla^2 + v_{\text{eff}}(\mathbf{r}) \right] \psi_i(\mathbf{r}) = \varepsilon_i \psi_i(\mathbf{r}), \quad i = 1 \dots N \quad (2.18)$$

with the electronic density of N electrons of spin s

$$\text{KS3} \quad \rho(\mathbf{r}) = \sum_{i=1}^N \sum_s |\psi_i(\mathbf{r}, s)|^2. \quad (2.19)$$

The expressions 2.16-2.19 are the celebrated Kohn-Sham equations. The wavefunctions $\psi_i(\mathbf{r})$ are the so-called Kohn-Sham orbitals. Note that these are exact expressions: if the exchange-correlation energy functional $E_{\text{xc}}[\rho(\mathbf{r})]$ was known exactly, then the above equations would allow one to calculate the potential that included the effects of exchange and correlation exactly. The remaining task is to find an expression for the exchange-correlation functional and solve the Kohn-Sham equations self-consistently, such that the occupied electronic states generate a charge density that produces the same electronic potential which was used to construct the equations.

2.2.2 Approximations to the XC-Functional

The framework of density-functional theory given above requires appropriate approximations for the unknown exchange-correlation functional $E_{\text{xc}}[\rho(\mathbf{r})]$ to be of practical use. These approximations are physically motivated and are not part of the Kohn-Sham formalism. The simplest but remarkably successful approximation to the exchange-correlation functional is the *local-density approximation* (LDA) that uses only the exchange-correlation energy of a homogeneous electron gas:

$$\text{LDA :} \quad E_{\text{xc}}^{\text{LDA}}[\rho(\mathbf{r})] = \int \varepsilon_{\text{xc}}^{\text{hom}}(\rho(\mathbf{r}))\rho(\mathbf{r})\text{d}\mathbf{r}. \quad (2.20)$$

Although this relation is exact only for a homogeneous electron gas, it showed to give very useful results for most applications. An extension of this expression is the so-called *generalized-gradient approximation* (GGA) that additionally includes derivative information of the electron density:

$$\text{GGA :} \quad E_{\text{xc}}^{\text{GGA}}[\rho(\mathbf{r})] = \int \varepsilon_{\text{xc}}(\rho(\mathbf{r}), |\nabla\rho(\mathbf{r})|)\rho(\mathbf{r})\text{d}\mathbf{r}. \quad (2.21)$$

Note that these local approximations to the exchange-correlation functional are only valid for an electron gas of slowly varying density $\rho(\mathbf{r})$. They are fundamentally inappropriate to treat e.g. Van der Waals interaction between non-overlapping subsystems.

2.2.3 Solving the Kohn-Sham Equations

For an infinite solid, the Kohn-Sham formalism leads to an infinite number of non-interacting electrons in the static potential of an infinite number of ions. The wavefunctions of the electrons extend over the entire solid and require an infinite basis-set. The task of handling these two infinities is drastically simplified by the usage of periodic systems and the application of Bloch's theorem.

Bloch's theorem In periodic systems, an electronic wavefunction $\psi_i(\mathbf{r})$ can be written as a plane wave modulated by a periodic function $f_i(\mathbf{r})$:

$$\psi_i(\mathbf{r}) = \exp[i\mathbf{k} \cdot \mathbf{r}] \cdot f_i(\mathbf{r}). \quad (2.22)$$

The periodic function of a solid can be expressed in terms of reciprocal lattice-vectors \mathbf{G}

$$f_i(\mathbf{r}) = \sum_G c_{i,G} \exp[i\mathbf{G} \cdot \mathbf{r}]. \quad (2.23)$$

Then, every electronic wavefunction can be written as sum of plane-waves:

$$\psi_i(\mathbf{r}) = \sum_G c_{i,G} \exp[i(\mathbf{k} + \mathbf{G}) \cdot \mathbf{r}]. \quad (2.24)$$

The infinite number of electrons in an infinite system occupy a finite number of electronic states at each of the infinite number of \mathbf{k} points. This changes the task of calculating an infinite number of electronic wavefunctions to the task of calculating a finite number of electronic wavefunctions for an infinite number of \mathbf{k} vectors. Calculations of finite systems can be performed by using periodic super-cells which are large enough to separate the periodic images of the system by a sufficiently large vacuum region.

k-point sampling Each of the occupied states at the infinite number of \mathbf{k} -points contributes to the electronic potential in the system. The calculation of the potential therefore requires an infinite number of numerical steps. But the electronic wavefunctions at \mathbf{k} -points that are very close together are almost identical. The electronic wavefunction over a certain region of \mathbf{k} -space can be approximated by those of a single \mathbf{k} -point. Then only a finite number of \mathbf{k} -points need to be sampled. Special sets of \mathbf{k} -points in the Brillouin zone have been developed for insulators and semiconductors. The Fermi-surface of metals is more complex and calls for a denser set of \mathbf{k} -points. The computed total energy converges with the number of \mathbf{k} -points and in principle the error from the \mathbf{k} -point sampling can be reduced to zero for a sufficiently dense set of \mathbf{k} -points.

Basis set The wavefunction can be represented by different basis sets that can be separated into two groups. On the one hand there are the so-called *all-electron approaches* which consider both core and valence electrons explicitly in the calculation. In contrast to these methods there are also the so-called *pseudo-potential approaches* that do not include the core-electrons explicitly. Instead, a pseudo potential is constructed that models the core-electrons implicitly and only the valence-electrons are included in the calculation. The valence electrons then are modeled with local orbitals or with plane-waves. An introduction to pseudo-potential theory is given in Sec. 2.3.

Cutoff energy In an expansion of the electronic wavefunction in terms of an plane-wave basis set, the coefficients $c_{i,\sigma,\mathbf{k}+\mathbf{G}}$ for the plane-waves with small kinetic energy are much more important than those with larger kinetic energy. This allows one to create a finite plane-wave basis set by truncating the basis set to include only plane waves that have kinetic energies less than some particular cutoff energy :

$$|\mathbf{k} + \mathbf{G}|^2 \leq E_{\text{cut}}. \quad (2.25)$$

The error imposed by neglecting contributions with higher energy decreases with increasing cutoff energy. There is no ‘correct’ value of E_{cut} , rather, it depends on the system and the desired accuracy of the calculation. Usually one requests a certain accuracy for the total energy or a system-characteristic energy-difference and increases E_{cut} until the calculations converged to the requested accuracy (see Appendix A). Note that the maximum \mathbf{G} -value and thus the maximum energy of the electronic states in a plane-wave basis-set increases with the number of plane waves included. This allows one to create a sufficiently large basis set systematically by increasing the cutoff energy E_{cut} and include as many plane waves as required. In contrast to this, a basis set of localized orbitals is an expansion in angular momentum eigenstates that does not allow a systematic creation of a sufficiently large basis set.

Plane-wave representation of Kohn-Sham orbitals The usage of plane-waves as a basis-set (Eq. 2.24) to represent the Kohn-Sham orbitals $\psi_i(\mathbf{r})$ for a periodic system reduces the Kohn-Sham equations (Eq. 2.16-2.19) after an integration over \mathbf{r} to a particularly simple expression:

$$\sum_{\mathbf{G}'} \left[\frac{\hbar^2}{2m} |\mathbf{k} + \mathbf{G}|^2 \delta_{\mathbf{G}\mathbf{G}'} + V_{\text{ion}}(\mathbf{G} - \mathbf{G}') + V_{\text{H}}(\mathbf{G} - \mathbf{G}') + V_{\text{xc}}(\mathbf{G} - \mathbf{G}') \right] c_{i,\mathbf{k}+\mathbf{G}'} = \varepsilon_i c_{i,\mathbf{k}+\mathbf{G}}. \quad (2.26)$$

Here the kinetic energy is diagonal and the various potentials are given in terms of their Fourier transforms. This equation is solved by the diagonalization of the Hamiltonian matrix given in brackets. The required computing time depends on the rank of the Hamiltonian matrix which increases with the cutoff radius E_{cut} . The matrix rank can be reduced by the

pseudo-potential approximation (Sec. 2.3) that allows one to neglect the chemically inert core electrons in the calculation. The diagonalization of the Hamiltonian is the most expensive task within a density-functional calculation and requires approaches that are far more sophisticated than just applying conventional matrix diagonalization algorithms.

2.3 Electron-Ion Interaction: Pseudo-Potentials

The tightly bound wavefunctions of the core-electrons and the rapidly oscillating wavefunctions of the valence-electrons in the core-region are difficult to represent with Gaussians or plane-waves. With increasing atomic number, the number of contributions from core-electrons to the total energy increases. This gives rise to a smaller ratio between differences in total energies and the total energy of similar sized systems one is typically interested in. This is effectively a loss of relative accuracy. The basic idea of pseudo-potential theory is to distinguish between core and valence electrons and to treat them in a different way. The physical motivation is the fact that the highly localized core wavefunctions cannot take part in the atomic bonding. The core-electrons are removed and the ionic potential and the wavefunctions of the valence-electrons are replaced by a pseudo potential and pseudo wavefunctions. Outside a certain core-region they are identical, but inside this region the pseudo potential is weaker and the pseudo wavefunctions have less or no nodes and can thus be represented by a smaller set of plane waves than the true valence wavefunction. This is schematically shown in Fig. 2.1. The shape (hardness) of the atomic pseudo potentials determines the size of the

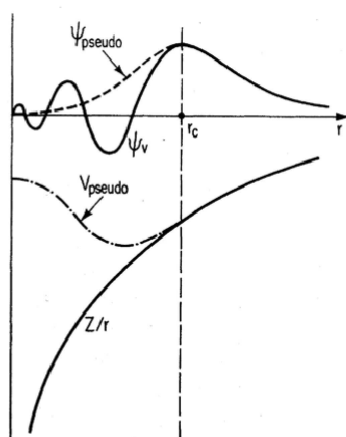


Abbildung 2.1:

Schematic illustration of all-electron (solid lines) and pseudo-electron (dashed lines) potentials and their corresponding wave-functions. The core cutoff radius at which all-electron and pseudo-electron values match is denoted by r_c . [46]

basis set that is required for a calculation. Consequently, the art of constructing a pseudo potential is to find a ‘soft’ shape which minimizes the numerical costs while retaining the accuracy of the approach. At the same time the pseudo wave-functions must yield the same integrated charge inside the core cutoff radius as the corresponding all-electron wave-function

to reproduce the scattering properties of the real atom (*norm-conservation*). Furthermore, it must describe different bonding configurations accurately (*transferability*). Formally the pseudo potentials can be written in a semi-local form in terms of a local pseudo potential $V^{\text{loc}}(r)$ and l -dependent components $\delta V_l^{\text{ps}}(r)$ that vanish outside the core cutoff radius. An alternative representation is the fully separable form with a fully non-local short-range term that is usually used in plane-wave calculations because of its better scaling with system-size. The ghost-states that are possibly introduced by the transformation from the semi-local to the fully separable form can be traced and removed. The transferability and thus the validity of the pseudo potentials in different bonding environments depends on the choice of the core cutoff radius, the linearization of the core-valence exchange-correlation, the frozen-core approximation and the transformation from the semi-local into the fully separable form of the pseudo potential. The pseudo potentials used in this work are generated with the program fhi98PP [60]. They are derived from a scalar-relativistic all-electron calculation of a free atom as reference state. There are separate pseudo potentials for calculations with LDA and GGA descriptions of the exchange-correlation functional. The linearization of the exchange and correlation between core and valence electrons in pseudo-potential calculations can result in systematic errors as compared to the all-electron approach. This can be accounted for by the *non-linear core-correction* [61] which is especially important for group I and II elements and for magnetic systems.

2.4 Minimization of the Kohn-Sham Energy

The Kohn-Sham equations are considered to be solved self-consistently, when the charge density that would be produced by the Kohn-Sham-orbitals gives rise to the same potential that was used to determine these orbitals. A density-functional calculation starts with selecting or creating the pseudo potentials for the electron-ion interaction. Then initial values for the wavefunctions and the electronic density are guessed: $\psi_i^{(0)}(\mathbf{r})$ and $\rho^{(0)}(\mathbf{r})$. The Kohn-Sham energy functional is minimized by iteratively improving the wavefunctions $\psi_i^{(n)}(\mathbf{r})$ with appropriate algorithms (e.g. Damped Joannopoulos, Williams-Soler, conjugate gradients).

2.5 Forces in the Ionic System

The solution of the time-independent Schrödinger equation gives the system's energy and wavefunction for the current configuration of fixed ion positions. The determination of the equilibrium geometry and dynamic simulations require the knowledge of the forces that are acting on the ions in the system. The expensive calculation of forces via a finite-difference scheme of the energy can be avoided through the Hellmann-Feynman theorem [62].

Let λ be a parameter in the Hamiltonian with an eigenfunction $|\Psi\rangle$. Treating the total energy with first order perturbation theory gives the Hellmann-Feynman theorem in its

differential form

$$\frac{dE}{d\lambda} = \frac{\langle \Psi | \partial \mathbf{H} / \partial \lambda | \Psi \rangle}{\langle \Psi | \Psi \rangle}. \quad (2.27)$$

Consider the parameter λ as the Cartesian coordinate X_α of the nucleus α and no external fields, then the Hellmann-Feynman theorem yields

$$\frac{dE}{dX_\alpha} = - \sum_{\beta \neq \alpha} \frac{Z_\alpha Z_\beta}{R_{\alpha\beta}^3} (X_\alpha - X_\beta) - Z_\alpha \int \rho(\mathbf{r}_1) \frac{(x_1 - X_\alpha)}{r_{1\alpha}^3} d\mathbf{r}_1. \quad (2.28)$$

This expression of the force on the nucleus α due to the other nuclei and the electron density is nothing but the expression that would be derived from purely classical electrostatic interaction. The Hellmann-Feynman theorem allows one to calculate the forces on the nuclei directly from the nuclear configuration in question and does not require the consideration of two or more different neighboring configurations to derive the forces from the slope of the energy-curve. Equation 2.28 holds true only for pure Coulomb potentials, i.e. all-electron calculations. With pseudo potentials in a fully separable form the Hamiltonian separates in local and non-local contributions from the pseudo-potential interaction. The explicit expression of the Hellmann-Feynman theorem then depends on the type of pseudo potential used [47, 60]. Strictly speaking, there is one term missing in Eq. 2.28 that comes from the derivative of the basis set with respect to the positions of the ions. This gives an additional contribution to the forces on the ions, called *Pulay forces* [63]. If one uses e.g. Gaussians as a basis set, the basis functions are ‘pinned’ to the position of the ions. This dependence results in a non-vanishing value of the aforesaid derivative and hence non-vanishing Pulay forces. The individual wavefunctions of a plane wave basis set, however, are independent of the ion positions, which results in vanishing Pulay forces.

Once the electronic ground-state is found, the forces on the ions can be calculated and used to relax a given structure. Usually equilibrium coordinates of the ions are not known a priori. Instead, a (reasonable) initial geometry is assumed, the forces on the ions are calculated and the ions are moved in the corresponding directions to minimize the total energy. In each step the self-consistent electronic structure is determined which corresponds to constraining the movement of the ions to the Born-Oppenheimer surface.

Kapitel 3

Thermodynamic Concepts in Surface Physics

In this chapter, we explain the thermodynamic concepts that are employed in the description of surfaces and of crystal growth later in this work. For further discussions of the relationship between thermodynamics and surface physics, we refer the interested reader to recent monographs [29, 64, 65].

3.1 Physical Events During Growth

Real surfaces under atmospheric conditions are complex systems with a non-periodic structure and numerous kinds of adsorbates. Still, one can often gain insight by combining the experimental findings of surfaces prepared in UHV with theoretical investigations of periodic surface unit cells. Clean semiconductor surfaces are nowadays prepared by e.g. cleavage, annealing, or condensation of monolayers on the surface with e.g. molecular-beam epitaxy (MBE) or metal-organic chemical vapor deposition (MOCVD). In all stages of preparation, a vast zoo of atomistic processes can possibly take place on the surface. Some of these events affect the sample mainly, such as diffusion (on terraces, along or across steps, by hopping or exchange), nucleation (of a 2D or 3D island), attachment and detachment (to steps, kinks, or islands), defect formation, and segregation. Other events, however, manifest an interplay of the surface with the gas phase, like desorption, adsorption, and dissociation.

A stable surface with no net growth is in thermodynamic equilibrium with the gas phase and the substrate. In growth experiments, however, it depends on the particular growth conditions if the resulting structures are ruled by thermodynamic equilibrium or by the kinetic interplay of atomistic processes. A kinetic description of growth under non-equilibrium conditions can be based on the effective rates of atomistic processes (see e.g. Ref. [66] for a description of this concept). A so-called *kinetic effect* is the situation that the atomistic

kinetics bring the system to a metastable state which is qualitatively different from the thermodynamic equilibrium. In Chap. 9 we present a DFT study of atomistic events that possibly trigger kinetic effects during QD growth. However, many aspects of QD growth and stability can be explained with a thermodynamic rationale, as we shall see in Chap. 7 and 8. These results refer to growth conditions close to thermodynamic equilibrium, i.e. to high mobilities of the deposited atoms, low deposition rates, or a sample annealing during a growth interruption. In the following section, we introduce the concept of surface energy that allows for a thermodynamic classification of crystal growth modes.

3.2 Surface Energy and Chemical Potential

A system is in the state of thermodynamic equilibrium at the minimum of the Gibbs free enthalpy $G(T, p, N)$ with respect to the inner variables at constant temperature T , pressure p , and number of particles N [67]. With the common Legendre transformations, this condition can be reformulated as the minimum of the Helmholtz free energy $F(T, V, N)$ at constant T , volume V , and N . The changes of these potentials due to infinitesimal changes in their according thermodynamic variables are

$$dG = -SdT + Vdp + \mu dN \quad \text{and} \quad dF = -SdT - pdV + \mu dN. \quad (3.1)$$

The chemical potential μ is given accordingly by

$$\mu = \left(\frac{\partial G}{\partial N} \right)_{T,p} = \left(\frac{\partial F}{\partial N} \right)_{T,V}. \quad (3.2)$$

The difference between the Helmholtz free energy and the Gibbs free enthalpy is the grand-canonical potential $\Omega(T, V, \mu)$. It reacts on infinitesimal changes in its thermodynamic variables as

$$d\Omega = -SdT - pdV - Nd\mu, \quad (3.3)$$

where we made use of the Gibbs-Duhem relation $SdT - Vdp + Nd\mu = 0$. This is the thermodynamic potential of choice for the description of surfaces, where processes typically happen at constant temperature T , pressure p , and chemical potential μ . With Gibbs' idea of dividing surfaces, a surface system can be decomposed in a region A that represents the solid with n_A particles in a volume V_A , a second region B that represents a vapor phase with n_B particles in a volume V_B , and a transition region S between A and B that mimics the surface. In the limit of a vanishing volume of S , the total volume and number of particles reduces to $V = V_A + V_B$ and $N = n_A + n_B$. The thermodynamic potentials F and G are then composed of the contributions from regions A and B , and a surface term. In the same limit, the Gibbs free enthalpy of the interface $G_S = N_S \mu_S$ vanishes as N_S goes to zero. Müller and

Saúl [64] gave an in-depth discussion of the different ways to derive this latter term. One of them [65, 68] is to express the grand-canonical potential Ω for constant pressure as

$$\Omega = -p(V_A + V_B) + \Omega_s \quad \text{where} \quad \Omega_s = \gamma A \quad (3.4)$$

to reflect the fact that the interface term should be proportional to the interface area A . The term γ , the *surface free energy*, is connected to the Helmholtz free energy of the surface by

$$F_S = \Omega_S = \gamma A \quad \text{and} \quad dF = \gamma dA + Ad\gamma. \quad (3.5)$$

Whereas the dividing surface in a single-component system can always be chosen such that N_S vanishes, this requirement can in general not be fulfilled simultaneously for all species of a multi-component system, like surfaces of III-V semiconductors studied in this work. For such systems, the Helmholtz free energy can be generalized to n components and the surface free energy per area and its differential reads

$$\gamma = \frac{1}{A}\Omega_S = \frac{1}{A} \left(F_S - \sum_{i=1}^n N_i^s \mu_i \right) \quad , \quad d\gamma = -\frac{1}{A} \left(S_S dT + \sum_{i=1}^n N_i^s d\mu_i \right) \quad (3.6)$$

where N_i^s is the excess of species i in the surface region. The relative stability of different structures of a surface with different stoichiometries, i.e. different ratios $N_1^s : N_2^s : \dots : N_n^s$, can thus be discussed by comparing the according surface free energies. A reasonable approximation [65] of many comparative studies of the surfaces of III-V semiconductors is to neglect the effects of pressure variation and entropy changes. The remaining variable is the dependence of the surface free energy on the chemical potentials.

The bulk chemical potentials of crystalline phases are the negative cohesive energies of the most stable structure at $T = 0$ and $p = 0$. The difference between the chemical potentials of a compound bulk system μ_{AB}^{bulk} and the according elemental bulk phases μ_{bulk}^A and μ_{bulk}^B defines the heat of formation of the compound

$$\Delta H_f^{AB} = - \left(\mu_{AB}^{bulk} - \mu_A^{bulk} - \mu_B^{bulk} \right). \quad (3.7)$$

This gives the range for the actual chemical potentials for a multi-component surface in equilibrium: Firstly, the chemical potential μ_i of each species i must be smaller than its bulk value μ_i^{bulk} , since its gas phase would condensate to the elemental bulk phase otherwise. Secondly, the j -rich conditions are fixed by $\Delta\mu_j = \mu_j - \mu_j^{bulk} = 0$. The chemical potentials of the species of a multi-component surface in equilibrium are thus

$$- \Delta H_f^{AB} \leq \Delta\mu_j \leq 0. \quad (3.8)$$

One possible representation of the grand-canonical potential of the surfaces of III-V semiconductors is then in terms of the majority species V:

$$\begin{aligned} \Omega_S(\Delta\mu_V) &= E(N_{IIIa}, N_{IIIb}, N_V) \\ &- \mu_{IIIa-V}^{bulk} N_{IIIa} - \mu_{IIIb-V}^{bulk} N_{IIIb} - \left(\mu_V^{bulk} + \Delta\mu_V \right) (N_V - N_{IIIa} - N_{IIIb}) \end{aligned} \quad (3.9)$$

where $E(N_{\text{IIIa}}, N_{\text{IIIb}}, N_{\text{V}})$ is the total internal energy, and the indices IIIa, IIIb, and V refer to Ga, In, and As, respectively. The relative stability of different structures of a surface, such as the reconstructions of III-V semiconductor surfaces, are compared in so-called surface phase diagrams that compile the different grand-canonical potentials with the according linear dependencies on the chemical potential(s). (A phase diagram for different reconstructions of GaAs(001) and InAs(001) is given in the right panel of Fig. 6.8). Practical aspects of calculating bulk chemical potentials and surface free energies with density-functional theory (Sec. 2.2) and the many-body potential (Sec. 5.2) are given in Sec. 5.4.2 and in the appendix A, respectively.

The surface free energy depends on the crystallographic orientation (hkl). This is commonly represented in the so-called Wulff plot [69, 70], a spherical plot of the surface energy with respect to the normal vector of the surface. The surface energy is a continuous function of the Miller indices and exhibits minima with discontinuous derivative (*cusps*) at those (hkl) that represent stable surfaces. Those orientations with a continuous derivative of the surface energy with respect to (hkl) form step structures of the most nearby stable surface orientation, these are the so-called *vicinal* surfaces. (These steps may even be extended to form a hill-and-valley structure for strongly varying surface energies [71].) The crystal inherent symmetries can strongly decrease the irreducible part of the Wulff plot. For cubic systems, the remaining part is the so-called *stereographic triangle*, a projection of the spheric segment between (001), (011), and (111) to the meridian plane. All surface orientations can be regarded as linear combinations of those in the corner. Despite the complexity of the high-index surfaces inside the stereographic triangle, some of them were found to have a surprisingly low surface energy, like GaAs(2 5 11) [72] surfaces, others were identified as dominant facets at early stages of QD growth, like InAs(137) [18]. The knowledge of all relevant surface free energies allows one to construct the equilibrium crystal-shape, that is given by the minimum total surface-energy at a certain chemical potential for a given amount of material.

The comparisons of QD nanostructures with different stoichiometry later in this work are based on the grand-canonical potential, too. These systems undergo deformations due to the lattice mismatch of GaAs and InAs, thereby introducing an additional dependency of the surface free energies on the surface strain. The concepts of stress and strain introduced in Sec. 4.1 allow one to interpret a change in the surface area as the consequence of a surface-stress tensor σ_{ij} that involves a strain tensor ε_{ij} . A subtle point of the application of Gibbs' concept of a dividing surface to the case of strained surfaces is that the localization of the dividing surface may change during deformations [64]: One can then either consider the localization as fixed (Eulerian coordinates) or instead treat the Gibbs's surface as attached to a piece of matter (Lagrangian coordinates). This discrimination plays no role at undeformed surfaces, but leads to e.g. a different stress dependence of surface energies in the case of deformations. In particular, the linear term $dF_S^{(1)}$ of an expansion of the Helmholtz free energy of the surface in terms of the strain tensor using either Eulerian (E) or Lagrangian (L)

coordinates reads

$$dF_S^{(1)} = A(\varepsilon)\gamma^E(\varepsilon) = A_0\gamma^L(\varepsilon) = A_0 \sum_{i,j} \sigma_{ij}\varepsilon_{ij}. \quad (3.10)$$

The relation between surface stress and surface energy reads in either coordinates

$$\sigma_{ij}^E = \gamma_0 + \left(\frac{\partial \gamma^E}{\partial \varepsilon_{ij}} \right)_{T,\mu}, \quad \sigma_{ij}^L = \left(\frac{\partial \gamma^L}{\partial \varepsilon_{ij}} \right)_{T,\mu}. \quad (3.11)$$

This so-called Shuttleworth equation [73] describes a fundamental difference between surfaces of solids and of liquids: The molecules of a liquid are mobile and can freely adjust to deformations without the boundary condition of a long-range order. Then the derivative of the surface energy with respect to deformations vanishes, leaving behind the equivalence of surface energy γ_0 and surface stress σ_{ij}^E (in Eulerian coordinates). In case of solids, however, this identification does not hold, and the trace of the surface stress given by

$$Tr(\sigma_{ij}^E) = 2\gamma_0 + \underbrace{\left(\frac{\partial \gamma^E}{\partial \varepsilon_{xx}} + \frac{\partial \gamma^E}{\partial \varepsilon_{yy}} \right)_{T,\mu}}_{\sigma_{xx}^E + \sigma_{yy}^E}, \quad Tr(\sigma_{ij}^L) = \underbrace{\left(\frac{\partial \gamma^L}{\partial \varepsilon_{xx}} + \frac{\partial \gamma^L}{\partial \varepsilon_{yy}} \right)_{T,\mu}}_{\sigma_{xx}^L + \sigma_{yy}^L} \quad (3.12)$$

determines if the surface exhibits intrinsic tensile ($\sigma_{xx} + \sigma_{yy} > 0$) or compressive ($\sigma_{xx} + \sigma_{yy} < 0$) surface strain. In Sec. 6.4, we will determine the intrinsic surface stress and the strain dependency of the surface energy for several GaAs and InAs surfaces numerically with the many-body potential developed in this work and compare them with results of previously performed DFT calculations [74]. This is an important test to verify that the many-body potential captures the strain stabilization of surfaces that appear as QD side facets (see e.g. Ref. [75, 76]). Note that a system under lateral strain $\varepsilon = \frac{\Delta x}{x} = \frac{\Delta y}{y}$ will relax perpendicular to the strain plane. In calculations of the intrinsic surface stress that employ slabs with fixed bottom layers, this elastic response needs to be known *a priori*. We will derive general expressions for such elastic response of cubic systems in Sec. 4.3 and apply these results in our numerical calculations.

3.3 Crystal Growth

The interplay of the dependence of the surface energy on the crystallographic orientation with the interface energy of a thin film on a substrate can be employed to classify elementary modes of crystal growth with a thermodynamic rationale. Bauer [77] opposed the surface energy of the substrate γ_s with the surface energies of a possibly deposited film γ_f and the energy γ_i of the interface that is shared among them. This allows one to distinguish three of the experimentally observed growth modes shown in the upper panel of Fig. 3.1:

Franck-van der Merwe	$\gamma_f + \gamma_i \leq \gamma_s$ for all θ
Volmer-Weber	$\gamma_f + \gamma_i > \gamma_s$
Stranski-Krastanov	$\gamma_f + \gamma_i \begin{cases} > \gamma_s & \theta \leq \theta_0 \\ \leq \gamma_s & \theta > \theta_0 \end{cases}$.

In the Franck-van der Merwe growth mode [78] the crystal grows in a layer by layer fashion, whereas in the Volmer-Weber growth mode [79] three-dimensional islands form. A combination of these two modes is the Stranski-Krastanov growth mode [80] that starts with the formation of a 2D film, the so-called *wetting layer*, and proceeds with the appearance of 3D islands after the film has reached a certain *critical thickness* θ_0 . A driving force for 3D island formation can be the lattice mismatch between substrate and deposited material due to a different lattice constant, studied in this work. The elastic energy stored in the strained wetting layer can be relieved in 3D islands by mechanisms of plastic relaxation, such as defect formation, or by elastic deformation of the upper island part. The latter process does not relieve the strain energy at the base of the islands, hence, one would always expect the formation of defects for a sufficiently large base area.

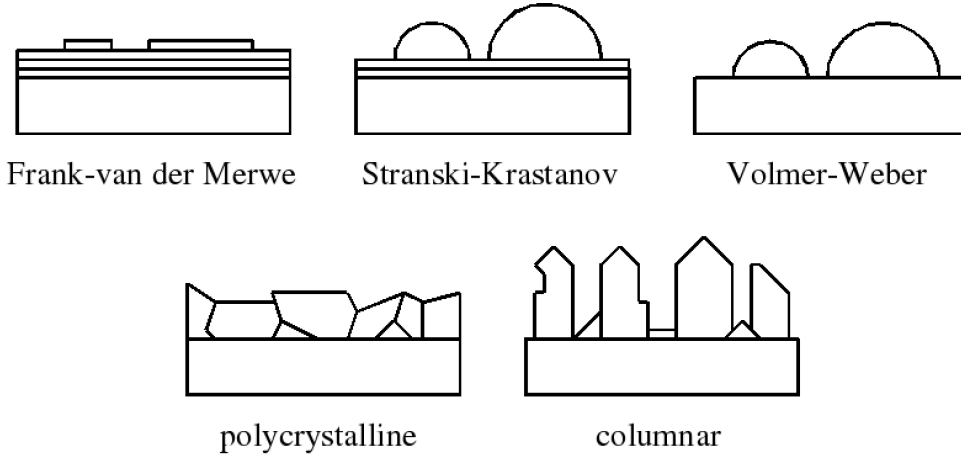


Abbildung 3.1: The appearance of the crystal growth modes in the upper panels can be distinguished by relations between surface and interface energies, γ_s , γ_f , and γ_i . The ones in the lower panel are due to kinetic effects.

The above classification covers all cases of the relationships between the surface energies, but is limited to thermodynamic equilibrium. In this context, this would require that the diffusion of the adsorbed atoms is able to establish the net mass transport required for the particular growth shape. Under experimental conditions that do not ensure thermodynamic equilibrium of the adsorbates with respect to diffusion, like e.g. low temperature and high deposition rate, the picture can change significantly. In fact, kinetic effects extend the variety of

growth modes by at least polycrystalline and columnar growth that are shown together with the aforementioned growth modes in Fig. 3.1. The experimentally observed sample features therefore leave some room for interpretation, particularly when it comes to distinguishing equilibrium and kinetic effects. In fact, the terms for the above growth modes are mostly applied in a phenomenological manner, based on experimental characterizations of the detailed atomic structure after the growth process with e.g. atomic force microscopy (AFM) or scanning tunneling microscopy (STM). (Appealing in-depth reviews of these methods were given recently by Giessibl [81] and Hofer et al. [82].) Additional degrees of freedom in III-V heteroepitaxy are e.g. the formation of ordered alloys [83], the dependence of the surface energies on the elemental chemical potentials in the growth chamber, intermixing and segregation processes, as well as strain effects due to the lattice mismatch of GaAs and InAs. One aspect of the latter is the influence of strain on the relative stability of differently shaped QDs.

3.4 Nucleation Theory

In this study we focus on the investigation of QD nanostructures as obtained in growth experiments close to thermodynamic equilibrium. In this case, the morphology of the system is determined by the minimum of the grand-canonical potential in each stage of evolution. The transition from one state of aggregation A (e.g. a vapor phase) to another state B (e.g. a crystal phase) starts out with the conglomeration of building units of the latter (e.g. crystallites) initiated by local density fluctuations of the starting phase [84]. A direct consequence of the locality of such fluctuations is that these conglomerates have a finite size and are thus accompanied by energy contributions from broken bonds. The fluctuations are present even in the thermodynamic equilibrium of one state, but increase in approaching the phase equilibrium with equal chemical potentials $\mu_A = \mu_B$. As long as the initial state is more stable ($\mu_A < \mu_B$), these conglomerates will decay on the same time scale as the fluctuations. If, however, the final state becomes more stable ($\mu_B < \mu_A$) although the system is still in the initial state, *supersaturation* is reached. In this situation, the transition is determined by the balance between energy gain due to the formation of the stable state and energy cost due to the formation of broken bonds. The different dependency of these contributions from the volume of the conglomerate imposes effectively an energy barrier for the transition in terms of the grand-canonical potential. This maximum of the difference in grand-canonical potentials marks the volume of the *critical nucleus*, where the energy contributions are equal and the conglomerate can gain energy by either dissolving or continuing growth. Below or above this volume, the conglomerate can gain energy only by dissolving or continuing growth, respectively. Note that this concept allows one to distinguish between the critical nuclei for forming a 2D island on a surface, for forming a 3D island on a surface (e.g. in the Stranski-Krastanov growth mode), and for forming a certain shape of a 3D island out of another shape. In this study, we don't sample all possible configurations of equal size, but rather assume that the

most favorable final state exhibits the smallest barrier from the common initial state. To be more precise, in our calculation of the critical nucleus for the formation of a ‘hut’-shaped QD (Sec. 7.7) we vary the size of the QD under the constraint of an approximately constant shape. For Ge islands on Si(001) there is some experimental indication that islands with sizes of about the critical nucleus are already bound by those facets of the ‘hut’-shaped QD’s that finally forms [85]. The alternative mechanism of nucleationless formation of islands from morphological instabilities of the strained film was proposed for material combinations with small lattice-mismatch [86, 87].

Note that the concept of a (‘thermodynamic’) critical nucleus employed in this study describes the transition between two distinct states (e.g. film and ‘hut’-shaped QD). This is not to be confused with the (‘kinetic’) critical nucleus i^* of rate-equation approaches (see e.g. Ref.[66]), where i^* is the maximum number of atoms which is not yet stable against break-up. (In other words: A conglomerate of $i^* + 1$ atoms would be stable.) These concepts need to be distinguished, particularly for the case that a group of atoms is larger than the ‘kinetic’ critical nucleus, but smaller than the ‘thermodynamic’ critical nucleus for the formation of a 3D island: Then the ‘kinetically stable’ 2D island would correspond to a ‘thermodynamically unstable’ 3D island.

Our investigations of thermodynamic nucleation of 3D islands (Chap. 7 and 8) are footed on *classical nucleation theory*. An instructive case is the formation of a homogenous liquid droplet from a vapor phase [84]. The resulting change in the thermodynamic potential is

$$G_1 = \mu_v n_v \quad \rightarrow \quad G_2 = \mu_v (n_v - n_l) + \mu_l n_l + \gamma_l A_1 \quad (3.13)$$

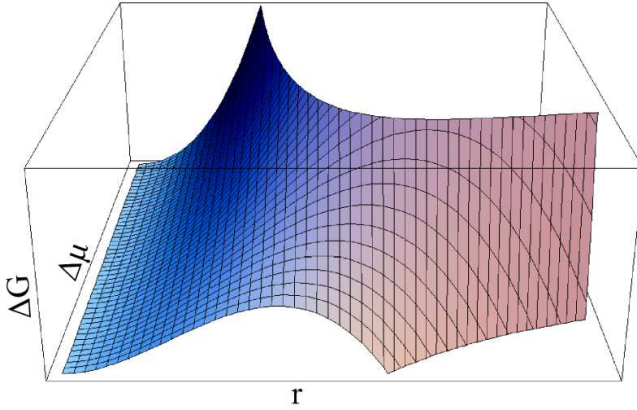
where $\mu_{l,v}$ and $n_{l,v}$ are the chemical potentials and the numbers of particles in the liquid and vapor phase, respectively. For simplicity, we assumed that the surface free energy γ_l is constant at all points of the droplet surface A_1 . The difference in the thermodynamic potential $\Delta G = G_2 - G_1$ in terms of the radius r of the droplet reads

$$\Delta G = -n_l(\mu_v - \mu_l) + \gamma_l A_1 = -\frac{4\pi r^3}{3v_l} \Delta\mu + \gamma_l 4\pi r^2 \quad (3.14)$$

with the volume per particle in the liquid v_l and $\Delta\mu = \mu_v - \mu_l$. This quantity is shown in Fig. 3.2 as a function of the droplet radius and the difference in chemical potentials. In the regime of liquid stability ($\Delta\mu < 0$) ΔG is monotonically increasing, thus the system can gain energy by the nucleus decay for all droplet radii. In a supersaturated situation ($\Delta\mu > 0$), however, ΔG exhibits a maximum, the critical nucleus, at

$$r_c = \frac{2\gamma_l v_l}{\Delta\mu}, \quad \Delta G(r_c) = \frac{16\pi}{3} \frac{\gamma_l^3 v_l^2}{\Delta\mu^2} = \frac{1}{3} \gamma_l A. \quad (3.15)$$

A droplet of the critical radius r_c can gain energy by either growing or decaying. Smaller nuclei tend to decay whereas larger ones are most likely to grow further. The critical radius r_c and

**Abbildung 3.2:**

The formation energy ΔG of a liquid droplet from a vapor phase depends on the droplet radius r and the difference in chemical potentials $\Delta\mu$. In classical nucleation-theory, the critical nucleus is given by the maximum of ΔG . Additional influences that affect the critical nucleus, such as elastic interactions in stacked QD layers (Fig. 8.9), can be interpreted as an effective change of $\Delta\mu$.

the energy barrier $\Delta G(r_c)$ for the formation of a droplet of a radius r_c depend quantitatively on the difference of chemical potentials. In Sec. 8.3.4 we will use this dependence to interpret the elastic interaction energy in a stack of QD layers as an effective chemical potential.

The application of classical nucleation-theory to semiconductor heterostructures involves several complications: The surface energy of a crystal is by no means a constant, but instead an anisotropic function of the orientation given by the Wulff construction denoted above. This implies the formation of edges and kinks of length L_j that appear as additional (positive) energy contributions κ_j . Furthermore, there can be reconstructions of different stoichiometry for the same orientation that possibly result in a piece-wise defined linear dependency of the surface energy on the chemical potential. The strain tensor that is due to the lattice mismatch of InAs and GaAs causes additional effects that can play a major role: The surface energies can exhibit a different dependency on the strain tensor. Furthermore, the amount of energy that is released by elastic relaxation depends on the particular shape and morphology of the homogenous film or QD, and groups of QDs interact among themselves by long-range elastic forces.

Previous studies (see e.g. Ref. [40]) combined the strain tensor as obtained from continuum-elasticity theory with density-functional theory calculations of the surface energies and their dependencies on (biaxial) strain. This approach is valid for large enough QDs (i.e. more than 5000-10000 atoms) and so far neglected the contributions from edges and kinks, but could still provide great insight to QD growth. In this work, we account for all these contributions simultaneously with the many-body potential developed in Chap. 5. Our results for the critical nucleus of 3D island formation, elastic interaction of QDs, and a transition between two different 3D shapes are presented in Chap. 7. The influence of vertically stacked QDs on the size of the critical nucleus is studied in Chap. 8.

Kapitel 4

Continuum-Elasticity Theory and Atomistic Strain

The lattice mismatch between two materials can lead to the Stranski-Krastanov growth mode described in the previous section. Thereby, the island, the wetting layer and the substrate undergo elastic deformations that depend on the material properties, the crystallographic orientation of the substrate, and the island shape. In this chapter, we will expound those elements of *continuum-elasticity theory* (CET) that are needed to describe such deformations of continuous media, and how to determine them within atomistic approaches. The particular properties of GaAs and InAs, and a detailed investigation of the deformations accompanying InAs QDs on GaAs(001) substrates are given in Sec. 6 and Sec. 8, respectively.

4.1 Introduction

Continuum-elasticity theory describes the change of shapes of continuous media upon external forces. This deformation is characterized by relations to the undeformed medium that serves as reference. The fundamental quantity is the displacement vector \mathbf{u} between the initial position $\mathbf{R} = (x_1, x_2, x_3)$ and the final position $\mathbf{R}' = (x'_1, x'_2, x'_3)$ of a point in the continuous medium:

$$\mathbf{u} := \mathbf{R}' - \mathbf{R}. \quad (4.1)$$

The deformation in a volume V of the medium is then completely given by the values of $\mathbf{u}(\mathbf{r})$ for every point \mathbf{r} in the volume V . The assumption of a continuous medium allows one to define the displacement vector at $\mathbf{r} + \delta\mathbf{r}$ in an infinitesimal neighborhood δV of point \mathbf{r} . For small displacements it can be written as [88]

$$u_i(\mathbf{r} + \delta\mathbf{r}) = u_i(\mathbf{r}) + \frac{\partial u_i(\mathbf{r})}{\partial x_1} \delta x_1 + \frac{\partial u_i(\mathbf{r})}{\partial x_2} \delta x_2 + \frac{\partial u_i(\mathbf{r})}{\partial x_3} \delta x_3, \quad i = 1, 2, 3. \quad (4.2)$$

The partial derivatives $\partial_j u_i = \partial u_i / \partial x_j$ describe the overall distortion of the media that can be decomposed to deformation and rigid rotation by symmetrization and anti-symmetrization, respectively,

$$\varepsilon_{ij} = \frac{1}{2} \left(\frac{\partial u_i(\mathbf{r})}{\partial x_j} + \frac{\partial u_j(\mathbf{r})}{\partial x_i} \right), \quad \omega_{ij} = \frac{1}{2} \left(\frac{\partial u_i(\mathbf{r})}{\partial x_j} - \frac{\partial u_j(\mathbf{r})}{\partial x_i} \right). \quad (4.3)$$

The symmetric part ε is called the *strain tensor*. The internal energy $E(V, \varepsilon)$ of a crystal with unstrained volume V can be expanded in terms of the strain tensor:

$$E(V, \varepsilon) = E(V) + V \sum_{i,j=1}^3 \sigma_{ij} \varepsilon_{ij} + \frac{V}{2} \sum_{i,j,k,l=1}^3 \varepsilon_{ij} c_{ijkl} \varepsilon_{kl} + \dots \quad (4.4)$$

where the *stress tensor* σ and the (adiabatic) *elastic constants* c_{ijkl} are given by

$$\sigma_{ij} = \frac{1}{V} \left(\frac{\partial E(V, \varepsilon)}{\partial \varepsilon_{ij}} \right) \Bigg|_{\varepsilon=0}, \quad c_{ijkl} = \frac{1}{V} \left(\frac{\partial^2 E(V, \varepsilon)}{\partial \varepsilon_{ij} \partial \varepsilon_{kl}} \right) \Bigg|_{\varepsilon=0}. \quad (4.5)$$

(The isothermic elastic constants are given similarly by an expansion of the Helmholtz free energy [89].) The minimum of the internal energy in the above truncated expansion at constant volume and entropy relates strain and stress in a tensor formulation of Hooke's law:

$$\sigma_{ij} = c_{ijkl} \varepsilon_{kl}. \quad (4.6)$$

Note, that the stress tensor σ_{ij} is symmetric due to its definition as derivative of the total internal energy with respect to the symmetric strain tensor ε in Eq. 4.5. The elastic constants c_{ijkl} are relating two symmetric tensors and are thus symmetric with respect to the two pairs of indices. These inner tensor symmetries strongly reduce the number of independent tensor components and allow the introduction of a more compact notation. In this so-called Voigt notation the indices are transformed like 11 \rightarrow 1, 22 \rightarrow 2, 33 \rightarrow 3, 23 or 32 \rightarrow 4, 13 or 31 \rightarrow 5, and 12 or 21 \rightarrow 6.

The above framework can be extended by a variational principle through employing minimum principles of thermodynamic potentials. This will allow the calculation of the equilibrium strain tensor for a given stress state. In this context, stress and strain form a pair of thermodynamic variables, similar to pressure and volume. For the focus of this work, the variables of choice are temperature and strain, rather than entropy and stress. Accordingly, the characteristic thermodynamic potential is the free energy given by

$$F = E - TS \quad \text{and} \quad dF = \sigma_{ij} d\varepsilon_{ij} - SdT. \quad (4.7)$$

The elastic response of the material to a certain stress is then determined by the minimum of the free energy with respect to the possible relaxations. For isothermal deformations the elastic energy reads

$$F = \frac{1}{2} c_{ijkl} \varepsilon_{ij} \varepsilon_{kl}. \quad (4.8)$$

For most crystal structures, the inherent symmetries can be used to determine a strongly simplified expression [88] in terms of the strain tensor.

4.2 Elastic Constants of Cubic Systems

For structures with cubic symmetry that are studied in this work, the elastic energy density given in Eq. 4.8 reduces to [88]

$$F(\varepsilon) = \frac{c_{11}}{2}(\varepsilon_{xx}^2 + \varepsilon_{yy}^2 + \varepsilon_{zz}^2) + 2c_{44}(\varepsilon_{xy}^2 + \varepsilon_{xz}^2 + \varepsilon_{yz}^2) + c_{12}(\varepsilon_{xx}\varepsilon_{yy} + \varepsilon_{xx}\varepsilon_{zz} + \varepsilon_{yy}\varepsilon_{zz}) \quad (4.9)$$

where the elastic constants are given in Voigt notation. For a properly chosen strain-tensor the elastic energy in Eq. 4.4 can be solved for the elastic constants by taking the second derivative of the internal energy. This can be done numerically with a unit cell based on the equilibrium lattice constant that is deformed according to the applied strain tensor ε

$$\mathbf{x}' = [1 + \varepsilon]\mathbf{x} = \left[1 + \begin{pmatrix} \varepsilon_{xx} & \varepsilon_{xy} & \varepsilon_{xz} \\ \varepsilon_{xy} & \varepsilon_{yy} & \varepsilon_{yz} \\ \varepsilon_{xz} & \varepsilon_{yz} & \varepsilon_{zz} \end{pmatrix} \right] \mathbf{x} \quad (4.10)$$

and the internal energy is minimized by relaxing all internal degrees of freedom. The elastic constants can then be calculated with employing e.g. the following strain tensors:

$$\begin{aligned} \varepsilon_{xx} = x & & \partial_x^2 E &= c_{11} \cdot V_0 \\ \varepsilon_{xx} = \varepsilon_{yy} = \varepsilon_{zz} = x & & \partial_x^2 E &= (c_{11} + 2c_{12}) \cdot 3V_0 \\ \varepsilon_{zz} = \frac{x^2}{4-x^2}, \varepsilon_{yz} = x & & \partial_x^2 E &= c_{44}^{(0)} \cdot V_0 \end{aligned} \quad (4.11)$$

where we used $\partial_x^2 E = \partial^2 E / \partial x^2$ for brevity. The second derivative can be determined numerically by e.g. a finite difference expression for numerically well-behaved data (like from a many-body potential, see Chap. 2) or a fit to a polynomial (for numerically less well-behaved data, like from DFT calculations, see Sec. 2).

Note that in the strain tensor for the calculation of c_{44}^0 the four tetragonal bonds of an atom in a zinc blende unit cell are no longer equivalent, which leads to a relaxation of the anion lattice with respect to the cation lattice along the crystallographic direction [111]. The elastic constants with and without consideration of the internal relaxation are denoted c_{44} and $c_{44}^{(0)}$, respectively. The relative relaxation is given by the Kleinman parameter ξ which can vary from 0 for no internal relaxation to 1 when all four bonds adopt equal length [90]. The numerical calculation of c_{44} is more tedious and would in principle require internal relaxation for each point that enters the numerical derivative, but Nielsen et al. [91, 92] derived a procedure that reduces the numerical effort to only two independent calculations. They showed that

within adiabatic and harmonic approximations, a displacement \mathbf{u}_τ and a strain ε increase the energy per unit cell with volume V with k atoms by

$$\Delta E = \frac{1}{2} \sum_{k,k'} \mathbf{u}_k \Phi(k, k') \mathbf{u}_{k'} + V \sum \mathbf{u}_k D(k) \varepsilon + \frac{1}{2} V \varepsilon c^{(0)} \varepsilon \quad (4.12)$$

with the tensors of force constants Φ , internal relaxation D , and elastic constants at vanishing internal strain $c^{(0)}$. In cubic crystals the above expression reduces for certain combinations of displacement and strain, particularly for $\mathbf{u} = u \cdot (1\ 1\ 1)$ and $\varepsilon_{\alpha\beta} = \frac{1}{2} \varepsilon_4 (1 - \delta_{\alpha\beta})$ the force reads:

$$\mathbf{F} = \mu \omega_\Gamma^2 \left[\zeta \frac{a}{4} \varepsilon_4 + u \right] \cdot \begin{pmatrix} 1 \\ 1 \\ 1 \end{pmatrix} = F \cdot \begin{pmatrix} 1 \\ 1 \\ 1 \end{pmatrix} \quad (4.13)$$

where μ is the reduced mass of the atoms, ω_Γ is the frequency of the TO phonon at the Γ point, and ζ is the Kleinman parameter. Similarly, the stress is given by

$$\sigma_{\alpha\beta} = \sigma_4 (1 - \delta_{\alpha\beta}) \quad \text{with} \quad \sigma_4 = c_{44}^{(0)} \varepsilon_4 + \Omega^{-1} \Phi \zeta \frac{a}{4} u. \quad (4.14)$$

The actual displacement for a given strain value ε_4 requires vanishing forces which yields the following stress-strain relation:

$$\sigma_4 = [c_{44}^{(0)} - \Omega^{-1} \Phi [\zeta \frac{a}{4}]^2] \varepsilon_4 = c_{44} \varepsilon_4. \quad (4.15)$$

Consequently, ω , c_{44} and ζ can be determined by applying firstly an atomic displacement $\mathbf{u} = u^{(1)}(1, 1, 1)$ and secondly a strain $\varepsilon = \varepsilon_4^{(2)}$ and calculating the resulting forces and stress:

$$I \quad u = u^{(1)}, \varepsilon = 0 \quad \rightarrow \quad \omega_\Gamma^2 = \frac{F^{(1)}}{u^{(1)} \mu} \quad \zeta^{(1)} = \frac{4\Omega \sigma^{(1)}}{a F^{(1)}} \quad (4.16)$$

$$II \quad u = 0, \varepsilon = \varepsilon_4^{(2)} \quad \rightarrow \quad \zeta^{(1,2)} = \frac{4u^{(1)} F^{(2)}}{a \varepsilon_4^{(2)} F^{(1)}}. \quad (4.17)$$

This procedure and the above strain tensors were used in this work to calculate the elastic constants with the many-body potential in Sec 6.1.

The elastic constants fully describe the elastic response of crystals. Additional commonly used quantities can be expressed in terms of these elastic constants: The bulk modulus B of cubic crystals can be determined by

$$B = (c_{11} + 2c_{12})/3 \quad (4.18)$$

or alternatively by applying isotropic strain ($\varepsilon_{xx} = \varepsilon_{yy} = \varepsilon_{zz} = x$) and determining the second derivative of the elastic energy directly or from fitting the latter to a polynomial. Expressing

the polynomial of the internal energy not in terms of the strain tensor, but rather in terms of the volume and pressure of the unit cell yields the Murnaghan equation-of-state [93].

The knowledge of the values of the elastic constants and the minimum principle of the free energy given in Eq. 4.9 are the only prerequisites to profit from the strength of continuum-elasticity theory: Given e.g. an uniaxial external deformation, i.e. $\varepsilon = \delta_{zz}\varepsilon_0$, the elastic response in the xy -plane is given by

$$\frac{d}{d\nu}F(\varepsilon_0(\delta_{zz} - \nu\delta_{xx} - \nu\delta_{yy})) = 0 \quad (4.19)$$

which yields the *Poisson ratio* ν for uniaxial strain. One can show that it depends on the direction of strain \mathbf{n} . This can also be expressed in terms of the *Young modulus* Y

$$\nu(\mathbf{n}) = \frac{1}{2} \left[1 - \frac{Y(\mathbf{n})}{c_{11} + 2c_{12}} \right] \quad (4.20)$$

that depends on the direction of strain \mathbf{n} as

$$Y^{-1}(\mathbf{n}) = \frac{c_{11} + c_{12}}{(c_{11} + 2c_{12})(c_{11} - c_{12})} + \left(\frac{1}{c_{44}} - \frac{2}{c_{11} - c_{12}} \right) (n_x^2 n_y^2 + n_x^2 n_z^2 + n_y^2 n_z^2). \quad (4.21)$$

The direction dependence vanishes for $c_{44} = c_{11} - c_{12}$, in this case the material exhibits no *elastic anisotropy*.

4.3 Biaxial Strain in Systems with Cubic Symmetry

In analogy to the uniaxial case above, one can define a Poisson ratio for isotropic two-dimensional deformations, that we will refer to as biaxial deformations, in compliance with most previous works. This kind of deformation occurs in the defect-free semiconductor heterostructures studied in this work where the crystal lattices of both materials need to adapt, i.e. one of them may experience tensile and the other compressive strain. The elastic energy associated with such deformations is of great importance for the structural stability and often determines whether it is possible to obtain pseudomorphic growth. In fact, the elastic energy stored in the biaxial strained film of deposited material is the driving force for the occurrence of the Stranski-Krastanov growth mode. Furthermore, biaxial strained GeSi/Si heterostructures increase the charge carrier mobility in high-speed transistors, an effect that already reached the stage of application [94]. The use of epitaxial films on substrates with high-index orientation [23, 95, 96] makes it desirable to have general expressions of the elastic response to planar deformations. Marcus et al. [97] demonstrated a general scheme to calculate the elastic response upon biaxial external deformations numerically. Nevertheless, analytic solutions in terms of the Miller indices of the strain plane exist only for a few selected cases in systems with cubic symmetry [98], and for thin films [99]. In this section, we

solve the problem of cubic systems under biaxial strain in linear-response CET and present general analytic expressions of the strain tensor, the Poisson ratio, and the elastic energy. These results enable us to investigate non-linear effects with DFT, presented later in this work in Sec. 6.2.

4.3.1 General Strain Tensor

Similar to the uniaxial case, the elastic relaxation upon biaxial strain in a plane (hkl) can be given in an orthogonal coordinate-system of the deformation with two axes (e_1, e_2) in the strain-plane (hkl) and a third (e_3) along the direction of relaxation [hkl]. The relation to the canonical coordinates can be given by a matrix \mathbf{T} :

$$\mathbf{T}(\mathbf{e}_1 \mathbf{e}_2 \mathbf{e}_3) = (\mathbf{e}_x \mathbf{e}_y \mathbf{e}_z). \quad (4.22)$$

The biaxial strain-tensor ε_s that transforms a position \mathbf{x}_s to \mathbf{x}'_s in this coordinate system of the deformation is

$$\mathbf{x}'_s = \varepsilon_s \mathbf{x}_s = \begin{pmatrix} \alpha_s & 0 & 0 \\ 0 & \alpha_s & 0 \\ 0 & 0 & -\nu\alpha_s \end{pmatrix} \mathbf{x}_s \quad (4.23)$$

where ν is the biaxial Poisson-ratio. A more general treatment is possible with introducing commensurability constraints [100, 101], but for the comparison with DFT calculations, we focus on the case of isotropic planar strain. The strain tensor ε_s can be combined with the free energy of Eq. 4.9 by transforming ε_s from the coordinate system of the deformation to the canonical coordinate-system of the crystal. This is advantageous as it allows us to use the well-known structure-specific expressions of the free energy in canonical coordinates. The above matrix \mathbf{T} transforms also the strain tensor ε_s in deformation coordinates $\{\mathbf{e}_1, \mathbf{e}_2, \mathbf{e}_3\}$ to the corresponding strain tensor ε in canonical coordinates $\{\mathbf{e}_x, \mathbf{e}_y, \mathbf{e}_z\}$. This yields the free energy in deformation coordinates

$$F(\varepsilon) = F(\mathbf{T}\varepsilon_s\mathbf{T}^T). \quad (4.24)$$

Together with the structure-specific free energy and the values of the elastic constants, Eq. 4.24 allows us to calculate the elastic response upon biaxial strain in arbitrary planes by determining the minimum of the elastic energy with respect to the biaxial Poisson-ratio:

$$\frac{\partial}{\partial \nu} F(\varepsilon) = 0. \quad (4.25)$$

A general procedure of transforming the strain tensor to canonical coordinates with a tensor-transformation law [102] was described in detail previously [97]. With this scheme Marcus [98] determined the elastic energy of cubic systems upon biaxial strain analytically for low-index planes and numerically for several high-index planes.

A rigorous analytic derivation requires the knowledge of the transformation matrix \mathbf{T} that is not unique for a given strain plane due to the freedom to choose the in-plane vectors \mathbf{e}_1 and \mathbf{e}_2 . But for the case of biaxial strain, i.e. for two orthogonal deformations of equal absolute value, the strain tensor is invariant under the particular choice of \mathbf{e}_1 and \mathbf{e}_2 . In other words, the elastic response can be calculated uniquely for a given plane of a structure with any choice of \mathbf{e}_1 and \mathbf{e}_2 , and thus depends solely on the elastic constants of the material, its crystal structure, and the normal of the biaxial-strain plane $\mathbf{e}_3 \parallel [hkl]$. This was already noted by Marcus [98] for the elastic energy. Without loss of generality we choose an orthonormal deformation coordinate-system that allows us to derive easily a general transformation matrix \mathbf{T} , similar to Lee [99]:

$$\mathbf{e}_1 = \mathbf{e}_2 \times \mathbf{e}_3, \quad \mathbf{e}_2 = \frac{1}{n_2} \begin{pmatrix} kl \\ hl \\ -2hk \end{pmatrix}, \quad \mathbf{e}_3 = \frac{1}{n_3} \begin{pmatrix} h \\ k \\ l \end{pmatrix} \quad (4.26)$$

with the normalization $n_2 = \sqrt{k^2l^2 + h^2l^2 + 4h^2k^2}$ and $n_3 = \sqrt{h^2 + k^2 + l^2}$. This defines the transformation matrix \mathbf{T} that allows us to transform the strain tensor from deformation coordinates to canonical coordinates:

$$\begin{aligned} \varepsilon &= \mathbf{T} \begin{pmatrix} \alpha_s & 0 & 0 \\ 0 & \alpha_s & 0 \\ 0 & 0 & -\nu\alpha_s \end{pmatrix} \mathbf{T}^T \\ &= -\frac{\alpha_s}{h^2 + k^2 + l^2} \begin{pmatrix} \nu h^2 - (k^2 + l^2) & hk(\nu + 1) & hl(\nu + 1) \\ hk(\nu + 1) & \nu k^2 - (h^2 + l^2) & kl(\nu + 1) \\ hl(\nu + 1) & kl(\nu + 1) & \nu l^2 - (h^2 + k^2) \end{pmatrix}. \end{aligned} \quad (4.27)$$

This strain tensor is obviously not altered by multiplying the Miller-indices with a common prefactor. Note, that the cubic symmetry of the crystal lattice enters the transformation matrix in the definition of the orthonormal deformation coordinate-system in Eq. 4.26. Hence the canonic representation of the strain tensor as given in Eq. 4.27 holds true only for materials with cubic symmetry. The corresponding result for non-cubic systems can in principle be obtained in a similar way using a proper orthonormal basis in Eq. 4.26.

4.3.2 General Linear Elastic Response

With the elastic energy of Eq. 4.9 and the canonic strain tensor of Eq. 4.27, we determined the elastic response of a system with cubic symmetry upon a biaxial deformation by minimizing the elastic energy with respect to the Poisson ratio ν , according to Eq. 4.25 with *MATHEMATICA* [103]. The resulting Poisson ratio and elastic energy upon biaxial strain in the (hkl) plane depend only on the elastic constants c_{ij} , the strain plane (hkl) , the biaxial

strain α_s , and the strained volume V :

$$\begin{aligned} \nu &= 2 \cdot \frac{c_{12}(h^4 + k^4 + l^4) + (c_{11} + c_{12} - 2c_{44})(h^2k^2 + h^2l^2 + k^2l^2)}{c_{11}(h^4 + k^4 + l^4) + 2(c_{12} + 2c_{44})(h^2k^2 + h^2l^2 + k^2l^2)} \\ &=: \nu^{(0)} \end{aligned} \quad (4.28)$$

$$\begin{aligned} F(\alpha^s) &= (c_{11} + 2c_{12}) \cdot \alpha_s^2 \cdot V \cdot \\ &\quad \frac{[(c_{11} - c_{12})(h^4 + k^4 + l^4) - (c_{11} - c_{12} - 6c_{44})(h^2k^2 + h^2l^2 + k^2l^2)]}{c_{11}(h^4 + k^4 + l^4) + 2(c_{12} + 2c_{44})(h^2k^2 + h^2l^2 + k^2l^2)}. \end{aligned} \quad (4.29)$$

These analytic results hold true for arbitrary biaxial strain and every material with cubic symmetry. Materials are usually called elastically isotropic if $2c_{44} = c_{11} - c_{12}$, i.e. if the Poisson ratio for uniaxial strain is independent from the direction of strain. The above equations show that for such materials the Poisson ratio for biaxial strain is independent from the strain plane, too. In that sense, elastic anisotropy with respect to uniaxial strain implies elastic anisotropy with respect to biaxial strain. Note that the analytic results of both, the Poisson ratio and the elastic energy are identical for values of (hkl) with constant ratio m given by

$$m = \frac{h^4 + k^4 + l^4}{h^2k^2 + h^2l^2 + k^2l^2} \quad (4.30)$$

such as (110), (211), and (321). The analytic Poisson-ratios for (100) and (110) from Eq. 4.28 are identical to those given in previous works [88, 98, 104]. In a comparison of the elastic-energy density upon biaxial strain in Fe, Cu, V, and Ni as obtained previously by Marcus [98], and our analytic expression with the same elastic constants, we find identical results for (100), (110), and (111), but different values for (211), (311), (310), (321), and (331).

The cubic symmetry of the crystal lattice is reflected in the invariance of the biaxial Poisson ratio and the elastic energy under exchange of the Miller indices of the strain normal. This symmetry is also apparent in Fig. 4.1 that shows a spherical plot of both quantities as a function of the normal vector of the biaxial strain-plane. These figures were obtained by multiplying the normalized vector (hkl) with ν or F as obtained from Eq. 4.28 and 4.29, respectively, using the experimentally observed elastic constants of GaAs and InAs as given in Ref [105]. The comparison of biaxial and uniaxial Poisson ratio of GaAs and InAs in the right panel shows that they are qualitatively very similar, but differ quantitatively by about a factor of two. Figure 4.1 illustrates the relationship between the elastic relaxation and the elastic energy: Biaxial strain in a plane perpendicular to an elastically soft direction, e.g. (001), allows for a comparably large relaxation along the plane normal with comparably small elastic energy.

Note, that these results allow for an approximative calculation of the transition between *fcc* and *bcc* phases, the so-called Bain path (see e.g. Ref. [106]). For this purpose, the elastic

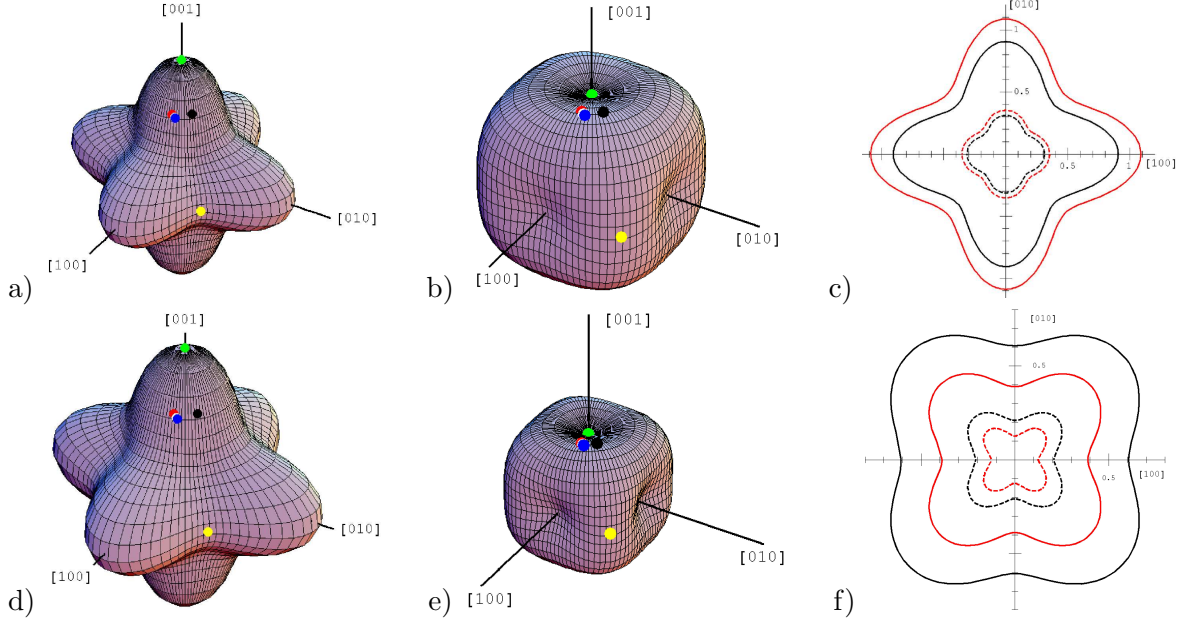


Abbildung 4.1: Poisson-ratio (left column) and elastic-energy density (middle column) of GaAs (top row) and InAs (bottom row) as an example of a cubic system under biaxial strain in arbitrary planes, together with the corresponding results for uniaxial strain (dashed lines in right column) in the $l = 0$ plane. The directional dependence corresponds to the normal vector of the strain plane. The colored dots mark selected orientations that will be discussed in Sec. 6.2: green= $(0\ 0\ 1)$, yellow= $(1\ 1\ 0)$, black= $(1\ 1\ 3)$, red= $(3\ 1\ 7)$, white= $(5\ 2\ 11)$, blue= $(7\ 3\ 15)$.

constants of the two cubic phases can be employed to calculate the elastic energy upon the particular biaxial strain along the path using Eq. 4.29. The quality of this (harmonic) approach will depend on the importance of non-linear elastic response.

4.4 Atomistic Strain-Tensor

Strain in a material system can affect several properties that are relevant for growth: It affects the surface energies [33], and can alter the relative stability of different surfaces [75] or different reconstructions of the same surface [107, 108]. Furthermore, strain can modify the energy barriers for surface diffusion, as observed both theoretically and experimentally (see e.g. Refs. [109, 110], or even alter the qualitative character of diffusion [111]. In addition, there are effects on a more mesoscopic level, such as the elastic interaction of steps [112] or islands [113]. Later in this work we will present our results of lateral and vertical elastic interaction of QDs, the latter effectively creating precursors for island nucleation (Sec. 8),

and discuss the strain dependence of diffusion on QD side facets (Sec. 9). Another aspect is that the change of the relative spatial position of cations and anions described by the strain tensor causes piezoelectric charges. For materials with non-negligible ionicity, this can have a strong impact on the electronic properties of nanostructures [114, 115, 116, 117], which is already used for band-gap engineering [94]. In this section we describe the determination of the strain tensor of heterostructures with InAs QDs that was provided for further usage in tight-binding calculations.

The strain tensor of a semiconductor nanostructure is often much more complex than the cases presented in the last sections. It can be determined numerically with both atomistic and continuum approaches (see e.g. Ref. [104] for a comparison). The latter are based on minimizing the internal energy in the equations of continuum-elasticity theory with the strain tensor as variable, and therefore naturally determine the strain tensor. In atomistic approaches, however, the internal energy of a structure is minimized by relaxing the positions of the atoms that are considered in the energy functional of the particular method, such that the strain tensor can be evaluated only afterwards. An assessment of local strain with Eq. 4.3 requires the comparison of a relaxed structure with a reference structure. Pryor et al. [104] gave a method for diamond and zinc blende lattices that compares the sides \mathbf{R}_{ij} of the strained tetrahedron formed by the four anion neighbors of a cation with those of the undistorted one \mathbf{R}_{ij}^0 as shown in Fig. 4.2 where the indices number the atoms.

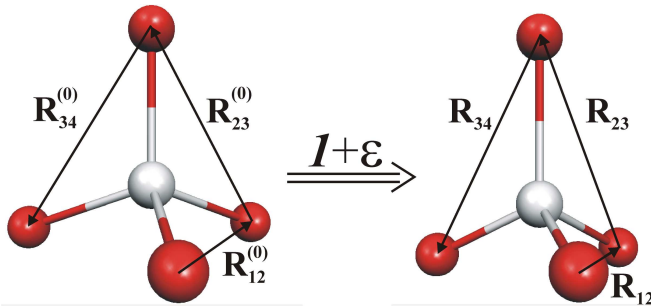


Abbildung 4.2:

The atomistic calculation of the strain tensor ϵ is based on the comparison of the sides \mathbf{R}^0 and \mathbf{R} of an ideal and a strained tetrahedron formed by the next-neighbor anions of a cation.

In general, the choice of the three considered tetrahedron sides is arbitrary as long as they are linearly independent. Note, that using a reference structure for a tetrahedron with As in the center and cations in the corners would require to determine systematically the structure of $\text{In}_x\text{Ga}_{1-x}\text{As}$ alloys, which is a field of research in itself. This scheme is applicable for heterostructures, too, as every In or Ga atom has four As neighbors in every compound

configuration. The local strain tensor of the distorted tetrahedron in this approach is

$$\begin{pmatrix} R_{12,x} & R_{23,x} & R_{34,x} \\ R_{12,y} & R_{23,y} & R_{34,y} \\ R_{12,z} & R_{23,z} & R_{34,z} \end{pmatrix} = \left[1 + \begin{pmatrix} \varepsilon_{xx} & \varepsilon_{yx} & \varepsilon_{zx} \\ \varepsilon_{xy} & \varepsilon_{yy} & \varepsilon_{zx} \\ \varepsilon_{xz} & \varepsilon_{xz} & \varepsilon_{zz} \end{pmatrix} \right] \cdot \begin{pmatrix} R_{12,x}^0 & R_{23,x}^0 & R_{34,x}^0 \\ R_{12,y}^0 & R_{23,y}^0 & R_{34,y}^0 \\ R_{12,z}^0 & R_{23,z}^0 & R_{34,z}^0 \end{pmatrix}. \quad (4.31)$$

The strain tensor is given in the same coordinate system as the atomic positions, therefore it might be necessary to either rotate the strain tensor to canonical coordinates or supply the distance vectors in the canonical coordinates of the crystal. In fact, we performed the latter transformation for free-standing QDs that oriented along the directions of the surface reconstructions, i.e. $\mathbf{e}_x = (110)$ and $\mathbf{e}_y = (1\bar{1}0)$. We used the following choice for the canonical \mathbf{R}^0 :

$$\{\mathbf{e}_{xyz}\} = a_0 \begin{pmatrix} 1 & 0 & 0 \\ 0 & 1 & 0 \\ 0 & 0 & 1 \end{pmatrix} \Rightarrow \{\mathbf{R}_0\} = \frac{a_0}{2} \begin{pmatrix} 1 & 0 & -1 \\ 1 & -1 & 1 \\ 0 & 1 & 0 \end{pmatrix}. \quad (4.32)$$

The strain tensor can be obtained from the $\{\mathbf{R}\}$ that corresponds to the position of the four anion neighbors of each cation and evaluating

$$\varepsilon = \{\mathbf{R}\} \cdot \{\mathbf{R}_0\}^{-1} - \mathbf{1}. \quad (4.33)$$

In this way, the atomistic strain tensor is given at the spatial positions of the relaxed cations, i.e. on a non-regular grid. Further processing like e.g. visualization and calculation of the piezoelectric potential usually require to interpolate the strain tensor from a non-regular to a regular grid. For the pictures shown later in this work, we used an interpolation with weighted Gaussian functions centered at the cation sites implemented by M. Winkelkemper, and a visualization tool developed by A. Schliwa.

Comparison: MBP vs Green's-Function Approach The strain tensor ε plays a crucial role during the self-assembled growth of lattice-mismatched QD nanostructures (see Chap. 7 and 8). Several approaches of calculating ε have been employed in previous studies, but only few quantitative comparisons of such methods are available (e.g. Ref. [104]). In a collaboration with R. Kunert and E. Schöll from the Technical University of Berlin, we compared the strain tensor as obtained with the atomistic method developed in this work (Chap. 5) with the results of a Green's function approach for a simple representative model structure [118]. The latter approach uses the numerically exact solution for the Green's tensor in k -space [119] in the homogeneous moduli approximation of continuum elasticity theory [120]. This method was successfully employed in previous studies of strain properties in various materials [121, 122].

As an example structure, we have chosen a circular plate-like inset of InAs with a radius of 29 Å embedded in a box of GaAs with dimensions of $L_x \times L_y \times L_z = 180 \text{ Å} \times 180 \text{ Å} \times 170 \text{ Å}$. This structure was relaxed with the many-body potential developed in this work (cf. Chap. 5

and App. B) until the maximum force on an atom in the system was below $0.01 \text{ meV}/\text{\AA}$. Then the atomistic strain tensor at the sites of the cations was calculated as described above, and interpolated onto a rectangular grid for ease of comparison. The compressed InAs inset appears as blue plate in the planar cuts of $Tr(\varepsilon)$ shown in the left panel of Fig. 4.3, surrounded by weakly affected GaAs. For a quantitative comparison with the strain tensor of the same structure, determined with the Green's function approach, we performed linescans along the (110) crystallographic direction in different heights above the InAs inset (right panel of Fig. 4.3).

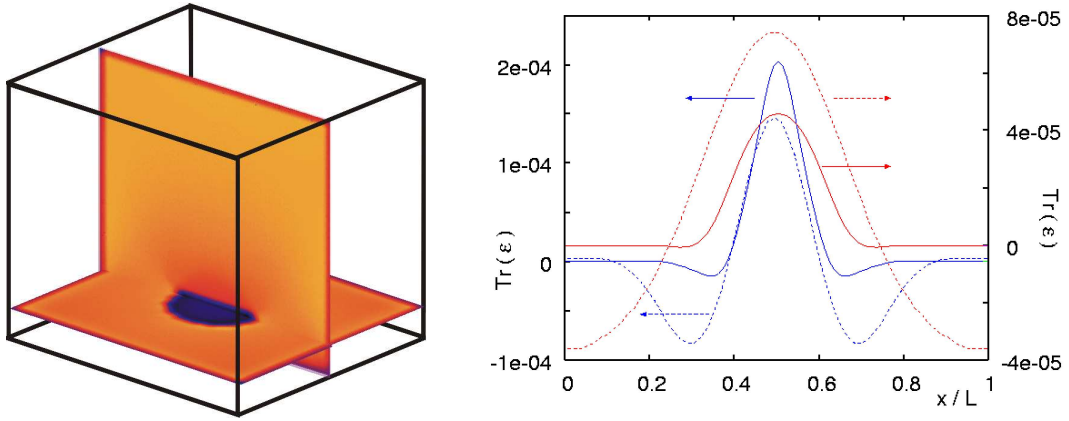


Abbildung 4.3: Comparison of $Tr(\varepsilon)$ for a simple InAs/GaAs heterostructure determined with the many-body potential developed in this work (right: dashed lines) and a Green's function approach (right: solid lines): The sample is a GaAs box with a circular monolayer inset of InAs that appears as blue plate in planar cuts of $Tr(\varepsilon)$ obtained with the prior method (left). Selected linescans (right) along the crystallographic direction (110) are in reasonable agreement in a height of 9 ML (blue) above the InAs inset, but show some discrepancy (text) in the border regions of weakly strained layers at a height of 17 ML (red).

Both methods yield an expansive strain of the central GaAs region that is directly above the InAs inset, and a similar range of values of $Tr(\varepsilon)$ in both investigated heights. The lateral extension of the region with $Tr(\varepsilon) > 0$ obtained by the two methods is in good agreement at a height of 9 ML (right panel: blue lines) and still reasonable for the weakly strained layers at a height of 17 ML (right panel: red lines). Regarding the GaAs border regions surrounding this tensile central area, both methods yield vanishing strain at small height, but show some discrepancy in the description of the weakly strained GaAs regions at larger height, namely an opposite sign of $Tr(\varepsilon)$ (right panel: red lines) in the border regions. With the applied periodic boundary conditions in mind, the compressively strained border region as obtained with the many-body potential (right panel: dashed red lines at $Tr(\varepsilon) < 0$) seems to be more consistent with the tensile strain of the central region. The Green's function

approach furthermore yields a weaker compression of the intermediate GaAs region above the corner of the InAs inset as compared to the many-body potential that exhibits two distinct minima of $Tr(\varepsilon)$ (right panel: dashed blue line). This finding is interesting in the context of investigations of growth correlations in stacked QD layers (see also Chap. 8) by kinetic Monte-Carlo simulations with strain tensors from Green's functions: An additional origin for the observed weak size correlations of vertically stacked QDs [123] could be the outlined underestimation of the compressive strain above the corner of the overgrown structure. It would be interesting to see if the compressive 'shadow' of the perimeter of the overgrown structure obtained with the many-body potential developed in this work would give rise to more pronounced size correlations in such kinetic simulations.

Kapitel 5

Many-Body Potential

Many-body potentials¹ are able to treat semiconductor nanostructures in full atomistic detail, in contrast to continuum-elasticity theory described in the previous section. Calculations of the strain tensor with continuum-elasticity theory (CET) show good agreement with atomistic valence force-fields [117, 124] in the far field, but discrepancies in the short-range regime [104]. The force fields are limited to certain lattice structures and were not yet adapted to the description of surfaces. Analytic many-body potentials, however, can be optimized to a much broader variety of bonding situations. Such potentials allow not only the calculation of strain tensors of structures modeled with millions of atoms, but also provide the corresponding cohesive energies e.g. for the growth investigations presented in Chap. 7 and 8. At the moment they seem to be the most promising approach for the description of long-range strain effects in large-scale systems with an atomically detailed consideration of surfaces, edges, and kinks. In this section we describe the many-body potential that we applied in this work, as well as the optimization of its interaction parameters and the final values. Detailed tests of the description of In, Ga, As, InAs, and GaAs bulk and surface properties are given in Chap. 6.

5.1 Introduction

In quantum mechanics, the internal energy E_{QM} of a set of i atoms is implicitly given by the Schrödinger equation and can be determined by electronic-structure calculations that aim to find a self-consistent solution for the unknown wave function and eigenvalues of the energy (Sec. 2.2). A many-body potential in contrast aims at calculating the internal energy E_{pot} of a set of atoms explicitly and solely from the atomic positions $\{\mathbf{X}_i\}$, without explicitly

¹The different terms *(semi-)empirical potential*, *interatomic potential*, or *many-body potential* in the literature pronounce the motivation of the functionals or the kind of reference data they were optimized for. In this work, we use only the term *many-body potential*.

considering electrons.

$$E_{\text{QM}} \approx E_{\text{pot}} = \mathcal{F}(\{\mathbf{X}_i\}). \quad (5.1)$$

The advantage is an increase in computation speed by typically several orders of magnitude as compared to electronic-structure calculations. The challenge is to find an explicit expression \mathcal{F} that allows one to study the phenomena of interest. (Note that the choice of not explicitly considering electrons already implies several limitations, such as the inability to investigate phenomena that arise from electronic excitations, spin properties, or electron-phonon coupling.) The complex quantum-mechanical nature of atomic bonds make the search for suitable functional forms a formidable task. Even more challenging is the description of *bond-making-and-breaking* that occurs during e.g. the diffusion of atoms on surfaces and the formation of surface reconstructions, as we shall see in Sec. 6.3 and 6.5. Many-body potentials found widespread application in molecular-dynamic (MD) and kinetic Monte-Carlo simulations [125]. They play an important role in multi-scale approaches where they are combined with electronic-structure methods such as DFT or tight-binding (see e.g. Ref. [76] for a recent review).

There is a variety of many-body potentials available in the literature (see e.g. Ref. [126] for a review). Some of them are expansions of the internal energy in terms of the bond lengths and angles (e.g. Keating valence force-field [124]), others are motivated by empirical considerations (e.g. Morse potential [127]), or low-order approximations of electronic-structure theories (e.g. embedded-atom method [128] and bond-order potentials [129, 130]). Some of them are fully equivalent [131] and some of them are subsets of others [132]. The following criteria can be used to classify all of them:

- *structural information*: usage of n -body configuration with $n - 1$ distances, $n - 2$ planar angles and $n - 3$ torsional angles;
- *flexibility*: given functional form of \mathcal{F} (additive or non-linear with respect to contributions of different bonds of the same atom) for all bonding situations or combination with data base for different bonding situations; and
- *functional form*: analytic functional with a set of parameters, or purely numerical representation of \mathcal{F} with e.g. splines or neural networks.

The description of a particular material system requires the proper adjustment of the according functional. For this purpose the potentials with given analytical form provide sets of parameters that need to be adjusted, as discussed in Sec. 5.3 and 5.4. Different sets of parameters were found for many material systems using the same analytical form. For the purpose of clarity, we refer to the analytical form as *functional* and consider the entity of functional and parameters as *potential*. In this work, we have chosen to employ a bond-order functional of the Abell-Tersoff type that showed to capture many effects of covalent bonding in semiconductor heterostructures in previous works.

5.2 Bond-Order Potentials

The Abell-Tersoff functional is motivated by the suggestion of Abell [133] to describe the previously observed universal binding-energy curves for solid cohesion and chemisorption as a sum of next-neighbor pair-interactions that are altered by the local environment. Tersoff developed a functional to describe the binding in a large number of Si solid-state structures [134]. It was improved several times [135, 136, 137] and extended to the compounds SiC, SiGe [138] and many other systems. Brenner [139] could improve the erroneous treatment of conjugacy and the overbinding of radicals by introducing additional *ad hoc* terms in the bond-order expression. These terms are sophisticated interpolations of a database of bond properties in different situations of discrete numbers of neighbors. This route of improving a potential by empirically introducing more terms in the functional increases the number of parameters that need to be adjusted and relies heavily on the choice of the particular terms. Pettifor and co-workers devised a systematic way of deriving bond-order potentials from approximations to tight-binding models [129, 130, 140].

5.2.1 Derivation from Tight-Binding Bond Model

Sutton et al. [141] used the variational principle of density-functional theory (Chap. 2.2) to formulate the *tight-binding bond model* that approximates the binding energy of a *sp*-valent solid by

$$E = E_{\text{bond}} + E_{\text{prom}} + E_{\text{rep}}. \quad (5.2)$$

The promotion energy E_{prom} accounts for the energy involved in changing the occupancy of orbitals during bond formation and can be neglected for most *sp*-valent solids [142]. The repulsive term E_{rep} accounts for electrostatic and exchange-correlation effects during the formation of the solid from atoms, and can be approximated an effective pair-potential between the atoms [141]. The energy of the attractive covalent bonds E_{bond} of a system with N atoms can be determined within a two-center orthogonal tight-binding approximation from the local density-of-states n_α and the on-site atomic energy levels ϵ_α by [141, 143]

$$E_{\text{bond}} = \sum_{\alpha} \int^{\epsilon_F} (\epsilon - \epsilon_{\alpha}) n_{\alpha}(\epsilon) d\epsilon \quad (5.3)$$

where ϵ_F is the Fermi energy and α is the orbital type, e.g. *s* and *p*. The energy difference can be rewritten in terms of the Hamiltonian and the on-site atomic orbitals with the Green's function

$$(\epsilon - H)G = 1 \quad \Rightarrow \quad (\epsilon - \epsilon_{\alpha})G^{i\alpha i\alpha} = 1 + \sum_{j\beta, j\beta \neq i} H^{i\alpha j\beta} G^{j\beta i\alpha} \quad (5.4)$$

with $G^{j\beta i\alpha} = \langle j\beta | (\epsilon - H)^{-1} | i\alpha \rangle$ and the two-center energy integral matrix elements $H^{i\alpha j\beta} = \langle i\alpha | H | j\beta \rangle$ [143]. Interpreting the imaginary part of the Green's function as local density-of-states allows one to express the *global* covalent bond energy E_{bond} as a sum of *local* covalent

bond energies E_{bond}^{ij} between atoms i and j

$$E_{\text{bond}} = \frac{1}{2} \sum_{i \neq j} E_{\text{bond}}^{ij} = \frac{1}{2} \sum_{j\beta, j \neq i} H^{i\alpha j\beta} \Theta^{j\beta i\alpha}. \quad (5.5)$$

The introduced *bond order* given by

$$\Theta^{j\beta i\alpha} = 2\text{Im} \int^{\epsilon_F} G^{j\beta i\alpha} d\epsilon \quad (5.6)$$

can be understood as one-half the difference between the electron occupancy in the bonding state $\frac{1}{\sqrt{2}}|i\alpha + j\beta\rangle$ and the anti-bonding state $\frac{1}{\sqrt{2}}|i\alpha - j\beta\rangle$. In saturated bonds with two electrons in the bonding state and none in the anti-bonding state, the bond order reaches a value of one, whereas it is less than one in the case of covalent bonds which are usually unsaturated. The further derivation of an analytic expression of the bond energy requires the determination of the matrix elements $H^{i\alpha j\beta}$ of the Hamiltonian with e.g. the two center approximation of Slater and Koster [144], and to calculate the bond order Θ . Pettifor and co-workers [129] derived an exact many-atom expansion of the bond order by expressing the diagonal matrix elements of the Green's function with a Lanczos recursion and the off-diagonal matrix elements as derivatives of the diagonal matrix elements. They show that the recursion coefficients can be expressed in terms of the moments of the local density-of-states.

Expanding the local density-of-states of tetrahedral semiconductors up to the second moment μ_2 results in a bond-order term that is similar to the empirically found Abell-Tersoff functional: The angular dependence $g(\theta_{ijk})$ of the strength of a bond between two atoms i and j on the position of a third atom k is similar to that of a σ bond obtained from the above procedure. In both cases, the overall functional form of the bond order is

$$\Theta = f_1(r_{ij}) [f_1(r_{ij}, g(\theta_{ijk}))]^{-1/2} \quad (5.7)$$

where f_1 and f_2 are functionals and r_{ij} is the the distance between atoms i and j . New developments and parameterizations for second order expansions of the local density-of-states were presented recently [145, 146], higher-order expansions are subject of development.

5.2.2 Abell-Tersoff Functional

In the Abell-Tersoff functional the total cohesive energy E_{coh} of a configuration of atoms is given by a sum over all atoms i and their neighbors j :

$$E_{\text{coh}} = \sum_{i,j < i} f_{ij}^c(r_{ij}) \left[V_{ij}^R(r_{ij}) - B_{ij}(r_{ij}) V_{ij}^A(r_{ij}) \right] \quad (5.8)$$

with the pairwise interatomic distance $r_{ij} = |\mathbf{r}_i - \mathbf{r}_j|$. The pairwise attractive and repulsive interaction V_{ij}^A and V_{ij}^R correspond to f_1 in Eq. 5.7 and to E_{rep} in Eq. 5.2, respectively. In

the Abell-Tersoff functional, both terms are represented by a Morse potential:

$$V_{ij}^R(r_{ij}) = \frac{D_{ij}}{S_{ij} - 1} \exp \left[-\beta_{ij} \sqrt{2S_{ij}} (r_{ij} - R_{ij}^0) \right], \quad (5.9)$$

$$V_{ij}^A(r_{ij}) = \frac{S_{ij} D_{ij}}{S_{ij} - 1} \exp \left[-\beta_{ij} \sqrt{2/S_{ij}} (r_{ij} - R_{ij}^0) \right]. \quad (5.10)$$

The bond-order term B_{ij} in the Abell-Tersoff functional corresponds to Θ in Eq. 5.5. It is usually less than unity and therefore weakens the attractive pair potential dependent on the bonds of an atom to all possible other bonding partners. The bond-order term in the Abell-Tersoff functional differs slightly in the literature [138, 147, 148, 149], but can easily be brought to a common form by introducing the additional parameters n and m in the bond-order terms:

$$B_{ij}(r_{ij}) = [1 + (\gamma_{ij} \chi_{ij}(r_{ij}))^{n_{ij}}]^{-\frac{1}{2n_{ij}}} \quad (5.11)$$

$$\chi_{ij}(r_{ij}) = \sum_{k \neq ij} f_{ik}^c(r_{ik}) \cdot g_{ik}(\theta_{ijk}) e^{[(\alpha_{ik}(r_{ij} - r_{ik}))^{m_{ik}}]}. \quad (5.12)$$

Analytical bond-order functionals that were derived from a moment expansion [130, 150, 151] as described in the previous section show a somewhat different functional form, but the overall angular dependence of the bond order for a σ bond is quite similar [130, 152]. However, a notable difference is that the moments expansion additionally yield π bonds that are absent in the Abell-Tersoff functional. Therefore, the latter gives an erroneous description of radicals that are important in e.g. hydrocarbons [139] but play a minor role in this work. The angular function $g_{ik}(\theta_{ijk})$ in the Abell-Tersoff functional allows one to model anisotropic interactions such as the sp^3 hybridization of III-V semiconductors and is given by

$$g_{ik}(\theta_{ijk}) = \delta_{ik} \left(1 + \frac{c_{ik}^2}{d_{ik}^2} - \frac{c_{ik}^2}{d_{ik}^2 + (h_{ik} - \cos \theta_{ijk})^2} \right) \quad (5.13)$$

where θ_{ijk} denotes the angle between \mathbf{r}_{ij} and \mathbf{r}_{ik} . The nearest neighbor approximation of the tight-binding scheme that was used in the previous section appears in the Abell-Tersoff functional as a cutoff function $f_{ij}^c(r_{ij})$ that limits the interaction range to neighbors within a certain distance:

$$f_{ij}^c(r_{ij}) = \begin{cases} 1 & r_{ij} - R_{ij}^c \leq -D_{ij}^c \\ \frac{1}{2} \left[1 - \sin \left(\pi \frac{r_{ij} - R_{ij}^c}{2D_{ij}^c} \right) \right] & |r_{ij} - R_{ij}^c| < D_{ij}^c \\ 0 & r_{ij} - R_{ij}^c \geq D_{ij}^c \end{cases} \quad (5.14)$$

Details on the implementation of the Abell-Tersoff functional and the analytic derivative for calculating the forces on individual atoms are described in Appendix B. A major part of this

work was to determine a new parameterization of the above functional for reliable studies of InAs quantum dots on GaAs substrates. In the next sections we discuss general aspects of fitting such a many-body potential and qualitative details of our fitting procedure together with the new parameters. The quantitative properties of In, Ga, As, InAs, and GaAs bulk and surface structures as obtained from experiment, density-functional theory, continuum-elasticity theory, and the many-body potential with our new parameterization and previous ones, are collected and compared in the following chapter.

5.3 Geometric Interpretation of Parameter Optimization

The goal of optimizing the parameters of a many-body potential is to reproduce the configurational energy of given structures $\{\mathbf{X}_i\}$ or other deduced properties, such as bulk elastic constants, and surface energies within a certain accuracy. The match between the result of the functional and a reference properties \mathcal{D}_i can be expressed analytically by a non-linear equation. This defines a set of r non-linear equations that relate the r reference properties and the p parameters of the potential by

$$\mathcal{F}_{\mathbf{P}}(\{\mathbf{X}_i\}_j) = \mathcal{D}_j, \quad j = 1 \dots r \quad (5.15)$$

where \mathcal{F} is the functional and \mathbf{P} is a particular choice of potential parameters. From the point of view of parameter optimization to known reference properties \mathcal{D}_j , this is an implicit equation for the parameters. Consequently, the task of optimizing p parameters for a set of r reference data points is equivalent to solving a set of r non-linear equations with p unknowns. In contrast to a set of linear equations, even for $p = r$ there may be no solution, there may be one or several solutions, or even a continuum of solutions [153]. Each single non-linear equation gives a relation between the parameters \mathbf{P} that would allow the correct description of the respective system property. This defines a solution manifold \mathcal{M}_i , i.e. a hypersurface in parameter space, given by the functional form of the potential and the system properties to be fitted. \mathcal{M}_{ij} is the intersection of two manifolds, corresponding to parameter sets which correctly describe two material properties i and j . Correspondingly, $\mathcal{M}_{1\dots r}$ is the solution manifold describing all material properties in the reference data set. In case there is no solution ($\mathcal{M}_{1\dots r} = \emptyset$), the chosen potential cannot reproduce the desired material properties exactly, but only with certain errors. The number and shape of intersections (i.e. the number of exact solutions), depends on the number of manifolds (i.e. the number of reference properties), their shapes and mutual location. If there is a continuum of solutions, the given set of reference properties is redundant for the given potential; if there is no solution, it is contradictory. Note that for noisy reference data there might be no solution, even if a potential would be able to model the physical interaction properly.

The concept of manifolds allows for a geometric formulation of the requirements to an ideal functional: It would define r manifolds \mathcal{M}_i that intersect in one point \mathbf{P}_0 only and

thereby define a unique set of parameters that reproduce the r reference properties exactly. For each additional reference data point, the perfect functional would define a manifold \mathcal{M}_{r+1} that contains \mathbf{P}_0 . This would allow one to apply the parameters \mathbf{P}_0 that were obtained from r reference data sets to the additional structure \mathcal{S}_{r+1} and obtain \mathcal{D}_{r+1} exactly.

In many cases it is not possible to exactly reproduce all reference properties at the same time, but rather an approximate solution needs to be found. Consequently, parameter fitting is done by minimizing a target function $\chi(P)$ which depends on the deviations of the reference properties \mathcal{D}^* and the corresponding properties $\mathcal{D}^\sim(P)$ as obtained by the potential with a parameter set P . The particular importance of different reference properties can be accounted for by assigning appropriate weights w_i . In this work, we used the target function

$$\chi(P)^2 = \sum_{i=1}^r \left(\frac{\mathcal{D}_i^* - \mathcal{D}_i^\sim(P)}{w_i} \right)^2, \quad (5.16)$$

but other forms might be better suited for fitting reference data with constraints. In the following example we will demonstrate several characteristic problems of fitting parameters of a many-body functional.

5.3.1 Example: Lennard-Jones Potential

We will try to describe the lattice constants and cohesive energy of an arbitrary material in face-centered cubic and simple cubic structures with a Lennard-Jones potential. This is certainly not the adequate potential to simultaneously capture *fcc* and *sc* structures, but it can serve to illustrate more general conclusions. Later we will discuss the consequences of choosing more complicated functionals.

Assume a cutoff radius that includes only the first neighbors of *fcc* (distance $r(\text{fcc}) = a_0(\text{fcc})/\sqrt{2}$) and *sc* ($r(\text{sc}) = a_0(\text{sc})$). First, we consider a *fcc* lattice with $a_0(\text{fcc}) = 4 \text{ \AA}$ and $E_0(\text{fcc}) = -2.5 \text{ eV}$. For this case the parameters $P_{LJ} = (c_1, c_2)$ can be easily determined from

$$E^{\text{LJ}}(r(\text{fcc})) = E_0(\text{fcc}), \quad \left. \frac{\partial E^{\text{LJ}}}{\partial r} \right|_{r(\text{fcc})} = 0. \quad (5.17)$$

Each condition is an implicit definition of a manifold \mathcal{M}_i in the parameter space of c_1 and c_2 (without loss of generality we set $c_1 \geq 0$ and $c_2 \geq 0$):

$$\mathcal{M}_1 : 12 \cdot 4c_1 \cdot \left[\left(\frac{c_2}{r(\text{fcc})} \right)^{12} - \left(\frac{c_2}{r(\text{fcc})} \right)^6 \right] = E_0(\text{fcc}), \quad \mathcal{M}_2 : 2 \cdot \left(\frac{c_2}{r(\text{fcc})} \right)^6 - 1 = 0. \quad (5.18)$$

This set of equations has a unique and exact solution that is given by the intersection of the corresponding manifolds as shown in Fig. 5.1. For this simple example, the parameters could easily be determined analytically, but for realistic cases this is no longer feasible. Similarly to *fcc*, we consider a *sc* structure with $a_0(\text{sc}) = 0.6 \cdot a_0(\text{fcc})$ and $E_0(\text{sc}) = 0.9 \cdot E_0(\text{fcc})$ and

thereby define additional manifolds \mathcal{M}_3 and \mathcal{M}_4 , respectively. Such relations between *fcc* and *sc* could represent e.g. Ga, In, or As (see Tab. 6.1- 6.3). The resulting set of manifolds (Fig. 5.1) no longer has a common intersection, but rather several crossings of subsets. The

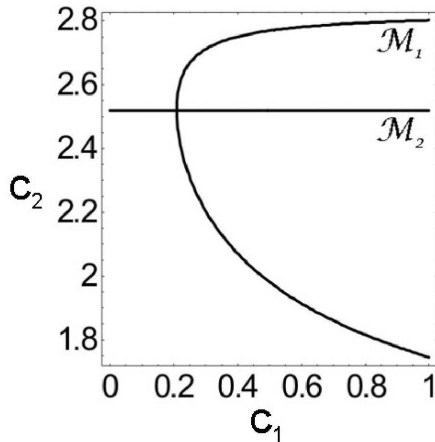


Abbildung 5.1:

Solution manifolds in the parameter space of a Lennard-Jones Potential. The reference data E_{coh} and a_0 for *fcc* and *sc* define \mathcal{M}_1 , \mathcal{M}_2 , and \mathcal{M}_3 , \mathcal{M}_4 , respectively. Intersections of a set of manifolds are exact solutions for the corresponding reference data.

large distance between the manifolds \mathcal{M}_{12} and \mathcal{M}_{34} in parameter space indicates that the Lennard-Jones Potential is not suitable for a simultaneous description of the two chemical environments *fcc* and *sc* for the given material (i.e., the given $a_0(fcc)/a_0(sc)$ and $E_0(fcc)/E_0(sc)$ ratios). Already for this very simple case, the character of the parameter solution depends strongly on the chosen subset of the reference data, even for an equal number of reference data and parameters: There are four different exact solutions for the subsets $\{a_0(fcc), E_0(sc)\}$, $\{a_0(sc), E_0(sc)\}$, $\{E_0(fcc), E_0(sc)\}$, and $\{E_0(fcc), a_0(sc)\}$. For $\{a_0(fcc), E_0(sc)\}$ there is only an approximate solution in the limit of $c_1 \rightarrow \infty$; and for $\{a_0(fcc), a_0(sc)\}$ there is a continuum of approximative solutions at constant c_2 , which gives a bad description of both structures. Subsets with three properties, as well as the complete set of four properties, define approximate solutions (i.e. different minima in the target function χ) which depend on the chosen weights w_i . The latter scale the contribution of the according manifolds and thereby shift the position of the minimum of χ , i.e. they result in different approximate solutions. The depth of these minima reflects the ability of the underlying functional to describe the particular choice of reference data. In this example, the subset $\{E_0(fcc), a_0(sc), E_0(sc)\}$ can be represented more accurately than any other subset with three reference data points. This means that a potential which has been fitted to the simple cubic structure (\mathcal{M}_{34}) describes the configurational energy of a *fcc* structure with lattice constant $a_0(sc)/0.6$ reasonably well (\mathcal{M}_1), but it cannot describe the *fcc* equilibrium lattice constant (\mathcal{M}_2 is not crossed).

5.3.2 Practical Consequences

This simple example illustrates some very basic characteristics of optimizing the parameters of a many-body functional: A set of fitted parameters is the (approximate) solution for a specific set of equations defined by the reference data, for a specific choice of error weights and for a specific construction of the target function. Furthermore, the sum of quadratic deviations in Eq. 5.16 for a set of reference data can be expressed as linear combination of sums of quadratic deviations for subsets of the reference data. Hence, for this form of target function, the minimum of χ for a set of r reference data is located (in parameter space) inside the polyhedron whose corners are defined by the different minima of χ for the possible subsets with $r - 1$ reference data. This means on the one hand, that the quality of the parameters for a sufficiently large set of reference data can not be systematically improved by including more reference data with similar bonding environment. And on the other hand, the quality of the description of a subset of reference data can decrease by including reference data with a different bonding environment. In other words, from a mathematical point of view, *it is not a priori known which subset of reference properties can be fitted within a requested accuracy*. Hence, *it is not necessarily the best choice to optimize all parameters for all reference data*. Instead, there can be conflicting subsets of reference data that cannot be fitted simultaneously with the requested accuracy. Thus, in practice, as soon as one assumes a non-ideal functional, one needs to distinguish between those properties that *should* be reproduced, and those that *need not* be reproduced and whose weights can be reduced for the benefit of the former. The difficulty of anticipating the conflicting subsets is similar to that of ‘postulating’ a functional: it requires a deep understanding of both the properties of the functional and the physical nature of the involved bonding environments. We meet with this obstacle of identifying conflicting subsets by performing extensive optimization attempts that combine different subsets of parameters and different subsets of reference data. This approach can be regarded as a systematic trial-and-error search. After having identified conflicting subsets of reference data and having reduced the weight of one conflicting subset, we repeated the search campaign until we successively optimized the potential parameters to an acceptable overall quality. During this procedure we tried to avoid overfitting effects by discarding those parameter sets that showed an improvement for the reference data, but a deterioration of a set of test data that were not explicitly included in the optimization. In all optimization steps we used the properties of high-index surfaces (see Sec. 6.3) as test data.

The parameters of the cutoff function were not varied in all optimization steps but rather were set to the values in Tab. 5.1 to include at most the second neighbor shell of the investigated bulk structures. Increasing the interaction range effectively creates additional contributions from the angular and/or pair-wise terms that enable the numerical fitting routine to distribute the energy contributions among different terms. Several attempts of fitting parameters with an increased cutoff radius for all terms or for the pair-interactions only were not promising and discarded. Note that the cutoff function creates a technical difficulty: If

a fitting step in parameter space leads to unstable structures and one of the included reference data requires a structure relaxation, the fitting algorithm faces the situation that atoms eventually leave the cutoff radius and do no longer interact at all. As a result, the algorithm would fail to reproduce the corresponding target quantity.

5.4 Determination of the Parameters

The elemental materials As, Ga, In, and the compound materials GaAs, InAs are of great technological importance and comprehensive experimental and theoretical results for the lattice constants, cohesive energies and bulk moduli of various phases are available (see e.g. Ref. [74, 105, 148, 154, 155, 156, 157, 158, 159, 160]). Nevertheless, only few analytical many-body potentials were developed for this material system. Among these, the bond-order functional of the Abell-Tersoff type [135, 138] that is used in this work is well suited to describe the covalent bonding character of semiconductors. Previously published parameterizations [147, 148, 149, 161, 162, 163] of this functional for elemental In, Ga, As, and the compound materials GaAs and InAs were optimized for equilibrium bulk properties. Our detailed tests of these parameter sets with respect to the description of bulk elasticity and surface properties pointed to the possibility of further optimizing them for quantitative investigations of the energetics of InAs/GaAs nanostructures. This implies the necessity to determine appropriate numerical values for the parameters R_{ij} , D_{ij} , β_{ij} , S_{ij} , γ_{ij} , α_{ij} , δ_{ij} , c_{ij} , d_{ij} , h_{ij} , n_{ij} , m_{ij} , R_{ij}^c , and D_{ij}^c introduced in Sec. 5.2. For this purpose, we optimize these parameters for the description of a set of reference data that represent the anticipated bonding configurations.

5.4.1 Reference Data

The reference data that we have chosen for the case of InAs/GaAs nanostructures are selected properties of several bulk and surface structures (see Chap. 6). We started with a collection of reference data that is based on previously published experimental and theoretical works and extended our reference data by results of additional DFT calculations using the program packages *fhi98md* [47] and *SFHInGX* [31]. We use norm-conserving pseudo potentials [60], Monkhorst-Pack k-point meshes [164], and the local-density approximation (LDA) to the exchange-correlation functional. The choice of the latter plays a minor role for the structural properties of the bulk phases: The scaling to experimental counterparts (see below) cancels the different overbinding behavior of LDA and GGA (generalized-gradient approximation), and the remaining relative differences are already within the achievable accuracy of the parameter fit. The LDA was found to be more consistent with the experimentally observed elastic constants of GaAs and InAs than GGA [74]. Furthermore, previous studies of the structure of $\text{In}_x\text{Ga}_{1-x}\text{As}$ surfaces using LDA found very good agreement with X-ray diffraction data (see e.g. Refs. [74, 165]). We successfully performed convergence tests with respect to energy cutoff

and number of \mathbf{k} -points for each physical property (Appendix A). The cohesive energies E_{coh} , lattice constants a_0 , and bulk moduli B were determined by fitting the equation of state to the empirical Murnaghan equation-of-state [93]. The surface calculations employed slabs passivated by pseudohydrogen atoms [166]. Non-stoichiometric surfaces require the consideration of atom exchange with a reservoir (see Sec. 3.2). The surface energy γ per area A is given by the total energy of the slab E_{tot} (after subtraction of the fixed lower part), the number of cations N_{III} and anions N_V , and the chemical potentials μ_V and μ_{IIIV} by Eq. 3.9. In the following we give the value of the surface energy γ for $\mu_{As} = -E_{coh}(As : \alpha)$, i.e. for very As-rich conditions, and for $\mu_{GaAs} = -E_{coh}(GaAs : \text{zinc blende})$ and $\mu_{InAs} = -E_{coh}(InAs : \text{zinc blende})$.

The consistency of mixing experimental and theoretical values of a_0 and E_{coh} was achieved by scaling the theoretical data without an experimental counterpart with the ratios of those theoretical data where experiments were available, too. To emphasize the vital importance of this issue we would like the reader to recall the overbinding effect of DFT calculations: This lowering of the absolute value of the cohesive energies does hardly alter the *relative* stability of different bulk phases, rather, it reduces the *absolute* values of all cohesive energies. The absolute value of the experimentally observed (unshifted) cohesive energy therefore appears higher than the corresponding theoretical value. A naive compilation of cohesive energies acquired by experiments and DFT calculations without scaling would alter the energy differences and could even end up in the situation that a ('DFT-overbound') meta-stable phase is energetically favorable over the experimentally observed phase. The goal of scaling the DFT results is therefore to preserve the relative stability of the theoretical results while achieving consistency with the experimental values. Due to a lack of experimental data for metastable structures, it is not completely clear if a multiplicative adjustment with a constant factor is preferable to an additive adjustment with a constant shift. Nevertheless, in our calculations, the difference between these two approaches was negligible as compared to the achievable accuracy of the parameter optimization.

5.4.2 Optimization Procedure

The values of the various included physical quantities need to be calculated with the Abell-Tersoff functional and the particular parameterization in each optimization step. In our case, the considered quantities are the bulk and surface properties given in Sec. 6.1 and 6.3, respectively. The parameter optimization of the functional starts with an initial guess for the parameters. In many cases, a good initial guess for the parameter values can be made up from previous parameterizations or from analytic expressions which may be deduced from the functional for simple structures (e.g. dimers, high symmetry bulk phases). The nearly 1000 initial guesses of this work were obtained by following the procedure described by Albe et al. [148], by using or scaling previous parameterizations [147, 148, 149, 161, 162, 163], and by fitting different subsets of parameters and reference data successively.

The numerical procedure is based on the sum of weighted quadratic differences of the

quantities as obtained from the potential (with a certain set of parameters) and the according reference values as given in Eq. 5.16. We minimized this deviation value with respect to the potential parameters by applying the Levenberg-Marquardt algorithm [153] that varies smoothly from a steepest-descent minimization to an inverse-Hessian minimization as it approaches the minimal deviation value. The gradients in parameter space were calculated numerically with Ridder’s method of polynomial expansion [153]. The numerical effort of optimizing one subset of parameters with one initial guess can be estimated as follows: Let us take the average CPU time for calculating one of the considered quantities as our unit of measure. Our minimization of the deviation value in a typically 10-dimensional parameter space requires the calculation of the Hessian matrix with $\mathcal{O}(100)$ matrix elements or line minimizations of the conjugate gradient. To ensure the numerical accuracy of each of these entries, we determine the numerical derivative based on $\mathcal{O}(10)$ calculations of the considered quantity. These operations have to be performed in each of the $\mathcal{O}(100)$ steps of minimizing the deviation value. For the number of initial guesses of this work the overall effort is then about $\mathcal{O}(10^8)$ times the calculation of the considered quantities with the many-body potential. Note that the latter include line minimizations for the bulk properties and high-dimensional conjugate-gradient relaxations of surface unit-cells. By highly optimizing these calculations to a total CPU time of $\mathcal{O}(10)$ seconds, we could reduce the total computational effort for the parameter optimization done in this work to $\mathcal{O}(10)$ CPU years.

5.4.3 Parameters

The parameters for each pair of species as obtained from our optimization are given in Tab. 5.1. In compliance with most previously published parameterizations, the parameters n_{ij} and m_{ij} were fixed in the optimization. The large value of D_{AsAs} leads to an undesirable overestimation of the cohesive energy of the As dimer, but was necessary to obtain proper surface energies: Some of the considered surfaces are terminated by As dimers, and these are only stable for large D_{AsAs} . Otherwise the angular terms of the potential would tend to continue the zinc blende lattice structure. Due to the limited interaction-range of the potential, the In-Ga interaction does not occur in the investigated zinc blende $\text{In}_x\text{Ga}_{1-x}\text{As}$ nanostructures, therefore no potential parameters for In-Ga are reported here. In principle, these parameters could be obtained in the manner described above, with the In-In and Ga-Ga parameters as initial guesses, or by an averaging scheme [138].

In order to assess the transferability of a many-body potential to bonding situations that were not included in the determination of its parameters, we need to investigate meaningful test cases. In the next chapter we demonstrate that the above parameterization based on bulk properties and reconstructed low-index surfaces is well suited to describe the energetic balance and atomistic structure of lattice-mismatched nanostructures such as InAs QDs on GaAs substrates. In particular, it describes several high-index facets that are known to form side-facets of QDs, but also the accompanying and energetically competing biaxially strained

Tabelle 5.1: Parameter sets for the different interactions

	Ga-Ga	As-As	In-In	Ga-As	In-As
R_{ij} [Å]	2.2625	1.9018	2.6639	2.3824	2.5492
D_{ij} [eV]	1.4159	7.9717	1.5052	1.9561	1.8900
β_{ij} [1/Å]	0.9079	1.2165	1.1847	1.5396	1.4549
S_{ij}	1.0646	2.3439	1.2440	1.1543	1.8578
γ_{ij}	1.4401	4.8650	4.0976	0.2992	2.2113
α_{ij} [1/Å]	0.7469	2.5408	1.2117	-1.3824	1.1816
δ_{ij}	0.0050	0.3609	0.0109	0.0424	0.0190
c_{ij}	1.4897	0.1749	1.0853	1.7796	3.9707
d_{ij}	0.8376	0.2140	0.9465	0.6450	0.9486
h_{ij}	-0.3373	-0.1261	-0.4652	-0.4060	-0.5102
n_{ij}	1.0	1.0	1.0	1.0	1.0
m_{ij}	1.0	1.0	1.0	1.0	1.0
R_{ij}^c [Å]	2.95	3.1	3.5	3.1	3.7
D_{ij}^c [Å]	0.15	0.1	0.1	0.2	0.1

InAs films on GaAs with reasonable reliability.

Kapitel 6

Applicability of Many-Body Potential to In, Ga, As, InAs, and GaAs

In this chapter we compare the applicability of the new parameterization of the Abell-Tersoff potential for In, Ga, As, GaAs, and InAs developed in Chap. 5 with previously published ones, which we name chronologically as T1 (Smith [161]), T2 (Ashu et al. [147]), T3 (Sayed et al. [162]), T4 (Nordlund et al. [163]), T5 (Albe et al. [148]), and T6 (Migliorato et al. [149]). For each of these parameterizations, we use the identical bond-order functions as the corresponding authors by choosing n_{ij} and m_{ij} in Eq. 5.11 and 5.12 properly. In fact, we used $n = 1$ for the parameterization developed in this work in compliance with most previous works, and in line with the results of the moments expansion of tight binding given in Eq. 5.5. For compound systems we apply the same combinations of interaction parameter sets as in the original works. The parameter values for the mutual interactions of In-In (T2), Ga-Ga (T1,T5), As-As (T1,T5), Ga-As (T1,T3,T5), and In-As (T2,T4,T6) are given in the corresponding publications. In this chapter we show that the many-body potential developed in this work allows reliable studies of InAs/GaAs QD nanostructures, which are presented in the following chapters.

6.1 Bulk Properties

For each pairwise interaction, the cutoff-radius of the many-body potential (Eq. 5.14) truncates the interaction range of the potential. The values of R_{ij}^c and D_{ij}^c in Tab. 5.1 were chosen similarly to previous parameterizations and limit the interaction to e.g. the first neighbor in any $\text{In}_x\text{Ga}_{1-x}\text{As}$ zinc blende structure. Thus, for this choice of cutoff-radii, the description of such systems with this potential is completely determined by the parameters of the

interaction terms Ga-As and In-As. Nevertheless, the elemental parameters (In-In, Ga-Ga, As-As) are needed because E_{coh} of the stable elemental crystal structures (i.e. α -Ga ($Cmca$), α -As ($A7$), and In(bct)) shown in Fig. 6.1) enters in the formula for the surface energy (see Eq. 3.9). A comparison of the lattice-parameters, cohesive energies and bulk moduli of

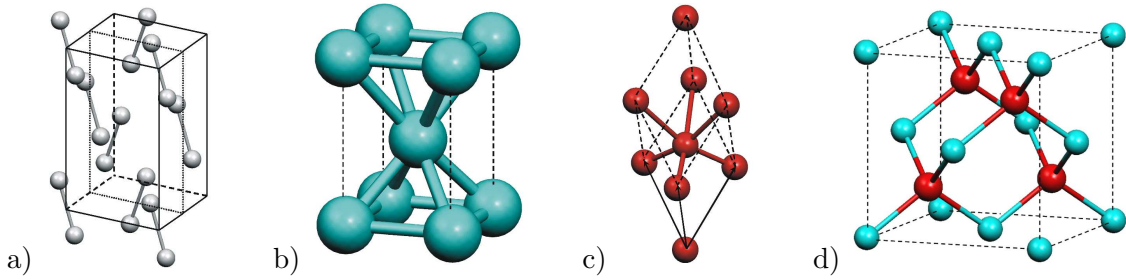


Abbildung 6.1: The conventional unit-cells of a) α -Ga ($Cmca$) (after [167]), b) α -As ($A7$) (after [168]), c) In (bct) (after [169]), and d) InAs (ZnS). The above color assignments to the atoms are used throughout this work.

stable and meta-stable Ga, In, and As bulk-structures as obtained from experimental works, (scaled) *ab-initio* calculations, and calculations with our new parameterization and previous ones is given in Tab. 6.1- 6.3. The corresponding comparison for GaAs and InAs in Tab. 6.4 and 6.5 additionally include the elastic constants.

In the calculations with the many-body potential, the lattice constants a_0 and cohesive energies E_{coh} were obtained by one-dimensional minimization of the cohesive energy E_{coh} with respect to a_0 . The structural parameters of phases with internal degrees of freedom, i.e. α -Ga and α -As, were calculated successively by minimizing E_{coh} with respect to each individual parameter while keeping the others fixed on the reference values and then iterating this procedure for all internal degrees of freedom. For these two structures, we adopt the nomenclature for the internal lattice-parameters as given by Albe and co-workers [148]. The bulk moduli B and elastic constants c_{11} and c_{12} were determined from the numerical second derivative of E_{coh} with respect to the volume under volume-conserving strain [170]. The elastic constants $c_{44}^{(0)}$, c_{44} , and the Kleinman parameter ξ were calculated according to the adiabatic and harmonic stress-method introduced by Nielsen et al. [92] as described in Sec. 4.2 of this thesis. Some of the bulk moduli in the tables below are given in brackets to indicate a technical artifact of the many-body potential: Equilibrium neighbor distances that are within the cutoff interval $[R_{ij}^c - D_{ij}^c, R_{ij}^c + D_{ij}^c]$ can lead to an unphysical influence of the curvature of the cutoff function (Eq. 5.14) on the curvature at the minimum of the equation of state. This can cause incorrect results for quantities that are given by second derivatives such as the bulk modulus.

Table 6.1 shows that the parameterization developed in this work reproduces the lattice-parameters and cohesive energies of all Ga structures with an error of only a few percent. This

ensures a reliable description of the Pauling relation between bond-length and bond-energy, as discussed in detail for T5 by Albe et al. [148]. In our optimization the bulk moduli of the meta-stable structures turned out to form a conflicting subset with the GaAs surfaces and capturing the surface properties required to tolerate a larger error on the bulk moduli. In

Tabelle 6.1: Equilibrium properties of Ga phases as obtained from experiments and *ab-initio* calculations, the potential developed in this work and previous ones.

	Ref.	T1	T5	this work
<i>diamond</i> -Ga	us-PP LDA [148]			
a_0 [Å]	5.680	5.7786	5.5369	5.5320
E_{coh} [eV]	2.458	2.5505	2.4854	2.3745
B [GPa]	46.5	44.072	27.960	18.894
<i>sc</i> -Ga	us-PP LDA [148]			
a_0 [Å]	2.626	2.6093	2.5992	2.6102
E_{coh} [eV]	2.699	2.9244	2.6950	2.6799
B [GPa]	61.3	74.607	43.056	30.130
α -Ga (<i>A11</i>)	exp. [154]			
a_0 [Å]	4.5192	4.3235	4.3819	4.4605
b_0 [Å]	7.6586	8.0612	7.6756	7.6749
c_0 [Å]	4.5258	4.4381	4.5195	4.5607
u	0.1539	0.16399	0.15943	0.15926
v	0.0798	0.087780	0.087669	0.087780
E_{coh} [eV]	2.810 [171]	2.8431	2.8063	2.8243
Ga-II (<i>bccTd</i>)	us-PP LDA [148]			
a_0 [Å]	5.901	6.3963	5.9088	5.9567
E_{coh} [eV]	2.784	2.5808	2.7582	2.8307
B [GPa]	66.8	(589 ^a)	50.882	36.607
<i>fcc</i> -Ga	us-PP LDA [148]			
a_0 [Å]	4.09	4.1557	4.0636	4.0750
E_{coh} [eV]	2.756	2.5611	2.7113	2.7793
B [GPa]	65.2	82.051	(1129 ^a)	(1374 ^a)

^a Value overestimated due to influence of cutoff function.

Tab. 6.2 we compiled the investigated properties of In bulk-structures that are reproduced within similar accuracy as for Ga. The bulk moduli are captured with a significantly higher accuracy as compared to those of the Ga bulk-structures, although they were not explicitly included in the optimization procedure as well. The properties of As bulk-structures (Tab. 6.3)

Tabelle 6.2: Equilibrium properties of In phases as obtained from experiments and *ab-initio* calculations, the potential developed in this work and previous ones.

	Ref.	T2	this work
<i>diamond</i> -In	LDA		
a_0 [Å]	6.564	8.0962	6.5575
E_{coh} [eV]	2.20	0.24934	2.1684
B [GPa]	28.49	(186 ^a)	24.785
<i>sc</i> -In	LDA		
a_0 [Å]	3.078	3.5291	3.0041
E_{coh} [eV]	2.44	0.22094	2.3913
B [GPa]	36.75	(503 ^a)	39.774
<i>bcc</i> -In	LDA		
a_0 [Å]	3.741	4.0884	3.6099
E_{coh} [eV]	2.44	0.20877	2.5375
B [GPa]	44.54	(909 ^a)	52.686
<i>bct</i> -In	exp [154]		
a_0 [Å]	3.2520	3.5783	3.2824
c_0 [Å]	4.9470	5.4417	4.9392
E_{coh} [eV]	2.52 [171]	1.2751	2.5209
<i>fcc</i> -In	LDA		
a_0 [Å]	4.737	5.0247	4.7316
E_{coh} [eV]	2.56	0.19760	2.5258
B [GPa]	47.39	(1520 ^a)	53.347

^a Value overestimated due to influence of cutoff function.

are reproduced with slightly larger deviations as compared to Ga and In. This is due to the dependence of the As-As parameters on the simultaneous optimization of As bulk-structures and surface properties of both GaAs and InAs. The tendency to minimize the number of dangling bonds of the surfaces is the driving force for several reconstructions with As dimers as prominent features. Consequently, the As-As interaction is crucial for capturing the surface energies of reconstructed surfaces. The angular terms of the cation-As interactions would favor a continuation of the underlying zinc blende lattice. The formation of As dimers can only be reproduced with the potential by a comparably strong As-As interaction. Despite the resulting overestimation of the binding energy of the As dimer, the degrees of freedom in terms of remaining parameters allow the potential to reproduce many bulk properties.

The energies per bond in different structures of the same element (or compound) were

Table 6.3: Equilibrium properties of As phases as obtained from experiments and *ab-initio* calculations, the potential developed in this work and previous ones.

	Ref.	T1	T5	this work
<i>diamond</i> -As	us-PP LDA [148]			
a_0 [Å]	5.913	6.0815	5.8086	5.9792
E_{coh} [eV]	2.487	2.2367	2.5100	2.6088
B [GPa]	52.6	40.476	47.520	34.482
α -As (<i>A7</i>)	exp. [154]			
a_0 [Å]	4.1320	4.0301	3.9056	4.0584
α [deg]	54.12	59.965	54.534	56.424
u	0.22707	0.25000	0.23218	0.22618
E_{coh} [eV]	2.96 [171]	2.7344	2.9650	2.9087
<i>sc</i> -As	us-PP LDA [148]			
a_0 [Å]	2.64	2.6377	2.6111	2.7271
E_{coh} [eV]	2.89	3.3204	2.8874	2.7201
B [GPa]	96.8	92.355	81.071	52.550
<i>bcc</i> -As	us-PP LDA [148]			
a_0 [Å]	3.26	3.5845	3.2016	3.3215
E_{coh} [eV]	2.562	2.4368	2.4617	2.4470
B [GPa]	96.8	(945 ^a)	84.555	58.221
<i>fcc</i> -As	us-PP LDA [148]			
a_0 [Å]	4.217	4.3339	4.1264	4.2481
E_{coh} [eV]	2.442	2.4005	2.4707	2.4789
B [GPa]	93.0	81.274	87.790	(439 ^a)

^a Value overestimated due to influence of cutoff function.

found to approximately depend exponentially on the according bond lengths L to the next neighbors. This *Pauling relation* was found empirically [172] and can be motivated from a two-center approximation to pseudo-potential theory [133]. In Tab. 6.1-6.3 we have given the cohesive energy of the different structures *per atom*, but one can easily acquire the cohesive energy *per bond* from division by the number of neighbors within the cutoff radius. The particular number of neighbors, as well as the distances to them, depend on the crystal structure. The energy per bond versus the bond length as obtained with our many-body potential for the elemental and the compound materials are shown in Fig. 6.2 and 6.3 as semi-logarithmic graphs. These data show good agreement with the Pauling relation that is

obtained by fitting an exponential function to the values of the reference data.¹

The parameterization of this potential was particularly optimized to capture the structural and elastic properties of the zinc blende structures of the compound materials GaAs and InAs. These are reproduced with high accuracy as shown in Tab. 6.4 and 6.5, a significant improvement to previous parameterizations. The deviation of about 0.5 eV for the cohesive energy of the NaCl structure of GaAs was necessary for the simultaneous description of the reconstructed low-index GaAs surfaces.

Note that these compound interactions are sufficient to describe heterogenous systems of

Table 6.4: Equilibrium properties of GaAs phases as obtained from experiments and *ab-initio* calculations, the potential developed in this work and previous ones.

	Ref.	T1	T3	T5	this work
GaAs (<i>ZnS</i>)	exp. [173]				
a_0 [Å]	5.653	5.6553	5.6438	5.6527	5.6527
E_{coh} [eV]	6.71	6.5015	6.5014	6.7087	6.7159
B [GPa]	74.8	79.941	74.942	73.485	75.195
c_{11} [GPa]	118.1	79.941	118.64	123.89	118.80
c_{12} [GPa]	53.2	79.941	53.090	48.281	53.393
c_{44} [GPa]	59.2	-0.014	68.988	39.190	58.616
ξ	0.77 [174, 175]	1.0002	0.5348	0.5480	0.6700
GaAs (<i>NaCl</i>)	us-PP LDA [148]				
a_0 [Å]	5.278	5.3489	5.6902	5.3202	5.3938
E_{coh} [eV]	6.168	5.1524	3.1348	6.1729	5.6236
B [GPa]	95.79	89.309	47.786	95.790	87.985
GaAs (<i>CsCl</i>)	us-PP LDA [148]				
a_0 [Å]	3.276	3.5992	3.5993	3.2680	3.2372
E_{coh} [eV]	5.73	3.7133	2.6523	5.5645	5.8438
B [GPa]	105.4	(17376 ^a)	(7473 ^a)	105.43	114.26

^a Value overestimated due to influence of cutoff function.

GaAs, InAs, and bulk interfaces formed by them. Their applicability to subtle effects of $\text{In}_x\text{Ga}_{1-x}\text{As}$ alloys [83, 177] needs to be tested separately which is beyond the scope of this work.

A survey of the accuracy achieved with the many-body potential for the lattice constants and cohesive energies of the different structures of all investigated elements and compounds

¹In the case of α -Ga, In (*bct*), and α -As, the energy per atom needs to be distributed to different bonds, because of the inequivalent neighbors in different distances. For this reason these structures were not included in the fit of an exponential Pauling relation. Instead, we distribute the energy per atom to the bonds by using the energy ratios that are obtained if one uses the occurring neighbor distances in the fitted Pauling relation.

Tabelle 6.5: Equilibrium properties of InAs phases as obtained from experiments and *ab-initio* calculations, the potential developed in this work and previous ones.

	Ref.	T2	T4	T6	this work
InAs (<i>ZnS</i>)	exp. [105]				
a_0 [Å]	6.0583	5.9084	6.0597	6.0587	6.0499
E_{coh} [eV]	6.20	7.1308	7.1310	6.2004	6.2042
B [GPa]	58.0	68.138	58.049	57.771	57.961
c_{11} [GPa]	83.29	68.138	83.605	82.917	83.355
c_{12} [GPa]	45.26	68.138	45.272	45.197	45.264
c_{44} [GPa]	39.59	0.012733	39.575	41.638	39.518
ξ	0.68 ^a	0.99978	0.65015	0.64078	0.64884
InAs (<i>NaCl</i>)	LDA				
a_0 [Å]	5.680	5.6539	5.7661	6.1427	5.6435
E_{coh} [eV]	5.56	5.4212	5.4566	3.0108	5.2801
B [GPa]	68.16	72.178	62.241	36.891	70.506
InAs (<i>CsCl</i>)	LDA				
a_0 [Å]	3.521	3.5998	3.5992	3.7787	3.5837
E_{coh} [eV]	4.94	4.3422	5.0665	2.4191	5.2270
B [GPa]	64.51	(27778 ^b)	(8727 ^b)	36.138	(879 ^b)

^a Value obtained with phenomenological theory in Ref. [176].

^b Value overestimated due to influence of cutoff function.

is given in Fig. 6.4. The agreement of the calculated lattice constants with the reference

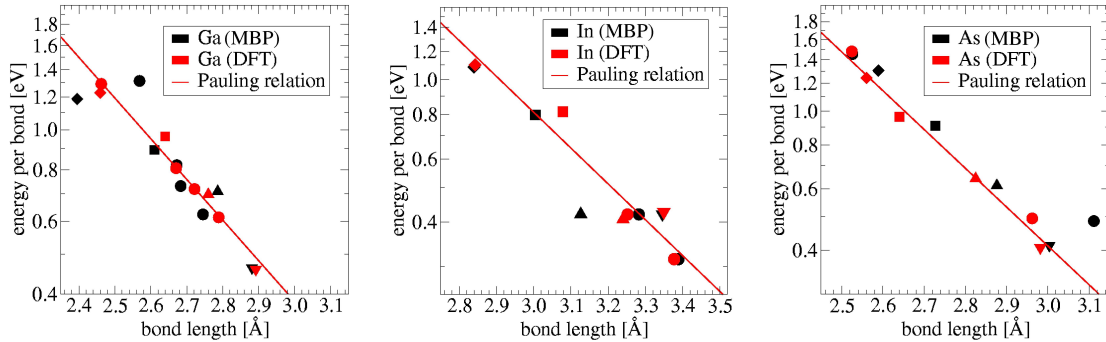


Abbildung 6.2: Pauling relation of Ga (left), middle (In), and As (right) as calculated with the many-body potential (black) and with DFT (red): Shown are the physically stable phases (\circ) α -As ($A7$), α -Ga ($Cmca$), and In (bct), as well as the meta-stable phases diamond (\diamond), sc (\square), fcc (∇), and bcc (\triangle) or $bccTd$ (\triangle) for Ga.

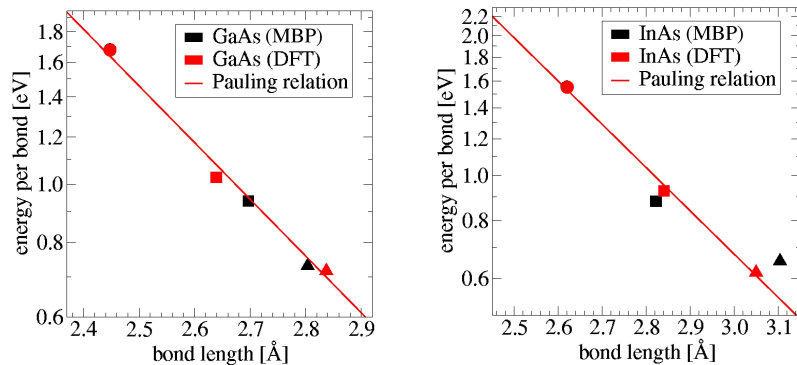


Abbildung 6.3: Pauling relation of GaAs (left) and InAs (right) as calculated with the many-body potential (black) and with DFT (red): Shown are the physically stable phases ZnS (\circ), as well as the meta-stable phases $NaCl$ (\square) and $CsCl$ (\triangle). (The results for the prior overlap.)

data is very good for all investigated phases. The cohesive energies of the most stable bulk phases are reproduced with high accuracy, only some of the metastable structures show small deviations.

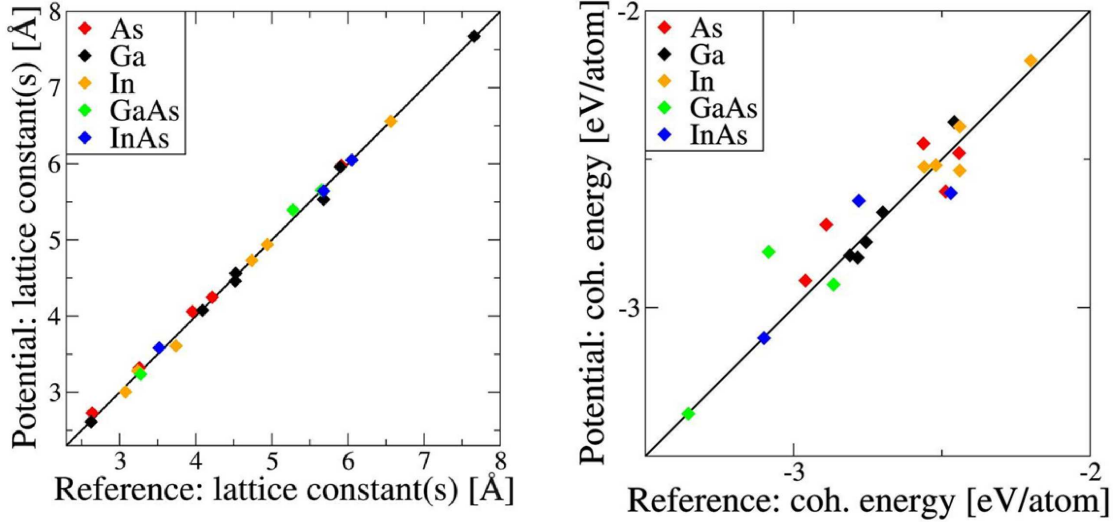


Abbildung 6.4: Survey of accuracy achieved with the newly developed many-body potential for the lattice constants (left) and cohesive energies (right) of the investigated elemental and compound phases (Tab. 6.1-6.5). The line would correspond to perfect agreement with the reference data.

6.2 Biaxial Poisson-Ratio and Elastic Energy

The applicability of the many-body potential developed in Chap. 5 to the description of the Poisson ratio for biaxial strain is of decisive importance for capturing the atomistic relaxation and elastic energy of pseudomorphic, lattice-mismatched interfaces and thin-films, like the InAs wetting layer that appears in Stranski-Krastanov growth of QDs (see Chap. 7 and 8). Although the strain is the driving force of self-assembly and can have an impact on the electronic structure, little is known about the role of non-linear elastic effects in InAs/GaAs heteroepitaxy: The linear-response approximation of continuum-elasticity theory (Chap 4) is valid for small deformations. For deformations larger than a few percent, however, this approximation may no longer be appropriate. In fact, the non-linear contributions to the elastic response upon biaxial strain turned out to be necessary to explain the experimentally observed light emission from $\text{In}_x\text{Ga}_{1-x}\text{As}$ [178] and $\text{In}_x\text{Ga}_{1-x}\text{N}$ [179] quantum well lasers. Even the phase stability of epitaxial films of noble metals is determined by non-linear elastic contributions [180]. Although such effects can in principle be considered in CET, the required higher-order elastic constants are often not known. Density-functional theory (DFT) calculations are a means to investigate non-linear effects numerically [180, 181], but until now they were applied mainly to isotropic strain and biaxial strain in low-index planes. The results of Sec. 4.3 now allow us to extend such investigations to a much wider range and enable us to

investigate linear and non-linear elastic response to biaxial strain in arbitrary planes. In this section we present an extensive comparison of results from CET and DFT calculations for the case of biaxially strained InAs and compare them to results with the many-body potential using our new parameterization and previous ones. Furthermore, we compare the predictions of CET for GaAs with results obtained with different parameterizations of the many-body potential.

In the linear response approximation of CET, the Poisson ratio ν and the elastic-energy density $F(\alpha^s)$ upon biaxial strain α^s is given analytically by Eq. 4.28 and 4.29. In this study we used the experimentally observed elastic constants of InAs [105]. The DFT calculations were performed with the *SFHingX*-package [31] using norm-conserving pseudo-potentials [60], Monkhorst-Pack \mathbf{k} -point meshes [164], and the local-density approximation for the exchange-correlation functional. We employ the results of Sec. 4.3 to reduce the numerical effort significantly: The strain tensor in canonical coordinates (Eq. 4.27) determines the strained unit cell and atomic coordinates for biaxial deformations in any plane. This allows us to perform the calculations for all strain planes with only a single zinc blende unit cell hosting 8 atoms in total². An energy cutoff of 20 Ry and a $5 \times 5 \times 5$ folding of one \mathbf{k} -point in the center of the Brillouin zone turned out to be sufficient to converge the value of $\nu^{(0)}$ introduced below (Eq. 6.2) to a remaining error of about 1% (see Appendix A). Alternatively, we obtained the biaxial Poisson-ratio and elastic energy numerically with the many-body potential using the new parameterization (Tab. 5.1) and the previously published parameter sets T2 (Ashu et al. [147]), T4 (Nordlund et al. [163]), and T6 (Migliorato et al. [149]) for InAs as well as T1 (Smith [161]), T3 (Sayed et al. [162]), and T5 (Albe et al. [148]) for GaAs. In these calculations, we used periodic supercells with two unit vectors of the strain plane and minimized the total energy $E(\varepsilon)$ for a certain biaxial strain α_i in the considered plane (hkl) with respect to the elastic response β_i perpendicular to this plane. These cells were generated from the crystal vectors given below and rotated to align the (hkl) direction of the bulk super cell with the Cartesian z -axis:

$$\begin{aligned} \{\mathbf{e}_i\}^{(001)} &= \left\{ \begin{pmatrix} 2 \\ 2 \\ 0 \end{pmatrix}, \begin{pmatrix} 2 \\ -2 \\ 0 \end{pmatrix}, \begin{pmatrix} 0 \\ 0 \\ 2 \end{pmatrix} \right\}, & \{\mathbf{e}_i\}^{(110)} &= \left\{ \begin{pmatrix} 0 \\ 0 \\ 1 \end{pmatrix}, \begin{pmatrix} 1 \\ -1 \\ 0 \end{pmatrix}, \begin{pmatrix} 2 \\ 2 \\ 0 \end{pmatrix} \right\} \\ \{\mathbf{e}_i\}^{(113)} &= \left\{ \begin{pmatrix} 2 \\ 1 \\ -1 \end{pmatrix}, \begin{pmatrix} 1 \\ -1 \\ 0 \end{pmatrix}, \begin{pmatrix} 1 \\ 1 \\ 3 \end{pmatrix} \right\}, & \{\mathbf{e}_i\}^{(137)} &= \left\{ \begin{pmatrix} 2 \\ 1 \\ -1 \end{pmatrix}, \begin{pmatrix} 3 \\ -2 \\ -1 \end{pmatrix}, \begin{pmatrix} 3 \\ 1 \\ 7 \end{pmatrix} \right\} \\ \{\mathbf{e}_i\}^{(3715)} &= \left\{ \begin{pmatrix} 3 \\ 3 \\ -2 \end{pmatrix}, \begin{pmatrix} 3 \\ -2 \\ -1 \end{pmatrix}, \begin{pmatrix} 5 \\ 2 \\ 11 \end{pmatrix} \right\}. \end{aligned}$$

²The *SFHingX*-package is particularly convenient for such kind of calculations as it allows one to perform algebraic operations in the input file and to enter the strain tensor explicitly (see Appendix A).

This procedure used in the calculations with the many-body potential is equivalent to applying the strain tensor to only one unit cell which was used in the DFT calculations.

Biaxial strain can lift the equivalence of the atomic bonds inside the zinc blende (or diamond) unit cell, causing the atoms to relax their position with respect to each other. This is well known from the calculation of the elastic constants $c_{44}^{(0)}$ and c_{44} [92]. To investigate the role of such internal relaxations under biaxial deformations, we performed two kinds of calculations: In the first set, we scaled the unit cell and the position of the atoms according to the strain tensor and computed the total energy. In the second set, we additionally relaxed the atoms in the unit cell until the absolute value of the change in the total energy was less than 0.3 meV in the DFT calculations, or until the relative change in total energy was less than 10^{-3} in the calculations with the many-body potential. This procedure is similar to numerically calculating $c_{44}^{(0)}$ and c_{44} , respectively, and will be referred to as unrelaxed and relaxed in the following discussion. In any case, we determined the biaxial Poisson ratio ν numerically for different values of the strain α_i . To address the case of InAs/GaAs heteroepitaxy³ with about 6.9% lattice mismatch, we have chosen $\alpha_i \in \{\pm 0.07, \pm 0.05, \pm 0.03, \pm 0.01\}$. For each α_i , we calculated the total energy of the strained InAs unit cell at $\nu(\alpha_i) = \nu_a \pm j \cdot 0.05$, where ν_a is the analytic result and $j = 0 \dots 5$ ⁴. The elastic energy E_{el} is given by the difference in total energies of strained and unstrained unit cell. From the calculations using either DFT or the many-body potential, we find that the elastic energy for a particular strain α_i is well described by

$$E_{\text{el}}(\alpha_i, \nu) = E_{\text{el}}^{(0)}(\alpha_i) + E_{\text{el}}^{(1)}(\alpha_i) \cdot \nu + E_{\text{el}}^{(2)}(\alpha_i) \cdot \nu^2. \quad (6.1)$$

The minimum of the elastic energy with respect to ν yields the elastic response $\nu_i(\alpha_i)$ upon this particular strain α_i . The Poisson ratios for different α_i in different planes (hkl) as obtained from our calculations are shown in the left panel of Fig. 6.5. For this comparison we have exemplarily chosen biaxial strain in the (001), (110), and (111) plane that correspond to extremal values of Poisson ratio and elastic energy (Fig. 4.1), and strain in some examples of high-index planes. For a quantitative discussion of linear and non-linear contributions we performed linear regressions of the results from calculations with either DFT or the many-body potential according to

$$\nu(\alpha) = \nu^{(0)} + \nu^{(1)} \cdot \alpha. \quad (6.2)$$

According to the above equations, the dependency of the elastic-energy densities on α is well described by

$$E_{\text{el}}(\alpha) = E_{\text{el}}^{(2)}\alpha^2 + E_{\text{el}}^{(3)}\alpha^3 \quad (6.3)$$

³For the technologically relevant case of heteroepitaxial growth of InAs on GaAs substrates, the elastic energy is stored in the InAs film which is compressed to the lattice-constant of GaAs (see Sec. 7.3).

⁴For some strain planes we experienced problems in the internal relaxation upon large strain values with the parameterizations T1 and T6. In these cases we reduced the strain interval to $\alpha \in [-0.02, 0.02]$ at constant number of calculation points.

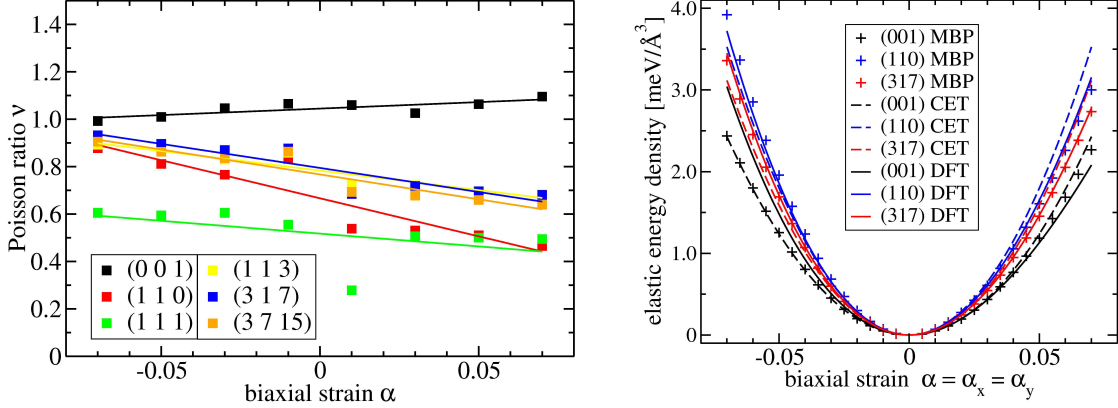


Abbildung 6.5: The Poisson ratio (left) of InAs for biaxial strain in different planes as obtained with either DFT (straight lines) or our MBP (crosses) shows a linear dependency on the strain and hence an anharmonic behavior of the associated elastic energy density (right: DFT). The results of linear-response CET in contrast are purely harmonic (left: dashed lines).

as shown in the right panel of Fig. 6.5. Note, that the slope $\nu^{(1)}$ leads to a non-linear elastic response (Eq. 4.27) that is not captured by the continuum-elasticity theory approach presented here. Under the assumption that the latter is valid for the comparably small strain values shown in Fig. 6.5, the different slopes $\nu^{(1)}$ could be interpreted as different contributions of the strain dependencies of the elastic constants in Eq. 4.28: The shear strain described by c_{44} is not present for biaxial strain in the (001) plane that shows a positive slope of the Poisson ratio. The negative slope of all other Poisson ratios, however, are due to the role of c_{44} in Eq. 4.28 and its strain dependence.

The biaxial Poisson ratio $\nu^{(0)}$ that corresponds to linear elastic response as obtained from our numeric calculations is compiled with the analytic result from Eq. 4.28 in Tab. 6.6 for different strain planes (hkl). The consideration of internal relaxations in the analytic expressions obtained from CET by employing c_{44} or $c_{44}^{(0)}$ in Eq. 4.28 is compared to numeric calculations without and with relaxation of the internal degrees of freedom, respectively. For both cases, we also provide the value of $\nu^{(1)}$ that leads to non-linear elastic response and is not present in the CET calculations. In both cases, i.e. with and without internal relaxations, the Poisson ratios of the investigated planes of biaxial strain as obtained from CET are in good agreement with calculations using either DFT or the many-body potential. This confirms that the consideration of internal relaxation in CET can be controlled by choosing either c_{44} or $c_{44}^{(0)}$ in Eq. 4.28. For the case of InAs studied here, the Poisson ratio varies between the smallest and the largest value by a factor of five whereas the range of elastic energy densities is about 30%.

Tabelle 6.6: Effect of internal relaxation on Poisson ratio $\nu^{(0)}$ of InAs under biaxial strains in selected planes as obtained from CET, DFT, and the newly developed many-body potential (MBP).

	without internal relaxation			with internal relaxation		
	CET $\nu^{(0)}$	DFT $\nu^{(0)}$	MBP $\nu^{(0)}$	CET $\nu^{(0)}$	DFT $\nu^{(0)}$	MBP $\nu^{(0)}$
(0 0 1)	1.09	1.05	1.10	1.09	1.04	1.10
(1 1 0)	0.34	0.40	0.34	0.67	0.67	0.70
(1 1 3)	0.54	0.60	0.56	0.81	0.78	0.82
(3 1 7)	0.58	0.63	0.59	0.83	0.79	0.85
(3 7 15)	0.52	0.57	0.53	0.79	0.77	0.81

In order to assess our newly developed parameterization, we additionally determined the elastic response upon biaxial strain in selected planes with previously published parameterizations for GaAs and InAs, employing internal relaxation in both cases. The resulting harmonic terms of the Poisson ratio and the elastic-energy density, $\nu^{(0)}$ and $E_{el}^{(2)}$, are shown in Tab.6.7 and 6.8, respectively, together with the according predictions of continuum elasticity theory (Eq. 4.28 and 4.29). The potential developed in this work reproduces the harmonic part of the biaxial Poisson ratio very well for all investigated strain planes in GaAs and InAs. The previously published parameterizations T3, T4, and T6 give comparable results for the biaxial Poisson ratio and the elastic energy, but they show deficiencies in capturing the surface energies (Tab. 6.10 and 6.9). The parameterizations T1 and T2 overestimate the biaxial Poisson ratio by a factor of 2 and show practically no dependence of the corresponding elastic energy on the applied biaxial strain. The values of the anharmonic term $E_{el}^{(3)}$ (Eq. 6.1) as obtained with T3-T6 and the potential developed in this work is comparably small: It ranges from -0.2 to -2.0 meV/Å³ for (001) and from -1.1 to -3.5 meV/Å³ for (110).

An interesting aspect of the elastic-energy densities given in Tab. 6.6 is that the formation of InAs QDs was reported only for GaAs substrate orientations that correspond to *minimal* or *moderate* elastic-energy densities of biaxially strained InAs, such as (001) and (113) [23], (114) [96] and (2 5 11) [95], but not for (110) and (111) substrates that would correspond to maxima in the elastic-energy density. In fact, STM experiments of heteroepitaxy of InAs on GaAs(110) and *ab-initio* calculations of the formation energies of misfit dislocations at this interface [182] suggested that in this case the formation of misfit dislocations is the dominant mechanism of strain relief at already a few monolayers of deposited InAs. The formation of either QDs or dislocations are obviously competing, but qualitatively different mechanisms of relieving compressive stress: In the case of QD formation, the atoms in the QD can adjust their comparably shortened bonds towards their equilibrium bond length and relax compressive stress in the QD at the expense of introducing additional stress in the

Tabelle 6.7: Poisson ratio for biaxial strain $\nu^{(0)}$ determined analytically from CET with the experimental elastic constants (Eq. 4.28) and numerically (Eq. 6.2) with the parameterization determined in this work and with previous ones.

$\nu^{(0)}$	CET	T1	T3	T5	this work
GaAs (0 0 1)	0.91	2.00	0.91	0.80	0.92
GaAs (1 1 0)	0.56	2.01	0.47	0.38	0.59
GaAs (1 1 3)	0.67	2.01	0.66	0.51	0.69
GaAs (1 3 7)	0.69	2.00	0.69	0.53	0.71
GaAs (3 7 15)	0.65	2.01	0.65	0.49	0.68
$\nu^{(0)}$	CET	T2	T4	T6	this work
InAs (0 0 1)	1.09	2.01	1.09	1.09	1.10
InAs (1 1 0)	0.67	1.99	0.69	0.64	0.70
InAs (1 1 3)	0.81	2.04	0.82	0.78	0.82
InAs (1 3 7)	0.83	2.03	0.84	0.81	0.85
InAs (3 7 15)	0.79	2.04	0.80	0.77	0.81

Tabelle 6.8: Elastic energy density for biaxial strain $E_{el}^{(2)}$ determined analytically from CET with experimental elastic constants (Eq. 4.29) and numerically (Eq. 6.1) with the parameterization determined in this work and with previous ones.

$E_{el}^{(2)}$ [meV/Å ³]	CET	T1	T3	T5	this work
GaAs (0 0 1)	0.77	0.00	0.76	0.84	0.76
GaAs (1 1 0)	1.02	0.00	1.09	1.14	1.00
GaAs (1 1 3)	0.94	0.00	0.98	1.04	0.93
GaAs (1 3 7)	0.93	0.00	0.99	1.03	0.91
GaAs (3 7 15)	0.95	0.00	0.97	1.06	0.94
$E_{el}^{(2)}$ [meV/Å ³]	CET	T2	T4	T6	this work
InAs (0 0 1)	0.50	0.00	0.49	0.49	0.48
InAs (1 1 0)	0.72	0.00	0.71	0.74	0.71
InAs (1 1 3)	0.65	0.00	0.64	0.66	0.64
InAs (1 3 7)	0.64	0.00	0.63	0.65	0.63
InAs (3 7 15)	0.66	0.00	0.65	0.67	0.65

substrate (as we shall see in Sec. 7.6). In the case of misfit dislocations the stress of the lattice-mismatched interface is released by the formation of a dislocation core. The interplay of the energy for forming a dislocation core and the amount of released elastic energy determines if and to what extent the formation of dislocations can eventually decrease the energy in the system. A reduction of the energy by dislocations is more likely for small formation energies of dislocation cores and large elastic energies due to the interface. This explains the above mentioned experimental trend that QD formation is observed on films with small and moderate elastic-energy densities, whereas dislocations are found on films with high elastic-energy densities. If a QD has eventually formed and is growing in volume keeping the same shape, the base area and hence the elastic-energy at the interface would increase. Possible mechanisms of strain relief are a change of the QD shape to a geometry with less base area (see Sec. 7.6), or the formation of dislocations. Both are observed experimentally [19].

6.3 GaAs and InAs Surfaces

In the previous sections we showed that the many-body potential developed in this work allows one to model structural properties of the compound semiconductors GaAs and InAs, as well as the elastic properties of heterostructures formed by these materials. In this section we will show that the many-body potential is furthermore able to model the structure and energetics of several surfaces reasonably well, an important ingredient for a reliable description of free-standing InAs QDs on GaAs substrates. Our choice of investigated surfaces in this study is motivated by recent high-resolution STM experiments that revealed the detailed atomistic structure of InAs QDs on GaAs substrates of low-index and high-index orientations.

The physics of surfaces of semiconductors such as GaAs and InAs, is dominated by unsaturated (*dangling*) bonds of the under-coordinated surface atoms. These atoms can lower the surface free energy by forming new bonds that tend to be saturated and to compensate charges (see e.g. Ref. [65] for an in-depth discussion). The emerging structures are the so-called *surface reconstructions* that can have a different periodicity than the bulk unit-cells. The possibly resulting variety of reconstructions of the same surface orientation typically differ in chemical stoichiometry. As a consequence (see Sec. 3.2), the surface free energy depends on the chemical potential and results in a phase diagram that allows one to identify the energetically most favorable surface reconstruction for a particular chemical potential.

The (2×4) reconstructions of the (001) surfaces of GaAs and InAs that were investigated in this work are shown in Fig. 6.6, each as 2×2 repetition of the 2×4 surface unit-cell in top view, i.e. along the crystallographic direction $[00\bar{1}]$. These geometries were obtained from DFT calculations [74, 183] and included the relaxation of the atomic positions in slab calculations. The nomenclature of reconstructions is identical for (001) surfaces of GaAs and InAs with the same topology, although the detailed atomic positions after relaxation differ slightly. These reconstructions and many others are investigated in great detail in the PhD thesis

of E. Penev [74]. The structures in Fig. 6.6 can be understood by noting that the $\alpha(2\times 4)$ reconstruction emerges from cutting a zinc blende bulk-structure in a step-like, stoichiometric fashion. Adding an As dimer per (2×4) surface unit-cell besides the two others leads to the $\beta(2\times 4)$ reconstruction. The removal of the two undercoordinated Ga atoms per surface unit-cell yields $\beta 2(2\times 4)$, and further removal of one As dimer per surface unit-cell finally results in the $\alpha 2(2\times 4)$, which is again stoichiometric. Obviously, the reconstructions $\beta(2\times 4)$ and $\beta 2(2\times 4)$ have the same stoichiometry of two As excess atoms per (2×4) surface unit-cell. The (110) surface that we have also included in our studies is shown below in Fig. 6.13 and appears as QD side facet on both, (001) substrates [19] and high-index substrates [95, 96, 184, 185, 186].

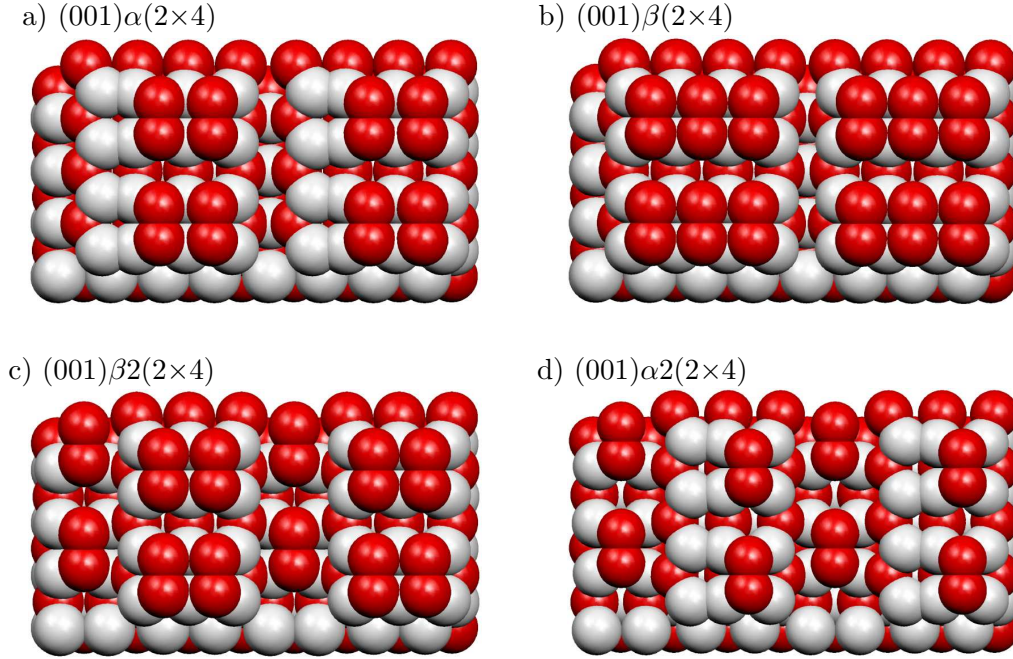


Abbildung 6.6: Low-index reconstructions of the (001) surface of GaAs and InAs. In the parameterization of the many-body potential we included GaAs(001) $\alpha(2\times 4)$, GaAs(001) $\beta(2\times 4)$, GaAs(001) $\beta 2(2\times 4)$, InAs(001) $\beta(2\times 4)$, and InAs(001) $\beta 2(2\times 4)$, as well as the (110) surfaces of GaAs and InAs shown in Fig. 6.13. (To guide the eye, we show a 2×2 repetition of the surface unit-cells, viewed along the crystallographic direction $[00\bar{1}]$.)

Furthermore, we investigated high-index surfaces that served as substrates for QD formation in experimental works ($\{113\}$ [184, 185, 186], $\{2\ 5\ 11\}$ [95]), or that were experimentally identified to appear as QD side facet on either (001) substrates ($\{137\}$ [18, 19]) or high-index substrates ($\{137\}$ [96], $\{2\ 5\ 11\}$ [185, 186]). These surfaces are shown in Fig. 6.7 as 2×2 repetition of the surface unit-cell viewed along the crystallographic direction $[00\bar{1}]$.

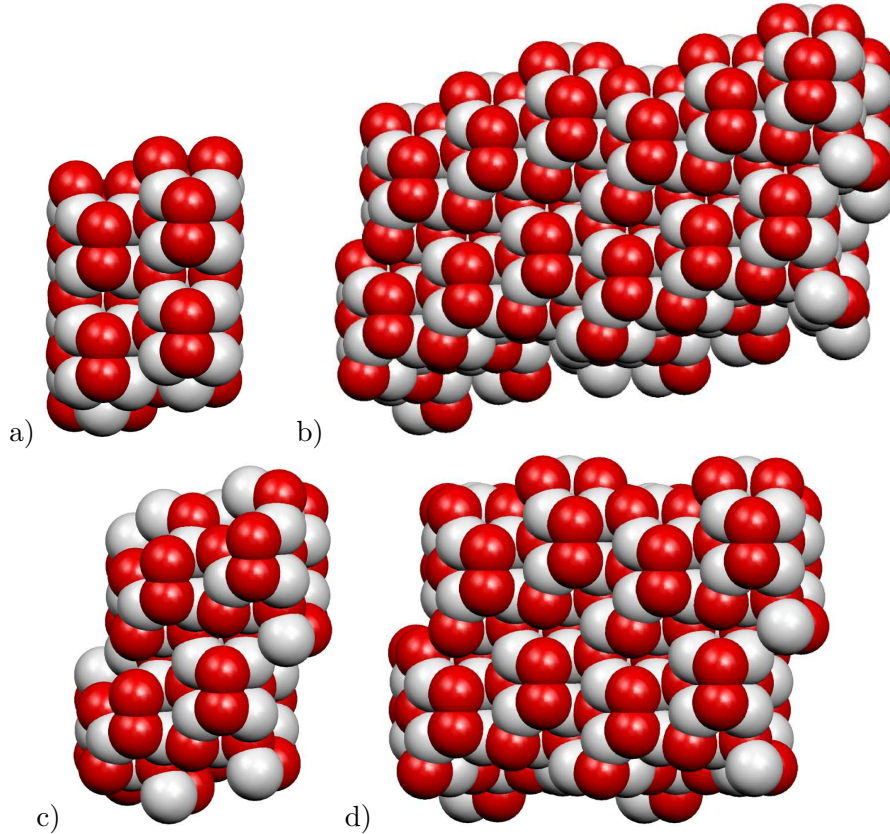


Abbildung 6.7: The newly parameterized many-body potential is transferable from the low-index surfaces of Fig. 6.6 to the high-index surfaces a) $(113) (2 \times 1)\text{-}\alpha$ [158], b) $(2\ 5\ 11)$, c) (137) , and d) $(3\ 7\ 15)$ of both, GaAs and InAs without loss of accuracy. (To guide the eye, we show a 2×2 repetition of the surface unit-cells, viewed along the crystallographic direction $[00\bar{1}]$.)

The surface calculations with the many-body potential proceeded by scaling the structures as obtained from DFT calculations with the corresponding bulk lattice constants as obtained with the particular parameterizations. We relaxed the atoms in a slab calculation by a conjugate-gradient algorithm [153] until the maximum force in the system was below $1\text{ meV}/\text{\AA}$. The surface energies were calculated with Eq. 3.9 and the cohesive energies as obtained from the according parameterization. Furthermore, we introduced two artificial observables in the optimization procedure to quantitatively account for the structural difference between relaxing the surfaces with DFT and with the Abell-Tersoff potential: Firstly, with the Abell-Tersoff potential, we calculated the maximum force in the geometry relaxed with DFT before. This value, F_0 , would vanish, if the geometry relaxed with DFT and with the

Abell-Tersoff potential respectively would be identical. Secondly, we calculated the average difference of all bond lengths $\langle \Delta r \rangle$ in the surface unit-cells after relaxation with either DFT, $R_{ij}(\text{DFT})$, or the many-body potential, $R_{ij}(\text{MBP})$, as

$$\langle \Delta r \rangle := \sum_{i=1}^{N-1} \sum_{j=i+1}^N \frac{2 \cdot \|R_{ij}(\text{DFT}) - R_{ij}(\text{MBP})\|}{N(N-1)}. \quad (6.4)$$

In our calculations we found no general, monotonous relationship between F_0 and $\langle \Delta r \rangle$, indicating that these two artificial quantities are not redundant as one might expect. Notwithstanding the many theoretical works on the structure of III-V semiconductor surfaces (see e.g. Schmidt [160] for a thorough discussion), there is still no general recipe how to describe them with a many-body potential. Our approach is therefore to include the (110) and several (2×4) reconstructions of the (001) surface of GaAs and InAs in the parameter optimization with the potential given in Sec. 5.2 in a numerical manner, similar to the bulk phases⁵. During this procedure we tried to avoid overfitting effects by discarding those parameter sets that showed an improvement for the reference data, but a deterioration of a set of test data that were not explicitly included in the optimization. In all optimization steps we applied our potential to the above high-index surfaces (113), (137), (3 7 15), and (2 5 11) with the same relaxation criteria as for the low-index surfaces, calculated the same quantities and used them as test data. This ensures the transferability of the many-body potential from the low-index surfaces for which it was optimized to those GaAs and InAs high-index surfaces that were not explicitly included in the optimization but are of particular importance as substrate and QD facets. A comparison of the results for GaAs and InAs for all investigated surfaces as obtained from *ab-initio* calculations and from calculations with our parameterization and previous ones is put together in Tab. 6.9 and Tab. 6.10, respectively.

This comparison shows clearly that the potential developed in this work achieves much higher overall accuracy in the description of the (110) and reconstructions of the (001) surfaces of both GaAs and InAs: The error of the surface energy of the investigated high-index facets of about 10 meV/Å² is very similar to the corresponding error for the low-index surfaces that were included in the optimization procedure. This is also indicated in the left panel Fig. 6.8 that shows both, the fitted low-index and the tested high-index surfaces. (The diagonal would correspond to perfect agreement with the reference data.) Additionally, Tab. 6.9 and 6.10 show that the maximum initial force on the DFT-relaxed high-index facets F_0 and the average bond-deviation $\langle \Delta r \rangle$ after relaxation with our potential is very similar to those of the low-index surfaces. This trend of surface energies and initial force is a clear indication that our parameterization for low-index facets is transferable to the investigated high-index facets without loss of accuracy. The reason is that these high-index

⁵The focus of our study are surfaces that are stable at As-rich conditions, therefore e.g. the $\zeta(4x2)$ reconstruction [159] is not considered here.

Table 6.9: Surface energies γ and relaxation differences F_0 and $\langle \Delta r \rangle$ of GaAs surfaces as obtained from *ab-initio* calculations, the potential developed in this work and previous ones.

GaAs(001) α (2x4)	LDA [156]	T1	T3	T5	this work
γ [meV/Å ²]	65.	71.902	89.002	80.044	49.814
F_0 [eV/Å]	0.001	6.486	8.430	4.797	2.905
$\langle \Delta r \rangle$ [Å]	0.	0.1474	0.1675	0.1325	0.1111
GaAs(001) β (2x4)	LDA [183]				
γ [meV/Å ²]	58.	110.25	89.754	114.79	63.523
F_0 [eV/Å]	0.001	4.083	5.246	4.849	1.033
$\langle \Delta r \rangle$ [Å]	0.	0.1259	0.1701	0.1090	0.1165
GaAs(001) $\beta 2$ (2x4)	LDA [156]				
γ [meV/Å ²]	56.	111.02	100.58	115.41	63.670
F_0 [eV/Å]	0.001	6.167	7.929	4.587	0.9273
$\langle \Delta r \rangle$ [Å]	0.	0.1389	0.1599	0.1075	0.1156
GaAs(110) (cleavage)	LDA[156]				
γ [meV/Å ²]	52.	13.893	10.707	57.693	62.477
F_0 [eV/Å]	0.001	4.923	7.424	0.5510	0.5262
$\langle \Delta r \rangle$ [Å]	0.	0.05371	0.09824	0.1023	0.1009
GaAs(113) (2x1)- α [158]	LDA [158]				
γ [meV/Å ²]	47.	83.891	73.859	102.21	51.973
F_0 [eV/Å]	0.001	2.0442	1.741	4.426	0.6975
$\langle \Delta r \rangle$ [Å]	0.	0.1453	0.1292	0.1320	0.08517
GaAs(137)	LDA [183]				
γ [meV/Å ²]	57.4	72.291	60.747	85.634	51.743
F_0 [eV/Å]	0.001	8.320	11.23	4.593	0.8018
$\langle \Delta r \rangle$ [Å]	0.	0.1632	0.1168	0.07964	0.08723
GaAs(2 5 11)	LDA [72]				
γ [meV/Å ²]	53.	76.479	67.386	103.08	63.100
F_0 [eV/Å]	0.001	10.05	13.90	4.580	0.8647
$\langle \Delta r \rangle$ [Å]	0.	0.1577	0.1155	0.1030	0.09209
GaAs(3 7 15)	LDA [72]				
γ [meV/Å ²]	55.	74.332	64.225	99.494	60.987
F_0 [eV/Å]	0.001	7.036	10.83	3.971	0.8229
$\langle \Delta r \rangle$ [Å]	0.	0.1519	0.1139	0.1076	0.1060

Table 6.10: Surface energies γ and relaxation differences F_0 and $\langle \Delta r \rangle$ of InAs surfaces as obtained from *ab-initio* calculations, the potential developed in this work, and previous ones.

InAs(001) α 2	LDA [74]	T2	T4	T6	this work
γ [meV/Å ²]	47.	70.131	62.721	44.136	35.758
F_0 [eV/Å]	0.001	9.392	6.315	10.37	2.846
$\langle \Delta r \rangle$ [Å]	0.	0.1814	0.1847	0.2233	0.1552
InAs(001) β 2	LDA [74]				
γ [meV/Å ²]	45.	102.72	102.03	78.993	53.280
F_0 [eV/Å]	0.001	6.432	1.036	1.573	0.7562
$\langle \Delta r \rangle$ [Å]	0.	0.1596	0.1205	0.1711	0.1092
InAs(110)	LDA [156]				
γ [meV/Å ²]	41.	10.298	16.241	-0.00074	47.215
F_0 [eV/Å]	0.001	1.790	2.455	0.6952	0.3915
$\langle \Delta r \rangle$ [Å]	0.	0.03072	0.1032	0.1027	0.1044
InAs(113) (2x1)- α [158]	LDA [183]				
γ [meV/Å ²]	45.2	77.408	80.201	53.788	41.560
F_0 [eV/Å]	0.001	7.827	4.673	8.131	1.995
$\langle \Delta r \rangle$ [Å]	0.	0.1884	0.1100	0.1793	0.09198
InAs(137)	LDA [183]				
γ [meV/Å ²]	43.0	65.958	69.256	42.092	40.425
F_0 [eV/Å]	0.001	4.679	5.110	8.196	1.953
$\langle \Delta r \rangle$ [Å]	0.	0.1343	0.06926	0.1327	0.0872
InAs(3 7 15)	LDA [183]				
γ [meV/Å ²]	41.5	67.672	70.208	45.990	49.160
F_0 [eV/Å]	0.001	6.756	4.987	8.665	2.054
$\langle \Delta r \rangle$ [Å]	0.	0.1475	0.1089	0.1390	0.09640

surfaces are reconstructed truncations of the zinc blende bulk dominated by As-dimer motifs which also appear as the most prominent feature of the reconstructed low-index surfaces that were included in the fitting procedure. Furthermore, we found that the applicability of the potential to surface reconstructions with two As layers (e.g. GaAs(001) $c(4 \times 4)$ [156] and $\text{In}_{2/3}\text{Ga}_{1/3}\text{As}(001)$ $\alpha 2(2 \times 3)$ [187]) is rather limited due to an overestimation of the according surface energies. From the viewpoint of possible reference structures (Sec. 5.3) for the fitting procedure, these structures form a subset which is in conflict with the subset formed by the As bulk properties and the other surface reconstructions. Consequently, we did not consider these two reconstructed surfaces in our optimization of the potential parameters. The relative

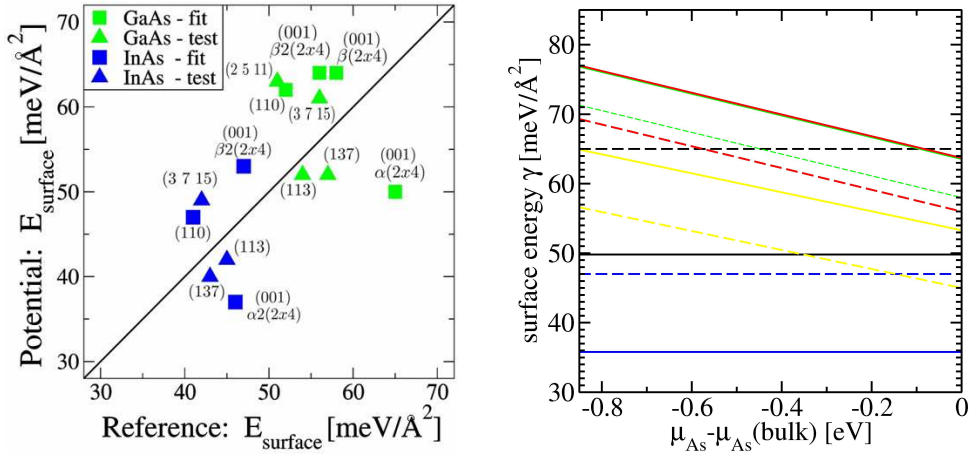


Abbildung 6.8: The many-body potential (MBP) developed in this work is transferable from the fitted low-index (left: \square) to the not-fitted high-index (left: \triangle) surfaces without loss of accuracy. The phase diagram (right) shows the deviation of the MBP results (solid lines) from DFT data (dashed lines) for GaAs(001) $\alpha(2 \times 4)$ (black), GaAs(001) $\beta(2 \times 4)$ (green), GaAs(001) $\beta 2(2 \times 4)$ (red), InAs(001) $\alpha 2(2 \times 4)$ (blue), and InAs(001) $\beta 2(2 \times 4)$ (yellow). The total energy of nanostructures investigated in the following chapters are corrected (Eq. 7.1) by the deviation per area.

ve stability of different surface reconstructions depends on the applied chemical potential(s) (Eq. 3.9). In the right panel of Fig. 6.8 we compare the surface energies of different reconstructions of GaAs(001) and InAs(001) obtained with MBP (solid lines) and DFT (dashed lines) calculations with respect to the applied chemical potential of As. There is no common trend of the deviations of the MBP results for different surface reconstructions. Therefore the order of surface reconstructions upon a change of μ_{As} is not reproduced by the MBP. In fact, the MBP yields the $\alpha(2 \times 4)$ and $\alpha 2(2 \times 4)$ reconstruction of GaAs(001) and InAs(001) as the most stable reconstructions in the whole range of allowed values of μ_{As} . In the DFT results, however, GaAs(001) $\beta 2(2 \times 4)$ and InAs(001) $\beta 2(2 \times 4)$ are most stable at As-rich conditions.

Despite these deviations of the surface energies from the DFT results, we could signi-

ificantly improve the description of InAs and GaAs surfaces as compared to the previously published parameterizations T1-T6. A survey of the surface energies acquired with DFT and the different MBP (see Tab. 6.9 and 6.10) is presented in Fig. 6.9. The degree of agree-

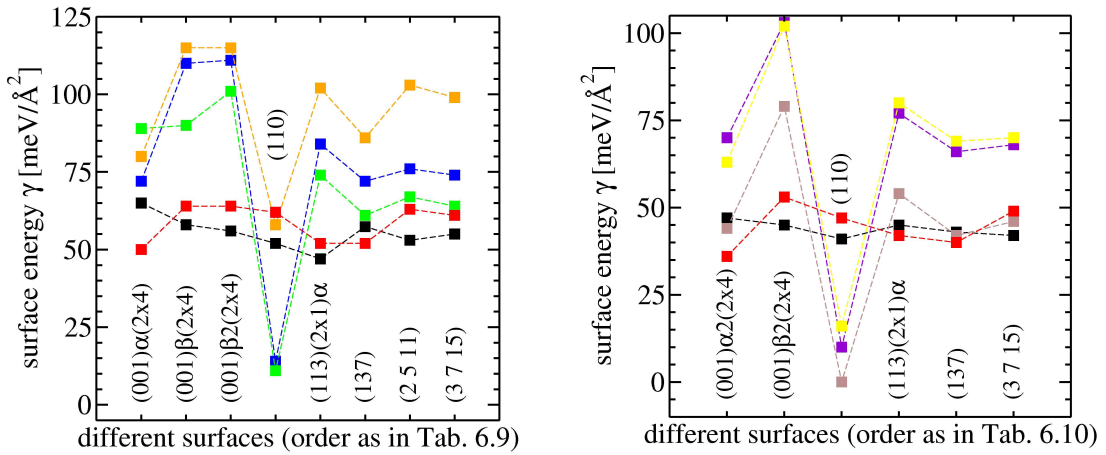


Abbildung 6.9: A comparison of the surface energies as obtained from DFT calculations (black) and the MBP developed in this work (red) shows the improvement to the previously published parameterizations T1 (blue), T2 (violet), T3 (green), T4 (yellow), T5 (orange), and T6 (brown) for GaAs (left) and InAs (right). The dashed lines have no physical meaning, they are shown for ease of comparison.

ment with the DFT results depends strongly on the investigated surface/reconstruction for all previously published parameterizations. The results acquired with our newly developed parameterization, however, do not show this behavior. Rather, they are afflicted with errors of approximately $10 \text{ meV}/\text{\AA}^2$ for all investigated surfaces/reconstructions. Furthermore, we find some remarkable similarities in the observed errors: The surface energies of the $\beta(2\times 4)$ and $\beta 2(2\times 4)$ reconstructed (001) surfaces are larger than that of the $\alpha(2\times 4)$ and $\alpha 2(2\times 4)$ reconstructed surfaces for all parameterizations, whilst the results of the DFT calculations show the opposite trend. Nearly all parameterizations (except T5 and ours) dramatically underestimate the surface energy of the GaAs(110) and InAs(110). The surface energies of the investigated high-index surfaces are distinctly overestimated by most parameterizations (T1, T2, T4, and T5). Note that none of these parameterizations is able to capture the surface energies accurately enough to provide a proper phase diagram of e.g. the different reconstructions of the (001) surfaces of GaAs and InAs. In studies that rely on the latter, such as e.g. molecular-dynamic simulations of changes in the surface reconstruction, one should therefore use different functionals. Recently, Murdick et al. [146] presented a much more accurate phase diagram for reconstructions of the GaAs(001) surface with a functional that accounts for π and σ bonds, and employs an additional Coulomb interaction term (summarized under the

term BOP+CE). This MBP is also able to give a good description of clusters and defects, in contrast to any known parameterization of the Tersoff functional. Despite these very convincing properties of the BOP+CE parameterization for GaAs, the relative deviation of the lattice constant a_0 (0.3%) and the elastic constant c_{44} (16%) of *zinc blende* GaAs might be too large in some quantitative studies of strain effects in e.g. lattice-mismatched nanostructures. To give a quantitative example, we can employ Eq. 4.29 to estimate the resulting deviation for the elastic energy density $F(\alpha^s)$ of GaAs that is biaxially strained to the experimental lattice constant of InAs. For this (somewhat artificial) case we find that the small deviation of a_0 already results in an underestimation of $F(\alpha^s)$ by 5%. The influence of c_{44} depends on the plane of biaxial strain and ranges from no effect for $\{001\}$ planes to an (additional) underestimation of $F(\alpha^s)$ by up to 8% for $\{111\}$ planes. The corresponding deviations obtained with our newly developed parameterization (of a less sophisticated functional) are 0.1% and 0.2%, respectively. These different advantages show once more (see e.g. Ref. [188] for a similar conclusion) that the choice of a MBP for a certain application should be guided by the detailed knowledge of those modeling ingredients that are of utmost importance to capture the anticipated physical behavior.

6.4 Surface Stress

A further test of applicability of our potential to the modeling of free-standing QDs is the description of strained surfaces. For this reason we calculated the variation of the surface free energy γ in Lagrangian coordinates (see Sec. 3.2) of the above surfaces upon biaxial strain ε_s in the surface plane (Eq. 4.23), i.e. the surface stress σ as given by the Shuttleworth equation (Eq. 3.11). In this work it was calculated from the corresponding surface energies at $-0.04 \leq \alpha_s \leq 0.04$ and a fit of $\gamma(\varepsilon)$ to a third-order polynomial $\gamma(\varepsilon) = \sum_{n=0}^3 \gamma^{(n)} \varepsilon^n$. The trace of the surface stress is then related to the polynomial coefficients by

$$\gamma^{(1)} = Tr(\sigma_{ij}) = \left(\frac{\partial \gamma}{\partial \varepsilon_{xx}} + \frac{\partial \gamma}{\partial \varepsilon_{yy}} \right)_{\varepsilon=0} = \sigma_{xx} + \sigma_{yy}. \quad (6.5)$$

The elastic response of the slab upon biaxial strain is determined by the biaxial Poisson-ratio ν that we determined analytically from continuum-elasticity theory in Sec. 4.3 for arbitrary planes of biaxial strain. In our slab calculations of the surface stress, we scaled the fixed bottom layers according to the particular biaxial strain and the corresponding biaxial Poisson ratio as given in Eq. 4.23. Then the upper layers were relaxed until $|\mathbf{F}_{max}| < 0.001 \text{eV}/\text{\AA}$. The surface energies $\gamma_{\varepsilon_{ij}}^{(hkl)}$ of slabs under biaxial strain ε_{ij} are determined with the area of the unstrained surface unit cell $A_0^{(hkl)}$ as

$$\gamma_{\varepsilon_{ij}}^{(hkl)} (\mu^V) = \frac{1}{A_0^{(hkl)}} \left[E_{\varepsilon_{ij}}^{(hkl)} - N^{\text{III}} \mu_{\varepsilon_{ij}}^{\text{III-V}} - (N^{\text{V}} - N^{\text{III}}) \cdot \mu^{\text{V}} \right], \quad (6.6)$$

$$\text{where } \mu_{\text{bulk}}^{\text{V}} - \Delta H_{\varepsilon_{ij}}^{\text{III-V}} < \mu^{\text{V}} < \mu_{\text{bulk}}^{\text{V}}. \quad (6.7)$$

For each surface normal (hkl) the chemical potential of the strained bulk compound material $\mu_{\varepsilon_{ij}}^{\text{III-V}}$ was calculated from bulk supercells with the same periodicity of the surface unit cells in the surface plane. For each strain value, ε_s the chemical potential $\mu_{\varepsilon_s}^{\text{III-V}}$ of the strained compound material is the cohesive energy per formation unit in the bulk supercells scaled with the applied strain and the (hkl)-specific biaxial Poisson ratio ν_{hkl} . Figure 6.10 shows the surface energies for a set of biaxially strained surface unit cells after relaxation: The

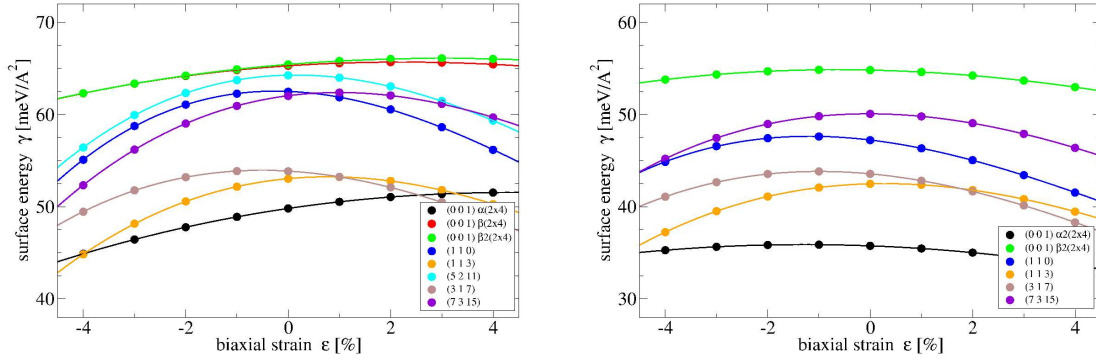


Abbildung 6.10: Dependence of surface energy on strain for GaAs (left) and InAs (right) surfaces.

agreement of the *intrinsic* surface stress with DFT calculations of Penev [74] is not very good. In many cases the sign of the surface stress σ is opposite, indicating that the intrinsic tensile or compressive character of the surface stress as obtained from DFT calculations is not captured by the many-body potential in this work for all surfaces. Still, the many-body potential *does* capture an effect that is of even greater importance for the investigation of InAs/GaAs QD nanostructures presented in the following chapters: The surface energies are reduced at compressive strain by several percent as compared to the surface energies at $\varepsilon_s = 0$. This lowering of the surface energy of particularly the surfaces that appear as QD side facets is meanwhile accepted to play an important role in compensating the additional surface energy upon QD formation, and thereby effectively stabilizing the QDs [75, 76]. This effect is qualitatively captured with our many-body potential.

6.5 Adatom Diffusion on Surfaces: Limitations of MBP

6.5.1 Ga / GaAs(001) $\beta 2(2 \times 4)$: Comparison of MBP with DFT

The description of potential-energy surfaces (PES) of adsorbed atoms on surfaces are usually quite a challenge for many-body potentials. The motivation or derivation of the latter are based on a focus of configurations that can hardly cover the variety of possible stable and intermediate bonding situations within a single functional. We investigated exemplarily the adsorption of a Ga atom on the $\beta 2(2 \times 4)$ reconstruction of the GaAs(001) surface, and compare the results to *ab initio* results by Kley et al. [157] and a previous study by Salmi et al. [189] employing the T3 parameterization of the Tersoff potential. Additionally, we performed similar PES calculations with the parameterization T5 [148]. Firstly, we relaxed a super cell containing 3×5 units of reconstructed (2×4) unit cells without adatom, keeping the lowest layers in the slab fixed. The resulting total energy is used to define the zero level of the adatom adsorption energy. Secondly, we determined the PES for Ga adsorption by positioning the Ga adatom on a grid of lateral positions to be held fixed, and relaxing its height in the different lateral positions as well as the upper layers of the supercell until the absolute maximum force in the system was below $1 \text{ meV}/\text{\AA}$. The lateral spacing of the PES grid of $\Delta x = \Delta y = a_0/25$ results in more than 5.000 points that allow a highly resolved PES with negligible interpolation artifacts. The calculated differences of the total energies to that of the clean surface yields the PES of adatom binding energies shown in Fig. 6.11 for the parameterization determined in this work. The topology of the PES obtained with the

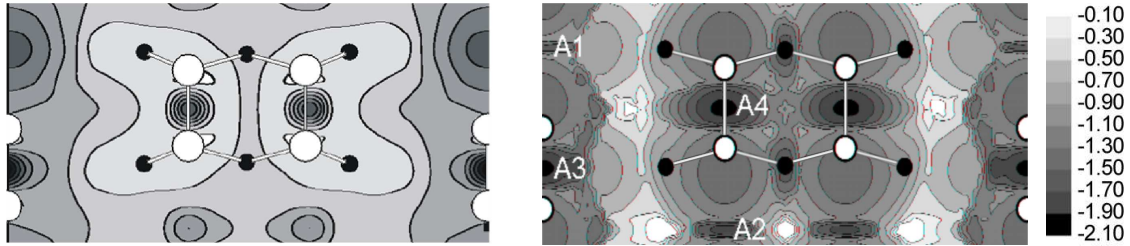


Abbildung 6.11: The adsorption energies (eV) of a Ga atom on GaAs(001) $\beta 2(2 \times 4)$ as obtained with our many-body potential (right) show similarities with according DFT calculations [157] (left), but exhibit several additional minima. The topmost Ga (black) and As (white) atoms are indicated.

parameterization determined in this work and with T5 are in qualitative agreement with the PES calculated previously using T3 and molecular dynamics [189]: The locations of the most stable adsorption sites are similar and the ranges of adatom binding energies of about 2 eV are comparable to the corresponding range of 1.75 eV from DFT calculations [157]. Nevertheless, compared to the corresponding PES calculated with DFT [157], all these results with Tersoff potentials exhibit additional minima that lead to artificial, additional transition-states which

hamper a quantitative comparison of diffusion barriers. The absolute depths of the realistic minima of the adsorption energy depend quantitatively on the parameterization as shown in Tab. 6.11. The parameterization determined in this work underestimates the adsorption

Tabelle 6.11: Adsorption energies (eV) of a Ga adatom at local minima on GaAs(001) β 2(2x4) as obtained with DFT, with the parameterization determined in this work and with previous ones.

	previous calculations		new calculations	
	DFT [157]	T3 [189]	T5 [148]	this work
A1	-2.5	-2.45	-2.38	-1.71
A2	-2.2	-2.43	-2.30	-1.77
A3	-3.2	-3.35	-2.78	-1.95
A4	-2.6	-3.26	-2.68	-1.94

energy minima. The difference of the smallest and largest deviation as compared to the DFT results is 0.71 eV, 0.52 eV, and 0.82 eV for T3, T5, and the parameterization developed in this work, respectively.

To complete the picture of adsorption, we investigated the potential's ability to describe the effect of local changes in the hybridization (see Fig. 6.12). It was first observed by Kley et al. [157], that a Ga adatom has two stable adsorption geometries with either sp^2 or sp^3 configuration at a surface As dimer of the GaAs(001) β 2(2x4) reconstruction (left panel). In similar calculations with the many-body potential developed in this work, a Ga adatom in different heights above the As dimer and with different lengths of the latter exhibited only one stable configuration (middle panel), and thus the analytic many-body potential does not capture this local change of the hybridization. The reason for this deficiency is that there is only one minimum in the angular function (right panel). We expect that introducing an additional minimum in the angular term of the Tersoff potential would allow the description of such multiple minima. Note that the one and only minimum for adsorption of the Ga adatom on the As dimer observed with the many-body potential (middle panel) corresponds to the configuration where the As dimer is broken.

6.5.2 In / InAs(110): Analysis of Artifacts

The quality of the potential-energy surfaces as obtained with many-body potentials is a long-standing issue in the literature (see e.g. Ref. [189]). In the following discussion we address this issue through a detailed study of the observed adsorption energies that aims to distinguish between effects that stem from the rather sharp onset of the cutoff function and those that stem from the angular terms. For this study, we have chosen the adsorption of In on the

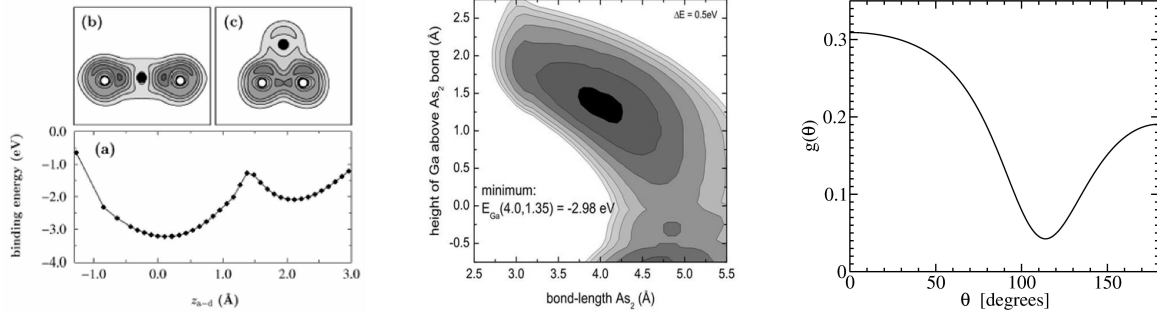


Abbildung 6.12: DFT calculations show two stable positions of a Ga adatom near an As dimer at the surface [157] (left). The MBP does not capture this local change in the hybridization (middle), because there is only one minimum in the angular term $g(\theta)$ (cf. Eq. 5.13) (right).

InAs(110) surface as a comparably simple case with relevance as side facet of larger QDs. A topview of the InAs(110) surface is shown in Fig. 6.13 with the unit cell used in the following calculations as a black frame and the In adatom at the most stable site (center of frame bottom). The dominant motifs are zigzag chains that consist of In and As which are slightly tilted against the surface plane and a trench between the zigzag chains. This configuration with three bonds per surface atom is energetically favorable as compared to As or In terminated surface structures for all allowed values of the As chemical potential [40]. The potential-energy surface of an In adatom on this surface was calculated with the many-body potential in the manner already described in Sec. 6.5.1 and is shown in the right panel of Fig. 6.13.

The corresponding DFT result is presented in detail later in Sec. 9.3.1 and shows two significant minima. The many-body potential reproduces the energetically most favorable adsorption sites in the trench, but gives rise to more structure and additional side minima. One might expect that the angular terms of the many-body potential would favor an sp^3 configuration with the In adatom at the position of an In or As atom of the next full layer that would correspond to the center of the dashed yellow circles in Fig. 6.13. But the observable effect in the PES is only the very weak minimum in the center of the PES plot, where the position of an In atom in the next full layer would be. Another possible origin of the deficient PES obtained with the many-body potential is the reduction of the number of contributions to the adsorption energy due to the limitation of the interaction range by the cutoff function (Eq. 5.14). We therefore investigated the number of neighbors and the height z of the In adatom after relaxation that contribute to the evaluation of the adsorption energy of the adatom at this height with the many-body potential. Both properties are shown in Fig. 6.14 for the same surface unit cell as above. The map of the number of neighbors that interact with the In adatom in the calculations with the many-body potential (left panel of Fig. 6.14)

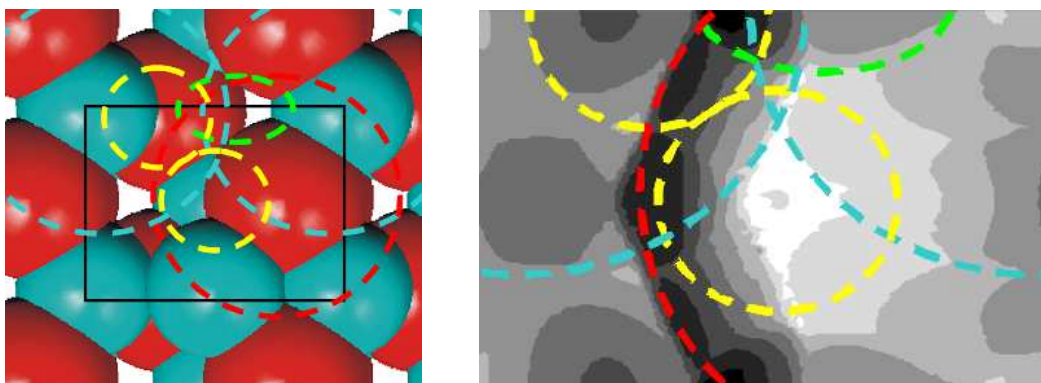


Abbildung 6.13: The most stable site of an In adatom on InAs(110) is in the trench (left: surface with adatom at bottom center of black frame). The PES (right, contour spacing: 0.15 eV) of In adsorption in the surface unit-cell (left: black frame) as obtained with the many-body potential is more rough than the corresponding DFT result (cf. Fig. 9.3, right). The dashed lines mimic the topology of the right panel of Fig. 6.14 and are explained in the text.

exhibits much less structure than the according PES (left panel of Fig. 6.13). In most regions it interacts with only one surface atom, and thus, several features of the PES are arising from the same set of interacting atoms. We can hence exclude that the additional structure of the PES as obtained with the many-body potential is due to a change in the number of contributions to the adsorption energy.

Additionally, we compiled the z -coordinate of the relaxed In adatom in the different grid points as observed in the PES calculation (right panel of Fig. 6.14). The centers of the dashed yellow circles in Fig. 6.14 again correspond to the positions of the In and the As atom in the next full layer. A strong influence of the angular terms would appear as a preference for the adatom in the region of the dashed yellow circles, but we find no trace of such an effect in the map of z -coordinates, similar to the PES. The overall topology resembles the PES, i.e. the height of the adatom is related to its adsorption energy in many positions. It appears that an understanding of the topology of adsorption heights of the adatom would provide an understanding of the PES topology and vice-versa. To visualize the degree of correlation between the adatom height and its adsorption energy, we mimicked features of the map of z -coordinates by the dashed red, blue, and green circles introduced to the right panel of Fig. 6.14, and transferred these circles without modification to the topview of the surface structure and the calculated PES (Fig. 6.13). (Additional circles due to the symmetry of the unit cell were not included.) We find that some of the features of the PES are in fact coinciding with the circles that were determined by mimicking the topology of adsorption heights. Interestingly, from a comparison of the transferred circles with the underlying surface

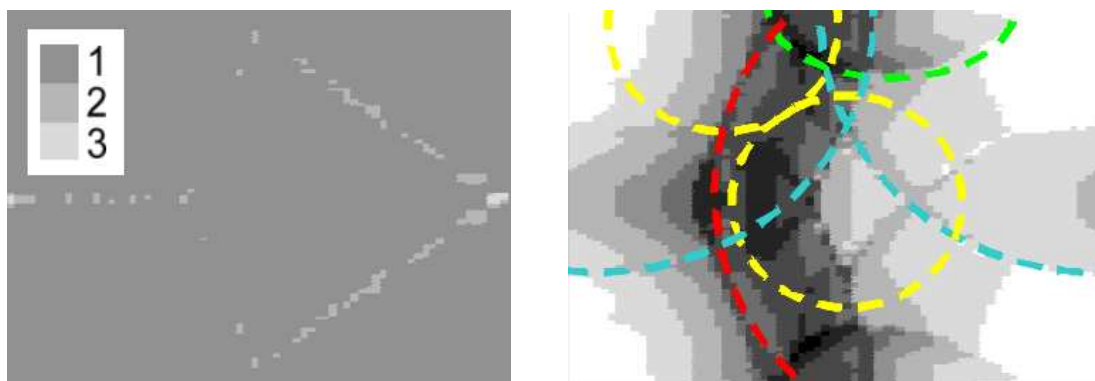


Abbildung 6.14: The number of neighbors N that are interacting with the In adatom in its different lateral positions (left) shows much less structure than the corresponding PES (Fig. 6.13). But the topology of observed z -coordinates of the relaxed In adatom (right, contour spacing: 0.25 \AA) can be correlated to the PES: To indicate this, we mimicked the topology of z with the dashed blue, red and green lines, and transferred them to the PES. The positions of In or As atoms in the next full layer (center of dashed yellow circles), however, are not apparent in the maps of N and z .

structure, we can identify the In and As atoms in the topmost zigzag chain as centers of the blue and red circles, respectively. These circular features of adsorption height and binding energy can thus be attributed to the onset of the spherical cutoff function around the topmost atoms. The origin of the green ellipse, however, is not apparent, it could be an effect of the cutoff of the angular function. We conclude that the major part of the PES as obtained with the many-body potential is determined by the interaction of the adatom with only one surface atom. The additional topological features as compared to DFT results are not due to the angular terms but instead resemble the onset of the spherical cutoff function.

Kapitel 7

Self-Assembled QD Growth

In the previous chapter we showed that our newly developed many-body potential captures many bonding-situations that typically occur in InAs/GaAs QD nanostructures with good overall accuracy. In the following we describe the route from atomistic representations of experimentally observed QD shapes to the relaxation with our many-body potential and the analysis of the changes in formation energy and the strain relief during QD growth. In particular, we demonstrate the convergence with substrate thickness, quantify the lateral elastic interaction of QDs, and identify the driving force for the experimental finding of a sequence of shapes with increasing QD size. With our atomistic approach, we can furthermore complete the thermodynamic interpretation of the shape transition by determining its dependency on the chemical potential of As and the lateral QD density.

7.1 Experimental Findings

Due to the large number of careful experiments in the last decade, we already have a good understanding of many aspects of quantum dot (QD) growth: The formation of QDs in Stranski-Krastanov growth mode is due to the lattice mismatch of deposited and substrate material. It could be realized for many different combinations of materials, and turned out to be of similar nature for various systems, such as InAs/GaAs(001) and Ge/Si(001) [19]. The QD nanostructures of these two materials are of major technological importance and very well characterized. The lattice mismatch can be systematically decreased by depositing alloyed instead of pure materials, such as $\text{In}_x\text{Ga}_{1-x}\text{As}$ on a GaAs substrate. Such an alloying is known to scale the characteristic lengths (like the transition coverage) for appropriate growth conditions (see e.g. Ref. [190]). Still, it depends strongly on the experimental conditions if semiconductor heteroepitaxy eventually leads to the self-assembled formation of coherent QDs. In fact, many combinations of temperature, As pressure, and growth rate will result in the formation of incoherent QDs, other coherent nanostructures (such as quantum wires,

dashes or rings), or no nanostructures at all. (In the latter case one often finds rough or stepped surfaces, possibly with defect formation.) The formation of QDs was observed on different substrates, e.g. $\{001\}$ [18], $\{113\}$ [184, 185, 186], and $\{25\bar{1}1\}$ [95], within rather small windows of experimental conditions. From *in-situ* RHEED measurements during MBE growth, it is known that the transition from 2D film growth to 3D island growth sets in at a coverage of about 1.7-1.9 ML of InAs on GaAs(001). The usage of direct-imaging methods (AFM, STM) after growth show lateral QD densities of about $10^9 - 10^{11} \text{ cm}^{-2}$. However, the QD density of a particular sample depends strongly on the growth conditions (see e.g. Ref. [191]), in particular on coverage, growth rate, flux ratio, and temperature. The effect of the latter on the detailed diffusion kinetics was shown to have a strong impact on the island density in GaAs homoepitaxy [28]. Additional effects in InAs/GaAs heteroepitaxy can be due to segregation, island coalescence, and transitions of the island shape. (The latter can significantly alter the elastic interaction between neighboring islands, as we shall see in Sec. 7.5.) The detailed shape of QDs exhibits characteristic side facets which depend on both, the material system and the substrate orientation. For InAs/GaAs(001) and Ge/Si(001) it was shown that the QD shapes additionally depend on the QD size (see Fig. 7.1) and undergo a transition from rather flat to steeper shapes (see e.g. Refs. [19, 192, 193]). In

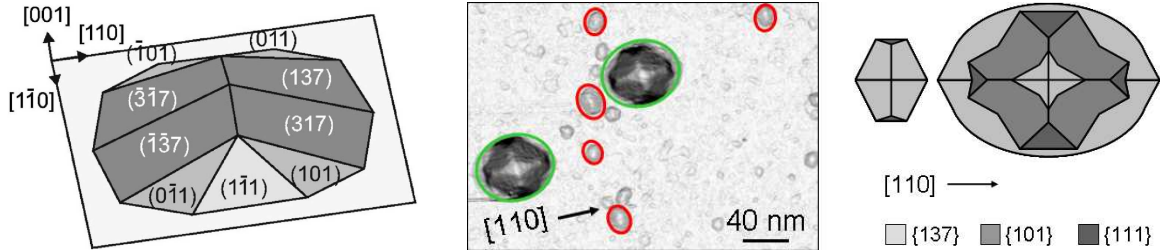


Abbildung 7.1: QD shapes as observed in high-resolution STM experiments by Márquez et al. [18] (left) and Costantini et al. [19] (middle and right). These shapes are referred to as *hut* and *dome* in this work.

fact, very recent STM experiments observed a similar shape transition for InAs QDs on GaAs(114) [96] which suggests that this is not a particular feature of (001) substrates. The importance of a shape transition during growth is due to its ability to explain the unusual bimodal distribution of QD sizes that is in contradiction to the expectation from conventional Ostwald ripening. For meaningful comparisons with theoretical results, the discrimination of kinetic and thermodynamic effects is of major importance. In this section and the following one, we focus on the question of which aspects of QD growth can be understood within a thermodynamic rationale. Our study is based on comparisons of formation energies calculated with the many-body potential developed in this work.

7.2 Calculations of QD Nanostructures

7.2.1 Initialization

The thorough investigation of realistic QD nanostructures requires the consideration of not only the QD itself, but additionally an appropriate amount of substrate material that is sufficient to converge the atomic forces that arise from the long-range strain field. Such convergence tests are presented in the next section. The lateral extension of the simulation cell with one QD defines the QD density per area (see Fig. 1.3). The densities used in our studies correspond to the experimentally observed density of 10^{11} QD/cm², and were varied to investigate effects on the lateral QD-QD interaction energy of one layer of freestanding QDs (Sec. 7.5) and of stacked layers of QDs (Sec. 8.3). The required vertical and lateral extension of the simulation cell results in systems with typically one million atoms. We developed a tool that allows us to easily initialize such systems with realistic surfaces, edges and kinks, as described in Appendix C. It is based on the definition of the QD side facets by plane equations that are specified by the corresponding Miller indices and the plane distance from the origin. These planes are chosen according to results of STM experiments (e.g. Ref. [18, 19]). Note that both the In and Ga atoms of the initial QD structures are located on a zinc blende lattice with the lattice constant of GaAs as obtained with our parameterization (Tab. 6.4). For all QD structures, the stoichiometry profile was chosen to generate a wetting layer of 1.75 ML of InAs and pure InAs QDs.

7.2.2 Relaxation and Formation Energy

We relax all investigated heterostructures with the many-body potential developed in Chap. 5 using an adapted version of the conjugate-gradient algorithm given in Ref. [153]. This method yields the closest nearby local minimum of the total energy which is adequate as long as the relaxation of the strained atomic bonds preserves the structure qualitatively. Investigations of structural changes (e.g. defect formation or changes in the surface reconstruction) as well as the search for the global minimum of the total energy for the given set of atoms would require other techniques. We performed slab calculations in which the positions of the atoms in the lowest four atomic layers were kept fixed, all other atoms were allowed to move freely, and periodic boundary conditions were applied in the substrate plane. The lateral sizes of the simulation boxes were held constant at multiples of the GaAs bulk lattice-constant to model an ideal GaAs bulk underneath the InAs wetting layer. For finite size effects such as wafer bending, different boundary conditions might be more appropriate. We relaxed the structures until the absolute value of the maximum force in the system was below 1 meV/Å to ensure that the total energy is well converged (see Fig. B.2 in the appendix).

Each surface i in a system with free standing QDs contributes to the total energy according to the particular surface free energy γ_i per area and the area A_i . These contributions to the total energy as obtained with the many-body potential are afflicted with errors per area δ_i as

discussed in Sec. 6.3. Determining the areas of the involved surfaces then allows us to perform a lowest order error-correction of the total energy by evaluating

$$E_{\text{tot}}^c = E_{\text{tot}} - \sum_i \delta_i A_i. \quad (7.1)$$

The stoichiometry of the surfaces, edges, and kinks of the QD nanostructures lead to a well-defined overall stoichiometry of the simulation cell that can be determined by simply counting the atoms of the different species, N_{Ga} , N_{In} , and N_{As} . Then the formation energy of an InAs/GaAs system \mathcal{S} with respect to an initial structure \mathcal{I} is given by

$$E_f(\mathcal{S}) = \Delta E_{\text{tot}}^c - \Delta N_{\text{Ga}} \cdot H_{\text{GaAs}}^f - \Delta N_{\text{In}} \cdot H_{\text{InAs}}^f - (\Delta N_{\text{As}} - \Delta N_{\text{In}} - \Delta N_{\text{Ga}}) \cdot \mu_{\text{As}} \quad (7.2)$$

where $\Delta X = X(\mathcal{S}) - X(\mathcal{I})$ denotes the differences of the energy and the numbers of atoms per species with respect to the initial system. The values of the heat of formation of GaAs and InAs, H_{GaAs}^f and H_{InAs}^f , are given by the cohesive energies of the corresponding zinc blende bulk structures. The freedom to choose the As chemical potential within $\mu_{\text{As}}^{\text{bulk}} - H_{\text{GaAs}}^f < \mu_{\text{As}} < \mu_{\text{As}}^{\text{bulk}}$ affects comparisons of QD nanostructures with different stoichiometries as we shall see in Sec. 7.6.

7.3 Wetting Layer

The self-assembled growth of QDs in the Stranski-Krastanov mode (Sec. 3.3) starts out with the formation of a wetting layer that covers the substrate completely, followed by the transition to 3D island growth. For the calculation of the critical nucleus, we need to determine the formation energy of the InAs wetting layer on the GaAs(001) substrate with respect to the increasing amount of InAs deposited. In Sec. 3.2 we have already noted that the relative stability of different reconstructions of the same surface depends on the chemical potentials. In the case of lattice-mismatched heteroepitaxy, the dependence of the surface energy on the amount of biaxial strain introduces an additional degree of freedom (Sec. 6.4). Previously performed DFT calculations of Penev [74] showed that the most stable surface reconstruction of InAs(001) under compressive strain (due to the lattice mismatch with the GaAs substrate) is the $\alpha 2(2 \times 4)$ reconstruction shown in Fig. 6.6 for a wide range of As pressures. This surface reconstruction is stoichiometric and therefore does not depend on the chemical potentials of the gas phase. Following this work, we determined the formation energy of a $\alpha 2(2 \times 4)$ surface reconstruction with the many-body potential developed in this work: The increasing InAs coverage is mimicked by successively replacing the Ga atoms of a GaAs(001) $\alpha 2(2 \times 4)$ surface reconstruction with In atoms. Similar to Ref. [74], we perform these replacements simultaneously for all atoms that are in the same row along the crystalline direction $[\bar{1}10]$, indicated by numbers 1-7 in the right panel of Fig. 7.2. The increment of the InAs coverage for this unit cell is therefore 0.25 ML InAs. We start the replacements from the topmost

rows and consider all combinations for each value of coverage Θ . A coverage of $\Theta = 1.00$ for example can be realized by replacing the Ga atoms in the rows 1-3 and one out of 4-7. The formation energies per unit area γ_f for all combinations of all values of coverage as obtained from relaxation with our potential are collected in the left panel of Fig. 7.2, together with the previously obtained results of DFT calculations. In all calculations we used a 4×2 repetition of the (2×4) surface unit-cell, and periodic boundary-conditions in the surface plane that correspond to an unstrained GaAs bulk lattice. In these calculations of the wetting layer we used 20 ML GaAs to achieve reliable values of the formation energies. Our calculations

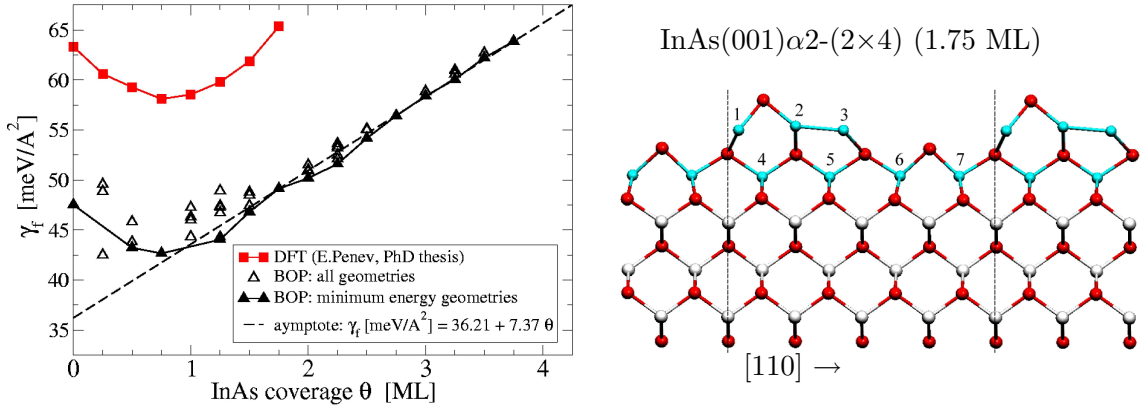


Abbildung 7.2: Formation energy of InAs(001) α_2 (2×4) wetting layer for different coverages (left) as obtained with DFT calculations [74] (red) and the many-body potential developed in this work¹ (black). The coverage is increased in increments of 0.25 ML by successively replacing Ga atoms with In atoms in rows along $[110]$ indicated by labels 1-7 (right panel).

with the many-body potential are shifted with respect to the previously performed DFT calculations for up to $\Theta = 1.75$ by approximately $15 \text{ meV}/\text{\AA}^2$ which reflects the errors in the surface energy per area already noted in Tab. 6.9 and 6.10. The curvature of $\gamma_f(\Theta)$ is very well reproduced with the many-body potential¹. Fitting the results for coverages up to 1.75 ML as obtained from calculations with DFT and the many-body potential to second-order polynomials yields

$$\gamma_f^{\text{DFT}}(\Theta) [\text{meV}/\text{\AA}^2] = 63.4 - 12.7\Theta + 7.9\Theta^2 \quad (7.3)$$

$$\gamma_f^{\text{MBP}}(\Theta) [\text{meV}/\text{\AA}^2] = 47.4 - 11.9\Theta + 7.5\Theta^2. \quad (7.4)$$

¹The deviations of $\Theta = 0.25$ and $\Theta = 1.00$ are due to contributions from In-Ga bonds that fall back on parameters for the In-Ga interaction: These were not included in the optimization, but instead determined from an averaging scheme [138]. This is the only case in this study, where In-Ga bonds come into play.

For InAs coverages beyond 1.75 ML, the formation energy as obtained with the many-body potential is not a continuation of the above polynomial, but rather a sequence of polynomials defined in sections with discontinuous derivatives at $\Theta = 1.75 + n$, where $n = 0, 1, \dots$. This behavior can be understood by realizing that the latter coverages correspond to complete layers of compressed InAs that comprise more elastic energy than intermediate coverages. This effect vanishes for sufficiently large coverages where the dominant part of the elastic energy is stored in the complete InAs layers. We performed analogous calculations with the many-body potential for a wetting layer of 1.75 ML InAs with the $\beta 2(2 \times 4)$ reconstruction and found similar agreement with the DFT calculations of Penev [74].

7.4 Convergence with Substrate Thickness

The elastic relaxation of a system with only a homogeneous InAs film is dominated by biaxial strain in the surface plane that affects mainly the film itself. The stress tensor due to a free-standing QD in contrast has components perpendicular to the surface plane that can result in a non-vanishing strain tensor deep in the GaAs substrate. This implies the possibility of finite-size effects in our investigations with the many-body potential where we keep the atoms in the lowest atomic layers fixed during the relaxation. We obviate such technical artifacts by convergence tests of the formation energy of QD nanostructures with respect to the vertical extension of the GaAs substrate. For this purpose, we initialized and relaxed *hut*-shaped and *dome*-shaped QDs with a wetting layer of 1.75 ML InAs on a GaAs(001) substrate of different vertical extension. In each case we determined the difference between the total energy of the relaxed QD structure and a homogeneous InAs film of 1.75 ML thickness on a GaAs substrate of the same size. This is the quantity that needs to be converged with respect to substrate thickness for the calculation of formation energies, the other terms in Eqs. 7.1 and 7.2 are not altered upon variation of the substrate thickness. The resulting values of $\Delta E_{\text{tot}}/\Delta N_{\text{tot}}$ as calculated for different lateral densities of QDs per unit area are shown in Fig. 7.3. An in-depth investigation of the variation of the relative stability of homogeneous films and differently shaped QDs with size will be presented in the following section. For these two differently shaped QDs of comparable size however, we find that the formation energy is converged to approximately 1 meV per atom for substrates of more than 60 Å thickness. This accuracy is sufficient in all cases studied of this work (c.f. Fig. 7.5, 7.7, or 8.6). The required amount of substrate corresponds to approximately two times the height of the *dome*-shaped or three times the height of the *hut*-shaped QD. In all following calculations we will use these relations to ensure that the formation energies are sufficiently converged. A rather surprising observation of Fig. 7.3 is that these two shapes exhibit a very different behavior with respect to the lateral QD density: The change in formation energy with variation of lateral QD density is an order of magnitude larger for the *hut*-shaped QD than for the *dome*-shaped QD. Previous investigations of truncated InAs pyramids with $\{101\}$ side facets on

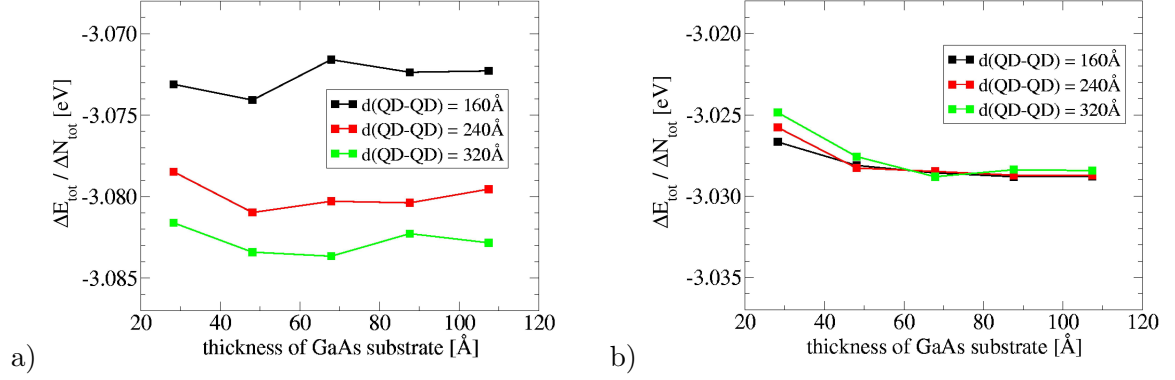


Abbildung 7.3: The convergence of the formation energies (Eq. 7.2) of a QD in either a) *hut* shape (with 1364 In atoms) or b) *dome* shape (with 2042 In atoms) with respect to the substrate thickness is determined by the energy difference ΔE_{tot} of the QD structures and homogeneous films with identical GaAs substrate per additional atom in the QD, ΔN_{tot} . The colors indicate different lateral QD densities.

a InP(001) substrate using finite-element calculations [194] already showed that the elastic interaction of islands of the same volume increases with decreasing aspect ratio of the QD. This trend reflects the increase of substrate area covered by QDs (all having the same angle of 45° between substrate and side facets) but does not explain the different elastic interaction of *hut*- and *dome*-shaped QDs observed in Fig. 7.3. This difference observed in our study can be understood by an analysis of the strain tensor ε in the substrate material below the QDs. Particularly instructive in this case is the visualization of the hydrostatic strain $\text{Tr}(\varepsilon)$: In Fig. 7.4 we plotted those values of $\text{Tr}(\varepsilon)$ in the (110) plane below the base center of the QDs that are within $[-0.005, +0.005]$. The absolute value of the hydrostatic strain in large portions of the substrate below the relaxed, free-standing InAs QDs is in fact less than 0.5 %. This value is exceeded only in the regions below the base center and at the base edges that comprise larger tensile and compressive hydrostatic strain, respectively, shown as yellow and black regions in Fig. 7.4. The difference in the hydrostatic strain in the substrate is due to the relative orientation of the QD side facets to the elastic principal axes. Our results on the direction dependence of the biaxial Poisson-ratio (see Fig. 4.1) allow us to understand this effect: Before the QD nanostructure is relaxed, the InAs is compressed to accommodate an ideal zinc blende structure with the lattice constant of GaAs. The stress tensor at the base of defect-free QDs has an effectively *tensile* part in the planes of the QD side facets. In these planes, the substrate in the vicinity of the base is subject to *compressive* stress. The resulting strain will be comparably small, if the stress (and hence the QD side facet) is parallel to elastically hard axes like [101] and [111]. However, if the stress (and hence the QD side facet)

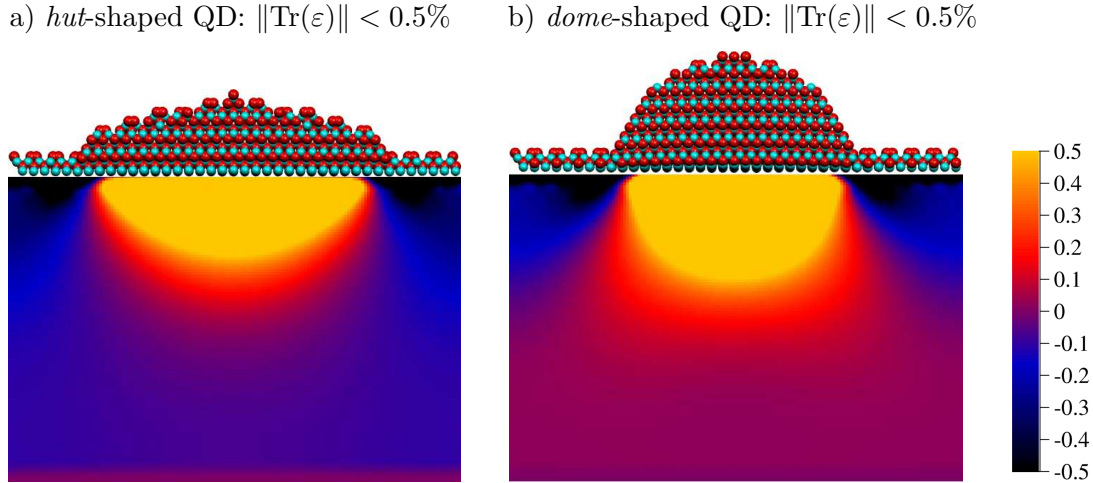


Abbildung 7.4: The trace of the strain tensor $\text{Tr}(\varepsilon)$ in the (110) plane of the GaAs substrate below the base center of a QD in either a) *hut* or b) *dome* shape reveals the origin of the different lateral interactions observed in Fig. 7.3: The hydrostatic strain due to a *hut*-shaped QD is much more extended in the substrate than those of a *dome*-shaped QD.

is parallel to an elastically softer axis like [137], the resulting strain in the substrate will be larger, just as we observe it.

It can easily be verified that the direction-dependencies of the biaxial Poisson-ratio for Ge and Si are similar to those of GaAs and InAs by employing the corresponding elastic constants in Eq. 4.28. Therefore we conclude that also in the case of Ge/Si(001) the lateral interaction between *hut*-shaped QD (with $\{105\}$ side facets) is stronger than those between *dome*-shaped QD (with $\{101\}$ side facets). For this material system, such a repelling interaction between islands was even observed experimentally by an elaborate sequence of QD growth, annealing, selective etching, and characterization of the surface with AFM (atomic force microscopy) [195]: For islands at close quarters, the direction of lateral movement could be correlated to the direction of the next-neighbor island [196].

Note that the above procedure of converging the formation energy with substrate thickness refers to the limit of negligible thickness of the InAs film as compared to the GaAs substrate. This assumption is appropriate for the majority of experimental investigations of InAs/GaAs QD nanostructures. However, there are cases where finite-size effects play the dominant role (see e.g. Ref. [197]).

7.5 Elastic Energy in Lateral QD Array

The strain tensor that a QD implies in the wetting layer and the substrate is of long-range character and can interact with those of other QDs at a distance R , as we have in the previous section. The according elastic interaction energy can be expressed in terms of a multi-pole expansion with the dipole-dipole elastic interaction as leading term [38, 113]. In this approximation, the interaction energy of an array of elastically coupled QDs reads

$$E_{\text{elastic}}(R) = \text{const} \cdot \left(\frac{1}{R}\right)^3 \cdot F(R) \quad (7.5)$$

where the prefactor contains the elastic moduli, the atomic volume, the lattice mismatch, and a shape function of the particular QDs, all being of constant value in this study. The function $F(R)$ comprises the density of the lateral QD array (right panel of Fig. 7.5), and a correction term that accounts for the deviation of the dipole-dipole approximation at small R . Previous works neglected the lateral QD-QD interaction [198], or used idealized QD shapes and characteristic values of surface and edge energies [38]. In this work, however, we apply the many-body potential developed in Chap. 5 to determine the elastic QD-QD interaction of realistic, atomically detailed InAs QDs without approximations (apart from the potential itself). In addition to the calculations with the *hut*-shaped QD from the previous section at more than 100Å thick GaAs substrate, we determined the formation energy $E_{\text{formation}}(R) = E^{(0)} + E_{\text{elastic}}(R)$ at small and intermediate values of R shown in the left panel of Fig. 7.5. We find that the long-range, repulsive interaction energy per atom is well described by the dipole-dipole elastic interaction of Eq. 7.5 with a power law for $F(R)$ as

$$E_{\text{elastic}}(R) = E^{(1)} R^{-3} R^\alpha, \quad \text{where } \alpha \approx 1.5. \quad (7.6)$$

The asymptote $E^{(0)}$ of an elastically non-interacting QD array was determined in two different ways, by either treating α as variable (leading to $\alpha = 1.4$) or by setting $\alpha = 1.5$ in the fitting of the formation energies. The difference in the resulting asymptotic value was not more than 0.7 meV. The elastic interaction energy at a certain value of R is then given by the difference between the corresponding formation energy and $E^{(0)}$ as shown in the left panel of Fig. 7.5. From similar calculations for larger QDs (# 6 and # 9 in Tab. 7.1) we find that the volume dependence of $E^{(1)}$ is well described by a linear relationship (inset in left panel of Fig. 7.5).

The resulting difference in elastic energy between an array of *hut*-shaped QDs that almost touch each other ($D = 100\text{\AA}$) and the asymptote of infinite distances is as big as 25 meV per atom, whereas it is negligible for the case of *dome*-shaped QDs. This finding has important implications for the investigation of the relative stability of these two shapes presented in the following section: If the QDs are closer to one another (due to increasing size or increasing lateral density), the formation energies of *dome*-shaped QDs is nearly unaffected by elastic interactions among neighboring QDs. The *hut*-shaped QDs instead repel each other with

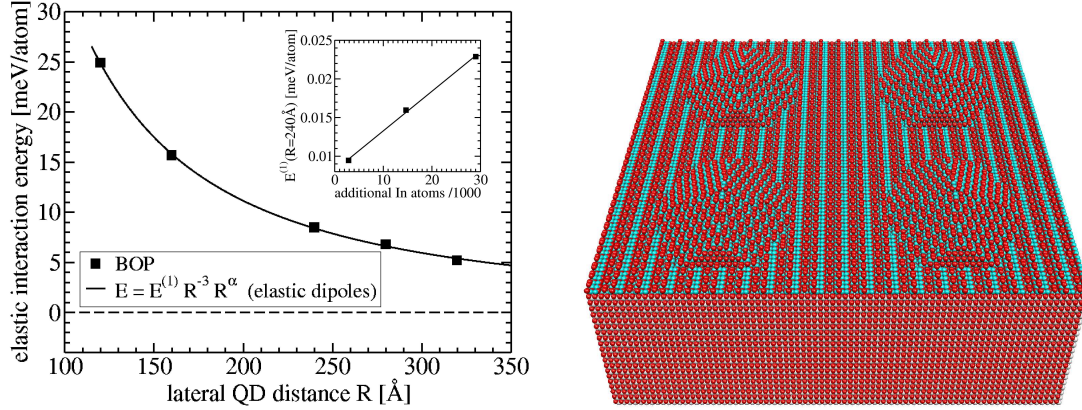


Abbildung 7.5: The elastic interaction of a lateral array of hut shaped QDs of size #3 in Tab. 7.1 (right: $R = 160\text{Å}$) can be determined from the formation energies at constant substrate thickness and is of repulsive character. In the investigated range of QD distances R , it follows the relation predicted for the interaction of elastic dipoles [113] (left). The inset (left) shows that the elastic interaction energy at constant lateral QD density depends linearly on the volume of the QD.

increasing elastic energy as their mutual distance shrinks. The resulting increase in formation energies is of the same order of magnitude as the difference in formation energy between *hut*-shaped and *dome*-shaped QD. Hence, with increasing QD size or lateral QD density, the different elastic interactions in a QD array tend to destabilize *hut*-shaped QDs in favor of *dome*-shaped QDs. This finding contradicts the previously applied approximation that QD shape-transitions are only slightly affected by lateral QD-QD interactions [37]. The origin of this discrepancy is that these authors assumed an elastically isotropic substrate, whereas our calculations include the elastic anisotropy of both GaAs and InAs.

These results allow a new interpretation of the experimental finding that the effective film-stress of a Si(001) wafer with a layer of self-assembled $\text{Si}_{0.8}\text{Ge}_{0.2}$ islands² is reduced when the QDs undergo a transition from *hut* shapes with $\{105\}$ facets to *dome* shapes with $\{101\}$ facets [199]. Transferring our findings from InAs/GaAs to Ge/Si, we conclude that the elastic interaction of *dome*-shaped Ge QDs with side facets in elastically hard planes is significantly weaker as for the case of *hut*-shaped Ge QDs with side facets that correspond to elastically softer planes. Therefore, we conclude that the reduction of substrate stress upon the shape transition is mainly due to the resulting difference in elastic interactions. The effect of reducing the substrate area that is covered by QDs [199] is comparably small. A detailed

²The growth behavior of depositing a SiGe alloy is only quantitatively different from depositing pure Ge. The advantage is an increase of the characteristic length-scales that makes it much more tractable experimentally.

investigation of the shape transition for the case of InAs/GaAs is presented in the following section.

7.6 Regimes of Thermodynamic Stability

It was first observed experimentally for the case of Ge/Si(001) that the bimodal distribution of QD sizes corresponds to two different shapes [192] with a small region of shape coexistence. The interpretation as shape transition during growth was confirmed by theoretical investigations [200] that showed, that the minimum-energy shape of islands on a lattice-mismatched substrate changes with volume. The slope of the formation energy with respect to the QD volume is then discontinuous at the intersections of different shapes, which leads to a discontinuous evolution of the chemical potential $\mu = \partial G / \partial N$ (Eq. 3.2) during growth. If the evolution of the chemical potential with island size would be continuous, the QDs would undergo the so-called *Ostwald ripening*, i.e. the larger ones would grow on the expense of the smaller ones, thereby creating a unimodal size distribution (see e.g. Ref. [201]). A discontinuous dependence of the chemical potential on the island volume instead was shown to produce a bimodal size distribution without introducing additional size-limiting effects [202]. The discontinuity in the above theoretical works was due the assumption of distinctively different minimum-energy shapes, but a very recent study could show that it is also observed in traversing the intermediate shapes along the shape-transition path-way [44]. The bimodal size distribution with different shapes are not specific to the material system Ge/Si, but in fact a more general aspect of QD growth. Recent high-resolution STM experiments revealed the shape of InAs QDs in atomic detail [18], and found a shape transition during growth for the case of InAs/GaAs, too [193, 203]. In fact, careful experimental investigations [19] revealed strong similarities with Ge/Si: In both cases, the size distribution is bimodal with small QDs that are rather flat and dominated by $\{105\}$ or $\{137\}$ side facets for Ge/Si or InAs/GaAs, respectively. The larger QDs are steeper and bound by $\{101\}$ side facets in both material systems. These detailed experimental studies also showed that the shape transition is reversible upon annealing. The previous theoretical investigations of the shape transition mentioned above are mostly based on material-unspecific continuum models. In this work, however, we employ our many-body potential to study this effect for the case of InAs/GaAs(001) in full atomistic detail. This enables us to specify the location of the discontinuity quantitatively, and to study its dependence on the chemical potential of the As gas phase. Furthermore, we will discuss the implications of the lateral elastic interactions found in the previous section.

In particular, we investigated the above shown *hut* shapes dominated by $\{137\}$ facets with a minor share of $\{\bar{1}11\}$ facets, and the *dome* shapes with mainly $\{101\}$ facets and minor areas of $\{137\}$, $\{111\}$, and $\{\bar{1}11\}$ facets on the top and the bottom, respectively. The resulting atomistic representations of these experimentally observed QD nanostructures are shown in the left panel of Fig. 7.6. Note that the $\{101\}$ facets of the *hut* shape given in Ref. [18] is not

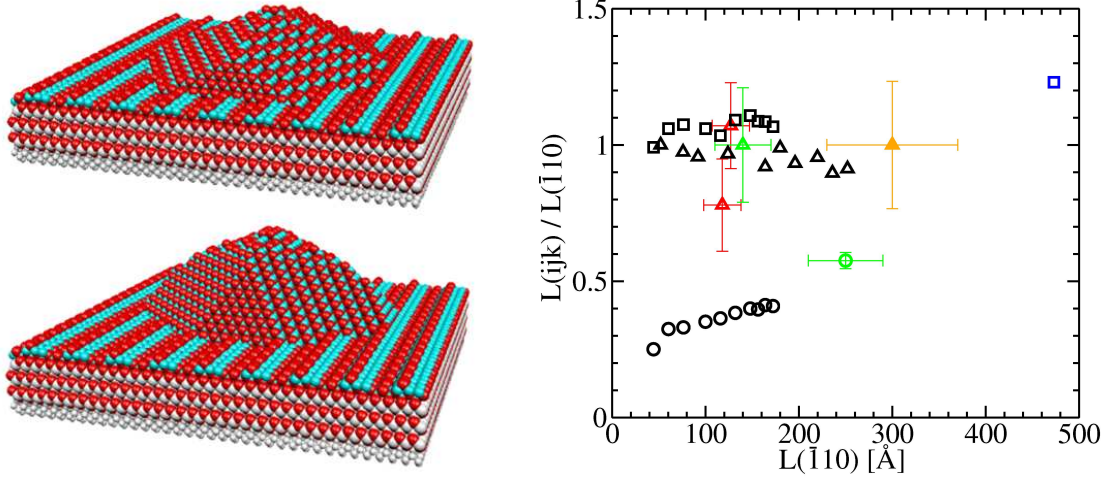


Abbildung 7.6: Atomistic representations of InAs QDs in *hut* shape (top left) and *dome* shape (bottom left) on a GaAs(001) substrate with 1.75 ML InAs as wetting layer. (The color scheme for the different atoms is again according to Fig. 6.1, apart from the bottom layers to indicate that they were kept fixed in the relaxation.) The ratios of characteristic lengths (right: ○= $L_{001}/L_{\bar{1}10}$ (*dome*), □= $L_{110}/L_{\bar{1}10}$ (*dome*), △= $L_{001}/L_{\bar{1}10}$ (*hut*)) used in this work (right: black) are close to experimentally observed values (right: Ref. [22] (red), Ref. [19] (green), derived from Ref. [19] (blue), Ref. [204] (orange)).

consistent with the given arrangement of the other planes, so we did not consider this facet in our study.

The thermodynamic stability of homogeneous films or QDs with different shapes can be compared by means of the according formation energies (Eq. 7.2) in dependence of the number of atoms (or, equivalently, the volume) of the particular structure. Perfect isomorphic scaling of a given structure can be achieved easily within continuum approaches, but in the atomistic approach presented in this work, a change of the QD volume involves integer changes in the number of atoms and the number of atomic layers of each facet. For different QD side facets, the distance between subsequent layers along the surface normal and their projection to the substrate plane can differ. This effectively leads to different (discrete) increments of the characteristic lengths, like the QD base length along $[110]$. In an atomistic approach like the one used in this work, the isomorphic volume-scaling of a given QD shape can only be done in an approximative manner. We determined typical ratios of characteristic lengths of experimentally observed QD shapes [18, 19, 22, 204, 205] and initialized the atomistic QD structures in different sizes [206] such that the chosen length ratios are similar, as shown in the right panel of Fig. 7.6. The parameters for isomorphic scaling as used in our initialization tool are given in Tab. 7.1 and 7.2 for the *hut* shape and the *dome* shape, respectively, together with

the total number of atoms in the QDs. The lengths given in Tab. 7.1 and 7.2 characterize

Table 7.1: *Hut*-shaped QDs: Miller indices of the side facets and distances from origin of the coordinate system, as well as the resulting characteristic lengths and the number of atoms.

#	$\ \mathbf{n}_{(\bar{1}\bar{1}1)}\ $	$\ \mathbf{n}_{(317)}\ $	$L_{[110]}$ [Å]	$L_{[\bar{1}10]}$ [Å]	ΔN_{In}
01	32	25	52	52	272
02	40	28.7	74	76	663
03	48	33	88	92	1384
04	60	39	120	124	3121
05	76	44	151	164	5716
06	83	47	178	180	7541
07	90	50	183	196	9721
08	99	53.7	210	220	13112
09	106.5	55.1	212	236	14848
10	112	58	230	252	18215

the QD shape uniquely and were determined as the distances between those atoms at the QD bottom that are not part of the surface reconstruction. The relative stability of different surface reconstructions of the substrate depends on both the local strain due to the presence of a QD and the chemical potential of As, as discussed in great detail in the Ph.D. thesis of E. Penev [74]. In this study, however, we focus on the formation energies of different structures with respect to a wetting layer (see Eq. 7.2) with the same surface reconstruction. The major part of the surface energy of the wetting-layer reconstruction will therefore cancel out and only the difference in substrate area that is covered by different QD shapes will contribute. The resulting change in the formation energy increases with QD size, but is only of a value of approximately 1 meV for the largest QD investigated in this work. Our particular choice of a $\beta 2(2 \times 4)$ reconstruction for the wetting layer is thus of minor importance for the kind of study presented in this section. The QD nanostructures were investigated in simulation cells with a side length of 480 Å along the crystalline directions (110) and ($\bar{1}10$) corresponding to a lateral QD density of $4 \cdot 10^{10} \text{ cm}^{-2}$. The lateral elastic interaction among the QD in the simulation cell and its periodic images are comparably small for this density (c.f. Fig. 7.5), but we will discuss the influence of higher densities in the next section. We relaxed each structure with our many-body potential, corrected the surface-energy errors of the total cohesive energy (Eq. 7.1), and calculated the formation energy with respect to a homogeneous InAs film of 1.75 ML thickness according to Eq. 7.2. Our results for the homogeneous InAs film and QDs in either *hut* or *dome* shape with increasing number of deposited In atoms are shown in Fig. 7.7 at As-poor conditions. We find that our calculated formation energies are very well described by an analytic expression that was proposed previously [33, 40, 198]: These works

Tabelle 7.2: *Dome*-shaped QDs: Miller indices of the side facets and distances from origin of the coordinate system, as well as the resulting characteristic lengths and the number of atoms.

#	$\ \mathbf{n}_{(101)}\ $	$\ \mathbf{n}_{(111)}\ $	$\ \mathbf{n}_{(\bar{1}11)}\ $	$\ \mathbf{n}_{(317)}\ $	$L_{[110]}$ [Å]	$L_{[001]}$ [Å]	$L_{[\bar{1}10]}$ [Å]	ΔN_{In}
01	26	28	28	25	44	11	44	224
02	31	38	34	33	64	20	60	654
03	37	44	41	39	82	25	76	1397
04	44	54	50	47	106	35	100	3087
05	50	61	57	54.4	120	42	116	5030
06	56	70	64	61	144	51	132	7677
07	62	76	70	69	164	59	148	11085
08	66	79	73	72	170	62	156	15314
09	68	82	76	76.4	178	68	164	13523
10	72	85	80	80.2	184	70	172	18365

show that the formation energy of a strained QD can be decomposed in a contribution from the elastic relaxation that scales linearly with the QD volume V , as well as contributions due to the formation of surfaces and edges that scale with $V^{2/3}$ and $V^{1/3}$, respectively:

$$E_{\text{QD}} = E_{\text{el}}V + E_{\text{surf}}V^{2/3} + E_{\text{edges}}V^{1/3}. \quad (7.7)$$

To be more precise, we find that the volume dependence of the formation energies per atom (Eq. 7.2) of QDs with respect to a wetting layer of 1.75 ML InAs are well captured by

$$\frac{E_{\text{f}}(\text{QD})}{\Delta N_{\text{In}}} = E'_{\text{el}} + E'_{\text{surf}}(\Delta N_{\text{In}})^{-1/3} + E'_{\text{edges}}(\Delta N_{\text{In}})^{-2/3} \quad (7.8)$$

if we assign an elemental volume of $V_0 = a_0^3/8$ to each In atom. The coefficients that we obtained by fitting the formation energies as obtained from our calculations for the *hut*-shaped and *dome*-shaped QDs to the above expressions are summarized in Tab. 7.3 for different values of the chemical potential. This finding allows us to identify three different regimes of thermodynamic stability: For a deposition of less than approximately 1900 In atoms on an InAs wetting layer of 1.75 ML thickness, the formation of a homogeneous InAs film is energetically most favorable. Beyond this amount of In atoms, our results predicts the onset of the Stranski-Krastanov growth mode, i.e. the transition from a 2D film to 3D islands. The number of In atoms in our simulation cell at the transition point corresponds to a coverage of 1.9 ML. This is in line with typical values of 1.7-1.9 ML deduced in experimental works. Previous theoretical works employing a hybrid approach of continuum-elasticity theory and density-functional theory [34] found a transition coverage of 1.6-1.8 ML InAs for the lateral QD density that we used in our calculation. In extension to previous theoretical works and in

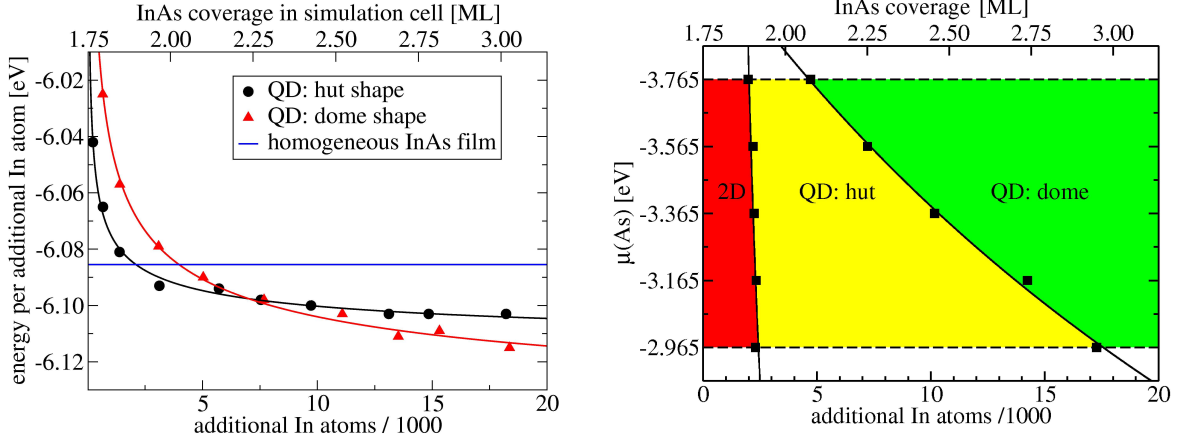


Abbildung 7.7: The formation energies (left) of *hut* (black) and *dome* (red) shaped QDs obtained with the many-body potential (points) are well described (lines) by previously suggested dependencies on the QD volume (Eq. 7.7). The three observed stability regimes depend additionally on the applied chemical potentials (left: $\mu_{\text{As}} - \mu_{\text{As}}^{\text{bulk}} = -0.6\text{eV}$), which is shown for the case of As in its allowed range (right).

agreement with experimental observations, we find two distinct regimes of QD-shape stability for coverages beyond the onset of the Stranski-Krastanov growth mode. In particular, the results in the left panel of Fig. 7.7 show that small QDs are energetically favorable in the *hut* shape, whereas larger ones are more stable in the *dome* shape.

An additional degree of freedom in this investigation is the stoichiometry of the different QDs: In the calculation of the formation energy (Eq. 7.2) we consider the In and Ga atoms to be in thermodynamic equilibrium with reservoirs of InAs and GaAs, respectively. The remaining excess or lack of As atoms instead leads to a dependence of the formation energy on the chemical potential of As, similar to the stoichiometry dependence of the surface free energies described in Sec. 3.2. The particular stoichiometry δN_{As} of a nanostructure with a QD of a certain size and shape is determined by the detailed atomic structure. It is naturally accessible in our approach by evaluating

$$\delta N_{\text{As}} = \Delta N_{\text{As}} - \Delta N_{\text{In}} - \Delta N_{\text{Ga}} \quad (7.9)$$

with the number of atoms per species in the QD nanostructure and the reference film (see Eq. 7.2 above). From this, we find that the dependence of the stoichiometry on the volume of the *hut*- and *dome*-shaped QDs (Tab. 7.1 and 7.2) is well described by contributions from the surface ($V^{2/3}$) and from edges ($V^{1/3}$), namely

$$\text{hut} : \delta N_{\text{As}}(\Delta N_{\text{In}}) = -0.111 \cdot (\Delta N_{\text{In}})^{2/3} + 0.820 \cdot (\Delta N_{\text{In}})^{1/3} \quad (7.10)$$

Tabelle 7.3: The formation energies of *hut*- and *dome*-shaped QDs in different sizes (Tab. 7.1 and 7.2) as obtained from relaxations with our many-body potential are well described by an earlier proposed dependence on volume, area, and kinks: E'_{el} , E'_{surf} , and E'_{edges} in Eq. 7.8 for different values of the chemical potential of As.

$\mu_{\text{As}} - \mu_{\text{As}}^{\text{bulk}}$	<i>hut</i>			<i>dome</i>		
	E'_{el}	E'_{surf}	E'_{edges}	E'_{el}	E'_{surf}	E'_{edges}
0.0	-6.107	0.03239	3.185	-6.152	1.319	0.4311
-0.2	-6.112	0.1868	2.124	-6.152	1.221	0.4987
-0.4	-6.115	0.2803	1.347	-6.154	1.154	0.3783
-0.6	-6.121	0.4232	0.3534	-6.154	1.051	0.5192
-0.8	-6.121	0.4367	0.0003241	-6.153	0.9468	0.5588

$$\text{dome} : \delta N_{\text{As}}(\Delta N_{\text{In}}) = -0.509 \cdot (\Delta N_{\text{In}})^{2/3} + 0.482 \cdot (\Delta N_{\text{In}})^{1/3}, \quad (7.11)$$

where the number of In atoms in the QD, ΔN_{In} , is proportional to its volume³. The resulting effect of the chemical potential on the formation energies is shown in the right panel of Fig. 7.7: The onset of the transition from 2D films to *hut*-shaped QD is only weakly affected by the value of μ_{As} . The transition from *hut*-shaped to *dome*-shaped QD instead changes significantly with the chemical potential of As. The upper and lower bound for μ_{As} are the cohesive energy of As (A7) bulk and its difference to the formation enthalpy of InAs zinc blende bulk. We found that the dependence of the transition coverages on the chemical potential are well described by a $1/N$ relation, which one would expect from solving Eq. 7.2 for $\mu(\text{As})$.

So far, we have discussed the transition from *hut*-shaped QD to *dome*-shaped QD only for a fixed lateral QD density of approximately $4 \cdot 10^{10} \text{ cm}^{-2}$. The quantitative results of the lateral elastic QD-QD interaction obtained in the previous section (see Fig. 7.5), however, allow us to present a complete picture of the shape transition as a function of both, the chemical potential of As, and the lateral QD density. To this end we employ the finding that the elastic interaction energy per atom (Eq. 7.6) at constant lateral QD density grows linearly with the QD volume (inset in left panel of Fig. 7.5). This allows us to isolate the lateral interaction-energy $E_{\text{elastic}}(R_1)$ for the QDs with fixed distance R_1 that were investigated above (Tab. 7.1, 7.2, and Fig. 7.7) by evaluating

$$E_{\text{QD}}(\infty) = E_{\text{QD}}(R_1) - E_{\text{elastic}}(R_1), \quad (7.12)$$

and to determine the formation energy of QDs at infinite distances $R = \infty$. In this way,

³Note, that these results from counting the atoms in the simulation cell differ from what one would expect by adding up the stoichiometries of the involved surfaces. The latter would lead to a nearly stoichiometric system for the case of the *dome* shape and an As excess for the *hut* shape that increases with ΔN_{In} , in contrast to our results.

we can also obtain these formation energies of non-interacting QDs for different chemical potentials of Arsenic, $E_{\text{QD}}(\infty, \mu(\text{As}))$. This yields directly (Eq. 7.12) the formation energies of the investigated *hut*- and *dome*-shaped QDs, $E_{\text{QD}}(R, \mu(\text{As}))$, in dependence of both, the QD-QD distances R and the value of the chemical potential $\mu(\text{As})$. We determined

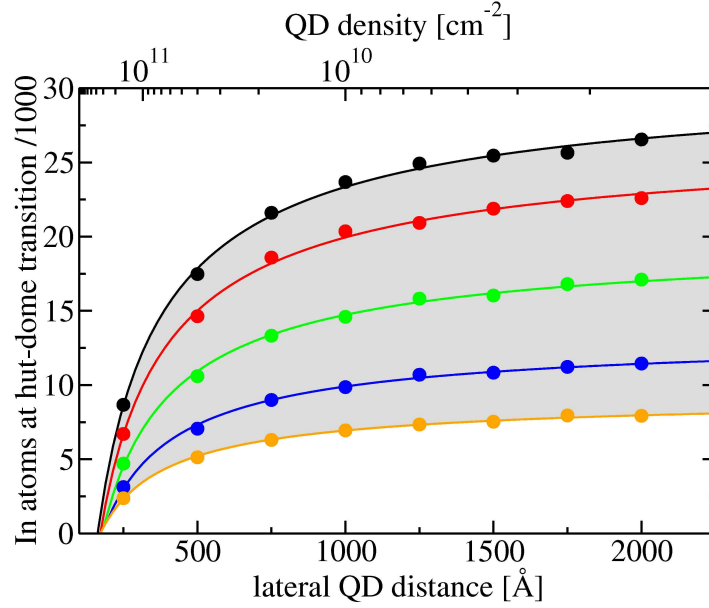


Abbildung 7.8: Number of In atoms in a QD on a wetting layer of 1.75 ML InAs at the transition from the *hut* shape to the *dome* shape as a function of the lateral QD density (or QD distance) and the chemical potential of As (colors). The allowed range of μ_{As} is indicated gray and ranges from $\mu_{\text{As}}^{\text{bulk}}$ (black line) to $\mu_{\text{As}}^{\text{bulk}} - \Delta H_f^{\text{InAs}}$ (orange line).

$E_{\text{QD}}(R, \mu(\text{As}))$ numerically for a number of tuples $(R, \mu(\text{As}))$ where $250 \text{ \AA} < R < 2000 \text{ \AA}$ and $\mu_{\text{As}}^{\text{bulk}} - \Delta H_f^{\text{InAs}} < \mu(\text{As}) < \mu_{\text{As}}^{\text{bulk}}$. (Note, that the left panel of Fig. 7.7 corresponds to one of these tuples.) For each tuple, we repeated the procedure of calculating the regimes of stability, i.e. we fitted the according formation energies of *hut*- and *dome*-shaped QDs to Eq. 7.7 and determined the number of In atoms in the QD at the intersection of the stability lines of these two shapes. This yields the transition point for the shape transition as a function of lateral QD density and chemical potential μ_{As} as shown in Fig. 7.8. The dependency of the calculated transition points on the QD distance for a given chemical potential is well described by

$$N(R)|_{\mu(\text{As})} = a(\mu(\text{As})) - b(\mu(\text{As})) \cdot R^{-3/4}. \quad (7.13)$$

In interpretation of Fig. 7.8 we find that As-poor conditions and high QD densities shift the transition from *hut*-shaped QD to *dome*-shaped QD to smaller QD volumes. The prior

dependence is a result of the different stoichiometries, the latter is due to the difference in elastic interactions. Note, that neglecting the elastic interaction and system stoichiometries that were determined from the facet stoichiometries only may cause large deviations from the experimentally observed transition points [193, 207].

7.7 Critical Nucleus

With the formation energies calculated above, we can now tie up to the previous work of Moll [198], and determine the critical nucleus for the formation of a QD on a wetting layer. In Sec. 3.4 we showed that the formation of a liquid droplet from a vapor phase is accompanied by a change in the thermodynamic potential ΔG with respect to the radius of the droplet. The two different phases in the case of QD growth are a homogenous film and a QD on a wetting layer, with the number of additional In atoms as variable. Therefore, we compare the formation energies γ_f of homogenous InAs films of increasing thickness with QDs of increasing volume on a wetting layer of constant thickness

$$\gamma_f(\mathcal{S}) = \cdot \left[\Delta E_{\text{tot}}^c - \Delta N_{\text{Ga}} H_{\text{GaAs}}^f - \Delta N_{\text{In}} H_{\text{InAs}}^f - (\Delta N_{\text{As}} - \Delta N_{\text{In}} - \Delta N_{\text{Ga}}) \mu_{\text{As}} \right] \quad (7.14)$$

where $\Delta X = X(\mathcal{S}) - X(\mathcal{I})$ is given in analogy to Eq. 7.2. Based on our results and those of previous experimental and theoretical works, we assume that the initial structure \mathcal{I} for QD formation is an InAs wetting layer of 1.75 ML thickness. The formation energies of the homogenous film and the QD structures refer to an identical area A given by the size of our super cells. The size-dependent formation energies of the QDs, $\gamma_f(\text{QD}, N)$, are fitted to Eq. 7.7. The obtained $\gamma_f(\text{QD}, N)$ is then subtracted from the formation energy of a homogenous film, $\gamma_f(\text{film}, N)$ as determined in Sec. 7.3⁴. This difference of the formation energy of a homogenous film and a *hut*-shaped QD with increasing amount of In atoms allows us to determine the size of the critical nucleus (Fig. 7.9: line in left panel). The critical nucleus is given by the number of additional In atoms at the maximum difference in formation energies. For values larger (lower) than zero, the film (QD) is energetically favored. Below the critical size of approximately 70 In atoms, the (unstable) QD can gain energy by dissolving without a barrier, but needs to overcome a barrier to gain energy by continued growth. If the QD is larger than the critical size but possibly still unstable, it can gain energy by further growth. The critical nucleus is the transition between these two regimes: There the QD can gain energy by either (barrier-less) dissolution or (barrier-less) growth. From our calculations we find that the energy barrier for forming the critical nucleus of a *hut*-shaped QD is 5.3 eV. Note that this result applies for growth conditions close to the thermodynamic equilibrium, e.g. high adatom mobility and low deposition rate.

⁴The formation energy of an extended wetting layer is the sum of formation energies of the involved surface unit-cells, and therefore a sequence of piecewise defined, linearly varying functions as shown in Fig. 7.2.

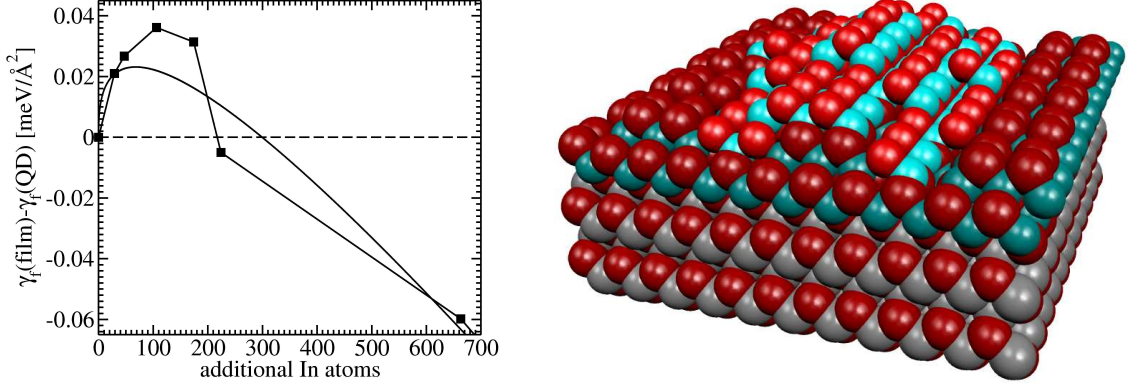


Abbildung 7.9: The difference between the formation energy of a homogenous InAs film and a *hut*-shaped QD on InAs wetting layer allows us to determine the size of the critical nucleus to be of approximately 70 In atoms (left) and the energy barrier of formation to be of 5.3 eV in our simulation cell with an area of $A = 2.3 \cdot 10^5 \text{\AA}^2$. Such a critical *hut*-shaped QD (right: size B in Tab. 7.4) is only a few monolayers high. (The atoms of the initial system are shown darker to guide the eye.)

So far, we implicitly assumed that the decomposition of formation energies given in Eq. 7.2 is valid in the regime of very small QDs. Our atomistic approach allows us to verify this presumption by extending our study to small, unstable *hut*-shaped QDs (Tab. 7.4). These structures were obtained by successively removing complete layers of the individual $\{137\}$ and the $\{111\}$ facets. Therefore, they do not follow the isomorphic scaling that we approximately achieved for the larger *hut*-shaped QDs (Tab. 7.1). The difference between the calculated

Tabelle 7.4: Unstable *hut*-shaped QDs: Miller indices of the side facets and distances from origin of the coordinate system, as well as the resulting characteristic lengths and the number of atoms.

#	$\ \mathbf{n}_{(1\bar{1}1)}\ $	$\ \mathbf{n}_{(317)}\ $	$L_{[110]}$ [Å]	$L_{[\bar{1}10]}$ [Å]	ΔN_{In}
A	19	19	16	19	29
B	19	20.5	24	20	47
C	22	26	38	35	106
D	23.5	28	48	44	174

formation energies of the small, unstable QDs and a wetting layer of according thickness (Fig. 7.9: symbols in left panel) allows us to determine the critical nucleus in an atomistic way. A comparison with the results that were obtained from the formation energies of larger

QDs (Fig. 7.9: line in left panel) shows good agreement for the size of the critical nucleus and reasonable agreement for the nucleation barrier. We conclude that the decomposition of the formation energy given in Eq. 7.2 is a good approximation even in the regime of very small QDs. Our results show that a many-body potential is able to resolve the energy differences that stem from the absence of an isomorphic scaling for very small atomistic structures.

An interesting aspect of our results is that a *hut*-shaped QD of about the critical size has a height of 2-3 atomic layers and therefore resembles a transition from a 2D to 3D island (right panel in Fig. 7.9). This explains the impression of a 'spontaneous' formation of QDs that was deduced from RHEED experiments: Growth interruptions just after the onset of the 2D-3D transition that can be observed as RHEED chevrons (see e.g. Ref. [208]) already yield samples with QDs of several nm base-length [18]. The possible uncertainties of the experiments (e.g. RHEED sensitivity) and of our approach do not allow a precise statement, if the island at the experimentally observed 2D-3D transition is *subcritical* or *supercritical*. However, our results suggest that the size of the islands at the 2D-3D transition observed in RHEED experiments is very close to the size of the critical nucleus. Islands of this size are still unstable, but the remaining barrier for a growth continuation is small, such that growth to eventually stable QDs can set in without significant time delay once the 2D-3D transition has occurred. If, on the contrary, the critical nucleus would have been much larger, then a growth interruption just after the onset of the 2D-3D transition would leave unstable islands behind that face a larger barrier for continuing 3D growth. They should therefore preferentially dissolve, in contrast to experimental findings (e.g. Ref.[18]). Note, that this is the first investigation of this kind that allows such quantitative explanations of the initial growth stage of InAs QDs on GaAs(001) without further assumptions.

Kapitel 8

QD Superlattices

In the previous chapter we found that many features of the self-assembled formation of InAs/GaAs QDs in the Stranski-Krastanov growth mode are well reproduced by the newly developed many-body potential. In this chapter we extend the application of the potential to an investigation the experimental finding of growth correlations in stacked layers of InAs QDs on a GaAs(001) substrate. We show that the dependence of the formation energy of an overgrown QD on its length and height favors a rather flat QD shape. Most importantly, we give the first quantitative investigation of the driving force of growth correlations in QD stacks, based on the size of the critical nucleus in different lateral positions relative to the overgrown QDs.

8.1 Experimental Findings

One of the prerequisites for utilizing QDs in future devices is a narrow distribution of the electronic spectra of the involved QDs. This can result directly from homogeneous sizes, shapes, and chemical compositions, but one might also think of combinations of different sizes, shapes, and compositions that exhibit similarities of the electronic properties of interest. Many experiments could demonstrate that the size distribution is narrow enough for realizing lasers with small frequency bandwidth and high intensity. One of the most interesting future applications, quantum computing, additionally requires a quantum-mechanical coupling (*entanglement*) of the electronic states of neighboring QDs [209]. The smallest formation unit of a quantum computer that is needed for procession of a logical *qubit* can be realized with two coupled QDs. The occurrence of this effect is connected with a sufficiently small spatial distance between the QDs, in practice either laterally or vertically. It was already demonstrated experimentally that the quantum states of a vertical arrangement of two QDs can couple with each other, and act as optically driven solid-state quantum gate [210]. Very recent investigations showed that the degree of coupling can be controlled experimentally and

is consistent with a theoretical description [211].

A possible route to devices with high densities of homogeneous QDs is the successive growth of stacked layers of spatially correlated QDs. Such growth correlations were revealed [2] already in the infancy of QD studies, and are still investigated as a possible route to the creation of ordered 3D arrays of QDs with a narrow size distribution. They are fabricated experimentally by successive growth steps: At first, a layer of self-assembled QDs is grown on a substrate by depositing e.g. InAs on GaAs(001). This layer of QDs is overgrown by a spacer layer of e.g. GaAs, which serves then as a substrate in another cycle of growing self-assembled QDs by depositing e.g. InAs. Under appropriate growth conditions, this procedure results in a crystalline, dislocation-free structure with QD layers stacked along the growth direction and separated by the material of the spacer layer. The above mentioned growth correlations are typically investigated by cross-sectional STM experiments (see e.g. Ref. [212] for a recent review): For this purpose, the sample is cleaved in e.g. the (110) or $(\bar{1}\bar{1}0)$ plane, and the exposed face is then investigated in a STM experiment. An exemplary result of stacked layers with vertically aligned QDs is shown in the left panel of Fig. 8.1.

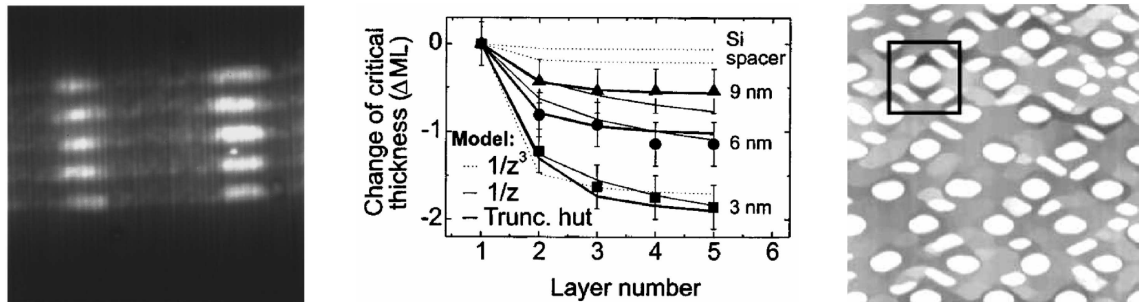


Abbildung 8.1: Cross-sectional STM experiments (e.g. Ref. [213]) revealed growth correlations in stacked QD layers (left). Systematic investigations showed that the critical thickness decreases with spacer thickness (middle, [214]), and that interstitial QDs possibly form between nearest neighbors (right, [215]).

Systematic experimental and theoretical investigations revealed a deeper insight in the nature of growth correlations in stacked QD layers: The elastic interactions between QDs of different layers depends on the elastic anisotropy of the materials and differs qualitatively for different crystal structures and substrate orientations (see e.g. Ref. [122]), whereas for InAs/GaAs(001) it results in a vertical alignment of QDs in subsequent layers (see e.g. Ref. [213]). The growth correlations manifest also in a decrease of the critical thickness with decreasing spacer thickness (middle panel of Fig. 8.1, observed for both, Ge/Si(001) [214] and InAs/GaAs(001) [216]). The lateral ordering of the QDs in the first layer can furthermore be controlled by patterning the GaAs substrate (e.g. with holes) that serve as preferential

nucleation sites. How many of the preferred sites given by the pattern are actually occupied by QDs depends on the relation between the QD density that would correspond to the particular growth conditions and the density of preferred sites offered by the substrate pattern. In particular, for too small pattern densities one observes QD growth in interstitial positions [215] as shown in the right panel of Fig. 8.1. Continuum-elasticity theory calculations suggested that the experimentally observed interstitial positions between nearest neighbors (instead of e.g. next-nearest neighbors) is due to the elastic anisotropy of the crystal lattice [215].

The theoretical interpretations of growth correlations in stacked QD layers are based on either kinetic or thermodynamic arguments. The prior apply to growth conditions that do not allow the system to reach an equilibrium state, but rather lead to a strong influence of the individual diffusion events [217, 218]. The activation barriers for the latter can be strongly influenced by the strain tensor that the overgrown QD causes at the substrate surface [109]. From a thermodynamic point of view, the preferred relative arrangement of QDs in subsequent layers is caused by an energy difference that alters the QD formation energy dependent on its position. The first suggestion of this relation [219] and later works are based on the qualitative assumption that nucleation is favorable in regions of tensile strain at the surface. The focus was consequently on the calculation of the surface strain-tensor above overgrown QDs with either continuum (e.g. Refs. [121, 122]) or atomistic approaches (e.g. Ref. [220]). Although these previous works provided a lot of insight already, they did not quantify the energetic gain for nucleation in a minimum of the surface strain tensor as compared to other non-preferred sites. This absence made it hard to judge the impact of the surface strain tensor arising from the overgrown QD as compared to possible kinetic effects. Our approach, however, enables us to settle this issue through a quantitative calculation of the size reduction of the critical nucleus in the preferred nucleation sites.

8.2 Truncated Pyramids in a QD Superlattice

The overgrowth of QDs with substrate material is not yet fully understood, but seems to be governed by an interplay of different processes that depends sensitively on the experimental growth conditions: After very fast (1-2 ML/s) InAs QD growth and GaAs overgrowth at moderate temperatures by MOCVD [221], the QDs exhibit a truncated-pyramid like shape [222], and consist of nearly pure InAs [20], indicating that In-Ga interdiffusion is negligible. Elevating the overgrowth temperature by about 100° already results in a significantly altered stoichiometry of the QDs that resembles an inverted cone profile [223] with a maximum In concentration of about 60% [224]. The intermixing of Ga and In is usually more apparent in MBE growth that takes place at much lower growth rates and results in e.g. a similarly reduced amount of In in the QDs [225] and the dissolution of the wetting layers [213]. Another source of substantial material redistribution is incomplete or interrupted overgrowth [226], which can lead to the formation of quantum rings or nanovoids (see e.g. Ref. [224] for a recent

study).

In this study we focus on the nature of QD overgrowth at comparably large deposition rates during growth and overgrowth. Consequently, we assume an atomically sharp interface between the GaAs(001) substrate and the InAs wetting layer, as well as negligible segregation of single In atoms to the GaAs environment. We mimic the formation of a truncated pyramid during overgrowth by investigating pyramids with $\{101\}$ facets of different base length that are truncated in different heights. They are located on 2 ML InAs wetting layer and embedded in a GaAs matrix, as sketched in the left panel of Fig. 8.2. In the relaxation with our many-body potential we do not relax the coordinates of the atoms in the two topmost layers individually, but rather fix the x and y coordinates of each atom, and relax these atoms under the constraint of a common z coordinate to mimic a sufficiently large capping layer. We then calculate the cohesive energy of each structure according to Eq. 7.2 and compare them at constant volume of the QD, as shown in the right panel of Fig. 8.2. The cohesive energies

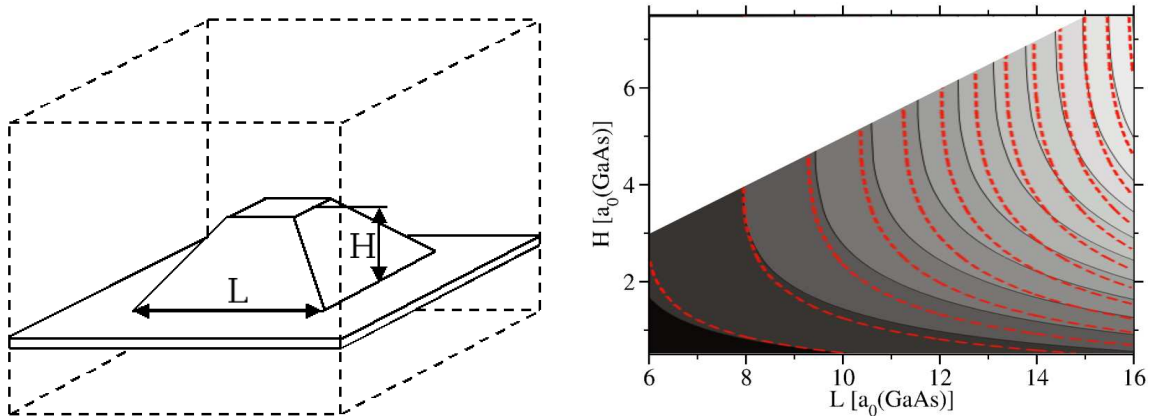


Abbildung 8.2: For a sequence of InAs $\{101\}$ pyramids with different base lengths and truncation-heights embedded in GaAs (left), we calculated the cohesive energies (right, gray scale: 0.1 eV spacing). For a given amount of InAs (right, red lines), the formation energy of the pyramids decreases (from light gray to black) with increasing base length and decreasing height, in line with the experimentally observed truncated pyramids.

of pyramids with base lengths $L/a_0(\text{GaAs}) \in [6, 16]$ and truncation heights $H/a_0(\text{GaAs}) \in [0.5, 7.5]$ are shown in gray scale in Fig. 8.2, together with the iso-volume lines in red. (The white region is due to the fact that for small base-lengths the maximum height is lower than the range of plotted heights.) From the comparison of cohesive energies at a constant pyramid volume, we can conclude that the shape of an InAs QD on a (001) wetting layer embedded in GaAs is energetically more favorable at large base length and small height. This result explains partially the driving force for the experimentally observed QD shapes that resemble

truncated pyramids. It depends strongly, however, on the detailed growth conditions, to which extent it effectively contributes or is ruled out by growth kinetics.

8.3 Growth Correlations in Stacked QD Layers

8.3.1 Initialization

In the following discussion, we address the experimental observation of growth correlations between QDs in stacked layers within a stationary approach using our newly developed many-body potential. In particular, we calculate the cohesive energy of a free-standing QD in different lateral positions above an overgrown QD, and thus determine the effective potential-energy surface for QD stacking. Note that this new kind of ansatz enables us to quantify the effect of elastic interaction among stacked layers of QDs. A sketch of the investigated systems in Fig.8.3 shows a side view of the two stacked QDs, together with a top view of the different lateral positions of the upper QD. The x and y axes of the shown structures correspond the crystallographic directions $[110]$ and $[\bar{1}10]$, respectively. In the case shown here we used a

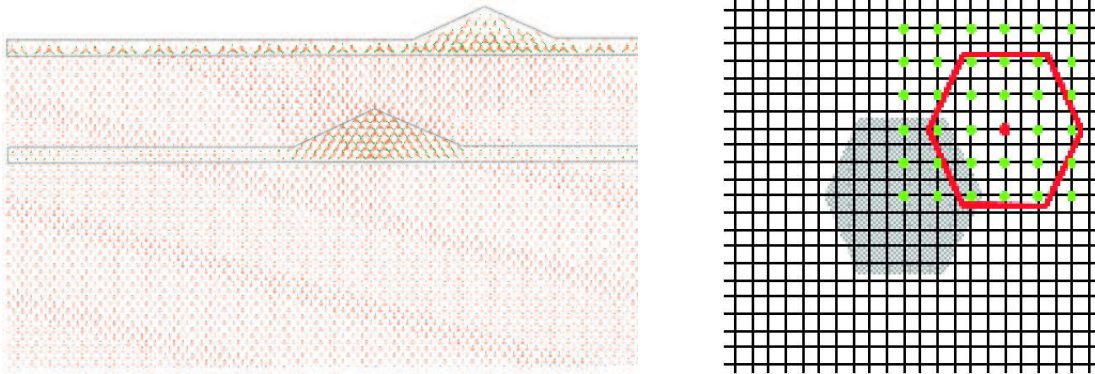


Abbildung 8.3: Setup of QD stack calculations: (a) A side view along $[\bar{1}10]$ shows the stacked QD layers and (b) a schematic top view indicates the different lateral positions (green points) of the upper QD. To guide the eye we plotted the lower capped QD as gray area and the upper free-standing QD as red frame.

spacer thickness of 4.6 nm GaAs between the two InAs layers, and assumed both QDs as *hut*-shaped with $\{317\}$ facets. In the results below, we will further investigate the role of spacer thicknesses, lateral QD density, and QD shapes. We have chosen the smallest *hut*- and *dome*-shaped QD investigated so far (*hut* #1 in Tab. 7.1 and *dome* #1 in Tab. 7.2) to keep the number of atoms in the investigated QD stacks below 1.5 million atoms. Throughout the following discussion, we use QDs formed by pure InAs and embedding material of pure

GaAs, in contrast to most experimentally observed stoichiometries. Our results can thus be understood as an upper bound for the elastic effects that are possibly weakened by intermixing of In and Ga.

For computational efficiency, we divide the QD stack in an upper part with the free-standing QD, the WL and a few substrate layers, and a lower part with the overgrown QD and the substrate below. Firstly, these two parts were pre-relaxed individually until the maximum force $|\mathbf{F}_{\max}|$ acting on an atom in the system was smaller than $0.1 \text{ eV}/\text{\AA}$. To preserve a planar interface between the two parts, we relaxed the lower part applying the constraint that the atoms in the upper layers (of the lower part) have a common height. In the relaxation of the upper part, the atoms in the lower layers were kept fixed. In the second step, we initialized the upper QD in different lateral positions by shifting all atoms relative to the upper super cell and applying periodic boundary-conditions. The increments of the lateral positions corresponded to four surface unit-cells to be in accordance with the periodicity of the assumed (2x4) reconstruction of the wetting layer. In the third step, the individual upper parts were joined again with the lower part, and the complete system was relaxed until $|\mathbf{F}_{\max}| < 0.001 \text{ eV}/\text{\AA}$ with keeping only the lowest layers of the system fixed. Finally, we calculated the formation energy of each structure according to Eq. 7.2 with the overgrown QD beneath a wetting layer of 1.75 ML InAs as initial structure, i.e. ΔN_{In} is the number of In atoms in the upper QD.

8.3.2 Potential-Energy Surface of Stacked QD Layers

The technical advantage of investigating QD growth correlations by a potential-energy surface is that not only the numbers of atoms of the different species, but also the area of all involved surfaces, is constant. Thus, in a comparison of total energies of different lateral positions of the upper QD, the errors of the surface energies as obtained from the many-body potential with respect to those obtained by DFT calculations cancel out exactly (Sec. 6.3). The remaining leading contributions are the elastic energy in the GaAs substrate and capping regions, in the InAs QDs, and in the two InAs wetting layers. These are well reproduced with the many-body potential as already shown in Sec. 6.2 and 6.4. To limit the computational effort¹, we performed this study in several steps.

Symmetry of PES

At first, we investigated the overall shape of the PES to identify possible symmetries that determine the irreducible scanning area by performing line scans in all quadrants, one of them indicated in the right panel of Fig. 8.3. To be more precise, we calculated the formation energies of the upper QD in different radial positions along the [100], [110], [010], [$\bar{1}10$]

¹Each calculated point of the investigated PES requires to relax up to 1.4 million atoms, dependent on lateral QD density and spacer thickness.

crystallographic directions with respect to the lower QD. To investigate the largest possible impact of the shape combinations on the overall structure of the PES, we have chosen the *hut* shape (that has less symmetry than the *dome* shape) for both QDs. The line scans in Fig. 8.4 show the energy gain δE per In atom of the upper QD in dependence of the lateral distance between the centers of upper and lower QD with respect to the smallest observed value of δE . The dominating feature of all line scans is the minimum that corresponds to the arrangement

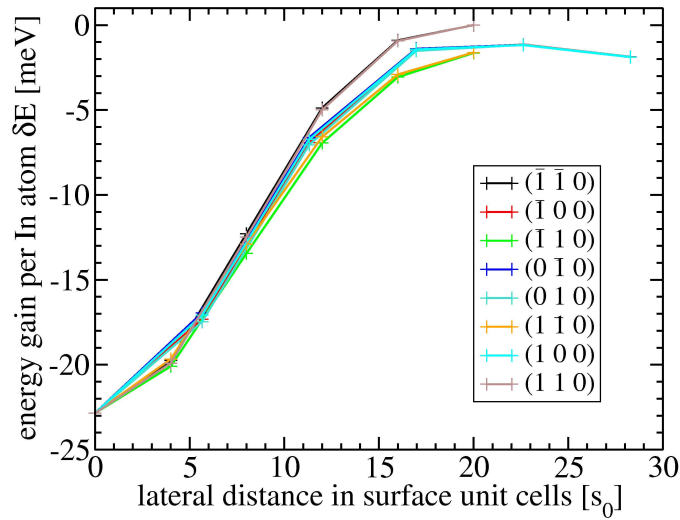


Abbildung 8.4: Line scans of the PES along the $\{100\}$, and $\{110\}$ directions in all quadrants of the PES of a freestanding *hut* QD above an overgrown QD *hut* show an energetic minimum for vertical stacking with high symmetry.

with the center of the upper (freestanding) QD above the apex of the lower (overgrown) QD. For several groups of line scans the formation energies are practically identical; these form the equivalent crystallographic directions of the PES calculation: $[110]=[\bar{1}\bar{1}0]$, $[\bar{1}10]=[1\bar{1}0]$, and $[100]=[010]=[\bar{1}00]=[\bar{1}\bar{1}0]$. From the difference between the first two groups we can conclude that the two possible interstitial sites between nearest-neighbor QDs are similar but not equivalent. There is however only one possible interstitial site between next-nearest neighbor QDs, which is reflected in the full equivalency of the directions in the last group. The smallest irreducible part of the PES is hence a quadrant that includes the two inequivalent nearest-neighbor interstitial sites. From the following calculations for this quadrant only, the full PES can be constructed by subsequent mirroring at the $[110]$ and $[\bar{1}\bar{1}0]$ axes.

Effect of QD Shapes

As a second issue, we investigated the effect of different shapes of the upper (free-standing) and the lower (overgrown) QD. To this end, we calculated the formation energies of the upper QD on top of the spacer layer above the lower QD for the four different combinations of *hut*-shape and *dome*-shape for the free-standing or overgrown QD. The QDs in either shapes were placed in different lateral positions in an area of 20×20 surface lattice constants $s_0 = a_0/\sqrt{2}$ in the quadrant of 40×40 s_0 as indicated in the right panel of Fig. 8.3. For one of the shape combinations (both QDs are *hut*-shaped), we calculated the PES for the full quadrant of 40×40 s_0 . The resulting PES for all combinations of shapes are compiled in Fig. 8.5. In

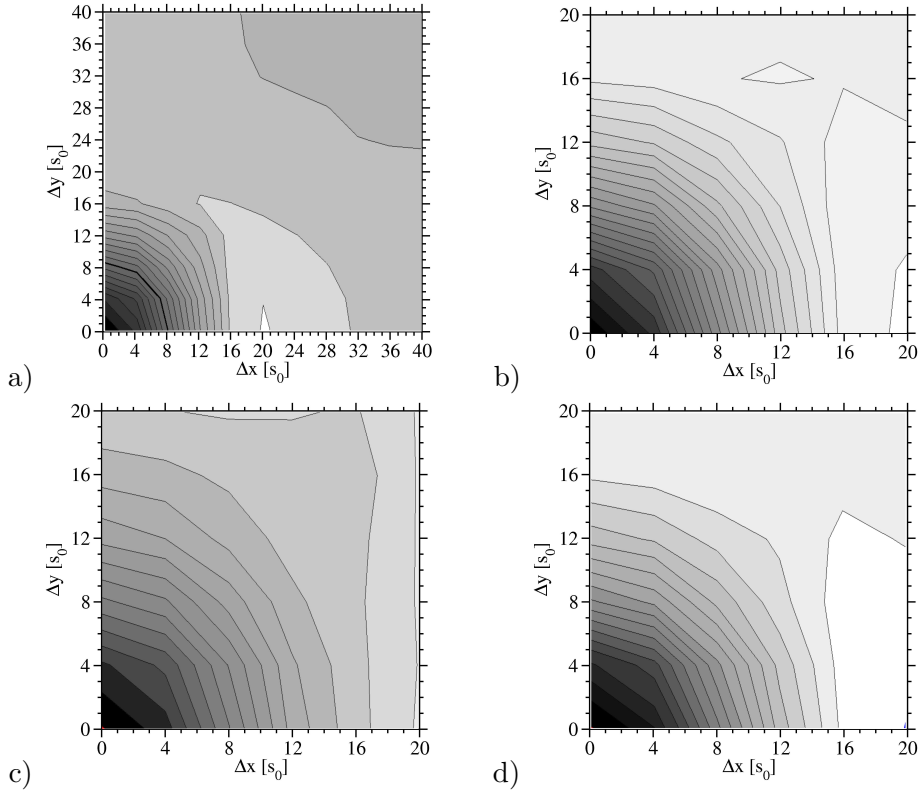


Abbildung 8.5: Potential-energy surface of total energies of free-standing QD in different lateral positions above overgrown QD (contour line spacing: 1 meV): *hut*-shaped QD above (a) *hut*-shaped of (b) *dome*-shaped QD, as well as *dome*-shaped QD above (c) *hut*-shaped of (d) *dome*-shaped QD. The x and y axes correspond to the crystallographic directions (110) and $(\bar{1}10)$, respectively.

all investigated combinations of QD shapes, the arrangement with vertically aligned QDs is

energetically most favorable, qualitatively in line with the experimentally observed vertical growth correlations in QD stacks. A comparison for Fig. 8.5 (a)-(d) shows clearly that the shape of the two QDs has practically no influence on the qualitative shape of the PES of the upper QD. An approximation by an array of interacting point sources of strain would thus be well justified. Due to negligible influence of the QD shapes, we can also limit the investigation of the full quadrant of $40 \times 40 s_0$ to one combination of shapes only, e.g. the case of two *hut*-shaped QDs shown in Fig. 8.5 (a): We find no further characteristic feature of the PES that is of comparable importance to the minimum for vertically aligned QDs. The additional minimum in the upper right edge corresponds to a weak preference for the interstitial sites between *next-nearest* neighbor QDs. For an understanding of the experimentally observed additional nucleation at interstitial sites between *nearest* neighbor QDs, one would need to extend this study to higher QD densities in the top layer.

For a more detailed study of the energy gain for vertical stacking of QDs of different shapes, we compare the line scans of the above PES along the crystallographic directions $[110]$, $[010]$, and $[\bar{1}10]$ shown in Fig. 8.6. These line scans reveal some interesting aspects of

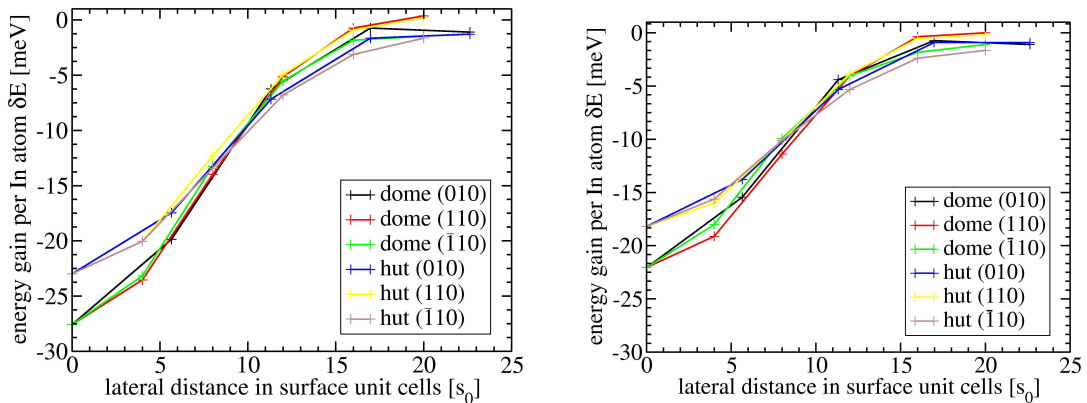


Abbildung 8.6: The line scans of PES of *hut*- and *dome*-shaped QD above overgrown *hut*-shaped (left) or *dome*-shaped QD (right) show an energy gain for vertical stacking of approximately 20-25 meV per In atom.

QD stacking: Firstly, by comparing the energy ranges of the two panels in Fig. 8.6, we find that the *hut*-shape is energetically more favorable by approximately 100 meV for the lower QD than the *dome*-shape, regardless of the shape of the upper QD. This is in accordance with the result of the previous section, that the formation energy of an embedded QD of given volume is smaller for rather flat shapes. Secondly, the vertically aligned arrangements with a *dome*-shaped QD on top are energetically favorable by nearly 5 meV as compared to those with a *hut*-shaped QD on top, independent from the shape of the overgrown QD. We find

thus no ‘shape inheritance’ from the overgrown QD to the free-standing QD. A further study of the relative shape stability of the upper QD in its lateral position might be accomplished in the way pointed out in Sec. 7.6. In this work though, we focus on the major effect due to vertical stacking that is of highest relevance for understanding experimental works.

8.3.3 Effect of Lateral QD-QD Spacing and Spacer Thickness

The calculations outlined above were repeated for the case of two *hut*-shaped QDs with different spacer thickness H and different lateral QD distance R . As a measure of the energy gain for vertical alignment in the different cases we compare the difference per atom δE between the formation energy at vertical alignment and at the energetically most favorable interstitial site in Fig. 8.7. The lateral QD distance obviously plays a role only at very small

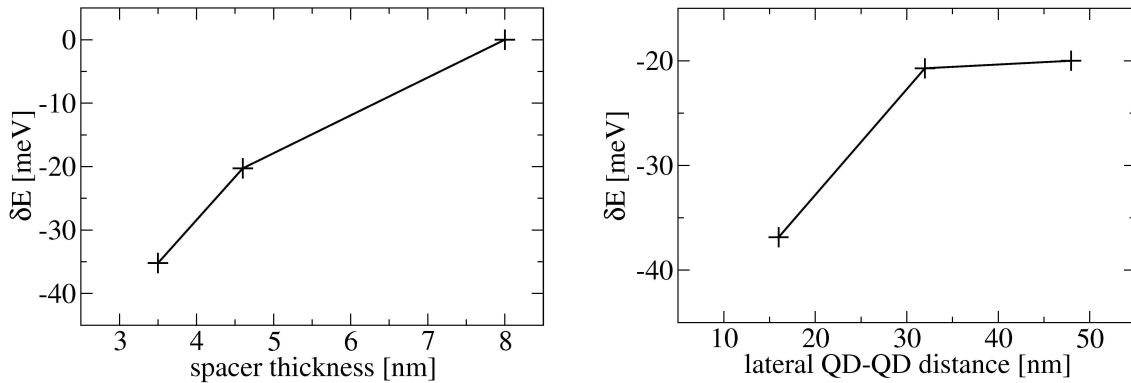


Abbildung 8.7: The energy gain δE for vertical alignment of two *hut*-shaped QDs with respect to the most favorable interstitial site is decreasing with increasing spacer thickness (left, $R=32$ nm) and vanishes at approximately 10 nm. The lateral QD distance at fixed spacer thickness (right, $H=4.6$ nm) plays only a role at values that are close to that of the QD base length.

values. Note that the maximum energy gain for vertical QD alignment of $\delta E \approx 35$ meV per atom obtained from our calculations is significantly larger than the previously reported value of 1 meV for PbSe/Pb_{1-x}Eu_xTe QD superlattices determined by a phenomenological argument [227]. This maximum energy gain for vertical alignment of the stacked QDs is decreasing with increasing spacer thickness and reaches a negligible value at a spacer thickness of $D_0 \approx 8$ nm, i.e. about 28 ML GaAs. A dependence of growth correlations on the spacer thickness was observed earlier in both, experimental (e.g. Refs. [214, 221, 228, 227]) and theoretical studies (e.g. Refs. [121, 123]). But a quantitative comparison of our results with experimental observations is hampered by the dependencies on growth conditions, and the different sizes and stoichiometries of the QDs. The most direct comparison is probably with

nearly pure [20] InAs QDs grown by MOCVD on GaAs(001) [221]: For these QDs of about twice the size of those studied in this work, the preference for vertical alignment vanishes at a spacer thickness of $D_0 \approx 9\text{-}12$ nm. We can compare this value to our results with QDs of a smaller base length L by noting that an increase of the characteristic system length would increase both the QD volume and D_0 . Therefore, the value of the spacer thickness with vanishing vertical alignment $D_0 \approx 8$ nm as calculated in this work can be considered as lower bound for stacked layers of QDs with a base length of $L > 5$ nm.

Together with the preference of vertical alignment, we conclude that QD stacks relieve elastic energy by a vertical overlap of the strain tensors of the upper and the lower QD. The difference between this *attractive* vertical interaction and the *repulsive* lateral interaction that we observed in Sec. 7.5 is an interesting effect that we can clarify by comparing the trace of the strain tensors in the investigated QD stack at different spacer thicknesses as shown in Fig. 8.8. The two QDs and their surroundings exhibit a qualitatively different strain

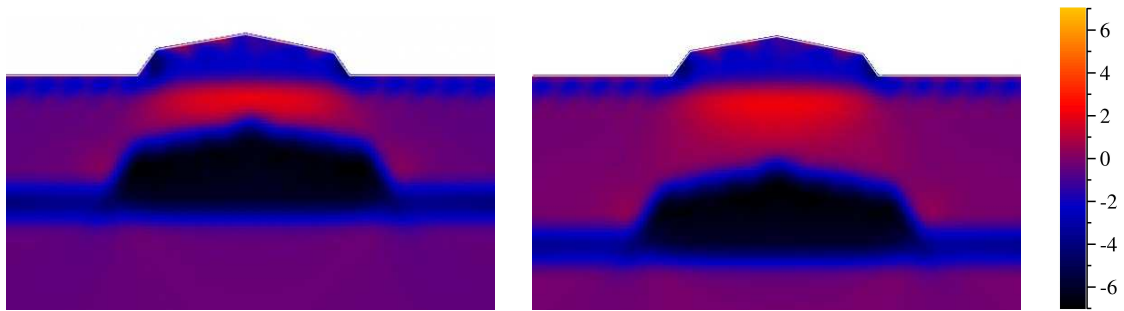


Abbildung 8.8: The trace of the strain tensor of vertically stacked QD with different spacer thickness of 3.5 nm (left) and 4.6 nm (right) shows the different overlap between the monopole-like lower QD and the dipole-like upper QD.

tensor, particularly at larger spacer thickness (right panel): The presence of the lower, highly compressed QD shows little effect on the embedding GaAs in its vicinity. The substrate below the upper, less compressed QD, however, is expanded, even for distances of about the size of the upper QD. This observation enables us to explain the origin of the lateral repulsive and the vertical attractive interaction within a simplified picture: The entity of compressed QD material and expanded substrate material below the free-standing QD can be regarded as a *elastic dipole*. The compressed material of the embedded QD on the other hand, is surrounded by only weakly expanded substrate material and therefore resembles more a *elastic monopole*. The lateral repulsive interaction is then due to the two surface dipoles of equal orientation. The vertical attractive interaction instead resembles more a dipole-monopole interaction with the ‘positive’ end of the dipole pointing towards the ‘negative’ monopole.

The few reports on experimentally observed anti-correlations (e.g Ref. [229]) were attribu-

ted to a transition from correlation to anti-correlation with increasing spacer thickness that was predicted qualitatively with both thermodynamic [121] and kinetic considerations [123]. In all cases of different spacer thickness, QD shapes and lateral QD distances studied in this work, however, we find a strong preference for vertical stacking, and no indication of an anti-correlation whatsoever. A thorough comparison to the previously mentioned theoretical works would require further calculations to systematically determine the energy gain of vertical or oblique arrangement for different QD sizes, shapes, and spacer thicknesses. In this study, however, we are interested in a quantitative understanding of the effect of QD stacking on the nucleation process itself.

8.3.4 Spatially Resolved Critical Nucleus

Furthermore, the results for the energy gain in different arrangements of stacked QDs presented above allow us to quantify the effect on the size of the critical nucleus. We will follow the procedure outlined in Sec. 7.7, but additionally consider the energy contribution from QD stacking. In the limit of vanishing elastic interaction ($\delta E = 0$), the formation energy of the upper QD, $\gamma_f^{(0)}(\text{QD})$, is equal to that of the freestanding QD (with no overgrown QD beneath) given by Eq. 7.14. Our results of the previous sections show that the average energy gain per atom δE due to stacking is well approximated by an isotropic function that depends on the lateral distance R between the centers of the upper and the lower QD in the stack. For the following study of the size of the critical nucleus at different R , we need to additionally consider that the energy gain depends on the volume V of the upper QD:

$$\gamma_f(\text{QD}, V, x, y) \approx \gamma_f^{(0)}(\text{QD}, V) + \delta E(V, R) \cdot \frac{\Delta N_{\text{In}}}{A} \quad (8.1)$$

where A is the area of the referred simulation cell. We performed additional calculations with smaller sizes of the upper QD (Tab. 7.4) to reveal the volume dependence of δE . It is reasonably well described by a proportionality to the base area of the upper QD (inset in left panel of Fig. 8.9) that senses the strain due to the overgrown QD beneath. With this result, we calculated the formation energies of *hut*-shaped QDs for different energy gains due to the stacking arrangement. The latter is comprised as an additional contribution to E_{surf} in the QD formation energy 7.7. Then we followed the procedure for determining the critical nucleus of a freestanding QD (Sec. 7.7), but now including the energy gain due to stacking (Eq. 8.1) within the observed range of $\delta E \in [5, 35]\text{meV}$. The obtained difference between the formation energy of a homogenous film and a *hut*-shaped QD for different energy gains due to different stacking arrangements is shown in Fig. 8.9. The energy gain reduces the energy barrier for nucleation $\Delta\gamma_c$ and the size of the critical nucleus N_c and can be interpreted as an additional chemical potential (see also Fig. 3.2). We find a linear relationship between $\Delta\gamma_c$ and N_c that gives the relationship between the two y axes shown in the right panel of Fig. 8.9:

$$\Delta\gamma_c = 2.52 \text{ eV} + 0.041 \text{ eV} \cdot N_c. \quad (8.2)$$

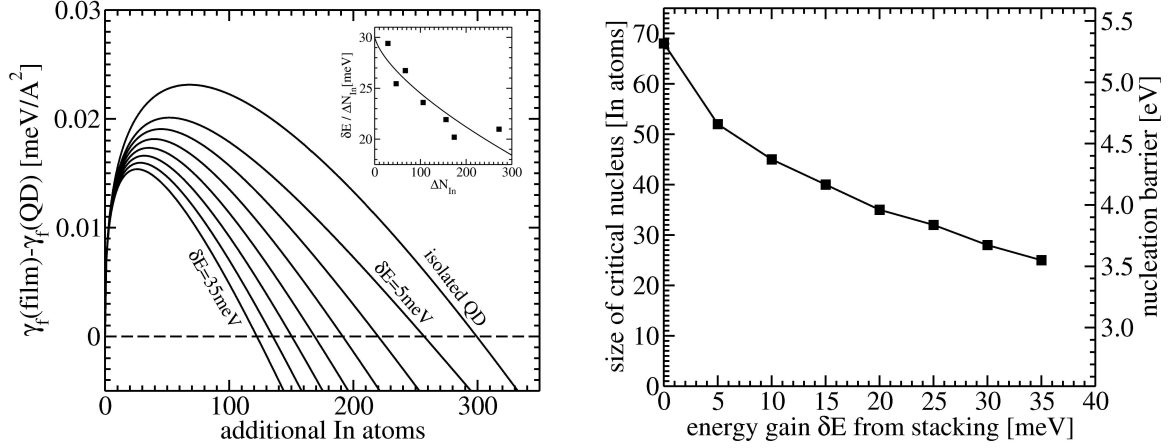


Abbildung 8.9: The energy gain δE due to stacking arrangement reduces both, the nucleation barriers and the size of the critical nucleus and leads to preferred nucleation above overgrown QDs. The value of δE depends on QD shape (Fig. 8.6), spacer thickness Fig.8.7, and lateral position with respect to overgrown QD (Fig. 8.5).

The critical nucleus of a free-standing QD of approximately 70 In atoms is reduced by the elastic interactions in the QD stack by up to a factor of 3 to approximately 25 In atoms (right panel) in the investigated range of energy gains δE . The energy barrier $\Delta\gamma_c$ for forming the critical nucleus is lowered from approximately 5.3 eV to approximately 3.5 eV. The resulting increase in the nucleation rate above the overgrown QDs can thus explain the strong tendency of the experimentally observed vertical growth-correlations in QD stacks within classical nucleation theory. Note that the above change of $\Delta\gamma_c$ by approximately 2 eV would increase the nucleation rate Γ at a temperature of 800 K by several orders of magnitude if we assume that Γ is proportional to $\exp(-\Delta\gamma_c/kT)$. A weakening of the preference for vertical alignment in experiments can be due to a reduced energy gain because of e.g. intermixing of Ga and In, or the formation of defects.

Kapitel 9

Kinetic Aspects of QD Growth

In the previous chapters, we found that many prominent features of InAs/GaAs(001) QD growth can be explained by a thermodynamic rationale based on total energy calculations with the many-body potential developed in this work. Nevertheless, the latter does not provide an adequate description of the adsorption of single adatoms on surfaces as shown in Sec. 6.5. A thorough understanding of adatom diffusion is, however, an inevitable prerequisite for investigating kinetic effects during growth in atomic detail. We therefore extended previous investigations of adatom diffusion on the substrate and wetting layer [74], by a DFT study of In diffusion on QD side facets that are apparent at different stages of growth.

9.1 Introductory Remarks

The growth of InAs QDs on GaAs(001) is accompanied by a shape transition from small, hut-shaped QDs to larger, *dome*-shaped QDs as discussed in depth in Chap. 7. These shapes are dominated by side facets that correspond to $\{137\}$ and $\{101\}$ surfaces, respectively (left panel of Fig. 7.6). The growth of QDs in either shape is governed by the adsorption and diffusion of In and As atoms on these side facets. A means of analyzing such atomic events are the corresponding potential-energy surfaces of adsorption that we determine in this chapter by density-functional theory calculations for the case of In/InAs(137) and In/InAs(101). Additional calculations try to investigate the role of breaking an As-dimer of the InAs(137) surface as a possible rate-limiting step for In incorporation, as well as the strain dependency of the diffusion barriers on the InAs(101) surface.

In our slab calculations for these two surfaces, we use 2×2 repetitions of the surface unit-cell that are oriented with the surface normal along the z -axis. The bottom side is passivated with pseudo hydrogen [166], and the In and As atoms in the bottom layers are not allowed to move during the performed relaxations. The individual points of the PES were determined in a two step procedure: First, for a given lateral position, we positioned the In adatom

in a height where it has 2.5 Å distance to the nearest surface atom, which turned out to save considerable CPU time as compared to starting the relaxation with the same height of the In adatom in all lateral positions. Second, we performed DFT calculations to relax the z -coordinate of the adatom with the constraint of fixed x - and y -coordinate, and the slab atoms (aside from the bottom layers.) In these DFT calculations with the fhi98md-package [47] we employed norm-conserving pseudo-potentials [60], Monkhorst-Pack \mathbf{k} -point meshes [164], and the generalized-gradient approximation (GGA-PBE) for the exchange-correlation functional [230]. The structures were relaxed until the change in the total energy was less than 1 meV.

9.2 Diffusion on Side Facets of Hut-Shaped QDs

9.2.1 Potential-Energy Surface of In/InAs(137)

It was first found experimentally that the InAs(137) surface is stable as side facet of small, *hut*-shaped InAs QDs on GaAs(001) [18]. It is somewhat surprising that this surface has a low formation energy (Tab. 6.10), although it lies inside the stereographic triangle (see Sec. 3.3) and does not even fulfill the electron-counting rule [231]. The surface energy of InAs(137) is further lowered by compressive strain (see Fig. 6.10) which makes it a favorable QD side facet, very similar to the strain-stabilized Ge(105) surface for the case of Ge/Si(001) QDs [76]. The atomic growth of *hut*-shaped InAs QDs is ruled by the diffusion and incorporation of In adatoms on this surface. The adsorption energy of an In adatom in different lateral positions as obtained from DFT calculations is shown in Fig. 9.1. To guide the eye, we present both the atomic structure (left panel) and the potential-energy surface, in a view along the $[00\bar{1}]$ crystallographic direction. (The grid of our calculations is indicated as tick marks at the border.) The adsorption energies at the most prominent local minima and transition states are collected in Tab. 9.1, relative to the most stable site. The most stable adsorption site M1 is a

Tabelle 9.1: Adsorption energies of a In adatom at prominent local minima (M1-M3) and transition states (T1-T4) on InAs(137) as obtained with DFT calculations, normalized to the most stable adsorption site.

site (Fig. 9.1)	M1	M2	M3	T1a	T1b	T2	T3	T4
adsorption energy [meV]	0	1	15	197	204	147	208	339

three-fold coordination with a surface As dimer and the nearby In atom one atomic layer above the dimer. Despite its rather complex structure, the PES reveals nearly isotropic diffusion of an In adatom on the InAs(137) surface: The diffusion between two equivalent sites M1 along As surface dimers in the same height (with respect to the (001) direction) involves two consecutive barriers of T1(a/b)-M1=197/204 meV and T2-M2=146 meV, whereas diffusion

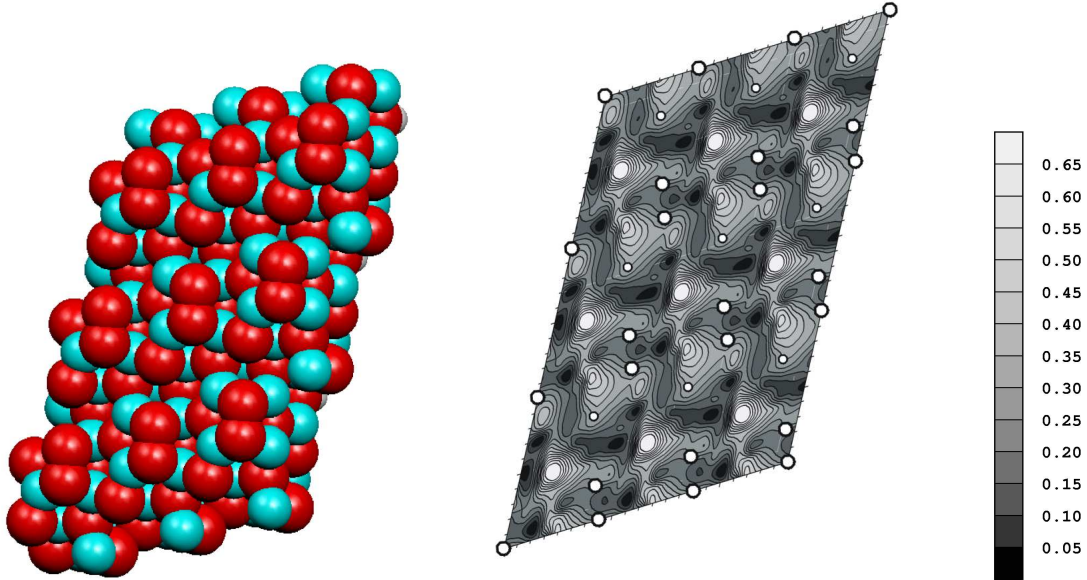


Abbildung 9.1: Potential-energy surface (right) of an In adatom on the InAs(137) surface (left), which appears as dominant side facet of small QDs, as obtained by DFT calculations (GGA-PBE). (The surface As dimer and the neighboring three-fold As atoms are indicated as large and small circles.)

between two equivalent M1 at As surface dimers in different heights can proceed by passing either a barrier of T3-M3=193 meV or T4-M1=339 meV. Thus, the dominant diffusion barrier between two equivalent M1 of the same height with respect to the (001) direction is very similar to those connecting two M1 of different height. Regarding growth of *hut*-shaped QDs, we conclude from these DFT calculations that the diffusion of In adatoms on the {137} facets is nearly isotropic along contour lines of *hut*-shaped QDs and perpendicular to them.

9.2.2 Binding Sites at As Surface-Dimer

The adsorption site of In at the As surface dimer is of particular interest for diffusivity: It was first found for the case of a Ga atom on a surface As dimer of the $\beta 2(2 \times 4)$ reconstruction of GaAs(001) [157], that the energy minimum of adsorption on top of the dimer is not the only stable adsorption site. In fact, forcing the adatom to break the As dimer turned out to result in an even more stable configuration. Similar investigations [74] showed that this effect is weaker for In/ $\text{In}_{2/3}\text{Ga}_{1/3}\text{As}(001)$ and negligible for In/GaAs(001)-*c*(4×4), mainly due to the elastic distortions that the In atom exerts on the As dimer. The energy gain for breaking

the surface As dimer of the InAs(137) is additionally altered by the presence of the three-fold coordinated As atom nearby the dimer that possibly limits the range of elastic relaxation of the broken dimer. Our constraint-free relaxation by DFT calculations from two different starting configurations, one with the In atom on top of the dimer and the other one with the In atom in the center of the dimer, showed two stable adsorption sites. Both minima are of nearly the same depth and differ only by 27 meV in favor of the broken-dimer configuration. The energy barrier for breaking the As dimer can be determined by forcing the In atom to move from the on top position to the center of the broken dimer. We therefore performed a linear interpolation of the coordinates of the In adatom, the dimer, and the slab atoms that correspond to the two stable configurations, fixed the atomic coordinates of the In adatom and relaxed all other atoms (aside from the bottom layers). The resulting binding energies show a similar behavior as observed in previous studies [74, 157], shown in Fig. 9.2. The reference

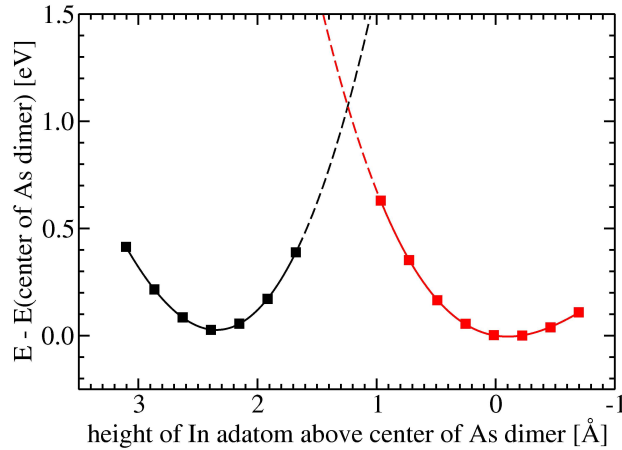


Abbildung 9.2: Binding energy of an In atom at a surface As dimer of InAs(137) as obtained by DFT calculations (GGA-PBE): The adsorption site on top of the As dimer (black) is slightly higher in energy than the configuration with the In atom in the center of the broken dimer (red). The barrier for As dimer breaking is estimated with third-order polynomials (lines) to be of approximately 1 eV.

points for the binding energy and the height of the In atom are the adsorption energy and the height of the broken-dimer configuration, respectively. We estimate the energy barrier for breaking the As dimer from a fit of the adsorption energies to third-order polynomials to be of approximately 1 eV. This energy barrier is a factor of five higher than the diffusion barriers reported in the previous section. Nevertheless, it needs to be overcome in a growth process to achieve the incorporation of In at this site. From the relation of these barriers, we conclude that the diffusion of In atoms on the (137) surface is faster than their incorporation.

The breaking of the As dimer on the $\{137\}$ surface for the incorporation of In atoms is thus of higher importance as a possible rate-limiting step than the diffusion of In atoms on the $\{137\}$ surface.

9.3 Diffusion on Side Facets of Dome-Shaped QDs

9.3.1 Potential-Energy Surface of In/InAs(101)

In a later stage of growth, the QDs undergo a transition from the *hut* shape with mainly $\{137\}$ side facets to the *dome* shape dominated by the steeper $\{101\}$ facets (Chap. 7). The $\{101\}$ surfaces of zinc blende and diamond semiconductors are very well studied and in fact often serve as an educational example, because they do not reconstruct and can be described by comparably small simulation cells. In this section, however, we focus on the question of how the diffusion barriers are affected by strain to understand the influence of the strain tensor of *dome*-shaped QDs on the diffusion of In atoms on its side facets. The adsorption energies of an In atom in different lateral positions on the InAs(101) surface as determined with DFT calculations, similarly to the proceeding outlined in the previous section, are shown in Fig. 9.3. Again, we indicate the grid of our calculations by tick marks and use the most stable

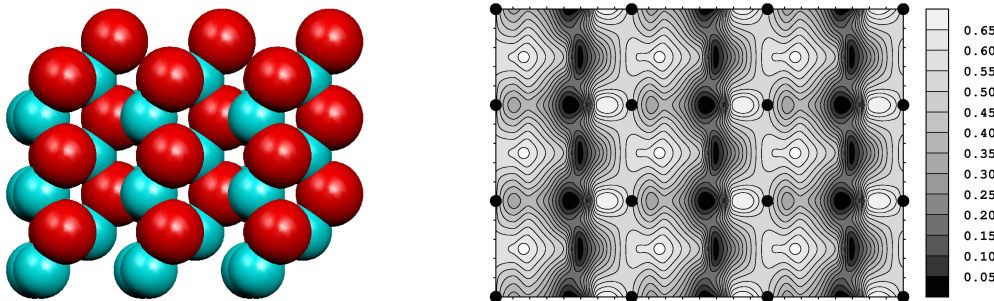


Abbildung 9.3: Potential-energy surface (right) of an In adatom on the InAs(101) surface (left), which appears as dominant side facet of larger QDs, as obtained by DFT calculations (GGA-PBE).

adsorption site for calibration of the energy scale. The binding energies at the most prominent adsorption sites are summarized in Tab. 9.2. The diffusion on this surface is obviously highly anisotropic due to the particular geometry with motifs that resemble zigzag-chains of In and As atoms (left panel in Fig. 9.3). The barrier for diffusion perpendicular to a zigzag chain (T3-M1) is more than 3 times larger than those parallel to the zigzag chains (T1-M1). In the context of *dome*-shaped QD, we can therefore conclude that the diffusivity of In on the side facets is highly anisotropic and dominantly perpendicular to the contour lines of the QD, i.e. from the bottom of the QD to its apex.

Tabelle 9.2: Adsorption energies of a In adatom at local minima (M1-M3) and transition states (T1-T3) on InAs(101) as obtained with DFT calculations, normalized to the most stable adsorption site.

site (Fig. 9.3)	M1	M2	M3	T1	T2	T3
adsorption energy [meV]	0	30	310	164	385	524

9.3.2 Dependence of Diffusion Barriers on Biaxial Strain

The directed diffusion to the apex of the *dome*-shaped QD takes course perpendicular to the contour lines and thus perpendicular to the iso-strain lines of the QD. An understanding of the diffusion kinetics therefore requires the knowledge of the dependency of the diffusion barrier on the strain. The results of the elastic response upon a biaxial strain ε that we reported in Sec. 6.2 now enable us to study this effect by scaling a unit cell of the (101) surface accordingly, including non-linear elastic response (see Fig. 6.5) for the fixed bottom layers. From our DFT calculations of the binding energies in the trench minima (M1,M2) and the transition state connecting them (T1) upon biaxial compressive strains of $-8\% \leq \varepsilon \leq 0\%$ we obtained the strain-dependent diffusion barriers shown in Fig. 9.4. Both energy barriers

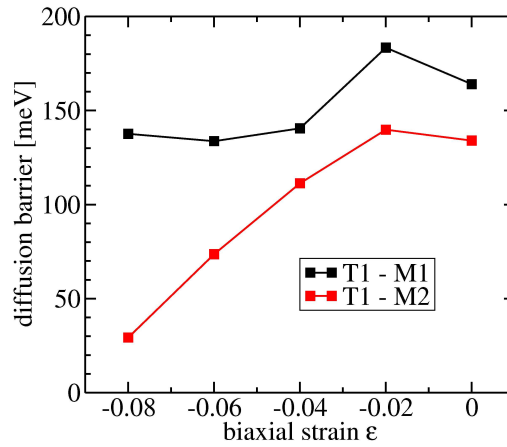


Abbildung 9.4: Dependence of energy barriers for diffusion of In atom in trench between zigzag chains of InAs(101) on compressive biaxial strain as obtained by DFT calculations (GGA-PBE).

for In diffusion on the (101) surface are reduced upon biaxial strain in the surface plane. The effective barrier for diffusion in the trench between two zigzag chains, i.e. perpendicular to the QD contour lines, is lower at the compressively strained bottom of the QD and higher near the more relaxed top. The $\{137\}$ side facets at the top of *dome*-shaped QDs (see e.g.

Ref. [19]) are not strain stabilized like the $\{137\}$ side facets of a *hut*-shaped QD. So, from a thermodynamic point of view, one might either expect the formation of a (001) facet at the relaxed top of the QD (as this surface is lowest in energy in the absence of strain) or the continuation of the $\{101\}$ facets beyond the top truncation of $\{137\}$ facets (as this would maximize the amount of unstrained InAs). This indicates that the remaining $\{137\}$ facets at the relaxed upper parts of a *dome*-shaped QD are explainable as a kinetic effect: From our calculated strain dependence of the diffusion barrier at compressive biaxial strain (Fig. 9.4), we can conclude that the diffusion of In atoms on the $\{101\}$ facets of *dome*-shaped QDs near the bottom is faster than near the top. This suggests that the $\{101\}$ facets grow from top to bottom, which could be an explanation of the experimentally observed remains of $\{137\}$ facets on the top of *dome*-shaped QDs. Note that this mechanism is a kinetic effect, in contrast to the many aspects that turned out to be consistent with a thermodynamic rationale in the previous chapters. We hope to get further insight from ongoing work that aims to combine the QD strain-tensor as obtained from the many-body potential with strain-dependent energy barriers for adatom diffusion determined with density-functional theory calculations.

Summary and Outlook

Semiconductor quantum-dots (QDs) are a promising ingredient for future technologies, such as new opto-electronic devices, single-electron transistors, and quantum computers. The key challenges for modern solid-state physics in this context are the identification of required electronic properties and adequate semiconductor nanostructures, as well as their controlled and robust fabrication. The small size of such structures (a few nm in length) calls for a consideration of both atomic details and long-range strain. Both aspects have a significant bearing on e.g. simulations of epitaxial growth and electronic-structure calculations of strained nanostructures. The goal of this work is to study the growth and stability of InAs/GaAs(001) QD nanostructures in atomic detail.

At first, we would like to draw attention to our continuum-elasticity theory (CET) results for the elastic response of cubic materials upon biaxial strain: We determined general analytic expressions for the strain tensor, the Poisson ratio, and the elastic energy for materials with cubic crystal symmetry under biaxial strain in arbitrary planes. The analytic strain tensor allows us to perform numerical calculations of elastic response upon biaxial strain in arbitrary planes with only one conventional cubic unit cell, a dramatic reduction of the numerical effort in e.g. density-functional theory (DFT) studies of such effects. The knowledge of the Poisson ratio enables an appropriate consideration of the elastic properties of the fixed bottom-layers in slab calculations of strained surfaces. With the general expression of the elastic energy we found that QD formation occurs surprisingly on substrate orientations that correspond to small and moderate elastic energies of biaxially strained InAs, but not on those that correspond to high elastic energies where instead the formation of dislocations was observed. A comparison of the elastic response from CET and DFT calculations enabled us to isolate non-linear contributions to the elastic response systematically and describe them by a simple polynomial expansion. The general expression of the elastic energy should in principle allow one to predict the energy barriers of the so-called Bain path between *bcc* and *fcc* structures for any material with cubic symmetry in an approximative manner. The quality of this harmonic approach will depend on the importance of non-linear elastic response.

A very reliable and well established method for the investigation of the atomic structure and thermodynamic stability of bulk and surface structures are DFT calculations. The numerical effort, however, limits this high-accuracy method to systems with irreducible simulation

cells of not more than about 1000 atoms. However, the lattice-mismatch of QD nanostructures causes long-range strain tensors that require typically three orders of magnitude more atoms in the simulation cell and other approaches of modeling. The methodical progress of this work is the development of an interatomic many-body potential that allows us to transfer information obtained by DFT calculations to QD nanostructures that are represented by million-atom simulation cells. In this part of the work we experienced fundamental drawbacks of this approach that hinder a reliable assessment of interatomic potentials in general. The common origin is that only a rather small subset of physical properties can be captured simultaneously with acceptable accuracy, but unfortunately there is little knowledge on how to identify conflicting subsets. The particular choice of a subset of reference data for the parameter optimization is therefore often guided by the application in mind. This requires a basic understanding of the relevant processes already in the stage of parameterization and usually yields parameters that are suitable only for a certain group of applications, which often limits the meaning of a comparison of different parameterizations. The numerical parameter optimization itself poses a non-linear optimization problem that can be tedious and time-consuming although sophisticated algorithms are available.

The interatomic many-body potential developed in this work is a significantly improved parameterization of the Abell-Tersoff functional for In, Ga, As, GaAs, and InAs. It was thoroughly checked and compared with previous parameterizations regarding the description of situations that are supposedly relevant for modeling the formation of InAs QDs on GaAs substrates. This comparison was based on a consistent set of reference data from experiments and DFT calculations, some of the latter performed in this work. The newly developed parameterization captures many more bulk and surface properties simultaneously with higher overall accuracy and is transferable to strained GaAs and InAs. With our newly developed parameterization, it is possible for the first time to perform reliable atomistic relaxations of realistic InAs/GaAs nanostructures with reconstructed surfaces using million-atom simulation cells, and to quantitatively study the resulting strain tensors and total energies with dependable contributions from strained bulk and surface configurations. This can be considered a successful length-scale extension from a few nanometers of the DFT unit-cells used in calculating reference data to a length of $0.5 \mu\text{m}$ in the largest simulation cell investigated with the many-body potential. Our atomistic approach has some advantages over the previously very successful hybrid approaches: The modeling of QD nanostructures with newly appearing (substrate or QD) surfaces involves no additional calculations of the surface properties. The atomic structure is well-defined, in particular, the side facets are either multiples of surface unit cells or terminated by e.g. edges and kinks. The stoichiometry of the QD nanostructures is thus a natural quantity and allows us to consistently capture the influence of chemical potentials. The energy contributions are implicitly included in their full complexity, in contrast to hybrid approaches that e.g. neglected lateral interactions between QDs in previous studies.

An important aspect of this work is the clarification of the role of thermodynamic effects during QD formation that is driven by the balance between energy gain due to strain relief

and energy cost due to formation of QD side facets and edges. We use recent atomically resolved STM images of InAs QDs to set up QD nanostructures in atomic detail, apply our potential to relax them, and compare the resulting total energies. In this way we could identify three regimes of thermodynamic stability that are in line with the experimentally deduced coverage at the 2D to 3D growth transition, and the shapes of small and larger QDs: For coverages just above 1.75 monolayers InAs the film is most stable, followed by small hut-shaped QDs dominated by $\{317\}$ facets and larger dome-shaped QDs dominated by $\{101\}$ facets. An analysis of strain-tensors revealed that the coincidence of the side facets with either elastically hard or soft axes causes a qualitative difference of the lateral interactions: The elastic interaction-energy of hut-shaped QDs follows a power-law dependence on the lateral QD distance, but is negligible for dome-shaped QDs, a fact that was not considered in previous works. With the well-defined stoichiometry of our atomistic QD nanostructures, we can show that the QD volume at the hut-dome transition can be altered by up to an order of magnitude for different values of the QD density and the chemical potential of As. Using classical nucleation-theory we determine the critical nucleus of QD formation for the case of growth conditions close to thermodynamic equilibrium: We find that the energy barrier to form the critical nucleus of approximately 70 In atoms is 5.3 eV. Our results suggest the concurrence of the formation of critical nuclei with the onset of the 2D-3D transition observed in RHEED experiments.

This fruitful combination of an interatomic many-body potential and a thermodynamic rationale enabled us also to explain growth correlations in stacked QD layers. From potential-energy surfaces of free-standing QDs in different lateral positions above overgrown QDs, we find a nearly isotropic energetic preference for the experimentally observed vertical alignment of QDs in subsequent layers. The QD shapes have no significant influence on this finding. The energy gain for vertical alignment decreases with increasing amount of GaAs between the stacked QD layers from a value of approximately 35 meV per atom for 3.2 nm to a negligible value at 8 nm, in consistency with experimental results for nearly pure InAs QDs grown by MOCVD. The calculated energy gain for vertical alignment reduces the size of the critical nucleus by up to a factor of 4 as compared to an elastically isolated QD. The observed vertical attractive and the lateral repulsive interaction of hut-shaped QDs is explainable within a simple elastic dipole-monopole and dipole-dipole interaction, respectively.

Our investigations of the stability of QD nanostructures show that great insight can be gained from the application of a many-body potential. Considering the ongoing discussion about thermodynamic and kinetic effects in the field of self-assembled growth, it is surprising that we found such a large number of experimentally observed features of InAs QD formation to be consistent with a thermodynamic rationale. We hope that our development of the many-body potential and the demonstration of its capabilities in describing QD nanostructures opens the way for further studies in this direction. The still ongoing projects of this work are the evolution of elastic contributions during the shape transition, the atomically detailed growth front of partially grown facets, as well as structural effects on the electronic

structure by tight-binding calculations in a close collaboration with A. Kleinsorge. But it might also be of fundamental interest to clarify if the shape transition observed on (001) substrates is connected to the substrate orientation or a more general feature. Another promising investigation should be to find an upper bound of the Ga content in freestanding InAs QDs by calculating the coverage at the 2D-3D transition of $\text{In}_x\text{Ga}_{1-x}\text{As}/\text{GaAs}(001)$ at different stoichiometries x and comparing it with experimentally deduced transition coverages. In the context of stacked layers of QDs it would be interesting to see if the energy gain of certain spatial arrangements is only due to a minimization of the distance between the QD in proximate layers or rather mediated by elastically soft/hard axes.

Although such thermodynamic studies provide a lot of insight, it is essential to also know the regimes where kinetic effects govern the growth of QD nanostructures. In extension to our thermodynamic studies, we performed DFT calculations of the potential-energy surfaces for In adsorption on the InAs(137) and InAs(101) that appear as dominant side facets of hut-shaped and dome-shaped QDs. The diffusion barriers on the (137) surface in the two main directions along As surface dimers of equal height with respect to the (001) direction, and perpendicular to them, differ only by a few meV. The In incorporation could be kinetically limited due to the high barrier of approximately 1 eV for breaking surface As dimers. The highly anisotropic diffusion on InAs(101) is mainly perpendicular to the contour lines of dome-shaped QDs. The diffusion barriers are lowered near the QD bottom, which supports the interpretation of remaining (137) facets on top of dome-shaped QDs as kinetic effect. For the realization of technical applications the highest priority for future studies has probably a qualitative understanding of intermixing and segregation effects that take place during QD overgrowth.

Appendix

A. DFT Calculations

In several parts of this work we present new results from DFT calculations, in particular for the structural and elastic properties of stable and metastable In and InAs bulk phases (Tab. 6.2, 6.5, and 6.6), and the potential-energy surface for adsorption of In on InAs surfaces (Chap. 9). We performed extensive and systematic convergence tests of the bulk calculations with respect to the number of \mathbf{k} -points, and the cutoff energy. In the surface calculations we successively optimized the parameters of the electronic minimization with the Williams-Soler algorithm [47] to achieve optimal convergence of the structural relaxation. In Fig. A.1 we show exemplarily the convergence tests of the InAs zinc blende lattice constant and the Poisson ratio ν (cf. Sec. 4.3) for InAs under biaxial strain in the (113) plane. For the calculation of

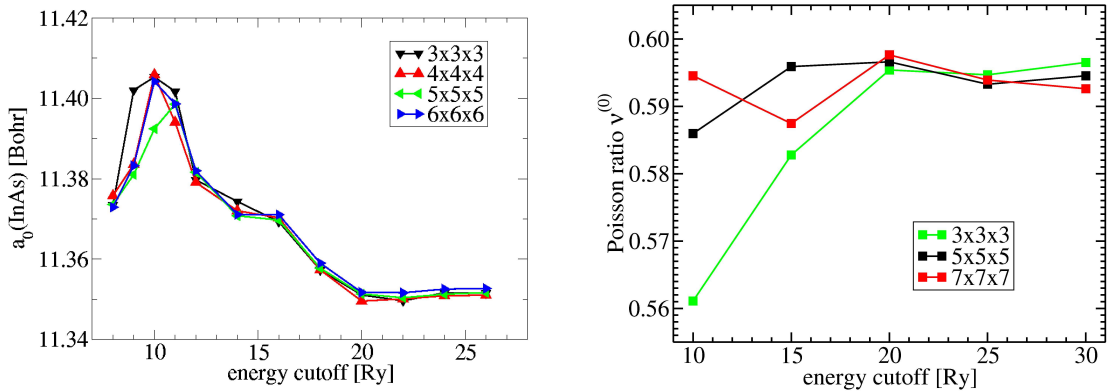


Abbildung A.1: Examples of convergence tests performed in the DFT calculations of this work: the lattice constant a_0 of InAs (left) and the Poisson ratio $\nu^{(0)}$ (cf. Eq. 6.2) for biaxial strain in the (113) plane (right) as a function of plane-wave cutoff and of the density of the Monkhorst-Pack \mathbf{k} -point grid [164].

the biaxial Poisson-ratio we employed the results of Chap. 4 and entered the strain tensor

directly in the input file of the SFHIngX package:

```
...
// --- biaxial strain and Poisson ratio from script
include "./strain.sx";
include "./poisson.sx";
eps = strain; // taken from ./strain
nu = poisson; // taken from ./poisson
// Miller indices that define plane of biaxial strain
h=1;
k=1;
l=3;
// components of strain tensor in canonical coordinates
fac = -eps/(h*h+k*k+l*l);
hh = 1+fac*(nu*h*h-(k*k+l*l));
kk = 1+fac*(nu*k*k-(h*h+l*l));
ll = 1+fac*(nu*l*l-(h*h+k*k));
hk = fac*h*k*(nu+1);
hl = fac*h*l*(nu+1);
kl = fac*k*l*(nu+1);
// ZnS unit cell (a0 = lattice constant)
structure {
cell = a0 * [ [ hh, hk, hl ],
              [ hk, kk, kl ],
              [ hl, kl, ll ] ];
// atomic positions in unit cell times strain tensor
species {
include species_1;
atom { coords = a0/2*[0 , 0 , 0 ];}
atom { coords = a0/2*[ hk+hl, kk+kl, kl+ll ];}
atom { coords = a0/2*[hh +hl, hk +kl, hl +ll ];}
atom { coords = a0/2*[hh+hk , hk+kk , hl+kl ];} }
species {
include species_2;
atom { coords = a0/4*[ hh+ hk+ hl, hk+ kk+ kl, hl+ kl+ ll];}
atom { coords = a0/4*[ hh+3*hk+3*hl, hk+3*kk+3*kl, hl+3*kl+3*ll];}
atom { coords = a0/4*[3*hh+ hk+3*hl, 3*hk+ kk+3*kl, 3*hl+ kl+3*ll];}
atom { coords = a0/4*[3*hh+3*hk+ hl, 3*hk+3*kk+ kl, 3*hl+3*kl+ ll];} }
}
...
```

Note that the convergence of $\nu^{(0)}$ in the right panel of Fig. A.1 is more sensitive to the cutoff energy than that of a_0 in the left panel. The origin of this effect is the change of the size and shape of the unit cell (`cell`) for different values of the applied biaxial strain (`eps`) in the calculation of $\nu^{(0)}$: The resulting difference in the plane-wave basis sets of the differently deformed unit cells introduces an additional error in the comparison of the total energies during the determination of $\min(E_{\text{el}}(\alpha_i, \nu), \nu)$ (Eq. 6.1) and the linear regression $\nu(\alpha) = \nu^{(0)} + \nu^{(1)}\alpha$ (Eq. 6.2 and Fig. 6.5). The correction of this error with the scaling hypothesis presented by Rignanese et. al [232] as demonstrated in the thesis of E. Penev for total energies of biaxially strained surfaces [74] is advantageous for large systems as it allows us to limit the calculations to comparably small cutoff energies and numbers of \mathbf{k} -points. The general strain tensor of biaxially deformed zintlende bulk material derived in this work, however, limits the irreducible simulation cell to a single unit cell. This allows us to easily perform calculations at increased cutoff energy and number of \mathbf{k} -points to systematically reduce the above error due to comparing total energies obtained with different plane-wave basis sets.

B. Implementation of the Many-Body Potential

The main application of the empirical potential in this work is the description of large systems with up to millions of atoms. Similar to other numerical methods in computational physics, it is of major importance to minimize the computational effort. The bottlenecks of relaxing a large system with an empirical potential are the evaluation of the force and energy functions, the determination of the interacting neighbor atoms, and the efficiency of the relaxation algorithm itself. Our Fortran 77 implementation uses the analytic derivative of the energy functional given in the following, determines the list of neighboring atoms with a linked-cell algorithm (see e.g. Ref. [125]) and performs minimizations with a conjugate-gradient algorithm taken from Ref. [153]. Furthermore, the code performs efficient access management of arrays, loop nesting with recycling of intermediate results, and separate treatment of fixed and non-fixed degrees of freedom.

The typical convergence behavior of the total energy and the absolute value of the maximum force F_{max} on an atom in the system during the relaxation with our implementation is shown in the left panel of Fig. B.1 for a system with more than one million atoms. All relaxations in this work were performed until F_{max} was less than 1 meV/Å. We found this sufficient to converge the total energy of the investigated systems to below 1 meV, as exemplarily shown in the left panel of Fig. B.1. This level of convergence corresponds to an average error of 10^{-6} meV per atom in a million-atom system. For an assessment of the CPU time spent in each relaxation step, we monitored the calculations of three systems with different sizes: an InAs wetting layer, a *hut*-shaped InAs QD, and a *dome*-shaped InAs QD on a GaAs(001) substrate. The results shown in Figure B.1 clearly indicate an order N behavior,

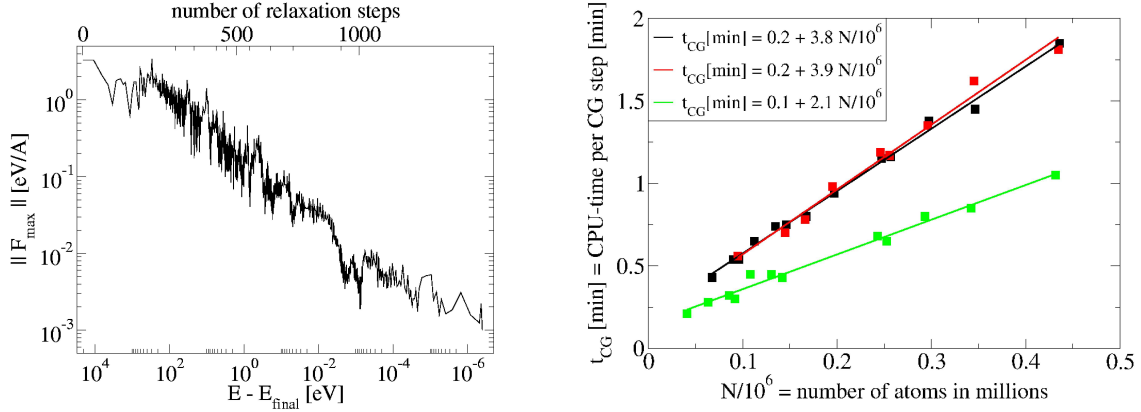


Abbildung B.1: A typical evolution of the maximum force in the system F_{\max} and the convergence of the total energy with respect to the final value during relaxation (left) shows that a force limit of $F_{\max} < 1$ meV/Å is sufficient to provide well converged total energies. The implementation of the force and energy evaluation as well as the relaxation were optimized to achieve a linear scaling of the computational effort per relaxation step with the number of involved atoms (right).

i.e. the computational effort scales linearly with the number of involved atoms.

The relaxation of a QD nanostructure transfers it from a stressed state to a stress-free strained state with a strain tensor that is determined by the system-inherent stress sources and the material response. The required number of relaxation steps depend not only on the number of atoms involved, but also on the complexity and the range of elastic response. In our calculations, the number of steps ranges from less than 100 for heterostructures with a wetting layer only to about 1000 if large QDs are present. The line-minimization algorithm used to determine the step width along the conjugate-gradient direction assumes a parabolic dependence of the energy on the step width. The quality of this assumption depends on the system itself and leads to the different slopes in Fig. B.1.

Analytic Force Expression

For empirical potentials with analytic energy functional the force on each atom can be given in closed analytical form as well. The numerical evaluation of the latter is usually significantly faster than a numeric derivative employing the energy functional only. The x component of the force on atom L defined as

$$F(x_L) = -\frac{dE_{\text{coh}}}{dx_L} \quad (\text{B.1})$$

is determined by the energy functional E_{coh} of Eq. 5.8- 5.14 where some parameters can be merged for computational efficiency:

$$\begin{aligned} V_{ij}^{R1} &:= \frac{D_{ij}}{S_{ij} - 1} \cdot e^{\beta_{ij} \sqrt{2S_{ij}} R_{ij}^0} \quad , \quad V_{ij}^{R2} := \beta_{ij} \sqrt{2S_{ij}} \quad , \\ V_{ij}^{A1} &:= \frac{S_{ij} D_{ij}}{S_{ij} - 1} \cdot e^{\beta_{ij} \sqrt{\frac{2}{S_{ij}}} R_{ij}^0} \quad , \quad V_{ij}^{A2} := \beta_{ij} \sqrt{\frac{2}{S_{ij}}} \quad , \\ G_{ik}^1 &:= \delta_{ik} \left(1 + \frac{c_{ik}^2}{d_{ik}^2}\right) \quad , \quad G_{ik}^2 := \delta_{ik} c_{ik}^2 \quad . \end{aligned}$$

Applying the chain rule in the analytic derivative leads to nested sums with delta functions due to

$$\frac{dr_{ij}}{dx_L} = (\delta_{iL} - \delta_{jL}) \cdot \frac{x_{ij}}{r_{ij}} \quad (\text{B.2})$$

with the Kronecker symbol δ_{ij} . These expressions can be simplified by using

$$\begin{aligned} \sum_i \sum_{j \neq i} (\delta_{iL} - \delta_{jL}) f_{ij} &= \sum_{i \neq L} [f_{Li} - f_{iL}] \quad , \\ \sum_i \sum_{j \neq i} (\delta_{iL} - \delta_{jL}) (a_{ij} + b_{ij}) &= \sum_{j \neq L} (b_{Lj} - b_{jL}) \quad \text{for } a_{ji} = a_{ij}, b_{ji} \neq b_{ij}, \quad \text{and} \\ \sum_i \sum_{j \neq i} \sum_{k \neq i, j} [\delta_{iL} f_{ijk} - \delta_{jL} g_{ijk} - \delta_{kL} h_{ijk}] &= \\ \sum_{j \neq L} \sum_{k \neq j \neq L} f_{Ljk} - \sum_{i \neq L} \sum_{j \neq i \neq L} h_{ijL} - \sum_{i \neq L} \sum_{k \neq i \neq L} g_{iLk} + \sum_{i \neq L} \sum_{j \neq i \neq L} [f_{Lij} - g_{iLj} - h_{ijL}] \quad . \end{aligned}$$

The analytic force is then given by

$$\begin{aligned} F(x_L) &= \sum_{i \neq L} \frac{x_{Li}}{r_{Li}} \cdot \frac{df_{Li}^c(r_{Li})}{dx_L} \left[\frac{B_{Li}(r_{Li}) + B_{iL}(r_{iL})}{2} \cdot V_{Li}^A(r_{Li}) - V_{Li}^R(r_{Li}) \right] \\ &\quad - \sum_{i \neq L} \frac{x_{Li}}{r_{Li}} \cdot f_{Li}^c(r_{Li}) \left[\frac{B_{Li}(r_{Li}) + B_{iL}(r_{iL})}{2} \cdot V_{Li}^A(r_{Li}) V_{Li}^{A2} - V_{Li}^R(r_{Li}) V_{ij}^{R2} \right] \\ &\quad - \frac{1}{2} \sum_{i \neq L} \sum_{j \neq i \neq L} \left[(A_{Lij} + B_{Lij}^1 + B_{Lij}^2 + C_{Lij}^1 - C_{Lij}^2) - (B_{iLj}^2 + C_{iLj}^1) \right. \\ &\quad \quad \left. - (A_{ijL} + B_{ijL}^1 - C_{ijL}^2) \right] \end{aligned}$$

where the following combined terms were introduced

$$\frac{df_{ij}^c(r_{ij})}{dx_L} = \begin{cases} 0 & r_{ij} \leq R_{ij}^c - D_{ij}^c \\ df_{ij}^c(r_{ij}) \cdot \frac{x_{ij}}{r_{ij}} \cdot (\delta_{iL} - \delta_{jL}) & \text{else} \\ 0 & r_{ij} \geq R_{ij}^c + D_{ij}^c \end{cases} \quad ,$$

$$\begin{aligned}
A_{ijk} &= H_{ij} \cdot e^{[(\alpha_{ik}(r_{ij}-r_{ik}))^{m_{ik}}]} \cdot g_{ik}(\theta_{ijk}) \cdot df_{ik}^c(r_{ik}) \cdot \frac{x_{ik}}{r_{ik}} \quad , \\
B_{ijk}^1 &= H_{ij} \cdot e^{[(\alpha_{ik}(r_{ij}-r_{ik}))^{m_{ik}}]} \cdot f_{ik}^c(r_{ik}) \cdot dg_{ik}(\theta_{ijk}) \cdot d \cos_{ijk}^1(r_{ij}, r_{ik}) \quad , \\
B_{ijk}^2 &= H_{ij} \cdot e^{[(\alpha_{ik}(r_{ij}-r_{ik}))^{m_{ik}}]} \cdot f_{ik}^c(r_{ik}) \cdot dg_{ik}(\theta_{ijk}) \cdot d \cos_{ijk}^2(r_{ij}, r_{ik}) \quad , \\
C_{ijk}^1 &= H_{ij} \cdot e^{[(\alpha_{ik}(r_{ij}-r_{ik}))^{m_{ik}}]} \cdot f_{ik}^c(r_{ik}) \cdot g_{ik}(\theta_{ijk}) \cdot de_{ijk}(r_{ij}, r_{ik}) \cdot \frac{x_{ij}}{r_{ij}} \quad , \\
C_{ijk}^2 &= H_{ij} \cdot e^{[(\alpha_{ik}(r_{ij}-r_{ik}))^{m_{ik}}]} \cdot f_{ik}^c(r_{ik}) \cdot g_{ik}(\theta_{ijk}) \cdot de_{ijk}(r_{ij}, r_{ik}) \cdot \frac{x_{ik}}{r_{ik}} \quad , \text{ and} \\
H_{ij} &= f_{ij}^c(r_{ij}) \cdot V_{ij}^A(r_{ij}) \cdot \frac{\gamma_{ij}^n}{2} \cdot B_{ij}(r_{ij})^{1+2n_{ij}} \cdot \chi_{ij}(r_{ij})^{n_{ij}-1}.
\end{aligned}$$

The remaining expressions from applying the chain rule are

$$\begin{aligned}
df_{ij}^c(r_{ij}) &= -\frac{\pi}{4D_{ij}^c} \cos\left(\pi \frac{r_{ij} - R_{ij}^c}{2D_{ij}^c}\right) \quad , \\
dg_{ik}(\theta_{ijk}) &= \frac{-2 \cdot G_{ik}^2 \cdot (h_{ik} - \cos \theta_{ijk})}{(d_{ik}^2 + (h_{ik} - \cos \theta_{ijk})^2)^2} \quad , \\
d \cos_{ijk}^1(r_{ij}, r_{ik}) &= \left(\frac{x_{ij}}{r_{ij}} - \frac{x_{ik}}{r_{ik}} \cdot \cos \theta_{ijk}\right)/r_{ik} \quad , \\
d \cos_{ijk}^2(r_{ij}, r_{ik}) &= \left(\frac{x_{ik}}{r_{ik}} - \frac{x_{ij}}{r_{ij}} \cdot \cos \theta_{ijk}\right)/r_{ij} \quad , \text{ and} \\
de_{ijk}(r_{ij}, r_{ik}) &= m_{ik} \cdot \alpha_{ik} \cdot (\alpha_{ik}(r_{ij} - r_{ik}))^{m_{ik}-1}.
\end{aligned}$$

The expressions above are formulated for ease of implementation.

C. Initialization of QD Supercells

The investigation of QD nanostructures in atomic detail requires us to initialize supercells that contain the atomic coordinates. The physically relevant QD shapes can be deduced from high-resolution STM experiments as indicated in Fig. C.1 for Ref. [18]. In many cases it is sufficient to generate a supercell of the embedding bulk material and swap the atomic species to the QD material in the region of a given QD shape. The treatment of free-standing QDs however requires us to model the emerging surfaces that would be reconstructed in a real experiment.

The geometries of the InAs/GaAs QD nanostructures investigated in this work were generated with a newly developed tool named *CHEOPS*: The system is represented by the substrate orientation and reconstruction, the supercell basis for rotated and non-orthogonal super cells, the corners of the supercell, the composition profile, and the list of facets with

Miller indices, distance from origin, and reconstruction. The size of the supercell defines the density of QDs per unit area of the substrate (see Fig. 1.3). The initialization of QD nanostructures starts with cutting a sufficiently large, cubic supercell of zinc blende GaAs by these planes. Then, the emerging cleavage surfaces are covered with periodically repeated surface unit-cells as obtained after relaxation with DFT calculations. For this purpose, these cells are scaled to the employed GaAs lattice constant, rotated to canonical crystal coordinates and shifted along the surface normal. The stoichiometric composition is created by swapping Ga atoms to In atoms according to a specified profile, resulting in the QD nanostructure in its initial stage where both In and Ga atoms are located on a zinc blende lattice with the lattice constant of GaAs. This procedure is sketched in Fig. C.1 that shows the zinc blende unit cells of GaAs and InAs, as well as the surface unit-cells of InAs(001) $\alpha 2(2 \times 4)$ and InAs(137).

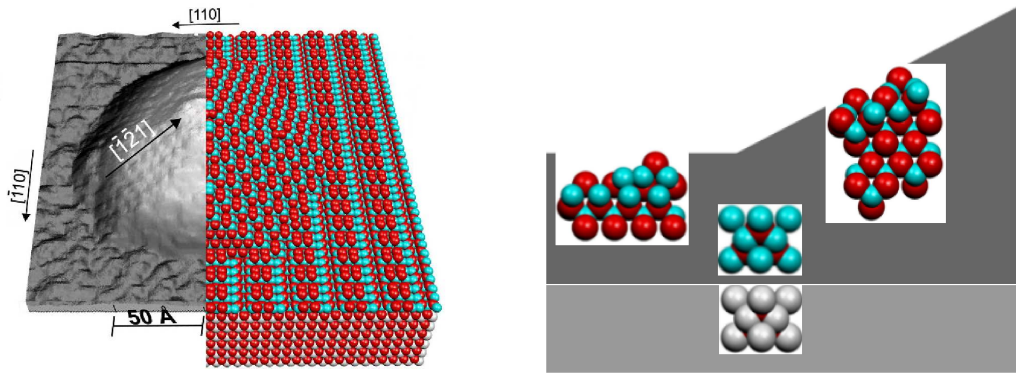


Abbildung C.1: The atomically resolved QD shapes from high-resolution STM experiments are used to derive atomistic representations of QDs (left) by means of the identified surfaces. The emerging surfaces in the atomistic representations are completed with reconstructed surface unit-cells as obtained from DFT calculations (right).

The overlap of reconstructions of neighboring surfaces at edges and kinks is treated by removing one atom from each pair of atoms which is closer than a certain threshold. Possibly occurring pairs of under-coordinated atoms at edges and kinks are modified to form dimers with a specified bond length. A similar procedure is used to create supercells of QDs with sockets or partially grown side facets, and of overgrown QDs. Systems with more than one QD, such as the QD stack structures in Sec. 8.3, were initialized by merging partial structures holding one QD each. The newly developed tool allows us not only to specify different reconstructions of the particular surfaces but also to incorporate more reconstructed surface unit-cells. Furthermore, it was extended to create *wurtzite* structures for InN/GaN QD nanostructures by M. Winkelkemper from the Technical University of Berlin.

D. Surface Area of QD Side Facets

The total cohesive energies E_{tot} of the investigated systems with freestanding QDs include errors in the surface free energy as described in Sec. 6.3 that can be corrected if the areas of the involved surfaces are known (Eq. 7.1). These areas are determined by the planes that were used to initialize the QD nanostructures, i.e. their Miller indices (hkl) and their distance from the origin d_{hkl} . Figure C.2 shows these planes for the case of the *hut* and *dome* shape that were investigated in this work.

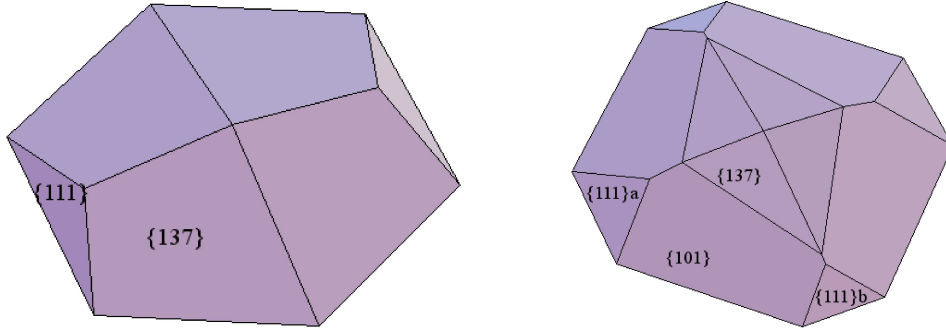


Abbildung C.2: Areas of QDs in *hut* (left) and *dome* (right) shape.

The corners of the involved QD facets are given by the intersections of the adjacent planes, and can be determined analytically by solving the set of linear equations defined by the plane equations. These points are then used to calculate the area of the corresponding surface, and one obtains, e.g. for the base area of the above *hut* and *dome* geometry:

$$A_{\text{base}}^{\text{hut}} = \frac{1}{2} \left(d_{001} - \sqrt{3}d_{111} \right)^2 + d_{001} \left(5\sqrt{3}d_{111} - 6d_{001} + \sqrt{59}d_{137} \right) + d_{111} \left(3d_{111} - \sqrt{177}d_{137} \right), \text{ and} \quad (\text{C.1})$$

$$A_{\text{base}}^{\text{dome}} = \left(\left(d_{001}^2 - 4\sqrt{2}d_{001}d_{101} + 8d_{101}^2 + 2\sqrt{3}d_{001}d_{111a} - 4\sqrt{6}d_{101}d_{111a} + 3d_{111a}^2 \right)^{1/2} + d_{001} - 2\sqrt{2}d_{101} + \sqrt{3}d_{111b} - 2\sqrt{2}d_{101} + \sqrt{3}(d_{111a} + d_{111b}) \right)^2 - \left(d_{001} - 2\sqrt{2}d_{101} + \sqrt{3}d_{111a} \right)^2 - \left(d_{001} - 2\sqrt{2}d_{101} + \sqrt{3}d_{111b} \right)^2. \quad (\text{C.2})$$

$$(\text{C.3})$$

Evaluating the expressions of all surfaces for a particular QD structure, i.e. for a particular choice of planes and distances from the origin, allows us to correct the error that the surface energies introduce to the total cohesive energy in lowest order.

Literaturverzeichnis

- [1] W. J. Schaffer, M. D. Lind, S. P. Kowalczyk, and R. W. Grant, *Nucleation and strain relaxation at the InAs/GaAs(100) heterojunction*, J. Vac. Sci. Technol. B **1**, 688 (1983).
- [2] L. Goldstein, F. Glas, M. N. Charasse J.-Y. Marzin, and G. LeRoux, *Growth by molecular beam epitaxy and characterization of InAs/GaAs strained-layer superlattices*, Appl. Phys. Lett. **47**, 1099 (1985).
- [3] O. Brandt, L. Tapfer, K. Ploog, R. Bierwolf, M. Hohenstein, F. Phillipp, H. Lage, and A. Heberle, *InAs quantum dots in a single-crystal GaAs matrix*, Phys. Rev. B **44**, 8043 (1991).
- [4] D. Leonard, M. Krishnamurthy, C. M. Reaves, S.P. Den Baars, and P. M. Petro, *Direct formation of quantum-sized dots from uniform coherent islands of InGaAs on GaAs surfaces*, Appl. Phys. Lett. **63**, 3203 (1993).
- [5] J. M. Moison, F. Houzay, F. Barthe, L. Leprince, E. André, and O. Vatel, *Self-organized growth of regular nanometer-scale InAs dots on GaAs*, Appl. Phys. Lett. **64**, 196 (1994).
- [6] J.-Y. Marzin, J.-M. Gérard, A. Izraël, D. Barrier, and G. Bastard, *Photoluminescence of single InAs quantum dots obtained by self-organized growth on GaAs*, Phys. Rev. Lett. **73**, 716 (1994).
- [7] M. Grundmann, J. Christen, N. N. Ledentsov, J. Böhrer, D. Bimberg, S. S. Ruvimov, P. Werner, U. Richter, U. Gösele, J. Heydenreich, V. M. Ustinov, A.Yu. Egorov, A. E. Zhukov, P. S. Kop'ev, and Zh. I. Alferov, *Ultrannarrow luminescence lines from single quantum dots*, Phys. Rev. Lett. **74**, 4043 (1995).
- [8] N. N. Ledentsov, V. M. Ustinov, A. Yu. Egorov, A. E. Zhukov, M. V. Maksimov, I. G. Tabatadze, , and P. S. Kop'ev, *Optical properties of heterostructures with InGaAs/GaAs quantum clusters*, Semiconductors **28**, 832 (1994).
- [9] C. Gobby, Z. L. Yuan, and A. J. Shields, *Quantum key distribution over 122 km of standard telecom fibre*, Appl. Phys. Lett **84**, 3762 (2004).

- [10] ARDA. *Solid state approaches to quantum information processing and quantum computing (V2.0)*. <http://qist.lanl.gov> (2004).
- [11] T. Maltezopoulos, A. Bolz, C. Meyer, C. Heyn, W. Hansen, M. Morgenstern, and R. Wiesendanger, *Wave-function mapping of InAs quantum dots by scanning tunneling spectroscopy*, Phys.Rev. Lett. **91**, 196804 (2003).
- [12] I. Vurgaftman, J. R. Meyer, and L. R. Ram-Mohan, *Band parameters for III-V compound semiconductors and their alloys*, J. App. Phys. **89**, 5815 (2001).
- [13] Blu ray Disc Association. <http://www.blu-raydisc.de>.
- [14] D. Bimberg, M. Grundmann, and N. N. Ledentsov, *Quantum Dot Heterostructures*, John Wiley & Sons, 1998.
- [15] M. Sugarawa, Ed., *Self-assembled InGaAs/GaAs quantum dots*, Academic Press, 1999.
- [16] V. A. Shchukin, N. N. Ledentsov, and D. Bimberg, *Epitaxy of nanostructures*, Springer Verlag, 2004.
- [17] J. Stangl, V. Hóly, and G. Bauer, *Structural properties of self-organized semiconductor nanostructures*, Rev. Mod. Phys. **76**, 725 (2004).
- [18] J. Márquez, L. Geelhaar, and K. Jaboci, *Atomically resolved structure of InAs quantum dots*, Appl. Phys. Lett. **78**, 2309 (2001).
- [19] G. Costantini, A. Rastelli, C. Manzano, R. Songmuang, O. G. Schmidt, K. Kern, and H. von Känel, *Universal shapes of self-organized semiconductor quantum dots: Striking similarities between InAs/GaAs(001) and Ge/Si(001)*, Appl. Phys. Lett. **85**, 5673 (2004).
- [20] H. Eisele, O. Flebbe, T. Kalka, F. Heinrichsdorff, A. Krost, D. Bimberg, and M. Dähne-Prietsch, *The stoichiometry of InAs quantum dots determined by cross-sectional scanning tunneling microscopy*, phys. stat. sol. (b) **215**, 865 (1999).
- [21] P. Offermans, P. M. Koenraad, J. H. Wolter, K. Pierz, M. Roy, and P. A. Maksym, *Atomic-scale structure and photoluminescence of InAs quantum dots in GaAs and AlAs*, Phys. Rev. B **72**, 165332 (2005).
- [22] J. Márquez, *Struktur von GaAs-Oberflächen und ihre Bedeutung für InAs-Quantenpunkte*. PhD thesis, TU Berlin, 12 2000.
- [23] K. Jacobi, *Atomic structure of InAs quantum dots on GaAs*, Prog. Surf. Sci. **71**, 185 (2003).

-
- [24] A. Di Carlo, *Microscopic theory of nanostructured semiconductor devices: beyond the envelope function-approach*, *Semicond. Sci. Technol.* **18**, R1 (2003).
- [25] R. Heitz, F. Guffarth, K. Pötschke, A. Schliwa, D. Bimberg, N. D. Zakharov, and P. Werner, *Shell-like formation of self-organized InAs/GaAs quantum dots*, *Phys. Rev. B* **71**, 045325 (2005).
- [26] G. E. Moore, *Cramming more components onto integrated circuits*, *Electronics* **38**, 8 (1965).
- [27] T. Hammerschmidt, A. Kersch, and P. Vogl, *Embedded Atom Simulations of Titanium Systems with Grain Boundaries*, *Phys. Rev. B* **71**, 205409 (2005).
- [28] P. Kratzer, and M. Scheffler, *Reaction-limited island nucleation in molecular beam epitaxy of compound semiconductors*, *Phys. Rev.Lett.* **88**, 036102 (2002).
- [29] K. Reuter, C. Stampfl, and M. Scheffler, *Ab initio atomistic thermodynamics and statistical mechanics of surface properties and functions*, In: *Handbook of Materials Modeling*, S. Yip, Ed. , Springer Verlag (2005).
- [30] G. Henkelman, G. Jóhannesson, and H. Jónsson. *Methods for Finding Saddle Points and Minimum Energy Paths*, 2000.
- [31] S. Boeck et al. <http://www.sfhingx.de>.
- [32] C. Priester, and M. Lannoo, *Origin of self-assembled quantum dots in highly mismatched heteroepitaxy*, *Phys. Rev. Lett.* **75**, 93 (1995).
- [33] N. Moll, M. Scheffler, and E. Pehlke, *Influence of stress on the equilibrium shape of strained quantum dots*, *Phys.Rev. B* **58**, 4566 (1998).
- [34] L. G. Wang, P. Kratzer, N. Moll, and M. Scheffler, *Formation and stability of self-assembled coherent islands in highly mismatched heteroepitaxy*, *Phys. Rev. Lett.* **82**, 4042 (1999).
- [35] X. Zhang, and P. Sharma, *Size dependency of strain in arbitrary shaped anisotropic embedded quantum dots due to nonlocal dispersive effects*, *Phys. Rev. B* **72**, 195345 (2005).
- [36] P. Kratzer, E. Penev, and M. Scheffler, *First-principles studies of kinetics in epitaxial growth of III-V semiconductors*, *Appl. Phys. A* **75**, 79 (2002).
- [37] J. Tersoff, and R. M. Tromp, *Shape transition in growth of strained islands: Spontaneous formation of quantum wires*, *Phys. Rev. Lett.* **70**, 2782 (1993).

- [38] V. A. Shchukin, N. N. Ledentsov, P. S. Kop'ev, and D. Bimberg, *Spontaneous ordering of arrays of coherently strained islands*, Phys. Rev. Lett. **75**, 2968 (1995).
- [39] I. Daruka, and A.-L. Barabási, *Dislocation-free island formation in heteroepitaxial growth: A study at equilibrium*, Phys. Rev. Lett. **79**, 3708 (1997).
- [40] E. Pehlke, N. Moll, A. Kley, and M. Scheffler, *Shape and stability of quantum dots*, Appl. Phys. A **65**, 525 (1997).
- [41] L. G. Wang, P. Kratzer, N. Moll, and M. Scheffler, *Size, shape, and stability of InAs quantum dots on the GaAs(001) substrate*, Phys. Rev. B **62**, 1897 (2000).
- [42] O. E. Shklyaeu, M. J. Beck, M. Asta, M. J. Miksis, and P. W. Voorhees, *Role of strain-dependent surface energies on Ge/Si(100) island formation*, Phys. Rev. Lett. **94**, 176102 (2005).
- [43] G.-H. Lu, and F. Liu, *Towards quantitative understanding of formation and stability of Ge hut islands on Si(001)*, Phys. Rev. Lett. **94**, 176103 (2005).
- [44] P. Kratzer, Q. K. K. Liu, P. Acosta-Diaz, C. Manzano, G. Costantini, R. Songmuang, A. Rastelli, O. G. Schmidt, and K. Kern, *Shape transition during epitaxial growth of InAs quantum dots on GaAs(001): Theory and experiment*, Phys. Rev. B **73**, 205347 (2006).
- [45] D. Bowler, R. Choudhury, M. J. Gillan, and T. Miyazaki, *Recent progress with large-scale ab initio calculations: The CONQUEST code*, phys. stat. sol. (b) **243**, 989 (2006).
- [46] M. C. Payne, M. P. Teter, D. C. Allen, T. A. Arias, and J. D. Joannopoulos, *Iterative minimization techniques for ab initio total-energy calculations: molecular dynamics and conjugate gradients*, Rev. Mod. Phys. **64**, 1045 (1992).
- [47] M. Bockstedte, A. Kley, J. Neugebauer, and M. Scheffler, *Density-functional theory calculations for poly-atomic systems: electronic structure, static and elastic properties and ab initio molecular dynamics*, Comp. Phys. Comm. **107**, 187 (1997).
- [48] W. Kohn, *An essay on condensed matter physics in the twentieth century*, Rev. Mod. Phys. **71**, 1253 (1998).
- [49] R. Jones, and P. R. Briddon, *Identification of Defects in Semiconductors, Semiconductors and Semimetals*, vol. 51, Academic Press, 1998.
- [50] R. G. Parr, and W. Yang, *Density-Functional Theory of Atoms and Molecules*, Oxford University Press, 1989.
- [51] R. M. Dreizler, and E. K. U. Gross, *Density Functional Theory*, Springer Verlag, 1990.

-
- [52] M. A. L. Marquez, and E. K. U. Gross, *Time-dependent density-functional theory*, Ann. Rev. Phys. Chem. **55**, 427 (2004).
- [53] M. Born, and R. Oppenheimer, *Zur Quantentheorie der Molekeln*, Ann. Phys. **84**, 457 (1927).
- [54] D. R. Hartree, *The wave mechanics of an atom with a non-Coulomb central field Part I. theory and methods*, Proc. Camb. Phil. Soc. **24**, 89 (1928).
- [55] V. Fock, *Näherungsmethode zur Lösung des quantenmechanischen Mehrkörperproblems*, Z. Phys. **61**, 126 (1930).
- [56] V. Fock, *'Selfconsistent field' mit Austausch für Natrium*, Z. Phys. **62**, 795 (1930).
- [57] G. Onida, L. Reining, and A. Rubio, *Electronic excitations: density-functional versus many-body Green's-function approaches*, Rev. Mod. Phys. **74**, 601 (2002).
- [58] P. Hohenberg, and W. Kohn, *Quantum density oscillations in an inhomogeneous electron gas*, Phys. Rev. **137**, A1697 (1965).
- [59] W. Kohn, and L. J. Sham, *Self-consistent equations including exchange and correlation effects*, Phys. Rev. **140**, 1133 (1965).
- [60] M. Fuchs, and M. Scheffler, *Ab initio pseudopotentials for electronic structure calculations of poly-atomic systems using density-functional theory*, Comp. Phys. Comm. **119**, 67 (1999).
- [61] S. G. Louie, S. Froyen, and M. L. Cohen, *Nonlinear ionic pseudopotentials in spin-density-functional calculations*, Phys. Rev. B **26**, 1758 (1982).
- [62] R. Feynman, *Forces in molecules*, Phys. Rev. **56**, 340 (1939).
- [63] P. Pulay, *Ab initio calculation of force constants and equilibrium geometries in polyatomic molecules. I. Theory*, Mol. Phys. **17**, 197 (1969).
- [64] P. Müller, and A. Saúl, *Elastic effects on surface physics*, Surf. Sci. Rep. **54**, 157 (2004).
- [65] F. Bechstedt, *Principles of surface physics*, 1st ed., Springer Verlag, 2003.
- [66] P. Ruggerone, C. Ratsch, and M. Scheffler, *Density functional theory of epitaxial growth of metals*, In: *"Growth and Properties of Ultrathin Epitaxial Layers"*, *The Chemical Physics of Solid Surfaces, Vol. 8*, D. A. King and D. P. Woodruff, Eds. , Elsevier Science (1997).
- [67] T. Fliessbach, *Statistische Physik*, 3rd ed., Spektrum Akademischer Verlag GmbH, 1999.

- [68] L. D. Landau, and E. M. Lifschitz, *Course on Theoretical Physics, vol. V: Statistical physics*, Pergamon Press, 1959.
- [69] G. Wulff, *On the question of speed of growth and dissolution of crystal surfaces*, Z. Kristallogr. **34**, 449 (1901).
- [70] M. von Laue, *Der Wulffsche Satz für die Gleichgewichtsform von Kristallen*, Z. Kristallogr. **105**, 124 (1944).
- [71] C. Herring, *Some theorems on the free energy of crystal surfaces*, Phys. Rev. **82**, 87 (1952).
- [72] L. Geelhaar, J. Márquez, P. Kratzer, and K. Jaboci, *GaAs(2 5 11): A new stable surface within the stereographic triangle.*, Phys. Rev. Lett. **86**, 3815 (2001).
- [73] R. Shuttleworth, *The surface tension of solids*, Proc. Phys. Soc. A **63**, 444 (1950).
- [74] E. Penev, *On the theory of surface diffusion in InAs/GaAs(001) heteroepitaxy*. PhD thesis, TU Berlin, 2002.
- [75] D. B. Migas, S. Cereda, F. Montalenti, and L. Miglio, *Electronic and elastic contributions in the enhanced stability of Ge(105) under compressive strain*, Surf. Sci. **556**, 121 (2004).
- [76] G.-H. Lu, M. Cuma, and F. Liu, *First-principles study of strain stabilization of Ge(105) facet on Si(001)*, Phys. Rev. B **72**, 125415 (2005).
- [77] E. Bauer, *Phänomenologische Theorie der Kristallabscheidung an Oberflächen. I*, Z. Kristallogr. **110**, 372 (1958).
- [78] F. C. Franck, and J. H. van der Merwe, *One dimensional dislocations. II. Misfitting monolayer and oriented overgrowth*, Proc. Roy. Soc. London Ser. A **198**, 216 (1949).
- [79] M. Volmer, and A. Weber, *Keimbildung in übersättigten Gebilden*, Z. Phys. Chem. **119**, 277 (1926).
- [80] I. N. Stranski, and L. Krastanov, *Zur Theorie der orientierten Abscheidung von Ionenkristallen aufeinander*, Sitzungsber. Akad. Wiss. Wien, Math.-naturwiss. Kl. II b **146**, 797 (1938).
- [81] F. J. Giessibl, *Advances in atomic force microscopy*, Rev. Mod. Phys. **75**, 949 (2003).
- [82] W. A. Hofer, A. S. Foster, and A. L. Shluger, *Theories of scanning probe microscopes at the atomic scale*, Rev. Mod. Phys. **75**, 1287 (2003).

-
- [83] G. P. Srivastava, J. L. Martins, and A. Zunger, *Atomic structure and ordering in semiconductor alloys*, Phys. Rev. B **31**, 2561 (1985).
- [84] I. V. Markov, *Crystal Growth for Beginners*, 1st ed., World Scientific, 1995.
- [85] D. E. Jesson, M. Kästner, and B. Voigtländer, *Direct observation of subcritical fluctuations during the formation of strained semiconductor islands*, Phys. Rev. Lett. **84**, 330 (2000).
- [86] P. Sutter, and M. G. Lagally, *Nucleationless three-dimensional island formation in low-misfit heteroepitaxy*, Phys. Rev. Lett. **84**, 4637 (2000).
- [87] R. M. Tromp, F. M. Ross, and M. C. Reuter, *Instability-driven SiGe island growth*, Phys. Rev. Lett. **84**, 4641 (2000).
- [88] L. D. Landau, and E. M. Lifschitz, *Course on Theoretical Physics, vol. VII: Elasticity Theory*, 4th ed., Pergamon Press, 1985.
- [89] G. Steinle-Neumann, and R. E. Cohen, *Comment on 'On the importance of the free energy for elasticity under pressure'*, J. Phys: Condens. Matter **16**, 8783 (2004).
- [90] L. Kleinman, *Deformation potentials in Si . I. Uniaxial strain*, Phys. Rev. **128**, 2614 (1962).
- [91] O. H. Nielsen, and R. M. Martin, *Quantum-mechanical theory of stress and force*, Phys. Rev. B **32**, 3780 (1985).
- [92] O. H. Nielsen, and R. M. Martin, *Stresses in semiconductors: Ab initio calculations on Si, Ge, and GaAs*, Phys. Rev. B **32**, 3792 (1985).
- [93] F. D. Murnaghan, *The compressibility of media under extreme pressures*, Proc. Nat. Acad. Sci. U.S.A. **30**, 244 (1944).
- [94] E. M. Fitzgerald, *Engineered substrates and their role in future microelectronics*, Mat. Sci. Eng. B **124**, 8 (2005).
- [95] Y. Temko, T. Suzuki, M. C. Xu, and K. Jacobi, *InAs quantum dots on the GaAs(-5-2-11)B surface*, Appl. Phys. Lett. **83**, 3680 (2003).
- [96] M. C. Xu, Y. Temko, T. Suzuki, and K. Jacobi, *Shape transition of self-assembled InAs quantum dots on GaAs(114)A*, Phys. Rev. B **71**, 075314 (2005).
- [97] P. M. Marcus, and F. Jona, *Strains in epitaxial films: The general case*, Phys. Rev. B **51**, 5263 (1995).

- [98] P. M. Marcus, *Epitaxial strain and epitaxial bending*, Surf. Sci. **366**, 219 (1996).
- [99] D. N. Lee, *Elastic properties of thin films of cubic systems*, Thin Sol. Films **434**, 183 (2003).
- [100] L. De Caro, and L. Tapfer, *Elastic lattice deformation of semiconductor heterostructures grown on arbitrarily oriented substrate surfaces*, Phys. Rev. B **48**, 2298 (1993).
- [101] K. Yang, T. Anan, and L. J. Schowalter, *Strain in pseudomorphic films grown on arbitrarily oriented substrates*, Appl. Phys. Lett. **65**, 2789 (1994).
- [102] J. F. Nye, *Physical Properties of Crystals*, Clarendon Press, 1957.
- [103] S. Wolfram, *The MATHEMATICA book*, 4th ed., Cambridge University Press, 1999.
- [104] C. Pryor, J. Kim, L. W. Wang, A. J. Williamson, and A. Zunger, *Comparison of two methods for describing the strain profiles in quantum dots*, J. Appl. Phys. **83**, 2548 (1998).
- [105] K.-H. Hellwege, Ed., *Landolt-Börnstein - Numeric Data and Functional Relationships in Science And Technology, volIII/17a: Semiconductors*, Springer Verlag, 1982.
- [106] P. Alippi, P. M. Marcus, and M. Scheffler, *Strained tetragonal states and Bain paths in metals*, Phys. Rev. Lett. **78**, 3892 (1997).
- [107] J. Dabrowski, E. Pehlke, and M. Scheffler, *Calculation of the surface stress anisotropy for the buckled Si(001)(1x2) and p(2x2) surfaces*, Phys. Rev. B **49**, 4790 (1994).
- [108] J. Dabrowski, E. Pehlke, and M. Scheffler, *Relation between the atomic structure and the surface-stress anisotropy: Calculations for the clean Si(001) surface*, J. Vac. Sci. Technol. B **12**, 2675 (1994).
- [109] E. Penev, P. Kratzer, and M. Scheffler, *Effect of strain on surface diffusion in semiconductor heteroepitaxy*, Phys. Rev. B **64**, 085491 (2001).
- [110] V. Cherepanov, and B. Voigtländer, *Influence of strain on diffusion at Ge(111) surfaces*, Appl. Phys. Lett. **81**, 4745 (2002).
- [111] B. D. Yu, and M. Scheffler, *Physical origin of exchange diffusion on fcc(100) metal surfaces*, Phys. Rev. B **56**, R15569 (1997).
- [112] L. E. Shilkrot, and D. J. Srolovitz, *Elastic field of a surface step: Atomistic simulations and anisotropic elastic theory*, Phys. Rev. B **53**, 11120 (1996).
- [113] V. A. Shchukin, and D. Bimberg, *Spontaneous ordering of nanostructures on crystal surfaces*, Rev. Mod. Phys. **71**, 1125 (1999).

-
- [114] A. J. Williamson, A. Zunger, and A. Cannen, *Prediction of strain-induced conduction-band minimum in embedded quantum dots*, Phys. Rev. B **57**, R4253 (1998).
- [115] O. Stier, M. Grundmann, and D. Bimberg, *Electronic and optical properties of strained quantum dots modeled by 8-band k - p -theory*, Phys. Rev. B **59**, 5688 (1999).
- [116] R. Santoprete, B. Koiller, R. B. Capaz, P. Kratzer, Q. K. K. Liu, and M. Scheffler, *Tight-binding study of the influence of the strain on the electronic properties of InAs GaAs quantum dots*, Phys. Rev. B **68**, 235311 (2003).
- [117] O. L. Lazarenkova, P. von Allman, F. Oyafuso, S. Lee, and G. Klimeck, *Effect of anharmonicity of the strain energy on band offsets in semiconductor nanostructures*, Appl. Phys. Lett. **85**, 8193 (2004).
- [118] R. Kunert, T. Hammerschmidt, P. Kratzer, and E. Schöll, *Strain field calculations of quantum dots — a comparison study of two methods*. ICPS proceedings, *in preparation*.
- [119] K. Portz, and A. A. Maradudin, *Surface contribution on the low-temperature specific heat of a cubic crystal*, Phys. Rev. B **16**, 3535 (1977).
- [120] A. G. Khachaturyan, *Theory of structural transformations in solids*, John Wiley & Sons, 1983.
- [121] V. A. Shchukin, D. Bimberg, V. G. Malyskin, and N. N. Ledentsov, *Vertical correlations and anticorrelations in multisheet arrays of two-dimensional islands*, Phys. Rev. B **57**, 12262 (1998).
- [122] V. Holý, G. Springholz, M. Pinczolit, and G. Bauer, *Strain induced vertical and lateral correlations in quantum dot superlattices*, Phys. Rev. Lett. **83**, 356 (1999).
- [123] M. Meixner, and E. Schöll, *Kinetically enhanced correlation and anti correlation effects in self-organized quantum dot stacks*, Phys. Rev. B **67**, 121202 (R) (2003).
- [124] P. N. Keating, *Effect of invariance requirements on the elastic strain energy of crystals with application to the diamond structure*, Phys. Rev. **145**, 637 (1966).
- [125] D. Frenkel, and B. J. Smit, *Understanding Molecular Simulation: From Algorithms to Applications*, 2nd ed., Academic Press, 2001.
- [126] A. E. Carlsson, *Beyond pair potentials in elemental transition metals and semiconductors*, Solid State Phys.: Adv. Res. Appl. **43**, 1 (1990).
- [127] P. M. Morse, *Diatomic molecules according to the wave mechanics. II. Vibrational levels*, Phys. Rev. **34**, 57 (1929).

- [128] M. S. Daw, S. M. Foiles, and M. I. Baskes, *The embedded-atom method: a review of theory and applications*, Mater. Sci. Rep. **9**, 251 (1993).
- [129] D. G. Pettifor, and I. I. Oleinik, *Analytic bond-order potentials beyond Tersoff-Brenner. I. Theory*, Phys. Rev. B **59**, 8487 (1999).
- [130] I. I. Oleinik, and D. G. Pettifor, *Analytic bond-order potentials beyond Tersoff-Brenner. II. Applications to the hydrocarbons*, Phys. Rev. B **59**, 8500 (1999).
- [131] I. J. Robertson, M. C. Payne, and V. Heine, *Multi-atom bonding in aluminum over a wide-range of coordination-number*, Euro. Phys. Lett. **15**, 301 (1991).
- [132] D.W. Brenner, *Relationship between the embedded-atom method and Tersoff potentials*, Phys. Rev. Lett. **63**, 1022 (1989).
- [133] G. C. Abell, and references therein, *Empirical chemical pseudopotential theory of molecular and metallic bonding*, Phys. Rev. B **31**, 6184 (1985).
- [134] J. Tersoff, *New empirical model for the structural properties of silicon*, Phys. Rev. Lett. **56**, 632 (1986).
- [135] J. Tersoff, *New empirical approach for the structure and energy of covalent systems*, Phys. Rev. B **37**, 6991 (1988).
- [136] J. Tersoff, *Empirical interatomic potential for silicon with improved elastic properties*, Phys. Rev. B **38**, 9902 (1988).
- [137] B.W. Dodson, *Development of many-body Tersoff-type potential for silicon*, Phys. Rev. B **35**, 2795 (1987).
- [138] J. Tersoff, *Modeling solid-state chemistry: Interatomic potentials for multicomponent systems*, Phys. Rev. B **39**, R5566 (1989).
- [139] D.W. Brenner, *Empirical potentials for hydrocarbon for use in simulating the chemical vapor deposition of diamond films*, Phys. Rev. B **42**, 9458 (1990).
- [140] D. G. Pettifor, *New many-body potential for the bond order*, Phys. Rev. Lett. **63**, 2489 (1989).
- [141] A. P. Sutton, M. W. Finnis, D. G. Pettifor, and Y. Ohta, *The tight-binding bond model*, J. Phys. C: Solid State Phys. **21**, 35 (1988).
- [142] J. C. Cressoni, and D. G. Pettifor, *Theory of structural trends within the sp bonded elements*, J. Phys.: Cond. Mat. **3**, 495 (1991).

-
- [143] P.A. Alinaghian, P. Gumbsch, A.J. Skinner, and D.G. Pettifor, *Bond-order potentials: a study of s- and sp-valent systems*, J. Phys.: Cond. Mat. **5**, 5795 (1993).
- [144] J. C. Slater, and G. F. Koster, *Simplified LCAO method for the periodic potential problem*, Phys. Rev. **94**, 1498 (1954).
- [145] R. Drautz, D. A. Murdick, D. Nguyen-Manh, X. W. Zhou, H. N. G. Wadley, and D. G. Pettifor, *Analytic bond-order potential for predicting structural trends across the sp-valent elements*, Phys. Rev. B **72**, 144105 (2005).
- [146] D. A. Murdick, X. W. Zhou, H. N. G. Wadley, D. Nguyen-Manh, R. Drautz, and D. G. Pettifor, *Analytic bond-order potential for the gallium arsenide system*, Phys. Rev. B **73**, 045206 (2005).
- [147] P. A. Ashu, J. H. Jefferson, A. G. Cullis, W. E. Hagston, and C. R. Whitehouse, *Molecular dynamics simulation of (100)InGaAs/GaAs strained-layer relaxation processes*, J. Cryst. Growth **150**, 176 (1995).
- [148] K. Albe, K. Nordlund, J. Nord, and A. Kuronen, *Modeling of compound semiconductors: Analytical bond-order potential for Ga, As, and GaAs*, Phys Rev B **66**, 035205 (2002).
- [149] M. A. Migliorato, A. G. Cullis, M. Fearn, and J. H. Jefferson, *Atomistic simulation of strain relaxation in $In_xGa_{1-x}As/GaAs$ quantum dots with nonuniform composition*, Phys. Rev. B **65**, 115316 (2002).
- [150] D. Conrad, and K. Scheerschmidt, *Empirical bond-order potential for semiconductors*, Phys. Rev. B **58**, 4538 (1998).
- [151] P. Alinaghian, S. Nishitani, and D. Pettifor, *Shear constants using angularly dependent bond order potentials*, Philos. Mag. B **69**, 889 (1994).
- [152] D. Pettifor, *Bonding and Structure of Molecules and Solids*, Oxford Science Publications, 1995.
- [153] W. H. Press, S. A. Teukolsky, W. T. Vetterling, and B. P. Flannery, *Numerical Recipes in F77: The Art of Scientific Computing*, 2nd ed., Cambridge University Press, 1992.
- [154] J. Donohue, *The Structure of Elements*, John Wiley & Sons, 1974.
- [155] L. Bosio, *Crystal-structures of Ga(II) and Ga(III)*, J. Chem. Phys. **68**, 1221 (1978).
- [156] N. Moll, A. Kley, E. Pehlke, and M. Scheffler, *GaAs equilibrium crystal shape from first principles*, Phys. Rev. B **54**, 8844 (1996).

- [157] A. Kley, P. Ruggerone, and M. Scheffler, *Novel diffusion mechanism on the GaAs(001) surface: The role of adatom-dimer interaction*, Phys. Rev. Lett. **79**, 5278 (1997).
- [158] J. Platen, A. Kley, C. Setzer, K. Jacobi, P. Ruggerone, and M. Scheffler, *The importance of high-index surfaces for the morphology of GaAs quantum dots*, J. Appl. Phys. **85**, 3597 (1999).
- [159] S.-H. Lee, W. Moritz, and M. Scheffler, *GaAs(001) surface under conditions of low As pressure: Evidence for a novel surface geometry*, Phys. Rev. Lett. **85**, 3890 (2000).
- [160] W. G. Schmidt, *III-V compound semiconductor (001) surfaces*, Appl. Phys. A **75**, 89 (2002).
- [161] R. Smith, *A semiempirical many-body interatomic potential for modeling dynamic processes in gallium-arsenide*, Nucl. Inst. and Meth. B **67**, 335 (1992).
- [162] M. Sayed, J. H. Jefferson, A. B. Walker, and A. G. Cullis, *Molecular dynamics simulations of implantation damage and recovery in semiconductors*, Nucl. Instr. and Meth. B **102**, 218 (1995).
- [163] K. Nordlund, J. Nord, J. Frantz, and J. Keinonen, *Strain-induced Kirkendall mixing at semiconductor interfaces*, Comput. Mater. Sci. **18**, 283 (2000).
- [164] H. J. Monkhorst, and J. D. Pack, *Special points for Brillouin-zone integrations*, Phys. Rev. B **13**, 5188 (1976).
- [165] L. Bellaiche, K. Kunc, M. Sauvage-Simkin, Y. Garreau, and R. Pinchaux, *Local aspects of the As stabilized 2×3 reconstructed (001) surface of strained $In_xGa_{1-x}As$ alloys: A first-principles study*, Phys. Rev. B **53**, 7417 (1996).
- [166] K. Shiraishi, *A new slab model approach for electronic structure calculations of polar semiconductor surface*, J. Phys. Soc. Jpn. **59**, 3455 (1990).
- [167] M. Bernasconi, G. L. Chiarotti, and E. Tosatti, *Ab initio calculations of structural and electronic properties of gallium solid-state phases*, Phys. Rev. B **52**, 9988 (1995).
- [168] L. F. Mattheiss, D. R. Hamann, and W. Weber, *Structural calculations for bulk As*, Phys. Rev. B **34**, 2190 (1986).
- [169] U. Häussermann, S. I. Simak, R. Ahuja, B. Johansson, and S. Lidin, *The origin of the distorted close-packed elemental structure of In*, Angew. Chem. Int. Ed. **38**, 2017 (1999).

-
- [170] M. J. Mehl, B. M. Klein, and D. A. Papaconstantopoulos, *First principles calculations of elastic properties of metals*, In: *Intermetallic Compounds: Principles and Practice, Vol I: Principles*, J. H. Westbrook and R. L. Fleischer, Eds. , John Wiley & Sons (1995).
- [171] C. Kittel, *Introduction to Solid State Physics*, Addison Wesley, 1985.
- [172] L. Pauling, *The nature of the chemical bond and the structure of molecules and crystals*, 3rd ed., Cornell Univ. Pr., 1960.
- [173] D. J. Dunslan, In: *Properties of GaAs*, M. R. Brozel and G. E. Stillmann, Eds. , 3rd ed., Inspec (1996).
- [174] C. N. Koumelis, and E. K. Rozis, *Internal strain of GaAs. I. Longitudinal case*, Acta Cryst. A **31**, 84 (1975).
- [175] C. N. Koumelis, and E. K. Rozis, *Internal strain of GaAs. I. Longitudinal case: erratum*, Acta Cryst. A **32**, 170 (1975).
- [176] R. M. Martin, *Elastic properties of ZnS structure semiconductors*, Phys. Rev. B **1**, 4005 (1970).
- [177] P. R. C. Kent, G. L. W. Hart, and A. Zunger, *Biaxial strain-modified valence and conduction band offsets of zinc-blende GaN, GaP, GaAs, InN, InP, and InAs, and optical bowing of strained epitaxial InGaN alloys*, Appl. Phys. Lett. **81**, 4377 (2002).
- [178] M. D. Frogley, J. R. Downes, and D. J. Dunstan, *Theory of the anomalously low band-gap pressure coefficients in strained-layer semiconductor alloys*, Phys. Rev. B **62**, 13612 (2000).
- [179] S. P. Lepkowski, and J. A. Majewski, *Pressure dependence of elastic constants in zinc-blende GaN and InN and their influence on the pressure coefficients of the light emission in cubic InGaN/GaN quantum wells*, Solid State Comm. **131**, 763 (2004).
- [180] V. Ovolins, C. Wolverton, and A. Zunger, *Effects of anharmonic strain on the phase stability of epitaxial films and superlattices: Applications to noble metals*, Phys. Rev. B **57**, 4816 (1997).
- [181] S. P. Lepkowski, J. A. Majewski, and G. Jurczak, *Nonlinear elasticity in III-N compounds: Ab initio calculations*, Phys. Rev. B **72**, 245201 (2005).
- [182] K. Shiraiishi, N. Oyama, K. Okajima, N. Miyagishima, K. Takeda, H. Yamaguchi, T. Ito, and T. Ohno, *First principles and macroscopic theories of semiconductor epitaxial growth*, J. Crystal Growth **237**, 206 (2002).
- [183] P. Kratzer. *unpublished*.

- [184] T. Suzuki, Y. Temko, and K. Jacobi, *Shape of InAs quantum dots grown on the GaAs($\bar{1}\bar{1}\bar{3}$)B surface*, Appl. Phys. Lett. **80**, 4744 (2002).
- [185] Z. M. Wang, H. Wen, V. R. Yazdanpanah, J. L. Shultz, and G. J. Salamo, *Strain-driven facet formation on self-assembled InAs islands on GaAs(311)A*, Appl. Phys. Lett. **82**, 1688 (2003).
- [186] Y. Temko, T. Suzuki, P. Kratzer, and K. Jacobi, *InAs quantum dots grown on the GaAs(113)A and GaAs($\bar{1}\bar{1}\bar{3}$)B surfaces: A comparative STM study*, Phys. Rev. B **68**, 165310 (2003).
- [187] P. Kratzer, E. Penev, and M. Scheffler, *Understanding the growth mechanisms of GaAs and InGaAs thin films by employing first-principles calculations*, Appl. Surf. Sci. **216**, 436 (2003).
- [188] D. A. Murdick, X. W. Zhou, and H. N. G. Wadley, *Assessment of interatomic potentials for molecular dynamics simulations of GaAs deposition*, Phys. Rev. B **72**, 205340 (2005).
- [189] M. A. Salmi, M. Alatalo, T. Ala-Nissila, and R. M. Nieminen, *Energetics and diffusion paths of gallium and arsenic adatoms on flat and stepped GaAs(001) surfaces*, Surf. Sci. **425**, 31 (1999).
- [190] J. A. Floro, E. Chason, R. D. Twisten, R. Q. Hwang, and L. B. Freund, *SiGe coherent islanding and stress relaxation in the high mobility regime*, Phys. Rev. Lett. **79**, 3946 (1997).
- [191] G. S. Soloman, J. S. Trezza, and Jr. J. S. Harris, *Effects of monolayer coverage, flux ratio, and growth rate on the island density of InAs islands on GaAs*, Appl. Phys. Lett. **66**, 3161 (1995).
- [192] G. Medeiros-Ribeiro, A. M. Bratkovski, T. I. Kamins, D. A. A. Ohlberg, and R. S. Williams, *Shape transition of Germanium nanocrystals on a Silicon(001) surface from pyramids to domes*, Science **279**, 353 (1998).
- [193] M. C. Xu, Y. Temko, T. Suzuki, and K. Jacobi, *Shape transition of InAs quantum dots on GaAs(001)*, J. Appl. Phys. **98**, 083525 (2005).
- [194] A. Ponchet, D. Lacombe, L. Durand, D. Alquier, and J.-M. Cardonna, *Elastic energy of strained islands: Contribution of the substrate as a function of the island aspect ratio and inter-island distance*, Appl. Phys. Lett. **72**, 2984 (1998).
- [195] U. Denker, A. Rastelli, M. Stoffel, J. Tersoff, G. Katsaros, G. Costantini, K. Kern, N. Y. Jin-Phillipp, D. E. Jesson, and O. G. Schmidt, *Lateral motion of SiGe islands driven by surface mediated alloying*, Phys. Rev. Lett. **94**, 216103 (2005).

-
- [196] M. Stoffel, A. Rastelli, S. Kiravittaya, and O. G. Schmidt, *Strain-mediated lateral SiGe island motion in single and stacked layers*, Phys. Rev. B **72**, 205411 (2005).
- [197] V. Y. Prinz, V. A. Seleznev, A. K. Gutakovsky, A. V. Chehovskiy, V. V. Preobrazhenskii, M. A. Putyato, and T. A. Gavrilova, *Free-standing and overgrown InGaAs/GaAs nanotubes, nanohelices and their arrays*, Physica E **6**, 828 (2000).
- [198] N. Moll, *Theorie der Form und Stabilität von Quantenpunkten auf III-V Halbleiter-Oberflächen*. PhD thesis, TU Berlin, 2002.
- [199] J. A. Floro, G. A. Lucadamo, E. Chason, L. B. Freund, M. Sinclair, R. D. Twisten, and R. Q. Hwang, *SiGe island shape transitions induced by elastic repulsion*, Phys. Rev. Lett. **80**, 4717 (1998).
- [200] I. Daruka, J. Tersoff, and A.-L. Barábasi, *Shape transition in growth of strained islands*, Phys. Rev. Lett. **82**, 2753 (1999).
- [201] M. Zinke-Allmang, L. C. Feldman, and L.H. Grabow, *Clustering on surfaces*, Surf. Sci. Rep. **16**, 377 (1992).
- [202] F. M. Ross, J. Tersoff, and R. M. Tromp, *Coarsening of self-assembled Ge quantum dots on Si(001)*, Phys. Rev. Lett. **80**, 984 (1998).
- [203] C. Manzano, *Scanning Tunneling Microscopy of self-organized semiconductor quantum dots*. PhD thesis, EPFL Lausanne, 2004.
- [204] K. Zhang, *Molecular beam epitaxy growth and structural property of self-assembled InAs quantum dots on GaAs*. PhD thesis, University of Hamburg, 8 2000.
- [205] K. Zhang, A. Foede, T. Schmidt, P. Sonntag, C. Heyn, G. Materlik, W. Hansen, and J. Falta, *X-ray interface characterization of buried InAs layers on GaAs(001)*, Phys. Stat. Sol. B **215**, 791 (1999).
- [206] T. Hammerschmidt, and P. Kratzer. Role of strain relaxation during different stages of InAs quantum dot growth. In *AIP Confer. Proc.: Physics of Semiconductors: 27th Int. Conf. on the Physics of Semiconductors (ICPS-27)* (2005), C. V. d. W. J. Menéndez, Ed. , vol. 772, American Institute of Physics, pp. 601–602.
- [207] A. Rastelli, M. Stoffel, J. Tersoff, G. S. Kar, and O. G. Schmidt, *Kinetic evolution and equilibrium morphology of strained islands*, Phys. Rev. Lett. **95**, 026103 (2005).
- [208] B. F. Lewis, T. C. Lee, F. J. Grunthaler, A. Madhukar, R. Fernandez, and J. Maserjian, *RHEED oscillation studies of MBE growth kinetics and lattice mismatch strain-induced effects during InGaAs growth on GaAs(100)*, J. Vac. Sci. Technol. B **2**, 491 (1984).

- [209] D. Loss, and D. P. Di Vencenzo, *Quantum computing with quantum dots*, Phys. Rev. A **57**, 120 (1998).
- [210] M. Bayer, P. Hawrylak, K. Hinzer, S. Farad, M. Korkusinski, Z. R. Wasilewski, O. Stern, and A. Forchel, *Coupling and entangling of quantum states in quantum dot molecules*, Science **291**, 451 (2001).
- [211] H. J. Krenner, M. Sabathil, E. C. Clark, E. Kress, D. Schuh, M. Bichler, G. Abstreiter, and J. J. Finley, *Direct observation of controlled coupling in an individual quantum dot molecule*, Phys. Rev. Lett. **94**, 057402 (2005).
- [212] R. S. Goldman, *Nanoprobng of semiconductor heterointerfaces: quantum dots, alloys and diffusion*, J. Phys. D: Appl. Phys. **37**, R163 (2004).
- [213] W. Wu, J. R. Tucker, G. S. Solomon, and Jr. J. S. Harris, *Atom-resolved scanning tunneling microscopy of vertically ordered InAs quantum dots*, Appl. Phys. Lett. **71**, 1083 (1997).
- [214] U. Denker, M. Stoffel, and O. G. Schmidt, *Quantitative evaluation of stress-field attenuation in stacks of self-assembled Ge islands*, Appl. Phys. Lett. **83**, 1432 (2003).
- [215] H. Heidemeyer, U. Denker, C. Müller, and O. G. Schmidt, *Morphology response to strain field interferences in stacks of highly ordered quantum dot arrays*, Phys. Rev. Lett. **91**, 196103 (2003).
- [216] A. J. Bennett, and R. Murray, *Nucleation and ripening of seeded InAs/GaAs quantum dots*, J. Crystal Growth **240**, 439 (2002).
- [217] M. Meixner, E. Schöll, V. A. Shchukin, and D. Bimberg, *Self-assembled quantum dots: Crossover from kinetically controlled to thermodynamically limited growth*, Phys. Rev. Lett. **87**, 236101 (2001).
- [218] S. Tan, P.-M. Lam, and J. C. S. Levy, *Monte-Carlo investigation of vertical correlations in self-organized multi-layer growth of islands*, Phys. A **303**, 105 (2002).
- [219] J. Tersoff, C. Teichert, and M. G. Lagally, *Self-organization in growth of quantum dot superlattices*, Phys. Rev. Lett. **76**, 1675 (1996).
- [220] I. Daruka, and A.-L. Barabási, *Molecular-dynamics investigation of the surface stress distribution in a Ge/Si quantum dot superlattice*, Phys. Rev. B **60**, R2150 (1999).
- [221] F. Heinrichsdorff, A. Krost, N. Kirstaedter, M.-H. Mao, M. Grundmann, D. Bimberg, A. O. Kosogov, and P. Werner, *InAs/GaAs quantum dots grown by metalorganic chemical vapor deposition*, Jpn. J. Appl. Phys. **36**, 4129 (1999).

-
- [222] H. Eisele, O. Flebbe, T. Kalka, C. Preinesberger, F. Heinrichsdorff, A. Krost, D. Bimberg, and M. Dähne-Prietsch, *Cross-sectional scanning-tunneling microscopy of stacked InAs quantum dots*, Appl. Phys. Lett. **75**, 106 (1999).
- [223] N. Liu, J. Tersoff, O. Baklenov, A. L. Holmes Jr., and C. K. Shih, *Nonuniform composition profile in In_{0.5}Ga_{0.5}As alloy quantum dots*, Phys. Rev. Lett. **84**, 334 (2000).
- [224] A. Lenz, H. Eisele, R. Timm, S. K. Becker, R. L. Sellin, U. Pohl, D. Bimberg, and M. Dähne, *Nanovoids in InGaAs/GaAs quantum dots observed by cross-sectional scanning tunneling microscopy*, Appl. Phys. Lett. **85**, 3848 (2004).
- [225] D. Zhi, H. Davock, R. Murray, C. Roberts, T. S. Jones, D. W. Pashley, P.J. Goodhew, and B. A. Joyce, *Quantitative compositional analysis of InAs/GaAs quantum dots by scanning transmission electron microscopy*, J. Appl. Phys. **8**, 2079 (2001).
- [226] L. G. Wang, P. Kratzer, M. Scheffler, and Q. K. K. Liu, *Island dissolution during capping layer growth interruption*, Appl. Phys. A **72**, 161 (2001).
- [227] G. Springholz, M. Pinczolits, P. Mayer, V. Holý, G. Bauer, H. H. Kang, and L. Salamanca Riba, *Tuning of vertical and lateral correlations in self-organized PbSe/Pb_{1-x}Eu_xTe quantum dot superlattices*, Phys. Rev. Lett. **84**, 4669 (2000).
- [228] Q. Xie, A. Madhukar, P. Chen, and N. P. Kobayashi, *Vertically self-organized InAs quantum box islands on GaAs(100)*, Phys. Rev. Lett. **75**, 2542 (1995).
- [229] X.-D. Wang, N. Liu, C. K. Shih, S. Govindaraju, and Jr. A. L. Holmes, *Spatial correlation-anticorrelation in strain-driven self-assembled InGaAs quantum dots*, Appl. Phys. Lett. **85**, 1356 (2004).
- [230] J. P. Perdew, K. Burke, and M. Enzerhof, *Generalized gradient approximation made simple*, Phys. Rev. Lett. **77**, 3865 (1996).
- [231] M. D. Pashley, *Electron counting model and its application to island structures on molecular-beam epitaxy grown GaAs(001) and ZnSe(001) surfaces*, Phys. Rev. B **40**, 10481 (1989).
- [232] G.-M. Rignanese, P. Ghosez, J.-C. Charlier, J.-P. Michenaud, and X. Gonze, *Scaling hypothesis for corrections to total energy and stress in plane-wave-based ab initio calculations*, Phys. Rev. B **52**, 8160 (1995).

Publications and Presentations

Publications

- R. Kunert, E. Schöll, T. Hammerschmidt, and P. Kratzer, *Strain field calculations of quantum dots — a comparison study of two methods*, ICPS proceedings, submitted
- T. Hammerschmidt, P. Kratzer, and M. Scheffler, *Quantitative Atomistic Investigation of Correlations in Stacked InAs/GaAs Quantum Dot Arrays: Role of the Critical Nucleus*, in preparation
- T. Hammerschmidt, P. Kratzer, and M. Scheffler, *Thermodynamic Shape-Stability of InAs Quantum Dots on GaAs(001) by Atomistic Investigations*, in preparation
- T. Hammerschmidt, P. Kratzer, and M. Scheffler, *General Expressions for Linear Elastic Response of Cubic Crystals upon Biaxial Strain and ab-initio Calculations of Non-Linear Contributions for InAs*, in preparation
- T. Hammerschmidt, P. Kratzer, and M. Scheffler, *Analytic Many-Body Potential for the Investigation of InAs/GaAs Surfaces and Nanostructures: Application to Elastic Interactions in Arrays of InAs Quantum-Dots*, in preparation
- 2005 T. Hammerschmidt, A. Kersch, and P. Vogl, *Embedded Atom Simulations of Titanium Systems with Grain Boundaries*, Phys. Rev. B **71**, 205409, (2005)
- 2004 T. Hammerschmidt, and P. Kratzer, *Role of Strain Relaxation during Different Stages of InAs Quantum Dot Growth*, In: Physics of Semiconductors: 27th Int. Conf. on the Physics of Semiconductors (ICPS-27). (Eds.) J. Menéndez, C.G. Van de Walle. AIP Confer. Proc. **772**. American Institute of Physics 2005, 601-602. ISBN 0-7354-0257-4.
- 2003 S.Boeck, A. Dick, C. Freysoldt, F. Grzegozewski, T. Hammerschmidt, L. Ismer, L. Lymperakis, M. Wahn, and J. Neugebauer, *SFHingX, User's Guide*
- 2001 T. Hammerschmidt, *Atomistic growth simulations of Titanium thin films and grains*, Annual Report 2001 Walter-Schottky-Institute, Technical University of Munich

Presentations

- 03/2006 German Physical Society Spring Meeting in Dresden, Germany. Talk: *Understanding Growth of InAs/GaAs Quantum Dot Nanostructures in Atomic Detail*
- 03/2006 American Physical Society March Meeting 2006 in Baltimore, Maryland, U.S.A, Talk: *Atomic-Scale Modeling of Shape Stability-Regimes and Stacking in InAs/GaAs Quantum Dot Nanostructures*
- 11/2005 SANDiE (Network of Excellence) workshop: Characterization and Modeling of Self-assembled Semiconductor Nanostructures, Eindhoven, Netherlands. Talk: *Understanding Growth of InAs/GaAs Quantum Dot Nanostructures in Atomistic Detail*
- 10/2005 IPAM Long Program: Bridging Time and Length Scales in Materials Science and Biophysics, Materials Modeling Seminar, UCLA, Los Angeles, USA. Invited Talk: *Growth Properties of InAs/GaAs Nanostructures studied with a DFT derived Many-Body Potential*
- 09/2005 Psi-k 2005, Schwäbisch Gmünd, Germany. Talk: *Growth Properties of InAs/GaAs Nanostructures studied with a DFT derived Many-Body Potential*
- 09/2005 European Conference on Surface Science (ECOSS-23) in Berlin, Germany. Talk: *Atomistic Investigation of InAs Quantum Dots at Different Growth Stages*
- 04/2005 Workshop *Probing Potential Energy Surfaces (PPES-III)* in Zermatt, Switzerland. Invited talk: *Empirical Potentials: From Quantum Mechanics to Quantum Dots*
- 03/2005 German Physical Society Spring Meeting in Berlin, Germany. Talk: *Atomistic Investigation of InAs Quantum Dots at Different Growth Stages*
- 02/2005 Theory Seminar of the Fritz-Haber-Institute. Invited talk: *Empirical Potentials: From Quantum Mechanics to Quantum Dots*
- 09/2004 Conference on Computational Physics (CCP) in Genoa, Italy. Poster: *Investigation of Diffusion on Semiconductor Surfaces with the Dimer Method and an Empirical Potential*
- 07/2004 International Conference on the Physics of Semiconductors (ICPS) in Flagstaff, USA. Poster: *Role of Strain Relaxation during Different Stages of InAs Quantum Dot Growth*
- 06/2004 CECAM workshop *Modeling of Self-Assembled Semiconductor Nano-Structures* in Lyon, France. Poster: *Investigation of Experimentally Observed InAs Quantum Dots with an Analytical Bond-Order Potential*

- 03/2004 German Physical Society Spring Meeting in Regensburg, Germany. Poster: *Investigation of Experimentally Observed InAs Quantum Dots with an Analytical Bond-Order Potential*
- 09/2003 Workshop *Modeling Statistics and Dynamics in Catalysis: From Ab-Initio Potentials to Rare Events* in Rottach-Egern, Germany. Poster: *Kinetic Effects in Quantum-Dot Growth: Preliminaries for a Multi-Scale Approach*
- 07/2003 Tutor at workshop *Application of Density-Functional Theory in Condensed-Matter Physics, Surface Physics, Chemistry, Engineering, and Biology* at FHI, Berlin
- 03/2003 German Physical Society Spring Meeting in Dresden, Germany. Poster: *A new InGaAs Bond-Order Potential for the Investigation of Kinetic Effects in Quantum-Dot Growth*
- 01/2003 Lecture series *Modern Concepts of Theoretical Physics - Nobel Prizes of the Last Decades*. Talk: *Bose-Einstein Condensation*
- 06/2002 European Materials Research Society (E-MRS) Spring Meeting in Strasbourg, France. Poster: *Embedded-Atom Simulation of Titanium-Growth including Grain-Boundaries*
- 05/2002 Joint Seminar of Inorganic Chemistry at ETH Zurich, Switzerland. Invited talk: *Multi-Scale Methods for Modeling Metal Growth*

Acknowledgments

This thesis was only possible with the help that so many people gave me during the past four years. I would like to gratefully acknowledge Prof. Dr. Matthias Scheffler for giving me the great opportunity to work at the Fritz-Haber-Institute and for his continuous support. The experience of this stimulating environment formed my notion of ideal scientific working conditions. I am deeply indebted to my supervisor Prof. Dr. Peter Kratzer for his untiring encouragement and guidance. He introduced me to the field of self-assembled nanostructures and was by my side through all problems and difficulties. Without his shining example of profound scientific work this thesis would not have been possible. I would also like to thank Prof. Dr. Ekehard Schöll and Prof. Dr. Mario Dähne for the supervision of my thesis at the Technical University of Berlin.

It is a pleasure to acknowledge my colleagues of the Theory Department for a wonderful working atmosphere, and particularly my office mate Mahbube Hortamani for her unbreakable good mood and the chance to gain insight into Persian culture. I would like to thank Evgeni Penev and Sladjana Stojkovic for giving me a perfect start at the FHI. A big *Thank you!* goes furthermore to Alexander Kleinsorge and Momme Winkelkemper for many discussions and the usage and further development of my code, to Andrei Schliwa for his tensor visualization tool, to Roland Kunert for our collaborative effort on strain tensors, to Bernhard Lehner for numerous debates about empirical potentials and their parameterization, to Maria Mignogna and Prof. Dr. Kristen Fichthorn for their engagement in applying our potential, and to the SFHIngX developer team, particularly Sixten Boeck, Alexej Dick, Lars Ismer, and Christoph Freysoldt for a great time in preparing the FHI 2003 workshop and the insight to electronic-structure calculations. This work strongly profited from funding of the SFB 296 of the German Science Foundation, the Wilhelm and Else Heraeus Foundation, the US National Science Foundation, and the European networks CECAM, Psi-K and SANDiE.

The nights in Berlin were much more enjoyable with Heidi Allende, Patrick Rinke, Jutta Rogal, Hendrik Braband, Miguel Márquez, and Jan Werschnik. I would also like to thank Hua Wu and Christian Bensch for very pleasant sessions of table tennis and no signs of mercy. I don't want to close without thanking my family for their unflinching support and my wife Franka for every single day.

Index

- Abell-Tersoff functional, 48
- Bain path, 39
- basis set, 19
- biaxial Poisson ratio, 37
- biaxial strain, 37
- Bloch's theorem, 18
- bond order, 48
- Born-Oppenheimer approximation, 13
- bulk modulus, 35

- continuum-elasticity theory, 32
- critical nucleus, 29, 119
- critical thickness, 28
- cutoff energy, 19

- density-functional theory, 14
- displacement vector, 32

- elastic anisotropy, 36
- elastic constants, 33
- elastic energy density, 34
- electron density, 14
- exchange energy, 14
- exchange-correlation energy, 16

- formation energy, 90
- Franck-van der Merwe growth, 28

- generalized-gradient approximation, 17
- GW approximation, 14

- Hartree-Fock theory, 13
- heat of formation, 25

- Hellmann-Feynman theorem, 21
- Hohenberg-Kohn theorem, 15
- Hooke's law, 33

- kinetic effect, 23
- Kleinman parameter, 34
- Kohn-Sham equations, 16
- Kohn-Sham formalism, 14

- Lennard-Jones potential, 51
- local-density approximation, 17

- Morse potential, 49
- Murnaghan equation, 36

- nucleation theory, 30

- Ostwald ripening, 97

- Pauling relation, 62
- Poisson ratio
 - biaxial strain, 37, 39
 - uniaxial strain, 36, 39
- potential-energy surface
 - adsorption, 82, 120
 - quantum dot stack, 111
- pseudo-potential theory, 20
- Pulay forces, 22

- quantum dot
 - critical nucleus, 104
 - dome shape, 94, 100, 138
 - hut shape, 94, 99, 138
 - isomorphic scaling, 98

- lateral elastic interaction, 93
- shape transition, 97, 102, 103
- stoichiometry, 101
- type I, II, 2

quantum dot stack, 108

Schrödinger equation, 12

self-consistent field, 16

Shuttleworth equation, 27

Slater determinant, 13

solution manifold, 50

stereographic triangle, 26

strain tensor, 33

Stranski-Krastanov growth, 28, 100

stress tensor, 33

supersaturation, 29

surface free energy, 25

surface phase-diagram, 26

Thomas-Fermi model, 14

Voigt notation, 33

Volmer-Weber growth, 28

wetting layer, 28, 90

Wulff plot, 26

Young modulus, 36